N° d'ordre 3267

THESE

En vue de l'obtention du : ***DOCTORAT***

Structure de Recherche : Laboratoire de la Matière Condensée et Sciences Interdisciplinaires
Discipline : Science de la Matière Physique (SMP)
Spécialité : Matière Condensée et Modélisation des Systèmes Énergétiques

Présentée et soutenue le 13/12/2019 par :

Zineb KERRAMI

Strained SnO_2

Properties and Applications as predicted by Density Functional Theory (DFT)

JURY

Hamid EZ-ZAHRAOUY	PES, Faculté des Sciences, Université Mohammed V-Rabat	Président
El Mustapha FEDDI	PES, ENSET, Université Mohammed V-Rabat	Rapporteur/Examinateur
Abdelkader KARA	PES, University of Central Florida, Orlando-USA	Rapporteur/Examinateur
Mohammed LOULIDI	PES, Faculté des Sciences, Université Mohammed V-Rabat	Rapporteur/Examinateur
Abdelilah BENYOUSSEF	PES, Académie Hassan II des Sciences et Techniques-Rabat	Examinateur
Omar MOUNKACHI	PA, Faculté des Sciences, Université Mohammed V-Rabat	Invité
Ari Paavo SEITSONEN	Docteur, École Normale Supérieure, Paris-France	Invité
Mohammed BENAISSA	PES, Faculté des Sciences, Université Mohammed V-Rabat	Directeur de thèse

Année Universitaire : **2019/2020**

ACKNOWLEDGEMENTS

The present thesis was carried out in the Laboratory of Condensed Matter and Interdisciplinary Sciences (LaMCScI) of Faculty of Sciences, University of Mohammed V in Rabat, Morocco, under the supervision of Prof. **Mohammed BENAISSA**.

First, and foremost, I would like to express my sincere gratitude and great appreciation to my supervisor, **Mohammed BENAISSA**, for giving me the opportunity to do this work as well as for his continuous support of my Ph.D. study, and related research, for his patience, motivation, and immense knowledge. During these years, I learned a lot about modern condensed matter physics and computer simulations as a powerful and a highly efficient tool to solve physical problems. My supervisor has provided enormous amounts of scientific guidance, invaluable advice and a critical scientific outlook. I am also thankful for encouraging me to attend numerous trainings, conferences, workshops and tutorials.

I would also thank the thesis committee for reviewing my work and giving their insightful and useful comments. It is an honor for me that they agree to judge this work.

I would like to express my thanks to Prof. **Hamid EZ-ZAHRAOUY**, from University Mohammed V-Rabat, Faculty of Science, for having accepted to be the chair of the jury members of the present thesis.

I would like to offer my thanks to Prof. **El Mustapha FEDDI** from, ENSET, Mohammed V University of Rabat, for reporting and reviewing my Ph.D. thesis.

I would like to thank Prof. **Abdelkader KARA** from University of Central Florida, for reporting and reviewing this Ph.D. thesis.

I would like also to thank Prof. **Mohammed LOULIDI** from Faculty of Science, University Mohammed V of Rabat, for reporting and reviewing my Ph.D. thesis.

I would like also to thank Prof. **Abdelilah BENYOUSSEF** from Hassan II Academy of sciences and techniques in Rabat**,** for reviewing my Ph.D. thesis.

I would like to thank Prof. **Omar MOUNKACHI** from Faculty of Science, University Mohammed V of Rabat, for reviewing my Ph.D. thesis. In addition, I would like to take this opportunity to express my appreciations and sincere gratitude to Prof. **Omar MOUNKACHI** who gave me the first guidance to the present research work, as my Master's supervisor. Also, I would like to thank him for his advises, comments, and his interesting and valuable scientific discussions that helped me a lot while working on my research.

I would like to thank Dr. **Ari Paavo SEITSONEN** from École Normale Supérieure de Paris, for reviewing this Ph.D. thesis.

I would like to thank all old and new members of the Laboratory of Condensed Matter and Interdisciplinary Sciences (LaMCScI). In particular, I am very grateful to my colleague Mr. **Anass SIBARI** with whom I shared beneficious discussions while working on my research.

Finally, my deep gratitude goes to my parents for their emotional, personal and financial supports and encouragements, to my brothers and sister, to my friends and everyone who helped and supported me in any way during my Ph.D. studies.

ABSTRACT

The present thesis has been devoted to the theoretical study of strained SnO_2 properties and its applications. Therefore, we employed a computational strategy, using Density Functional Theory (DFT), to modulate the energy band structure of SnO_2 by applying biaxial strain on its *ab* plane aiming to improve its suitability for thermoelectric conversion, electrochemical water splitting, and Carbon Monoxide (CO) sensing. The structural deformation together with changed interatomic distances caused by an applied strain leads directly to the variation of energy band structure.

The modulation of energy band structure presents the key source of the variation of the optical and transport properties of SnO_2. Indeed, we found that under a compressive strain, a wider bandgap results in an increased Seebeck coefficient, while under tensile strain, the electrical and thermal conductivities increase due to a narrowed bandgap. This interplay leads to a variation of the figure of merit under strain that reaches its highest value under compression at temperatures below 400 K. Furthermore, a narrowed bandgap under tensile strain induces visible-light absorption and charge carrier's mobility of SnO_2. Although, in order to adjust band edges positions relative to the water redox levels, compressive strain for pH $\geq$ 7 or larger pH value (pH $\geq$ 10) are needed. Moreover, under tensile strain, the weakening of the Sn–O bond at the surface enhance the adsorption energy and the charge transfer, which may facilitate SnO_2 interaction with CO molecule. Further, we found that tensile-strained (101) SnO_2 surface induce the highest charge transfer with CO molecule.

Keywords: Strain engineering; SnO_2; DFT; Thermoelectric conversion; Electrochemical water splitting; Hydrogen production; CO sensing.

RÉSUMÉ

La présente thèse a été dédiée à l'étude théorique des propriétés du SnO_2 sous contrainte et ses applications. Cela étant, nous avons utilisé des méthodes de calcul se basant sut la théorie de la densité fonctionnelle (DFT), pour moduler la structure de bande de SnO_2 en appliquant une contrainte biaxiale sur son plan *ab* visant à améliorer sa performance à la conversion thermoélectrique, décomposition de l'eau, et détection de carbone monoxyde. La déformation structurelle provoquée par une contrainte appliquée conduit directement à la variation de la structure de bande.

La modulation de structure de bande est la source principale de la variation des propriétés physiques du SnO_2. En effet, nous avons constaté que sous compression, une bande interdite plus large entraîne une augmentation du coefficient de Seebeck, alors que sous dilatation, les conductivités électriques et thermiques augmentent à cause d'une bande interdite réduite. Cet enjeu entraîne une variation du facteur de mérite sous contrainte qui atteint sa valeur supérieure en compression pour des températures inférieures à 400 K. De plus, un gap réduit sous traction induit l'absorption de la lumière visible et augmente la mobilité des porteurs des charges. Bien que, pour ajuster les niveaux énergétiques de la structure de bande relatifs aux niveaux d'oxydo-réduction de l'eau, une contrainte de compression pour $pH \geq 7$ ou une valeur de pH supérieure ($pH \geq 10$) est nécessaire. De plus, sous effet de tension, l'affaiblissement de la liaison Sn–O au niveau de la surface améliore l'énergie d'adsorption et le transfert de charge, ce qui peut faciliter l'interaction de SnO_2 avec la molécule CO.

Mots-clés : Contraintes mécaniques; SnO_2; DFT; Conversion thermoélectrique; Décomposition électrochimique de l'eau; Production d'hydrogène; Carbone Monoxyde (CO).

RÉSUMÉ DÉTAILLÉ

Dans la présente thèse nous avons étudié les propriétés du SnO_2 sous contrainte et ses applications en se basant sur des méthodes de calcul théoriques. En fait, l'ingénierie par contraintes mécaniques des propriétés physiques des matériaux a été l'objet d'intérêt des recherches scientifiques comme l'une des stratégies les plus utilisées pour moduler la structure de bande des semi-conducteurs. Les contraintes mécaniques peuvent être induites par plusieurs expériences telles que l'étirement piézoélectrique, la croissance et le dépôt par épitaxie, et dilatation thermique, durant lesquelles, les modifications structuralles provoquées conduisent au changement des distances interatomiques et bien sûr à la distribution de charge ce qui cause directement une variation des niveaux énergétiques de la structure de bande. Cela étant, nous avons utilisé des méthodes de calculs se basant sur la théorie de la densité fonctionnelle (DFT), pour moduler la structure de bande de SnO_2 en appliquant une contrainte biaxiale sur son plan *ab* visant à améliorer ses propriétés pour conversion thermoélectrique, décomposition électrochimique de l'eau, et détection de monoxyde de carbone.

Nous avons commencé par étudier l'effet combiné de la contrainte et de la taille sur les propriétés électroniques du SnO_2. En effet, nos résultats montrent que, sous contrainte de traction, la longueur de la liaison Sn-O augmente, ce qui conduit à un affaiblissement de l'hybridation des états O-p et Sn-s dans la bande de conduction, ce qui entraîne une diminution de l'énergie de la bande interdite. Tandis que sous contrainte de compression, un comportement opposé a été observé. D'autre part, la bande interdite diminue quand l'épaisseur des couches de SnO_2 augmente, à cause de l'effet du confinement quantique.

Grace aux changements observés au niveau de structure de bande et bande interdite, les propriétés physiques du SnO_2 ont été aussi influencées. En effet, concernant les propriétés de transport, nous avons constaté que la contrainte de compression entraîne une augmentation de la masse effective à cause de l'augmentation de la bande interdite ce qui entraîne une augmentation du coefficient de Seebeck, alors que par effet de traction, une bande interdite réduite entraîne diminution du coefficient de Seebeck à cause de la masse effective diminué. Les conductivités électriques et thermiques augmentent à cause d'une mobilité des porteurs des charges augmentés à cause d'une bande interdite réduite. Cet enjeu entraîne entre le coefficient de Seebeck, conductivité électriques, et thermiques entraine une variation du facteur de mérite (ZT) sous contrainte qui atteint sa valeur supérieure en compression pour des températures inférieures à 400 K.

À propos les propriétés photo-catalytiques du SnO_2 sous contraintes, nos résultats montrent qu'une bande interdite réduite sous traction semble d'entrainer une augmentation de l'absorption de la lumière visible et de la mobilité des porteurs des charges. Bien que, pour ajuster les niveaux énergétiques de la structure de bande relatifs aux niveaux d'oxydo-réduction de l'eau (H_2O/H_2), une contrainte de compression pour $pH \geq 7$ ou une valeur de pH supérieure ($pH \geq 10$) est nécessaire. Ces résultats sont d'un grand bénéfice pour SnO_2 afin d'élargir son application photo-catalytique.

Au sujet de la détection de la molécule CO par les surfaces (110), (101), et (100) du SnO_2, nos résultats montrent que la contrainte de traction qui affaiblie les liaisons interatomiques à la surface, entraine une diminution de la densité des charges au niveau de surface et augmente le transfert de charge entre molécule et surface, ce qui facilite l'adsorption de CO sur les sites actifs de la surface. En outre, nous avons constaté que la surface (101) contrainte de SnO_2 induisait le transfert de charge le plus élevé avec la molécule CO à cause de sa morphologie structurelle et faible liaison Sn-O à la surface. D'après nos résultats la contrainte de traction a servi d'améliorer l'interaction entre les surfaces du SnO_2 et la molécule CO, et alors, la détection de CO par SnO_2.

En conclusion, d'après les résultats présentés en cette étude, nous avons démontré la capabilité des contraintes mécaniques à ajuster la structure de la bande du SnO_2 et améliorer ses propriétés physiques pour les applications thermoélectriques, photo-catalytiques, et détection des gaz toxiques.

TABLE OF CONTENTS

LIST OF FIGURES

LIST OF TABLES

LIST OF ABREVIATIONS

2D	Two Dimensional
APW	**A**ugmented **P**lane **W**ave
BO	**B**orn-**O**ppenheimer
CBM	**C**onduction **B**and **M**inimum
COPD	**C**hronic **O**bstructive **P**ulmonary **D**isease
DFT	**D**ensity **F**unctional **T**heory
DNA	**D**eoxyribo-**N**ucleic **A**cid
DOS	**D**ensity **o**f **S**tates
DSSC	**D**ye **S**ensitized **S**olar **C**ell
EA	**E**lectron **A**ffinity
$\mathbf{E_{ads}}$	Adsorption Energy
FP	**F**ull **P**otential
FTO	**F**luorine **T**in **O**xide
GGA	**G**eneralized **G**radient **A**pproximation
HER	**H**ydrogen **E**volution **R**eaction
HF	**H**artree-**F**ock
HK	**H**ohenberg-**K**ohn
HPC	**H**igh **P**erformance **C**omputers
IE	**I**onization **E**nergy
IHME	**I**nstitute for **H**ealth **M**etrics and **E**valuation
ITO	**I**ndium **T**in **O**xide
KS	**K**ohn-**S**ham
LAPW	**L**inearized **A**ugmented **P**lane **W**ave
LDA	**L**ocal **D**ensity **A**pproximation
LDA+U	**Hu**bbard corrected **L**ocal **D**ensity **A**pproximation
LEDs	**L**ight **E**mitting **D**iodes
LIB	**L**i-**I**on **B**atteries
mBJ	**m**odified **B**ecke-**J**ohnson
MC	**M**onte **C**arlo
MD	**M**olecular **D**ynamics
MOS	**M**etal **O**xide**S**emiconductor
MOSFET	**M**etal **O**xide **S**emiconductor **F**ield-**E**ffect **T**ransistor
MOx	**M**etal **O**xides
NHE	**N**ormal **H**ydrogen **E**lectrode
PAW	**P**rojector **A**ugmented **W**ave
PBE	**P**erdew−**B**urke−**E**rnzerhof
PEC	**P**hoto-**E**lectro**C**hemical
PFM	**P**hase-**F**ield **M**ethod
QD	**Q**uantum **D**ot
QE	**Q**uantum **E**SPRESSO
QM	**Q**uantum **M**echanics
RTG	**R**adioisotope **T**hermoelectric **G**enerators
$\mathbf{SnO_2}$	Tin Oxide
TCO	**T**ransparent **C**onductive **O**xide
TF	**T**homas-**F**ermi
TMDs	**T**ransition **M**etal **D**ichalcogenides
VASP	**V**ienna **A**b initio **S**imulation **P**ackage
VBM	**V**alence **B**and **M**aximum
WHO	**W**orld **H**ealth **O**rganization
XC	**E**xchange-**C**orrelation

GENERAL INTRODUCTION

People on the earth gets most of its power from fossil fuels that are very harmful to the environment and human health. As a key part of the current global strategy, especially since the general awareness of increased environment pollution, climate change and global warming, urgent demand for clean and renewable energy sources, and effective monitoring systems to supervise and control air quality have been generated [1,2]. Therefore, a great deal of research and effort has been placed in solar energy conversion and toxic gas monitoring devices.

In fact, thermoelectric applications present one of the important aspects of clean energy sources as they have the ability to convert waste heat to an electric voltage [3]. However, the industry of these applications is still dominated by a large variety of intermetallic materials, such as (Sb_2Te_3) [4] and (Bi_2Te_3) [5] known by their toxic character and high cost, then, an alternative material is needed for long-term development of the thermoelectric generators. Moreover, photocatalysis presents another environment-friendly application that has recently seen a growing interest within researchers as it serves in the most promising technologies in water treatment and energy harvesting such as pollutants degradation, and hydrogen production [6-8]. Until now, TiO_2 was the most intensively used and studied photo-catalyst semiconductor combining several optimistic features [9-11]. Nevertheless, the fast recombination of the photo-generated electron/hole due to its low electron mobility (~1 $cm^2\ V^{-1}\ s^{-1}$) represents a serious obstruction for its efficiency [12,13]. Furthermore, gas sensing is becoming more and more an important application to ensure maximum safety for environment and human life. Therefore, a huge scientific interest has been dedicated to develop effective gas sensing devices. However, a transition from the understanding of the electronic interaction at the surface-molecule level to the actual improvement of sensing devices is still under study.

The scientists' interest and effort have been dedicated to develop advanced materials that combine both non-toxicity and high performance for the three discussed applications earlier. Tin oxide (SnO_2) presents a serious option due to its non-toxicity, low cost, and outstanding properties such as its high electron mobility (~200-250 $cm^2\ V^{-1}\ s^{-1}$) and high electron transfer efficiency [13,14]. However, its application has strong obstructions. Indeed, the wide band gap of SnO_2 i.e. 3.6 eV [15] inhibits its visible light absorption, which presents a serious limitation in sunlight conversion devices. Furthermore, SnO_2 application for thermoelectric conversion is limited due to its high thermal conductivity (i.e. $\gtrsim 40\ W\ m^{-1}\ K^{-1}$) compared to those of conventional thermoelectric materials [16,17]. In addition, the energy

band structure of SnO_2 did not match the redox potentials of water (H_2O), which presents another limitation for its application for photocatalytic water splitting and H_2 production. Many researchers have proposed solutions such as nano-structuring and doping in order to modulate SnO_2 band structure and enhance its applicability [18–20], however, its application is very limited so far.

Since it was discovered by Bardeen and Shockley in 1950 [21], that mechanical deformations induce important changes in materials properties, and further demonstrated by Welser et al. in 1992 that n-channel MOSFETs on a strained Si substrate exhibit a 70% higher effective mobility than those on unstrained substrates [22,23], strain engineering has became a successful strategy in modulating band structure and electronic properties for semiconductors in the majority of energy conversion applications [24–26]. Strain may be induced using experimental techniques that affect the electronic properties through the change on the interatomic bonding, lattice parameters and angles, such as piezoelectric stretching [27], epitaxial growth and deposition [28], and thermal expansion mismatch [29–31]. Previous reports have reported the effect of strain on the electronic properties of many materials. For example, Bissett et al. [32] demonstrated the effect of mechanical strain on 2D materials properties and its ability to alter their behavior. Further, Yan et al. [33] reported the strain effects on the electronic band structure of the group-III nitrides (AlN, GaN, and InN) grown in various orientations. In addition, Dhakal et al. [34] reported modified electronic properties of Transition Metal Dichalcogenides (TMDs) multilayer films through strain engineering via creating wrinkle structures in the range of 0-2%. In addition, previous experimental and computational reports have addressed the effect of strain on SnO_2 properties in order to enhance its applicability [35,36].

In the present thesis, we performed a computational study of strained SnO_2 properties. In fact, amongst the popular computational methods, Density Functional Theory (DFT) is considered as an accurate choice for electronic structure calculations. Therefore, we employed computational modeling and simulation methods within DFT in order to modulate the energy band structure of SnO_2 by applying a biaxial strain on it *ab* plane.

This thesis is organized as follows: First, in chapter I we provided a detailed bibliography of SnO_2 properties and applications. After, Chapter II offers detailed Quantum Mechanics (QM) and Density Functional Theory (DFT) basics to introduce and provide the necessary background of the computational methods for the calculations that have been performed in the following chapters. Then, the electronic properties of SnO_2 under strain and size combined-effect are presented and discussed in Chapter III. Next, Chapter IV presents enhanced thermoelectric properties of strained SnO_2 in its bulk state over a wide range of temperatures. In Chapter V we presented adjusted band energy of SnO_2 thin-films related to the redox potential level of water H_2O/H_2. In Chapter VI a comparative study of Carbon Monoxide (CO) adsorption on strained SnO2 surfaces have been discussed. Finally, a general conclusion addressing our important findings is presented.

CHAPTER I: GENERAL ASPECTS OF TIN OXIDE: PROPERTIES, APPLICATIONS, AND LIMITATIONS

Table of contents

CHAPTER I: GENERAL ASPECTS OF TIN OXIDE: PROPERTIES, APPLICATIONS, AND LIMITATIONS

I.1 Tin Oxide (SnO2)

Tin oxide is a Transparent Conductive Oxide (TCO) with the molecular formula SnO_2. It has attracted much attention in recent decades because of its unique and hugely useful properties for many applications such as gas sensing, optoelectronic and photocatalytic applications. Besides, its availability, low cost, purity and chemical and physical stability present promising qualities. SnO_2 is an n-type semiconductor with a large band gap of 3.6 eV [37]. Such large band gap presents an advantage in some applications and limitations in others depending on the application and its requirements.

I.1.1 Structural properties

SnO_2 possesses several polymorphs such as the rutile-type (*$P4_2/mnm$*), a-PbO_2-type (*Pbcn*), pyrite-type (*Pa3*), ZrO_2-type orthorhombic phase I (*Pbca*), fluorite-type (*Fm3m*), and cotunnite-type orthorhombic phase II (*Pnam*) with nine fold coordination [38,39] (see Figure I.8).

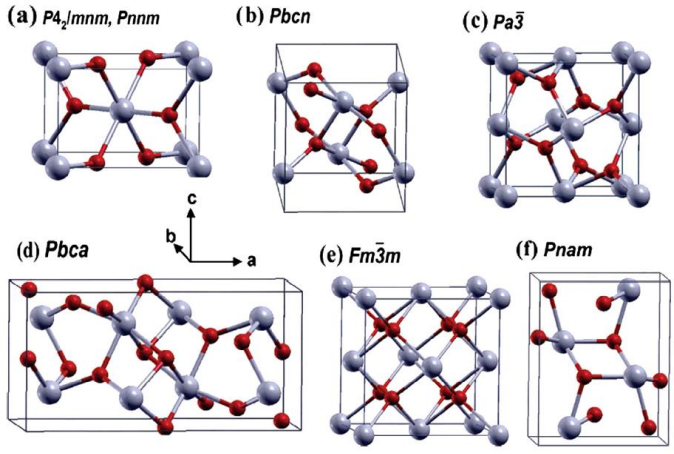

Figure I.1 Crystal structures of the SnO_2 polymorphs. (a) Rutile (*$P4_2/mnm$*) and $CaCl_2$ type (*Pnnm*), (b) a-PbO_2-type (*Pbcn*), (c) pyrite-type (*Pa3*), (d) ZrO_2-type (*Pbca*), (e) fluorite-type (*Fm3m*), and (f) cotunnite-type (*Pnam*). Reported in Gracia et al. [38].

All these structures are sequentially obtained depending on many factors such as temperature and pressure. Yet, the most commonly available and stable form of SnO_2 at ambient pressure is cassiterite, a phase with the tetragonal rutile structure and space group D4h [p42/mm] (Figure I.1 a) [38].

As illustrated in Figure I.2, the unit cell of rutile SnO_2 contains six atoms, two tin (Sn), and four oxygen (O). Each Sn atom is at the center of an octahedron formed by six O atoms placed at the corners, while each O atom is surrounded by three Sn atoms located at the corners of an equilateral triangle. Thus, the whole system made a structure of 6:3 coordinations. The lattice parameters are (a=b=4.737 Å, c=3.185 Å), the c/a ratio is 0.673, and the ionic radii for O_2^- and Sn^{4+} are 1.40 and 0.71 Å respectively. The metal atoms (cations) are located at the positions (0,0,0) and (1/2,1/2,1/2) in the unit cell, while the oxygen atoms (anions) are located at ±(u,u,0) and ±(1/2+u,1/2-u,1/2), where the internal parameter u takes the value 0.307 [40,41].

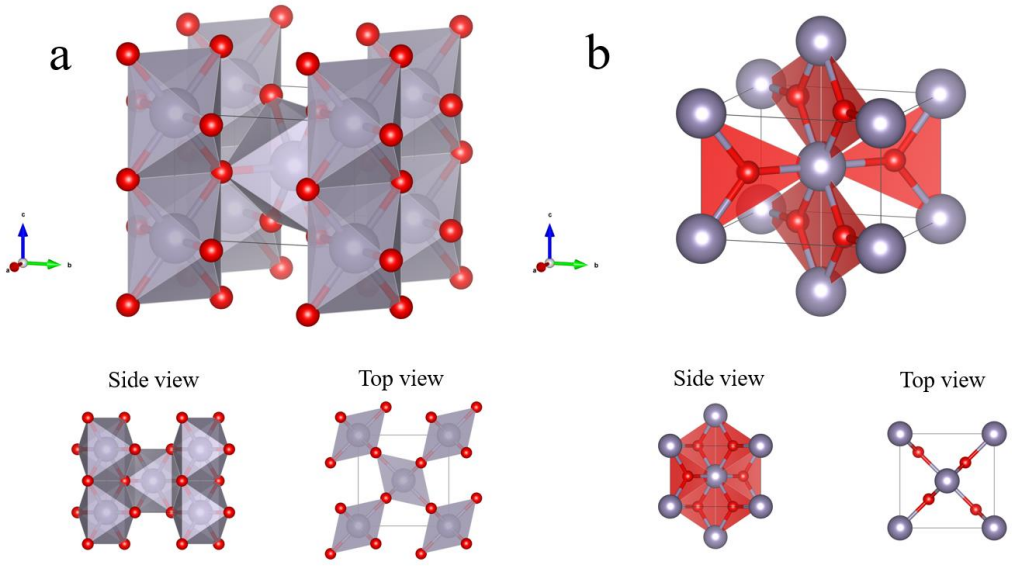

Figure I.2 Rutile unit cell, Sn coordination (a) and O coordination (b) with side and top view.

Generally, the structural defects such as vacancies and structural deformation are the origin of the electronic properties of semiconducting oxides. In the case of SnO_2, it exhibits a special stoichiometric detail due to the existence of oxygen vacancies within its crystalline structure during its exposure to air, which represents its predominant defect. Therefore, the chemical formula of this material could be in the form SnO_{2-x} with a value x dependent on the mode of elaboration of the layers and the partial pressure of oxygen in the surrounding atmosphere. Discussing this type of defect is essential to understand the electronic mechanisms of this material. In fact, it is reported that oxygen vacancies are the main type of defect, although, it is difficult to know the nature of all the defects present in SnO_2 and their influence on its electronic properties [42–45].

I.2.2 Physical Properties of Tin Oxide

I.2.2.1 Electronic structure and band gap

The valence band essentially arises from 2p states of O and admixture of p and d states of Sn. Just above these states, lies the bottom of the conduction band, which is mainly formed by O-2p and Sn-5s states hybridization. The valence band maximum and the conduction band minimum are located at the Γ point, thus forming a direct band gap. The band gap of SnO_2 is found in the Γ-X direction or Γ-M direction of the brillouin zone. The band gap of SnO_2 is 3.6-3.7 eV [37], which could vary depending of elaboration mode, oxygen vacancies, and the presence of impurities/dopants.

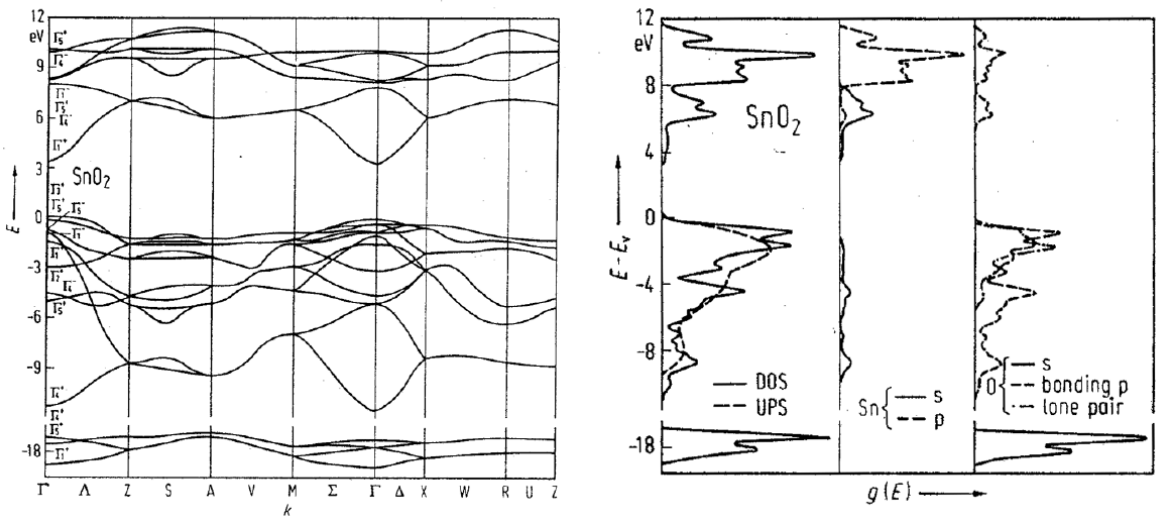

Figure I.3 Reported band structure of SnO2 (left) and projected density of states (DOS) (right) [46].

I.1.2.2 Electrical properties

Electrical conductivity occurs within semiconductors when photo-excited electrons can immigrate from the valence band to the conduction band. Electrical conductivity of SnO_2 depends on its charge carrier concentration and mobility, which is inversely proportional to their effective mass (m^*). This latter is a quantity used to express the mass that the electrons seem to have when moving within a periodic solid. The conduction band CB with a lower effective mass is described as having higher dispersity, and appears visually as having higher curvature at the band edges in contrast with CB with higher effective mass [47,48].

This relationship can be easily demonstrated to a parabolic approximation, and the energy *E(k)* of the CB at wave vector *k* close to the Brillouin zone center can be expressed as:

$$E(k) = E_0 + \frac{\hbar^2 k^2}{2m^*} \qquad \text{Eq I. 1}$$

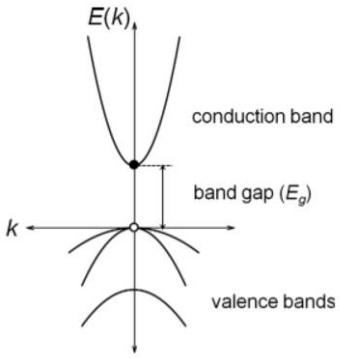

Figure I.4: Illustration of electron energy E as a function of wave vector k.

where E_0 is a constant representing the energy at the band center and m* is the electron effective mass. Then, the curvature of the CB and the VB is expressed as:

$$\frac{d^2 E(k)}{dk^2} = \frac{\hbar^2}{m^*} \qquad \text{Eq I. 2}$$

Electrical conductivity of semiconductors is directly related to charge carrier mobility and electron density by the Boltzmann equation:

$$\sigma = ne\mu \qquad \text{Eq I. 3}$$

where σ is the electrical conductivity expressed in S cm^{-1}, n is the density of free charge carriers, e is the electronic charge and μ is the charge carriers mobility. The electrical resistivity, expressed in Ω cm, is simply

$$\rho = \frac{1}{\sigma} \qquad \text{Eq I. 4}$$

The native defects within the crystalline structure of SnO_2 (oxygen vacancies or tin interstitial atoms) act as donors or acceptors. For instance, the electrons provided from oxygen vacancies can fix on Sn^{4+} atoms, and then they became Sn^{2+} and behave like electrons donors, which explain the *n*-type semiconducting of SnO_2. Therefore, the concentration of free electrons in pure SnO_2 is proportional to that of oxygen vacancies and the interstitial tin atoms. Reported electron density of SnO2 at ambient conditions is in the order of 10^{19} cm^{-3}, while its electron mobility is in the order of 10 cm^2/Vs, which result in electrical resistivity in the order of 10^{-4} Ωcm [49,50].

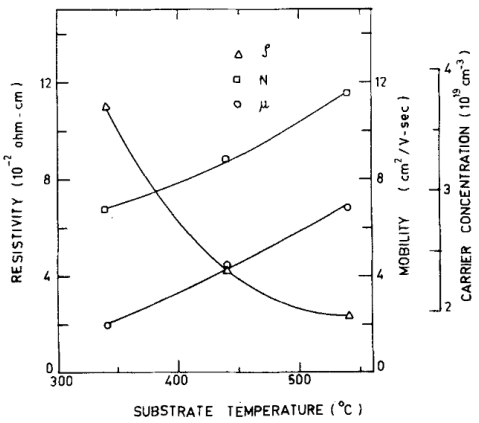

Figure I.5 Variation of resistivity ρ, mobility μ, and carrier concentration *n* in un-doped tin oxide films with substrate temperature. Reported by Shanthi et al. [50].

I.2.2.3 Optical properties

The optical transparency of a semiconductor is directly related to its native optical properties, mainly the optical band-gap that is the lowest energy allowed optical transition. When light come across a material, it interact with it in three different ways: reflection, absorption and transmission, depending on the nature of the material, its band-gap, and the wavelength of the incident light.

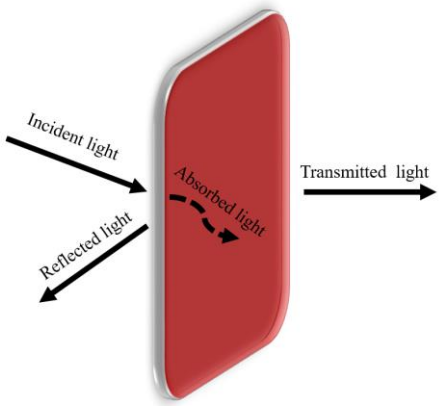

Figure I.6: Illustration of light absorption, transmission, and reflection.

SnO*2* as a transparent conductive oxide presents high absorption in the ultraviolet range, strong reflection in the infrared range, and high transparency (~85%) in the visible range (Figure I.12). The optical transmission of SnO_2 in the visible spectrum (400-800 nm) is due to its large band gap (3.6 eV). Besides, in the case of lower wavelengths < 400 nm (high energies) the transparency decreases and the light would be absorbed, while at long wavelengths > 800 nm (low energies) the light would be reflected. The absorption/transmission rate of SnO2 vary according to several factors such as synthesis method, elaboration protocol and conditions, and crystal morphology [51,52].

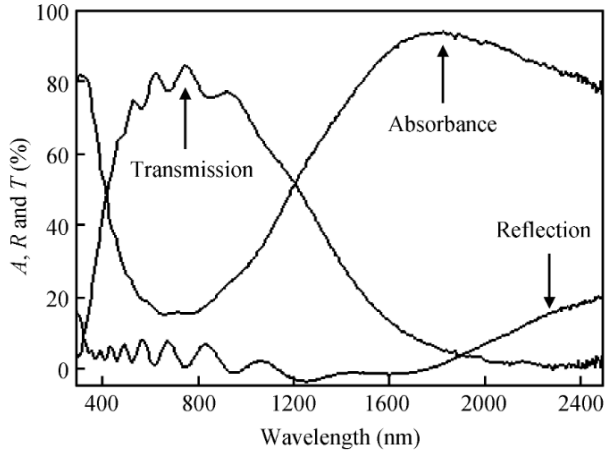

Figure I.7 The transmission, absorbance and reflectance spectra of SnO_2:F thin films reported by Rahal et al. [53].

I.3 Applications and limitations

I.3.1 Acid catalysis

Acid catalysts have been emerged as potential alternates solid catalysts to homogeneous liquid due to their non-toxic nature, enhanced selectivity, activity in moderate temperatures and the ease of separation [54,55]. SnO_2 is hugely used as a solid acid catalyst as reported by several researchers. For instance, Ahmed et al. [56] reported sulfated SnO_2 nanomaterials as an efficient catalyst for the preparation of 7-hydroxy-4-methyl, and Marakatti et al. [57] reported mesoporous SnO_2 as an efficient solid acid catalyst for the activation of carbonyl group in selected organic transformations. In addition, mesoporous SnO_2 presented higher catalytic performance compared to nano and bulk SnO_2 in the Prins, glycerol acetylation, and carbonization reactions. SnO_2 based nano-catalyst exhibit superior catalytic activity and high stability, as well as excellent recycling in solution- and gas-phase reactions, which is evident from various reports on catalytic hydrogenation of p-nitrophenol to p-aminophenol, catalytic oxidation of CO, methanol oxidation and oxygen reduction reaction [58–62].

I.3.2 Photocatalytic degradation of dyes and organic compounds

Photo-catalytic degradation of pollutants, organic molecules and poisonous chemicals in wastewater is very critical for environmental security. SnO_2 nano-materials is considered as a good photocatalyst for the degradation of dyes and organic molecules under UV light. The rapid recombination of the photo-generated electrons and holes presents an obstruction for efficient photocatalytic activity. Instead, modifying SnO2 by either cation and/or anion doping, composite formation, or nanostructures supported over different substrates could be good solutions [63,64]. For instance, Pan et al. [65] reported that the indium tin oxide nanoparticles show higher photo-degradation efficiency of rhodamine B than the commercial P25 TiO_2. Further, Zhao et al. [66] demonstrated enhanced Methyl Orange dye degradation (~92%) by Zn-doped SnO_2, which is found to be higher than that by undoped SnO_2 (~75%). Further, Sadeghzadeh-Attar et al. [67] reported simple and inexpensive photocatalytic degradation of Methylene Bleu (MB) by synthesized SnO_2 nanotubes (see Figure I.14).

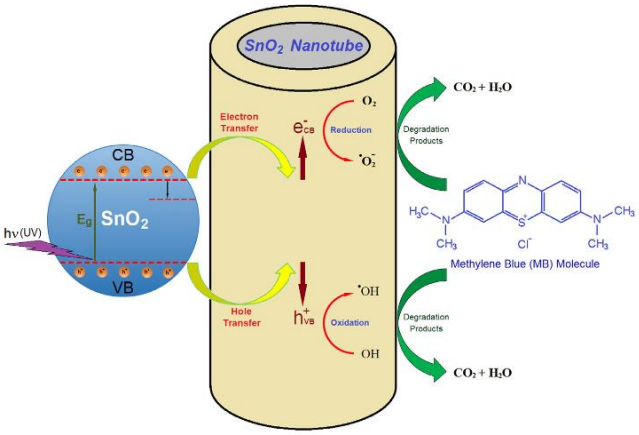

Figure I.8 Schematic illustration of the SnO_2 nanotube showing the proposed photo-degradation mechanism of MB dye under UV light illumination reported by Sadeghzadeh-Attar et al. [67].

I.3.3 Dye sensitized solar cells

Dye-Sensitized Solar Cells (DSSCs) are low-cost solar cells constructed by a metal oxide semiconductor that acts as a photo-anode, redox electrolytes, and dye molecules incorporated onto the photo-anode and the electrolyte [68,69].

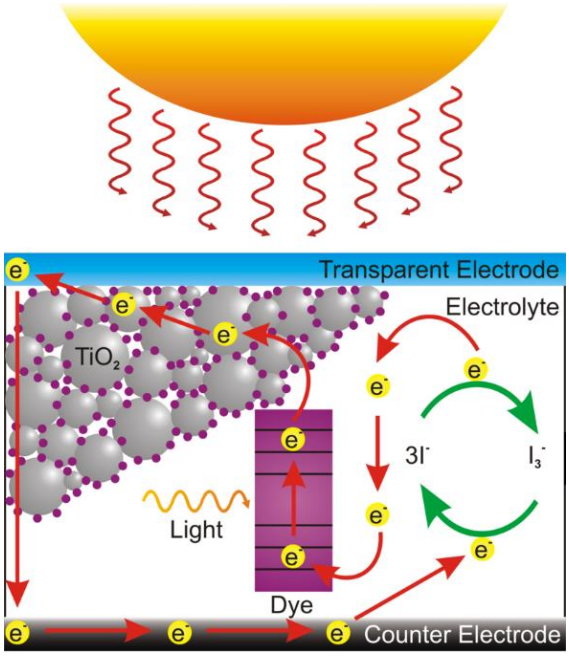

Figure I.9. Schematic representation of the components and the basic operating principle of a DSSC.

As illustrated in Figure I.9, the solar energy conversion by the DSSCs consists of dye molecules excitation by photon energy, which results in rapid migration of electrons onto the conduction band of the metal oxide semiconductors, thereby resulting in photocurrent. Mainly, TiO_2 is the current photo-anode in DSSCs [70,71]. Although, SnO_2 is believed to be a potential alternative of TiO_2 owing to its wider band gap and higher electron mobility, which present positive qualities to improve the photovoltaic performance of DSSCs [72]. In fact, Basu et al. [73] reported modified SnO_2 nanoparticles that acts as a photo-anode in order to facilitate the electron transport in this latter and enhance the power conversion efficiency of the DSSC solar cell. In addition, Milan et al. [74] reported enhanced photo-conversion efficiency (4.96%) of ZnO/SnO_2 composite due to the high carrier mobility of ZnO combined with the high stability under UV irradiation of SnO_2. Further, doped tin oxide nano-particles as photo-anodes were reported to have greater performance due to moderate up-shifting of the band edge by doping which facilitated electron injection from the sensitizer to the electrode, and prohibited electron recombination within the electrolyte [72]. Several reports on indium tin oxide (ITO) and fluorine tin oxide (FTO) DSSCs [75–77] firmly establish the importance of tin oxide based photo-anodes towards dye-sensitized solar cells.

I.3.4 Lithium ion batteries

Rechargeable lithium ion batteries are considered the most favored power sources for portable electronic devices due to their high capacity, and flexible design. SnO_2 is deemed as one of the promising anode materials of lithium ion batteries, owing to its high theoretical lithium storage capacity (~782 mAh/g), which is two times greater than that of conventional graphite anodes (372 mAh/g) [78–81]. However, practical applicability of SnO2 based anodes is significantly limited due to many factors, such as the poor capacity retention over large cycles, resulting from large volume changes during the charge/discharge processes [82,83]. Many researchers reported that the use of SnO_2 with specific structures like hollow spheres, nano-wires, and nano-flowers might solve some limitations [84–86]. For instance, SnO2 nano-boxes designed by Wang et al. [87] provide a capacity of 570 mAh/g after 40 cycles. Further, hybridization of SnO2 with carbonaceous materials that are good electron conductors could enhance the electrochemical performance of SnO_2 [88–90]. In fact, Paek et al. reported SnO_2/graphene nano-sheets (SnO_2/GNS) that showed much better performance in term of storage capacity (~810 mAh/g), coulombic efficiency and cycling life [91]. Further, doped (carbon-SnO_2) composites showed positive results, as the chemical functionalization of carbonaceous materials could potentially produce localized highly reactive regions and thus exhibit adjusted properties. In fact, many examples have been reported as anode materials in lithium ion batteries like doped-SnO_2/graphene, or SnO_2/carbon to have high flexibility, and enhanced rate capacity [92–95].

I.3.5 Bio-sensing

Bio-sensing is hugely useful for clinical applications, environmental monitoring and food analysis. Recently, SnO_2 based nanomaterials have demonstrated immense possibilities and gained wide popularity in bio-sensing applications. Several systems have been developed like graphene/SnO_2 composites as electrochemical sensor to detect insulin and estradiol, doped SnO_2 for glucose sensing, and SnO_2 quantum dot based DNA sensor for pathogen detection [96–102]. For instance, Masodha et al. [103] demonstrated that fluorine-doped SnO_2 (FTO) modified with dye-labeled monoclonal antibody materials is a suitable electrode for next generation cancer sensors, as this later is based on the photoluminescence and photocurrent conversion results from the reaction of monoclonal antibody with human alpha-fetoprotein (present in blood serum of hepatocellular cancer patient). Further, Liu et al. [104] studied DNA adsorption by Indium Tin Oxide nanoparticles (ITO) and reported the average DNA adsorption behavior on ITO compared to SnO_2 and In_2O_3. ITO nanoparticles are found to get enough DNA

binding affinity so that desorption can occur easily in the presence of complementary DNA (cDNA). This reversible ITO-DNA interaction makes ITO a very useful transparent electrode material for detection of various other targets like DNA, cDNA, DNA methylation, and pathogen [105–108].

I.3.6 Gas sensing

Detectors of various gases and odors play an important role for controlling human health, public safety, and environmental pollution [109,110]. Among the metal oxides, SnO2 presents the most suitable material for gas sensing under atmospheric conditions due to its high selectivity and sensitivity, easy designing and implementation, good reversibility and low manufacturing costs [111].

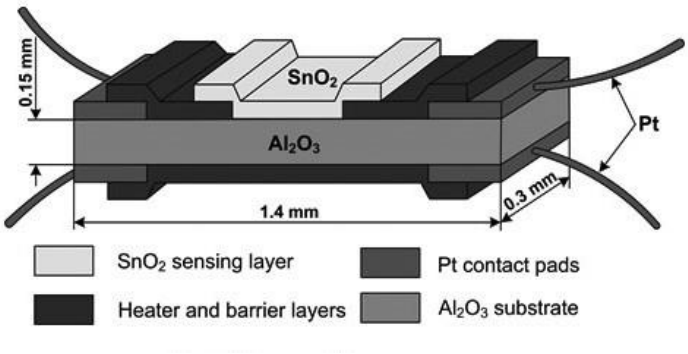

Figure I.10 Illustrated design of the gas sensor [112].

The response of a SnO_2 sensor occurs when its physical and chemical properties on the surface change during the adsorption of a chemical molecule. Several researchers reported enhanced SnO_2 sensitivity by nano-structuring, varying the crystal structure and morphology, and doping typically by noble metals or other metal oxides to create nanocomposites [113–115]. For instance, Wang et al. [116] reported high stability, selectivity and sensitivity of Pd-loaded SnO2 nanostructures, as well as fast recovery properties when detecting carbon monoxide gases. Further, Maeng et al. [117] reported highly sensitive SnO2 nano-slab network for NO2 sensing. Various hybrid materials like SnO_2/reduced graphene oxide composites, and reduced graphene oxide-multi walled carbon nanotube-tin oxide nanoparticle hybrids have been employed for high performance low temperature NO_2 sensing [118,119]. During the last decade, intense research has been conducted to understand the electronic and mechanical features that govern the sensing behavior of SnO2 towards various gases (NOx, ethanol, methanol, ammonia, acetone, CO, H_2 etc.) including trace amounts of toxic gases [120–125],

in that way, establishing the great suitability and huge potential of SnO2 for gas sensing applications.

I.3.7 Limitations

As discussed in the preceding parts, SnO2 has demonstrated its suitability in a wide range of applications due to its promising properties. However, SnO2 has also limitations and difficulties, amongst some will be treated in the following chapters. As reported by Miller et al. and Peelaers et al. [126,127], the wide band-gap of SnO2 prohibits its visible light absorption (see Figure I.18), and presents a serious obstruction of its application in sunlight conversion devices.

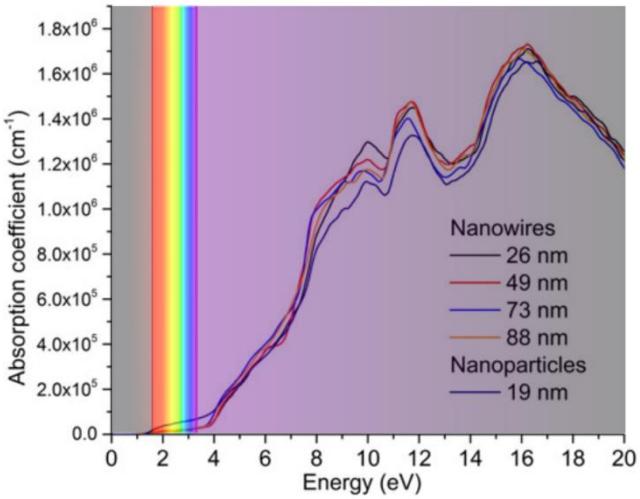

Figure I.11 Optical absorption coefficient of SnO_2 nanowires and nano-particles of varying thickness reported by Miller et al. [126].

Many researchers have provided solutions to overcome wide band-gap complication such as doping, and morphology engineering [128–130]. Ganose et al. [131] reported reduced band gap of SnO_2 through Pb doping, resulting in increased electrons affinity and improved charge carriers mobility, however, Pb-doped SnO_2 maintain its transparency in the visible spectrum. In fact, SnO_2 wide band-gap still its main inconvenient so far. Further, it has been reported that SnO_2 suitability is limited for thermal to electric energy conversion due to its large thermal conductivity (i.e. $\gtrsim$ 40 W m^{-1} K^{-1}) which result in low figure of merit ($\sim<$ 0.3) compared to those of intermetallic systems (see Figure I.12) [132–135].

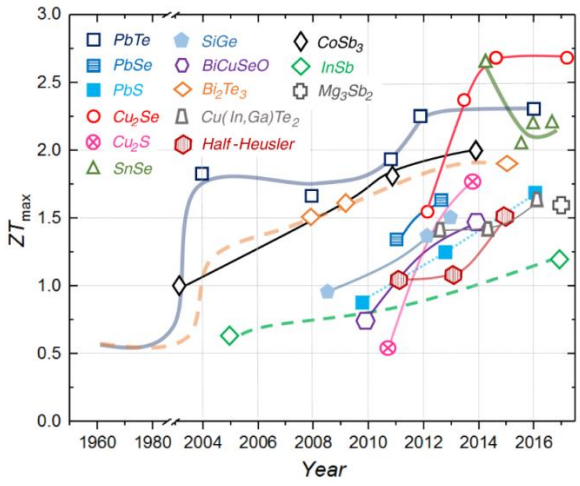

Figure I.12 Timeline of the maximum ZT values for several representative families of TE materials. Reported by He et al. [136].

Generally, SnO2 is a good material for photocatalytic applications as discussed in previous parts (see **I.3.2 Photocatalytic degradation of dyes and organic compounds**). However, its Electron Affinity (EA) and Ionization Energy (IE) are not suitable to oxidize and reduce many species and molecules. In fact, SnO2 band energy did not match the redox potential of water (H_2O). As reported in Figure I.13, the conduction band minimum (CBM) of SnO_2 compared to other semiconductors such as ZnO and TiO2 is located above the redox potential level of H^+/H_2 (outlined in red), which presents a serious disadvantage and complicates its wide application in photocatalysis especially for water splitting and Hydrogen Evolution Reaction (HER) [137].

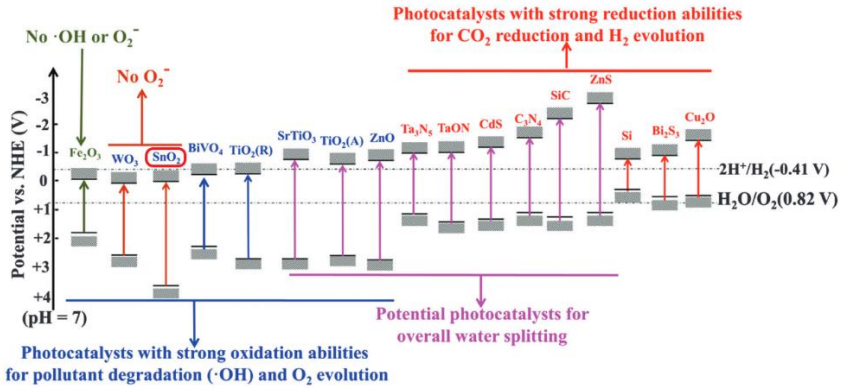

Figure I.13 Band positions and potential applications of some typical photo-catalysts (at pH = 7 in aqueous solutions). Reported by Li et al. [137].

Inspired by such reports, in the present thesis, we attempt to modulate the energy band structure and enhance the electronic and optical properties of bulk- and thin film-SnO_2 through an applied strain in order to overcome its limitations and improve its suitability in the previous discussed applications via computational strategies using density functional theory (DFT) calculations.

CHAPTER II: DENSITY FUNCTIONAL THEORY (DFT)

Table of contents

CHAPTER II: DENSITY FUNCTIONAL THEORY (DFT)

In many problems of materials science, the processes occurring at microscopic scale (on the order of nanometers and femtoseconds) govern the behavior of the material at the macroscopic scale (on the order of centimeters and milliseconds and beyond). Therefore, performing material simulations through several length and time scales has evident request as a tool for technological innovation. Thanks to the increasing availability of very fast computers and the development and understanding of efficient algorithms, numerical simulations have become predominant in any field of research. Fast and parallelized computers also called High Performance Computing (HPC) systems allow for solving complex and non-linear many body problems directly. Further, computer simulations are not only a connecting link between analytic theory and experiment, allowing analyzing theories, but they can also be used as an exploratory research tool under physical conditions that are not feasible in real experiments in a laboratory. Thus, computational methods have generated a new interdisciplinary research approach, which is often referred to as "Computational Materials Science" or "Computational Physics". This approach brings together elements from diverse fields of study such as physics, mathematics, chemistry, biology, engineering and even medicine and has the potential to handle multiscale and multi-disciplinary simulations in realistic situations.

Computational materials science involves computational tools for solving materials related problems. There exist different mathematical models for investigating problems at multiple length and time scales that help in understanding evolution of material structures (at different length scales) and how these structures effectively control material properties. With this understanding, we can select materials for specific applications, and design advanced materials for new applications. At electronic level, Density Functional Theory (DFT) is a popular computational tool, while Molecular Dynamics (MD) and Monte Carlo (MC) methods are considered as preferred tools for atomistic simulations. For materials problems at micron and mesoscale (between micro and nano) regimes, phase-field Method (PFM) is frequently used. It helps in understanding temporal evolution of microstructures at these length scales. There are also different models related to solid mechanics, transport phenomena for continuum level calculations. Besides, material problems that have important features at multiple length scales involves exchange of information between computational tools at different length scales.

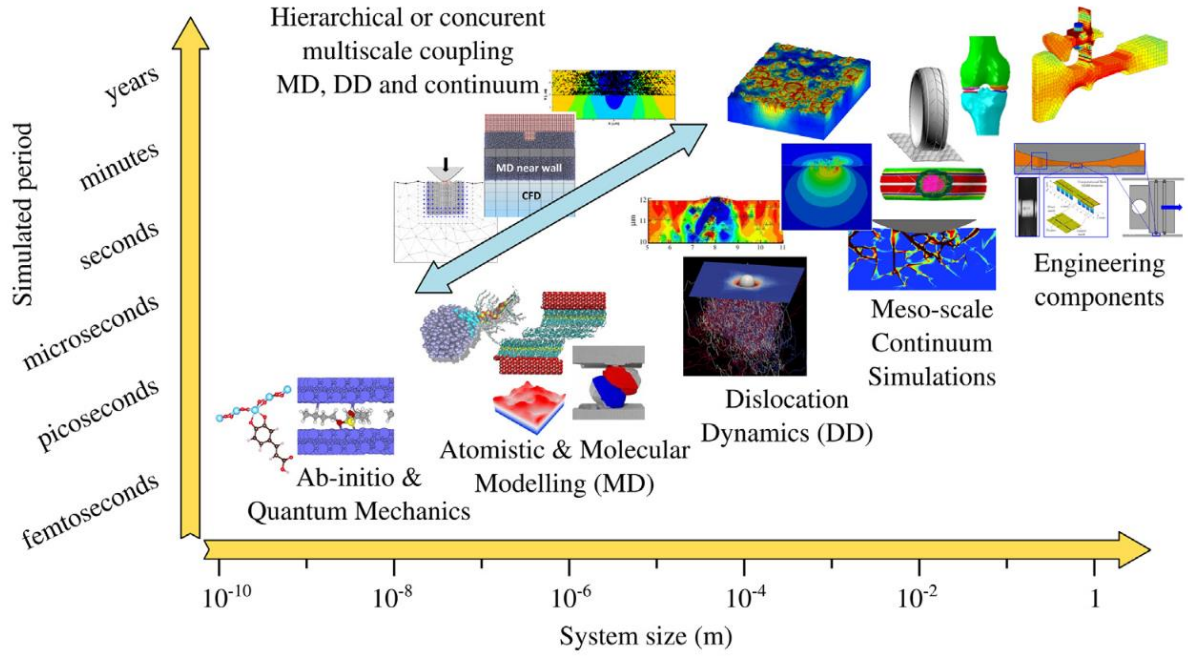

Figure II.1 Time vs length scales map of models developed in tribology highlighting the intrinsic link between multiscale/physics that needs to be captured to provide predictive tools for engineering applications [138].

As illustrated in Figure II.1, depending on the question at hand and on the desired accuracy with which specific structural features of the considered system are resolved, one has the choice between many different models, which often can be usefully employed on a whole span of length and time scales. Thus, before getting started with computer simulations, as always in research, it is important to establish first, which phenomena and properties one is primarily interested in and which questions one is going to ask. In the present thesis, the electronic structure is the main property we aim to predict, therefore Density Functional Theory (DFT) for our purpose is the accurate choice.

II.1 Basics of quantum mechanics

II.1.1 The Schrödinger equation

In order to describe the matter properties at the nano-scale Erwin Schrödinger used the Broglie's relations to develop the general form of the famous equation named after him, which is the time-dependent Schrödinger equation [139].

$$i\hbar \frac{\partial}{\partial t}\psi(\vec{r},t) = \hat{H}\,\psi(\vec{r},t) \qquad \text{Eq II. 1}$$

where $\hat{H}$ is the time dependent Hamiltonian, $\psi(\vec{r},t)$ is the time dependent wave function, and $\vec{r}$ is the position.

It is often impracticable to use a complete relativistic formulation of the formula. Therefore, Schrödinger himself proposed a non-relativistic approximation, which is nowadays often used, especially in quantum chemistry.

$$\hat{H} = \hat{T} + \hat{V} = -\frac{\hbar^2}{2m}\vec{\nabla}^2 + V(\vec{r}, t) \qquad \text{Eq II. 2}$$

Using the Hamiltonian for a single particle leads to the (non-relativistic) time-dependent single-particle Schrödinger equation:

$$i\hbar \frac{\partial}{\partial t}\psi(\vec{r}, t) = \left[-\frac{\hbar^2}{2m}\vec{\nabla}^2 + V(\vec{r}, t)\right]\psi(\vec{r}, t) \qquad \text{Eq II. 3}$$

while for N particles in three dimensions, the Hamiltonian is expressed as:

$$\hat{H} = \sum_{i=1}^{N} \frac{\hat{p_i}^2}{2m_i} + V(\overrightarrow{r_1}, \overrightarrow{r_2}, \dots, \overrightarrow{r_N}, t) = -\frac{\hbar^2}{2}\sum_{i=1}^{N}\frac{1}{m_i} + V(\overrightarrow{r_1}, \overrightarrow{r_2}, \dots, \overrightarrow{r_N}, t) \qquad \text{Eq II. 4}$$

Therefore the corresponding Schrödinger equation is:

$$i\hbar \frac{\partial}{\partial t}\psi(\overrightarrow{r_1}, \overrightarrow{r_2}, \dots, \overrightarrow{r_N}, t) = \left[-\frac{\hbar^2}{2}\sum_{i=1}^{N}\frac{1}{m_i}\nabla_i^2 + V(\overrightarrow{r_1}, \overrightarrow{r_2}, \dots, \overrightarrow{r_N}, t)\right]\psi(\overrightarrow{r_1}, \overrightarrow{r_2}, \dots, \overrightarrow{r_N}, t) \qquad \text{Eq II. 5}$$

II.1.2 Time-independent equation

Special cases are the solutions of the time-independent Schrödinger equation, where the Hamiltonian itself has no time-dependency (which implies a time-independent potential $V(\overrightarrow{r_1}, \overrightarrow{r_2}, \dots, \overrightarrow{r_N})$, and the solutions therefore describe standing waves which are called stationary states or orbitals). The time-independent Schrödinger equation is not only easier to treat, but the knowledge of its solutions also provides crucial insight to handle the corresponding time-dependent equation.

The time-independent equation is obtained by the approach of separation of variables, i.e. the spatial part of the wave function is separated from the temporal part via [140]:

$$\psi(\overrightarrow{r_1}, \overrightarrow{r_2}, \dots, \overrightarrow{r_N}, t) = \psi(\overrightarrow{r_1}, \overrightarrow{r_2}, \dots, \overrightarrow{r_N})\tau(t) = \psi(\overrightarrow{r_1}, \overrightarrow{r_2}, \dots, \overrightarrow{r_N}).e^{-i\omega t} \qquad \text{Eq II. 6}$$

Furthermore, the left hand side of the equation reduces to the energy eigenvalue of the Hamiltonian multiplied by the wave function, leading to the general eigenvalue equation

$$E\,\psi\,(\overrightarrow{r_1},\overrightarrow{r_2},\dots,\overrightarrow{r_N}) = \hat{H}\,\psi(\overrightarrow{r_1},\overrightarrow{r_2},\dots,\overrightarrow{r_N}) \qquad \text{Eq II. 7}$$

Again, using the many-body Hamiltonian, the Schrödinger equation becomes

$$E\,\psi\,(\overrightarrow{r_1},\overrightarrow{r_2},\dots,\overrightarrow{r_N}) = \left[-\frac{\hbar^2}{2}\sum_{i=1}^{N}\frac{1}{m_i}\nabla_i^2 + V(\overrightarrow{r_1},\overrightarrow{r_2},\dots,\overrightarrow{r_N})\right]\psi(\overrightarrow{r_1},\overrightarrow{r_2},\dots,\overrightarrow{r_N}) \qquad \text{Eq II. 8}$$

II.1.3 The wave function

In the last section, the term wave function was repetitively used. Therefore, and for a better understanding of the following a closer look at the wave function is taken. The first and most important postulate is that the state of a particle is completely described by its (time-dependent) wave function, i.e. the wave function contains all information about the particle's state. For the sake of simplicity the discussion is restricted to the time-independent wave function. A question always arising with physical quantities is about possible interpretations as well as observations. The Born probability interpretation of the wave function, which is a major principle of the Copenhagen interpretation of quantum mechanics, provides a physical interpretation for the square of the wave function as a probability density [141,142]

$$|\psi(\overrightarrow{r_1},\overrightarrow{r_2},\dots,\overrightarrow{r_N})|^2 d\overrightarrow{r_1}d\overrightarrow{r_2}\dots d\overrightarrow{r_N} \qquad \text{Eq II. 9}$$

Equation II.9 describes the probability that particles 1,2,...,N are located simultaneously in the corresponding volume element $d\overrightarrow{r_1}d\overrightarrow{r_2}\dots d\overrightarrow{r_N}$. Thus, what happens if the positions of two particles are exchanged, must be considered as well. Following merely logical reasoning, the overall probability density cannot depend on such an exchange, i.e.

$$\left|\psi(\overrightarrow{r_1},\overrightarrow{r_2},\dots,\vec{r}_i,\vec{r}_j,\dots,\overrightarrow{r_N})\right|^2 = \left|\psi(\overrightarrow{r_1},\overrightarrow{r_2},\dots,\vec{r}_j,\vec{r}_i,\dots,\overrightarrow{r_N})\right|^2 \qquad \text{Eq II. 10}$$

There are only two possibilities for the behavior of the wave function during a particle exchange. The first one is a symmetrical wave function, which does not change due to such an exchange. This corresponds to bosons (particles with integer or zero spin). The other possibility is an anti-symmetrical wave function, where an exchange of two particles causes a sign change, which corresponds to fermions (particles which half- integer spin) [143,144].

In this text only electrons are from interest, which are fermions. The anti-symmetric fermion wave function leads to the Pauli principle, which states that no two electrons can occupy the same state, whereas state means the orbital and spin parts of the wave function1 (the term spin coordinates will be discussed later in more detail). The antisymmetric principle can

be seen as the quantum-mechanical formalization of Pauli's theoretical ideas in the description of spectra (e.g. alkaline doublets) [145].

Another consequence of the probability interpretation is the normalization of the wave function. If Equation II.9 describes the probability of finding a particle in a volume element, setting the full range of coordinates as volume element must result in a probability of one, i.e. all particles must be found somewhere in space. This corresponds to the normalization condition for the wave function.

$$\int d\vec{r}_1 \int d\vec{r}_2 \ \dots \int d\vec{r}_N \, |\psi(\vec{r_1}, \vec{r_2}, \dots, \vec{r_N})|^2 = 1 \qquad \text{Eq II. 11}$$

Equation II.11 also gives insight on the requirements a wave function must fulfill in order to be physical acceptable. Wave functions must be continuous over the full spatial range and square-integral [146].

Another very important property of the wave function is that calculating expectation values of operators with a wave function provides the expectation value of the corresponding observable for that wave function. For an observable $O(\vec{r_1}, \vec{r_2}, \dots, \vec{r_N})$, this can generally be written as:

$$O = \langle O \rangle = \int d\vec{r}_1 \int d\vec{r}_2 \ \dots \int d\vec{r}_N \, \psi^*(\vec{r_1}, \vec{r_2}, \dots, \vec{r_N}) \hat{O} \, \psi(\vec{r_1}, \vec{r_2}, \dots, \vec{r_N}) \qquad \text{Eq II. 12}$$

II.1.4 The Born-Oppenheimer (BO) Approximation

The Born-Oppenheimer approximation consists in the separation of Schrodinger equation into nuclear and electronic parts based on the fact that the nuclei are much heavier than the electrons, while the electrons move much faster than the nuclei with respect to the center of mass. Hence, we can consider that the nuclei as fixed points and the electrons experience a potential generated by a specific fixed nuclei configuration. This implies that, the term relative to kinetic energy of the nuclei can be neglected, , then the Hamiltonian can be expressed as the sum of an operator depending only on the coordinates of the electrons ($\hat{H}_{elec}$) and another term depending only on the coordinates of the nuclei ($\hat{H}_{nucl}$):

$$\hat{H} = \hat{H}_{elec} + \hat{H}_{nucl} \qquad \text{Eq II. 13}$$

with

$$\hat{H}_{elec} = -\sum_{i=1}^{N}\frac{1}{2}\nabla_i^2 - \sum_{i=1}^{N}\sum_{A=1}^{M}\frac{Z_A}{r_{iA}} + \sum_{i=1}^{N}\sum_{j>i}^{M}\frac{1}{r_{ij}} \qquad \text{Eq II. 14}$$

and

$$\hat{H}_{nucl} = -\sum_{A=1}^{M-1}\sum_{B>A}^{M}\frac{Z_A Z_B}{R_{AB}} \qquad \text{Eq II. 15}$$

Solving Eq II.xx is now simply reduced to the solution of the electronic part

$$\hat{H}_{elec}\psi_{elec} = E_{elec}\psi_{elec} \qquad \text{Eq II. 16}$$

with the total wave function of the system given by the product of the electronic wave function ψ_{elec} and of the wave function ψ_{nucl} describing the nuclear motion:

$$\psi_{tot}(nuclei, electrons) = \psi_{nucl}\psi_{elec} \qquad \text{Eq II. 17}$$

and with the total energy of the system given by the sum of the electronic energy E_{elec} and nucler repulsion term E_{nucl}:

$$E = E_{elec} + E_{nucl} = E_{elec} + \sum_{A=1}^{M-1}\sum_{B>A}^{M}\frac{Z_A Z_B}{R_{AB}} \qquad \text{Eq II. 18}$$

The nuclear repulsion term, as well as the terms relative to the kinetic energy of the electrons and the electron-nuclear interaction can be computed analytically, but the presence of the electron-electron repulsion contribution does not allow to solve exactly equation II.8 for poly-electronic systems. In these cases, further approximations are thus necessary. Special approaches have been developed to solve this equation including the Thomas-Fermi, Hartree Fock, and density functional theory.

II.2 The Hartree-Fock approach

Hartree-Fock (HF) theory presents one of the simplest theories to solve the Schrodinger equation. The principle of the HF approximation is to replace the complex many-electron problem by a one-electron problem in which the electron-electron interaction is treated in an average way. This means that each electron is subject to an average non-local potential arising from the other electrons. Although this approximation can lead to a poor description of the electronic structure, since the correlation among the electrons is neglected, the HF theory represents the starting point for most ab initio quantum chemistry methods.

II.2.1 Orbitals and Slater Determinants

We define an orbital as a wave function for a single electron. A molecular orbital is thus a wave function describing an electron in a molecule. In particular, a spatial orbitalis definable as a function of the position vector (*r*), that describes the spatial distribution of a given electron so that $|\psi(\mathrm{r})|^2 dr$ is the probability to find the particle in a volume *dr*. Spatial orbitals are generally assumed to be orthonormal:

$$\int \psi^*(r)\psi_j(r)dr = \delta_{ij} \qquad \text{Eq II. 19}$$

where δ_{ij} is the Kronecker symbol ($\delta_{ij} = 1$ if $i = j$ and $\delta_{ij} = 0$ if i ≠ j).

However, in order to completely describe an electron, the specification of its spin state is also necessary. This condition is obtained through the definition of two orthonormal functions $\alpha(\omega)$ and $\beta(\omega)$ so that the two possible states of spin (spin up and spin down, respectively) are taken into account for each electron. The wave function describing both the spatial and spin distribution for an electron is called spin-orbital $\chi(x)$, where *x* indicates both space (r) and spin (ω) coordinates. Consequently, for each spatial orbital, two different spin-orbitals can be defined:

$$\chi(x) = \begin{cases} \psi(\mathrm{r})\alpha(\omega) \\ \psi(\mathrm{r})\beta(\omega) \end{cases} \qquad \text{Eq II. 20}$$

If the spatial wave functions are orthonormal, so are the spin orbitals:

$$\int \chi_i(x)^*\chi_j(x)dx = \delta_{ij} \qquad \text{Eq II. 21}$$

Having the expression of the wave function describing one electron, the approximations used for the multi-electron wave function can be considered. The simplest approximation is the orbital approximation. If we neglect the coupling between electrons, the electronic Hamiltonian in equation (2.5) becomes simply a sum of mono-electronic terms ($\hat{h}(i)$), since the interactions between the electrons are zero:

$$\hat{H}_{elec} = \sum_{i=1}^{N} \hat{h}(i) \qquad \text{Eq II. 22}$$

where $\hat{h}(i)$ will have a set of eigen functions that can be described through a set of spin orbitals:

$$\hat{h}(i)\chi_i(x_i) = \varepsilon_i\chi_i(x_i) \qquad \text{Eq II. 23}$$

Consequently, the multi-electron wave function will simply be the product of the spin orbital wave function for each electron (ψ_{el}^{HP}, the so called Hartree product):

$$\psi_{el}^{HP} = \chi_1(x_1)\chi_2(x_2)\dots\chi_N(x_N) \qquad \text{Eq II. 24}$$

and the electronic energy will be the sum of the energy of each spin orbital:

$$E_{elec} = \sum_{i=1}^{N} \varepsilon_i \qquad \text{Eq II. 25}$$

This assumption was proposed by Hartree and the product of the mono electronic wave-functions is called Hartree product. Nevertheless, according to the Pauli exclusion principle, the multi-electron wave-function must change its sign with respect to exchange of the electronic coordinates. This anti-symmetric condition is not satisfied by the Hartree product so that a better description is necessary. The Slater determinant (ψ_{el}^{SD}, see equation II.26) is an expression able to describe the multi-electrons wave function including the anti-symmetry requirements. For an N-electron system it is definable as:

$$\psi_{el}^{SD} = \frac{1}{\sqrt{N!}} \begin{vmatrix} \chi_1(x_1) & \chi_2(x_1) & \cdots & \chi_N(x_1) \\ \chi_1(x_2) & \chi_2(x_2) & \cdots & \chi_N(x_2) \\ \vdots & \vdots & \ddots & \vdots \\ \chi_1(x_N) & \chi_2(x_N) & \cdots & \chi_N(x_N) \end{vmatrix} \qquad \text{Eq II. 26}$$

where $\frac{1}{\sqrt{N!}}$ is a normalization constant. In the ψ_{el}^{SD}, the N electrons occupy the N spin orbitals without specifying which electron is in which orbital. Interchanging the space and spin coordinates of two electrons implies the interchange of two rows of the Slater Determinant, which changes the sign of the determinant, thus meeting the requirement of the anti-symmetric principle. In particular, while the Hartree product is truly an independent-electronic wave-function, the Slater determinant, as a consequence of its invariance with respect to the exchange of the electron coordinates, incorporates the so called exchange correlation, meaning that the motion of two electrons with parallel spins is correlated. However, since the motion of electron with anti-parallel spin is still not correlated, Slater determinants are referred as an uncorrelated wave function. A single Slater determinant is the simplest antisymmetric wave-function that can be used to describe the ground state of an N-electron system and it is used in the HF theory, that is thus referred to as a single-determinantal method.

II.2.2 Hartree-Fock energy

The HF energy can be derived applying the variational principle:

$$E_0^{HF} = \frac{\langle \psi_0 | \hat{H}_{elec} | \psi_0 \rangle}{\langle \psi_0 | \psi_0 \rangle} = \langle \psi_0 | \hat{H}_{elec} | \psi_0 \rangle \geq E_0^{exact} \qquad \text{Eq II. 27}$$

The best wave-function is the one which gives the lowest possible energy. This means that for a given electronic configuration, we can vary the spin orbitals so as to obtain the Slater determinant ψ_0 providing a minimal energy E_0. The principle is thus applied by minimizing the energy E_0^{HF} as a functional of the spin-orbitals. It can be shown that the obtained energy will be always higher or equal to the exact energy of the ground state (E_0^{exact}). By minimizing E_0^{HF} with respect of the choice of spin-orbitals, it is possible to derive the Hartree-Fock equations, which determine the optimal spin-orbitals. These equations are one electron eigen-value equations of the form:

$$\hat{F}(i)\chi_i(x_i) = \varepsilon_i \chi_i(x_i) \qquad \text{Eq II. 28}$$

Since in the case of the HF approximation, in order to introduce the electron-electron repulsion, each electron is subjected to a mean potential due to the presence of the other N-1 electrons, each spin orbital is function of an effective one-electron operator called Fock operator ($\hat{F}$) of the form:

$$\hat{F}(i) = -\frac{1}{2}\nabla_i^2 - \sum_A^M \frac{Z_A}{r_{iA}} + v(i)^{HF} \qquad \text{Eq II. 29}$$

$$\hat{F}(i) = \hat{h}_i + v(i)^{HF} \qquad \text{Eq II. 30}$$

In other words, the electron-electron interaction $\frac{1}{r_{ij}}$ in the Hamiltonian is substituted by a mono-electronic operator $v(i)^{HF}$ Hartree-Fock potential, representing the average potential experienced by the i^{th} electron due to the presence of the other electrons and given by:

$$v(i)^{HF} = \sum_i^N (\hat{J}_j(x_i) - \hat{K}_j(x_i)) \qquad \text{Eq II. 31}$$

where $\hat{J}_j$ is the Coulomb operator Eq II.32 and $\hat{K}_j$ is the exchange operator Eq II.33:

$$\hat{J}_j(x_1) = \int \chi_j^*(x_2)\frac{1}{r_{12}}\chi_j(x_2)dx_2 \qquad \text{Eq II. 32}$$

$$\widehat{K}_j(x_1)\chi_j^*(x_1) = \int \chi_j^*(x_2)\frac{1}{r_{12}}\chi_i(x_2)\chi_j(x_1)dx_2 \qquad \text{Eq II. 33}$$

As we can see from the previous equations, $v(i)^{HF}$ depends on the spin orbitals of the other electrons and consequently the Fock operator depends on its eigen-functions. The HF equtions are thus non linear and have to be solved in an iterative way. The procedure for solving the HF equations is called the Self Consistent Field (SCF) method: starting from an initial trial function for the spin orbitals, the mean field felt by each electron is computed to solve the HF equations Eq II.28. The obtained new spin orbitals are then used to compute the new mean fields so that an iterative cycle is established. It can be repeated until self-consistency is reached, so that the fields no longer change and the spin orbitals used to construct the Fock operator are the same as its eigein-functions. The HF equations are solved by introducing a finite set of spatial basis functions ψ_μ can be used to expand both the α and β spin orbitals. The larger and more complete is the set of the basis function ψ_μ, the greater the degree of flexibility in the expansion of the spin orbitals and the lower will be the expectation value E_0^{HF}. In the limit of a complete basis set the Hartree-Fock energy reaches a lower limit known as the Hartree-Fock limit.

II.2.3 Limits of the HF approach

A single determinant, like the one used in the HF formulation, is not able to express the exact wave-function since the explicit electron-electron interaction is not taken into account: in the HF method the probability of finding an electron at some location around an atom is determined by the distance from the nucleus but not from the distance to the other electrons. So that the correlation due to the coulomb interaction between the electrons (named Coulomb correlation) is completely neglected. Furthermore, although the use of Slater determinants allows to fully account for the correlation between electrons of parallel spin (electron exchange), the correlation between electrons of opposite spins is completely neglected so that the probability of finding two electrons having opposite spins in the same location of space is not equal to zero. The correlation energy (E_{corr}) is thus defined as the difference between the exact nonrelativistic energy of the system (E_0^{exact}) and the HF energy (E_0^{HF}) obtained in the limit of a complete basis set:

$$E_{corr} = E_0^{exact} - E_0^{HF} < 0 \qquad \text{Eq II. 34}$$

Different methods, like the post-HF methods, the Thomas-Fermi (TF), or the Density Functional Theory (DFT), have been proposed to introduce this correlation energy contribution.

II.3 Thomas-Fermi (TF) theory

Llewellyn Thomas and Enrico Fermi proposed (1927) a quantum mechanical theory for solving the electronic structure of many-body system [147,148]. This theory is formulated in terms of the electron density *ρ(r)*, instead of the wave function. The total energy of a system comprises three terms:

$$E_{TF}[\rho(r)] = A_1 \int \rho(r)^{\frac{5}{3}} dr + \int \rho(r) V_{ext}(r) dr + \frac{1}{2} \int \int \frac{\rho(r)\rho(r)'}{|r - r'|} dr dr' \quad \text{Eq II. 35}$$

where the first term represents the kinetic energy of the non-interacting electrons in a homogeneous electron gas, with $A_1 = \frac{1}{10}(3\pi^2)^{\frac{2}{3}}$, and the second term is the electrostatic energy between nucleus-electron interaction. The $V_{ext}(r)$ is the static coulomb potential generated by the nuclei, while the third term is the classical electrostatic Hartree energy originating from the classical Coulomb repulsion between electrons.

This method has been used to account for a rough description of electrostatic potential and the charge density. The inclusion of correlation energy was developed as an approximation. For realistic systems, this scheme allows for poor quantitative predictions, and it does not reproduce any usual shell structure of atoms in various complex systems. The approximation of the kinetic energy is the main source in this model. The TF model over simplifies the description of the electron-electron interaction, which is treated classically, exchange interaction is not taken into account. This theory was used as a precursor to develop the modern Density Functional Theory. In the following section, we will briefly revise the basis of the Density Functional Theory, which have been almost exclusively applied in this thesis.

II.4 Density Functional Theory (DFT)

The complexity of Hartree-Fock (HF) methods is due to its dependence of the multi-electron wave function $(x_1, x_2, \dots, x_N)$. On the other hand, Density Functional Theory (DFT) works based on the electronic charge density distribution $\rho\ (r)$ rather than many-electron wave function. DFT has been widely used due to its good accuracy and high computational efficiency. It takes into account the structure of molecules, surfaces, crystals and their interactions. The advantage of using electron density is a much reduced dimensionality compared to that of the

wave function. Indeed, this method is easy to apply to larger systems because it works with electron density. Detailed discussions of DFT can be found in many books [149,150] and review articles [151–153]. Although, the DFT method is accurate for ground states it insufficiently accounts for the form of exchange-correlation functional. Some approximation are therefore used to refine the model for the exchange-correlations interactions.

II.4.1 Hohenberg and Kohn (HK) Theorems

Modern DFT theory of many-body systems was introduced by Hohenberg and Kohn [154] in 1964. This theory is based on two theorems: The first states that the ground state energy of any interacting many particle system in an external potential $V_{ext}\ (r)$, which determines uniquely by its ground state density. This theorem is also valid for systems with degenerate ground states. Assume that there are two different potentials $V_{ext}\ (r)$ and $V'_{ext}\ (r)$, they differ by a constant, and give the same ground state electron density $n_0\ (r)$. These two external potentials will give two different Hamiltonians, $\widehat{H}$ and $\widehat{H}'$, and these Hamiltonians will have the same ground state electron density $n_0\ (r)$, but the normalized ground state wave functions, ψ and ψ ′ are different. Then it follows that:

$$E_0 = E'_0 + \int n_0(r)[V_{ext}(r) - V'_{ext}(r)]dr \qquad \text{Eq II. 36}$$

where E_0 and E'_0 are the ground states energies for $\widehat{H}$ and $\widehat{H}'$ respectively. Similarly,

$$E'_0 = E_0 + \int n_0(r)[V'_{ext}(r) - V_{ext}(r)]dr \qquad \text{Eq II. 37}$$

The second theorem states that the universal functional of the density is independent of the external potential $V_{ext}(r)$. The exact ground state density of the system is the global minimum value of this functional, and the exact ground state density $n_0(r)$ minimizes the functional. In other words, the calculation of the ground state density will minimize the energy. The universal functional $F[n(r)]$ is independent on the external potential and it can be written as:

$$F[n(r)] \equiv T[n(r)] + E_{int}[n(r)] \qquad \text{Eq II. 38}$$

where $T[n(r)]$ is the kinetic energy and $E_{int}[n(r)]$ represents the interaction energy of the particles. For another wave function ψ ′, the energy functional E[ψ′] can be calculated using variational principle:

$$E[\psi'] \equiv \langle\psi'|\hat{T} + \hat{V}_{int} + \hat{V}_{ext}|\psi'\rangle \qquad \text{Eq II. 39}$$

If ψ' is the ground state wave-function, ψ_0 the above has its global minimum and the total number of particles is conserved. According to the HK theorem I and the variational principle:

$$E[\psi'] = \int n_0(r) V_{ext}(r) dr + F[n_0(r)]$$

$$= E[n = 0(r)] \qquad \text{Eq II. 40}$$

Therefore, the above energy attains the minimum only when the electron density is equal to ground state energy.

II.4.2 Kohn-Sham (KS) formulation

In order to apply DFT formalism one needs a good method for the F[n(r)] functional. The Kohm-Sham(KS) [155] method consists in the replacing the problem of the original many body system with an auxiliary independent particles system that will have the same ground state density but is easier to solve. The main advantage of this approximation is that it allows to calculate the kinetic energy in as implest way. It clearly provides a picture of one-particle interacting electronic systems. This method was introduced in 1965 and Walter Kohn was awarded with Nobel prize in chemistry in the 1998, together with John Pople.

The auxiliary independent-particle Hamiltonian is:

$$\widehat{H}_{KS} = -\frac{1}{2}\nabla^2 + V_{KS}(r) \qquad \text{Eq II. 41}$$

In order to evaluate the kinetic energy of a system with N independent particles, they obtained the corresponding potential $V_{KS}(r)$, by solving the system of N one-electron Schrodinger equations:

$$\left(-\frac{1}{2}\nabla^2 + V_{KS}(r)\right)\psi_i(r) = \varepsilon_i \psi_i(r) \qquad \text{Eq II. 42}$$

Each of the N orbital $\psi_i(r)$ has one electron with the lowest eigen values ε_i, with the density:

$$\rho(r) = \sum_{i=1}^{N} |\psi_i(r)|^2 \qquad \text{Eq II. 43}$$

The normalization condition is:

$$N = \int \rho(r) dr \qquad \text{Eq II. 44}$$

The independent-particle kinetic energy $T_S[\rho(r)]$ of the non-interacting particles is:

$$T_S[\rho(r)] = -\frac{1}{2}\sum_{i=1}^{N} \int \psi_i^*(r) \nabla^2 \psi_i(r) dr \qquad \text{Eq II. 45}$$

The universal functional $F[\rho(r)]$ is:

$$F[\rho(r)] = T_S[\rho(r)] + E_H[\rho(r)] + E_{XC}[\rho(r)] \qquad \text{Eq II. 46}$$

where $E_H[\rho(r)]$ represents the classic electrostatic energy of the electrons

$$E_H[\rho(r)] = \frac{1}{2}\int\int \frac{\rho(r)\rho(r')}{|r-r'|} dr dr' \qquad \text{Eq II. 47}$$

and $E_{XC}[\rho(r)]$ is the exchange-correlation energy.

The Kohn-Sham potential $V_{KS}(r)$

$$V_{KS}(r) = V_{ext}(r) + V_H(r) + V_{XC}(r)$$

$$= V_{ext}(r) + \frac{\delta E_H[\rho(r)]}{\delta \rho(r)} + \frac{\delta E_{XC}[\rho(r)]}{\delta \rho(r)} \qquad \text{Eq II. 48}$$

where $V_H(r)$ is:

$$V_H(r) = \int \frac{\rho(r')}{|r-r'|} dr' \qquad \text{Eq II. 49}$$

and the exchange-correlation potential is:

$$V_{XC}(r) = \frac{\delta E_{XC}[\rho(r)]}{\delta \rho(r)} \qquad \text{Eq II. 50}$$

Equations (II.42), (II.43) and (II.48) are the KS equations. These equations are solved self-consistently because $V_{XC}(r)$ depends on the density.

The definition of the XC energy functional is:

$$E_{XC}(r) = T[\rho(r)] - T_S[\rho(r)] + E_{int}[\rho(r)] - E_H[\rho(r)] \qquad \text{Eq II. 51}$$

where $T[\rho(r)]$ and $E_{int}[\rho(r)]$ represent kinetic and electron-electron interaction energies of the interacting system, respectively.

II.4.3 Exchange-Correlation (XC) functional

The previous equations provide a good method for finding the ground state energy of an interacting system when the form of E_{XC} is known. However, the form of E_{XC} has been exactly calculated for only a few simple systems, therefore this term is generally unknown. The E_{XC} term is commonly approximated in electronic structure calculations within the local density approximation or the generalised-gradient approximation. In the last decades hundreds of authors have been publishing different forms for the E_{XC} functional. The first method was proposed by Perdew and is also called the Jacob'sladder [156]. He introduced the simple classes of exchange-correlation functionals, which are the following:

II.4.3.1 Local Density Approximation (LDA)

The simplest method to obtain the exchange-correlation energy is called the Local-density approximation (LSDA is also have been used, for Local Spin Density Approximation). In this method, the contribution to the exchange-correlation energy from each volume in space and the same density of homogeneous electron gas. The total exchange-correlation energy E_{XC} can be obtained by integrating over the entire space:

$$E_{XC}^{LDA}[\rho(r)] = \int \rho(r)\varepsilon_{XC}\big(\rho(r)\big)dr \qquad \text{Eq II. 52}$$

where $\varepsilon_{XC}\big(\rho(r)\big)$ represents the exchange-correlation energy per electron. The Exchange-correlation functional can be obtained by differentiating this equation:

$$V_{XC}(r) = \rho(r)\frac{d\varepsilon_{XC}\big(\rho(r)\big)}{d\rho(r)} + \varepsilon_{XC}\big(\rho(r)\big) \qquad \text{Eq II. 53}$$

In this approximation, the point r is to be assumed in the inhomogeneous electron distribution. At this point the electron density $\rho(r)$ in both $V_{XC}\rho(r)$ and $\varepsilon_{XC}\rho(r)$, has the same value as in the homogeneous electron gas. Initially, Ceperley and Alder [157] calculated the exchange-correlation energy for the homogeneous electron gas using Monte Carlo methods and after the parametrisation was done by Perdew and Zunger [158]. LDA only predicts the limit of slowly-varying densities. However, the density is rapidly varying in most systems, and the LDA is clearly a crude approximation in these cases. However, the LDA method can still be used in predicting physical properties in real systems. In the following equation, we establish the connection of the interacting and non-interacting systems using the coupling constant

variable λ (which varies in the range of [0, 1]) in the presence of the external potential $V_\lambda(r)$. The corresponding Hamiltonian [159] is:

$$\hat{H}_\lambda = -\frac{1}{2}\sum_i \nabla_i^2 + \frac{1}{2}\sum_i \sum_{j\neq i} \frac{\lambda}{|r_i - r_j|} + \hat{V}_{ext} + \hat{V}_\lambda \qquad \text{Eq II. 54}$$

The exchange-correlation hole $n_{XC}(r, r')$ is defined with density $n(r)$ in terms of pair correlation function and scaled Coulomb interaction [160,161] as:

$$n_{XC}(r, r') = n(r') \int_0^1 d\lambda [g(r, r'; \lambda) - 1] \qquad \text{Eq II. 55}$$

The exchange-correlation energy can be written in the form of a classical electrostatic interaction

$$E_{XC}[n] = \frac{1}{2} \int dr dr' |r - r'| \qquad \text{Eq II. 56}$$

The following sum rule holds which arises from pair correlation function

$$\int dr' n_{XC}(r, r') = -1 \qquad \text{Eq II. 57}$$

It shows that the exchange-correlation energy depends on the shape of the exchange-correlation hole. These two facts account for the success of the LDA. In spite of success of the LDA, it has some limitations. Indeed, which means if systems density varies slowly, the LDA performs well, and chemical properties are well reproduced. However, in strongly correlated systems, where an independent particle approach breaks down, the LDA is very inaccurate. Moreover, the LDA gives a very poor description of hydrogen bonding and it does not account for van der Waals bonding. Recently, the LDA functional has been developed and it differs only in their contribution to the many-body electron gas. The most common LDA functionals are Perdew-Wang (**PW**) [162], Perdew-Zunger (**PZ**) [163] and Vosko-Wilk-Nusair (**VWN**) [164] for varying densities.

II.4.3.2 Generalized Gradient Approximation (GGA)

The LDA method neglects the real charge density in inhomogeneous system which differs from that of homogeneous electron gas. A simple term E_{XC} have been raised for local derivatives of the electron density is called Gradient Expansion Approximation (GEA), however this is ineffective on the accuracy of DFT. The electron density as well as the each

coordinate of the system take into account from the gradient of the density and it is called as Generalized Gradient Approximation (GGA). It includes higher derivatives of the electron density and density gradient gives better results than the LDA method in many cases, such as binding energy of molecules, bond lengths, crystal lattice constants and so on. The more general form is:

$$E_{XC}^{GGA}[\rho(r)] = \int \rho(r)\varepsilon_{XC}\big(\rho(r)\big)\,\nabla\,\rho(r)dr \qquad \text{Eq II. 58}$$

The above equation should satisfy some fundamental conditions such as reduce to LDA, respect the sum rule for the exchange-correlation hole and respect limits for small and large gradients. However, the exchange GGA functional are written in the forms of LDA exchange and F_x enhancement factor, which depend on the local magnitude of the density gradient. This gradient is scaled according to the electron density

$$E_x^{GGA} = F_x(s^2)E_x^{LDA} \qquad \text{Eq II. 59}$$

where s is the measure of inhomogeneity of the system

$$s = \frac{|\nabla^n|}{2k_f n} \qquad \text{Eq II. 60}$$

The above s term is a logarithmic derivative of density and density is measured by changing as compared to the Fermi factor. Over the years, several exchange functional have been developed in GGA. The most important functionals such as B88 (Becke, 1988 [165]), PBE (Perdew et al., 1996) have earned great attention by physicists and chemists communities and they have been used in the construction of hybrid functional. The Beck's B88 exchange functional is:

$$E_x^{B88}(s) = 1 + \frac{\beta c_2 (c_1 s)^2}{1 + 6\beta(c_1 s)sinh^{-1}(c_1 s)'} \qquad \text{Eq II. 61}$$

where

$$c_1 = 2(6\pi^2)^{\frac{1}{3}} \qquad \text{Eq II. 62}$$

$$c_2 = \frac{4}{3}\left(\frac{4\pi}{3}\right)^{\frac{1}{3}} \qquad \text{Eq II. 63}$$

and the parameter $\beta = 0.0042$ is an empirical parameter which is fitted from the Hartree-Fock exchange energies of noble gas atoms.

Perdew [166] and Perdew, Burke, Ernzerhof (PBE) [167] of GGA-PBE exchange component is:

$$F_x^{PBE}(s) = 1 + k - \left(\frac{k}{1 + \frac{\mu s^2}{k}}\right) \quad \text{Eq II. 64}$$

which for small s^2

$$F_x^{PBE}(s) \sim 1 + \mu s^2 \quad \text{Eq II. 65}$$

where $\mu \approx 0.21951$, and in the large s^2 limit

$$F_x^{PBE}(s) \sim 1 + k \quad \text{Eq II. 66}$$

The proposed value of $k = 0.804$. After the introduction of PBE functionals, several functionals have been proposed to give accurate predictions using modified correlation and exchange functionals. However, the GGA functionals has always large and smalls limit but it differs only in changing of the functional of μ value. Another functional such as revPBE has the same form as PBE and it varies the value of k to 1.245. This revPBE functional is used to calculate the accurate atomization energy. The functional of revPBE [168,169] is:

$$F_x = 1 + k - \left(1 - exp\frac{mus^2}{k}\right) \quad \text{Eq II. 67}$$

Also, the PBEsol functional can be used to improve calculations on solids and it is able to account for the structure of solids with high accuracy. This PBEsol functional use the same correlation enhancement factor and a different $\beta = 0.046$ value. The corresponding PBEsol [170] functional is:

$$F_x = 1 + k - \left(\frac{k}{1 + \frac{\mu s^2}{k}}\right) \quad \text{Eq II. 68}$$

RGE2 [171] functional uses the same μ as PBEsol functional and k is taken from the PBE functional. The RGE2 functional form is:

$$F_x = 1 + k - \frac{k}{\left[1 + \frac{\mu s^2}{k} + \left(\frac{\mu s^2}{k}\right)^2\right]} \quad \text{Eq II. 69}$$

The RPBE [172] exchange functional use the PBE correlation functional with PBEsol β to get:

$$F_x = 1 + k\left(1 - \frac{1}{2}\frac{1}{1 + \frac{\mu s^2}{k} - \frac{1}{2}e^{\frac{-\mu s^2}{k}}}\right) \quad \text{Eq II. 70}$$

II.4.3.3 Hybrid Functionals:

Hartree-Fock uses the exact exchange energy but does not account for correlation at all. Becke proposed using a portion of the exact HF exchange energy along with conventional GGA correlation [173, 174]. The general form is:

$$E_{XC}^{Hyb}[\rho] = E_{XC}^{GGA}[\rho] + \alpha\left[E_X^{HF}[\phi_{sel}] - E_X^{GGA}[\rho_{sel}]\right] \quad \text{Eq II. 71}$$

The parameter α is a semi-empirical constant determined by fitting of experimental data, ϕ_{sel} are the selected orbitals to which the exact exchange is applied (correlated *d*-electrons), and ρ_{sel} is the density of the selected electrons. Applying this exact exchange to localized electrons has the same general effect as PBE+U that is to localize and better handle correlated electrons. The benefits of hybrids over the +U scheme is that there are no system dependent parameters to choose (such as the U value).

II.4.3.4 Hubbard corrected Local Density Approximation (LDA+U)

Strongly correlated systems usually contain transition metal or rare earth metal ions with partially filled *d* or *f* shells. Because of the orbital-independent potentials in LDA and GGA, they cannot properly describe such systems. For example, LDA predicts transition metal oxides to be metallic with itinerant *d* electrons because of the partially filled *d* shells. Instead, these transition metal oxides are Mott insulators and the *d* electrons are well localized. In order to properly describe these strongly correlated systems, orbital-dependent potentials should be used for *d* and *f* electrons. There are several approaches available nowadays to incorporate the strong electron-electron correlations between *d* electrons and *f* electrons. Of these methods including the self-interaction correction (SIC) method [175], Hartree-Fock (HF) method [176], and GW approximation [177], LDA+U method [41] is the most widely used one. In the LDA+U method, the electrons are divided into two classes: delocalized s, p electrons which are well described by LDA (GGA) and localized d or f electrons for which an orbital-dependent term $\frac{1}{2}U\sum_{i\neq j} n_i n_j$

should be used to describe Coulomb $d-d$ or $f-f$ interaction, where n_i are d– or f–orbital occupancies. The total energy in LDA+U method is given as [178]:

$$E_{xc}^{LDA+U}[\rho(r)] = E_{xc}^{LDA}[\rho(r)] + E^{U}[\{n_\sigma\}] - E^{dc}[\{n_\sigma\}] \qquad \text{Eq II. 72}$$

where σ presents the spin index (up or down), and $\{n_\sigma\}$ is the density matrix of *d* or *f* electrons for spin- σ, the first term is the standard LDA energy functional, the second term is the electron-electron Coulomb interaction energy given by

$$E^{U}[\{n_\sigma\}] = \frac{1}{2}\sum_{\{m\},\sigma}\{\langle m,m''|V_{ee}|m',m'''\rangle n_{mm',\sigma}n_{m''m''',-\sigma} - \left(\langle m,m''|V_{ee}|m',m'''\rangle - \langle m,m''|V_{ee}|m''',m'\rangle\right)n_{mm',\sigma}n_{m''m''',\sigma}\} \qquad \text{Eq II. 73}$$

where *m* denotes the magnetic quantum number, and V_{ee} are the screened Coulomb interactions among the *d* or *f* electrons.

The last term in equation (Eq II.72) is the double-counting term which removes an averaged LDA energy contribution of these *d* or *f* electrons from the LDA energy. It is given by [178]

$$E^{dc}[\{n_\sigma\}] = \frac{1}{2}UN(N-1) - \frac{1}{2}J[N_\uparrow(N_\uparrow-1) + N_\downarrow(N_\downarrow-1) \qquad \text{Eq II. 74}$$

where $N_\sigma = Tr\left(n_{mm',\sigma}\right)$ and $N = N_\uparrow + N_\downarrow$. U and J present Coulomb and exchange parameters.

As a simple approximation, if the exchange and non-sphericity is neglected, Eq II.xx is simplified to:

$$E_{xc}^{LDA+U} = E_{xc}^{LDA} + \frac{1}{2}U\sum_{i\neq j} n_i n_j - \frac{1}{2}UN(N-1) \qquad \text{Eq II. 75}$$

The orbital energies ε_i are derivatives of Eq II.76 with respect to orbital occupations n_i:

$$\varepsilon_i = \frac{\delta E}{\delta n_i} = \varepsilon_{LDA} + U\left(\frac{1}{2} - n_i\right) \qquad \text{Eq II. 76}$$

In this simple consideration, the LDA orbital energies are shifted by −U/2 for occupied orbitals ($n_i = 1$) and by +U/2 for unoccupied orbitals ($n_i = 0$), resulting in lower and upper Hubbard bands separated by U, which opens a gap at the Fermi energy in transition metal oxides.

In the general case, the effective single-particle potential is

$$V_{mm',\sigma} = \frac{\delta(E^U[\{n_\sigma\}] - E^{dc}[\{n_\sigma\}])}{\delta n_{mm',\sigma}}$$

$$= \sum_{\{m\}} \{\langle m, m''|V_{ee}|m', m'''\rangle n_{m''m''',-\sigma} - (\langle m, m''|V_{ee}|m', m'''\rangle$$

$$- \langle m, m''|V_{ee}|m''', m'\rangle)\, n_{m''m''',\sigma}\} - U\left(N - \frac{1}{2}\right) + J\left(N_\sigma - \frac{1}{2}\right) \quad \text{Eq II. 77}$$

which is used in the effective single-particle Hamiltonian

$$\widehat{H} = \widehat{H}_{LDA} + \sum_{mm'} |\, inlm\sigma\rangle\, V_{ee}\, \langle inlm'\sigma| \quad \text{Eq II. 78}$$

where *i* denotes the site, *n* the main quantum number, and *l* the orbital quantum number. The matrix elements of V_{ee} can be expressed in terms of complex spherical harmonics and effective Slater integrals F_k as [179]

$$\langle m, m''|V_{ee}|m', m'''\rangle = \sum_k a_k(m, m', m'', m''')F_k \quad \text{Eq II. 79}$$

where $0 \leq k \leq 2l$ and

$$a_k(m, m', m'', m''') = \frac{4\pi}{2k+1} \sum_{q=-k}^{k} \langle lm|Y_{kq}|lm'\rangle \langle lm''|Y^*_{kq}|lm'''\rangle \quad \text{Eq II. 80}$$

$$F_k \approx \int\int_0^\infty (r_1 R_i(r_1))^2 (r_2 R_i(r_2))^2 \frac{r_<^k}{r_>^{k+1}} dr_1 dr_2, \text{for } k > 0 \quad \text{Eq II. 81}$$

here, $r_<$ is the smaller of r_1 and r_2, and $r_>$ the larger.

The relations between the Slater integrals and the screened Coulomb and exchange parameters *U* and *J* are:

$$U = F_0;\ J = (F_2+F_4)/14, \qquad \text{for } 3d \text{ or } 4d \text{ systems,}$$

$$U = F_0;\ J = (286F_2+195F_4+250F_6)/6435, \text{ for } 4d \text{ or } 5f \text{ systems,} \quad \text{Eq II.82}$$

The ratio F_4/F_2 and F_6/F_2 are taken from atomic situations. $F_4/F_2 \sim 0.625$ for 3*d* transition elements [180], and $F_4/F_2 \sim 2/3$, $F_6/F_2 \sim 1/2$ for 4*f* lanthanides. The screened Coulomb

parameter *U* can be calculated from the constraint LDA method [181], so that the LDA+*U* method remains a first principle method (no adjustable parameters).

For the double-counting term, there are two different treatments: the so-called around mean field (AMF) and fully localized limit (FLL) (also called atomic limit) approaches. The former is more suitable for small *U* systems [182] and the latter is more suitable for large *U* systems. [183] The energies for the double counting are given by [47]:

$$E_{AMF}^{dc} = \frac{1}{2}\sum_{m\neq m',\sigma\sigma'}[U_{mm'} - \delta_{\sigma,\sigma'}J_{mm'}]\bar{n}\,\bar{n}$$

$$= \frac{1}{2}UN^2 - \frac{U+2lJ}{2l+1}\frac{1}{2}\sum_{\sigma}N_{\sigma}^2 \qquad \text{Eq II.83}$$

$$E_{FLL}^{dc} = \frac{1}{2}\sum_{m\neq m',\sigma\sigma'}[U_{mm'} - \delta_{\sigma,\sigma'}J_{mm'}]\bar{n}_{\sigma}\bar{n}_{\sigma'}$$

$$= \frac{1}{2}UN(N-1) - \frac{1}{2}J\sum_{\sigma}N_{\sigma}(N_{\sigma}-1) \qquad \text{Eq II.84}$$

where $\bar{n} = N/2(2l+1)$ is the average occupation of the correlated orbitals and $\bar{n}_{\sigma} = N_{\sigma}/(2l+1)$ is the average occupation of a single spin of the correlated orbitals. Note that, (Eq II.84) is the same as (Eq II.74). For a detailed comparison of the different double counting terms, please refer to [184].

II.4.3.5 Modified Becke-Johnson (mbJ) method

As mentioned in the previous discussions, LDA and GGA severely underestimate bandgaps. Becke and Johnson developed a method based on the Optimized Potential Method (OPE), which is a computationally very demanding method but does greatly improve bandgap predictions. They constructed a relatively simple model for the exchange term that produces similar band gaps as expensive OPE [185]. GGA or LDA correlation is used in conjunction with the BJ ex-change. Tran and Blaha modified the BJ functional (MBJ) which further improved predicted band gaps and is the form used in this thesis (**Chapter III, Section III.2 Strain effect on the electronic properties of bulk SnO2 and Chapter IV: ENHANCED THERMOELECTRIC PROPERTIES OF STRAINED SNO$_2$**).

Becke and Johnson (BJ) [186] was designed to reproduce the exact exchange potential in atoms, which can be a good starting point. The multiplicative BJ potential, which does not contain any empirical parameters

$$v_x^{BJ}(\vec{r}) = v_x^{BR}(\vec{r}) + \frac{1}{\pi}\sqrt{\frac{5}{6}}\sqrt{\frac{t(\vec{r})}{n(\vec{r})}} \qquad \text{Eq II. 85}$$

where

$$t(\vec{r}) = \frac{1}{2}\sum_{i=0}^{N} \nabla\psi_i^*(\vec{r}).\nabla\psi_i(\vec{r}) \qquad \text{Eq II. 86}$$

is the KS kinetic-energy density, and

$$v_x^{BR}(\vec{r}) = -\frac{1}{b(\vec{r})}(1 - e^{-x(\vec{r})} - \frac{1}{2}x(\vec{r})e^{-x(\vec{r})}) \qquad \text{Eq II. 87}$$

is the Becke Roussel (BR) exchange potential, which was proposed to model the Coulomb potential created by the exchange hole. In equation (Eq II.87), *x* is determined from a nonlinear equation involving n, $\nabla(\vec{r})$, $\nabla^2 n(\vec{r})$ and t, while b is calculated with

$$b = [x^3 e^{-x(\vec{r})}/(8\pi n)]^{1/3} \qquad \text{Eq II. 88}$$

It has been shown that the BJ potential can be further improved for the description of band gaps by using a modified version developed by Tran and Blaha (TB-mBJ) which introduces a parameter to change the relative weights of the two terms in the BJ potential

$$v_x^{BJ-mBJ}(\vec{r}) = cv_x^{BR}(\vec{r}) + (3c-2)\frac{1}{\pi}\sqrt{\frac{5}{6}}\sqrt{\frac{t(\vec{r})}{n(\vec{r})}} \qquad \text{Eq II. 89}$$

with

$$c = \alpha + \beta\left(\frac{1}{V_{cell}}\int_{cell}\frac{\nabla \mathrm{n}(\vec{r}')}{\mathrm{n}(\vec{r}')}d^3(\vec{r}')\right)^{1/2} \qquad \text{Eq II. 90}$$

where V_{cell} is the unit cell volume and α and β are two free parameters whose values are $\alpha = -0.012$ and $\beta = 1.023\text{bohr}^{(1/2)}$ according to a fit to experimental results. The way in which this linear combination is written makes sure that for any value of c the LDA exchange potential

is recovered for a constant electron density. For $c = 1$ the original BJ potential is recovered. This potential has yield satisfying results for many different systems, including transition-metal compounds [186–188].

II.5 Overview of DFT concepts and computational tools

II.5.1 Bloch Theorem

The description of crystal lattices is based on the assumption that the atoms adopt their equilibrium positions and form a structure that repeats itself periodically in three directions in space and in infinite way. In mathematical terms, if we call $V(\vec{r})$ the external potential acting on the electrons of such a system, the definition of a crystalline lattice:

$$V(\vec{r} + \vec{R}) = V(\vec{r}) \qquad \text{Eq II. 91}$$

where $\vec{R}$ is a translation vector of the direct network corresponding to a linear combination of the entire three unit vectors defining the network periodicity in the three spatial directions: $\vec{R} = l_1\vec{a}_1 + l_2\vec{a}_2 + l_3\vec{a}_3$.

Consequently, the total electronic Hamiltonian and all the physical quantities describing the periodic system are also characterized by the translational invariance network to the extent that the Hamiltonian operator commutes with the operators that generates translations through the network points. Any individual functions can therefore be written as the product of a function $u_{\vec{g}}$ that has the network periodicity by a plane wave $e^{i.\vec{g}\vec{r}}$ with $\vec{g}$ any vector in reciprocal space.

$$\phi(\vec{r}) = u_{\vec{g}}(\vec{r})e^{i.\vec{g}\vec{r}} \qquad \text{Eq II. 92}$$

Since there are an infinite number of vectors in reciprocal space, the Hamiltonian of such a system is therefore characterized by an infinite number of eigenvectors. This invariance property by translational symmetry has been described in a more advantageous way in the Bloch theorem which states that any single electron wave function of a crystal lattice $\phi_{\vec{k}}^{n}(\vec{r})$ can be expressed as the product of a planewave $e^{i.\vec{g}\vec{r}}$ with a function with same periodicity as the periodic potential $u_{\vec{k}}^{n}(\vec{r})$:

$$\phi_{\vec{k}}^{n}(\vec{r}) = u_{\vec{k}}^{n}(\vec{r})e^{i.\vec{g}\vec{r}}$$

with Eq II.93

$$u_{\vec{k}}^{n}(\vec{r}+\vec{R}) = u_{\vec{k}}^{n}(\vec{r})$$

$\vec{k}$ represents a wave vector of the first Brillouin zone of the reciprocal lattice and n corresponds to the band number.

The base of planewaves is complete and orthonormal and hence any normalizable continuous function can be developed on a plane-wave basis. The periodic function $u_{\vec{k}}^{n}(\vec{r})$ can therefore be decomposed on a discrete basis of plane waves whose wave vectors belong to the reciprocal lattice:

$$u_{\vec{k}}^{n}(\vec{r}) = \Omega^{-\frac{1}{2}} \sum_{\vec{k}} C_{\vec{K}}^{n,\vec{k}}\, e^{i.\vec{K}.\vec{r}} \qquad \text{Eq II. 94}$$

where $\vec{K}$ and Ω represents respectively a vector of the reciprocal lattice and the volume of the simulated lattice. The development of $\phi_{\vec{k}}^{n}(\vec{r})$ in the same base is:

$$\phi_{\vec{k}}^{n}(\vec{r}) = \Omega^{-\frac{1}{2}} \sum_{\vec{k}} C_{\vec{K}}^{n,\vec{k}}\, e^{i.(\vec{K}+\vec{k}).\vec{r}} \qquad \text{Eq II. 95}$$

From this equation, the only unknowns to be determined are the coefficients $C_{\vec{K}}^{n,\vec{k}}$.

The Bloch theorem allows to transform the problem of solving an infinite number of single-electron equations to the resolution of a finite number of single-electron equations for an infinite number of points k in a finite volume (Brillouin zone). To achieve optimal interpolation, methods to reach discrete sampling points in space were developed (e.g. sampling Monkhorst-grid VASP and Quantum espresso code).

II.5.2 K-points sampling

As a plane wave expansion is used, one is generally working in the reciprocal space. Therefore, we usually need to sample a few k-vectors in the reciprocal space (The first Brillouin zone) to calculate a well converged total energy.

DFT software packages usually save time by analyzing the symmetry of the system in question and using the symmetries of the point group of your system to reduce the BZ down to the so called “irreducible BZ”. The software then only picks a few points in the irreducible BZ to save even more computational time. In this dissertation we use the Monkhorst and Pack grid method for sampling the BZ. This method samples k-points uniformly in the BZ [189,190]. The

user only need specify the number of k-points they wish to sample in z, y, and z directions. The more k-points one samples the greater the accuracy, but the larger the computational cost. A large k-point grid is needed to accurately calculate the electronic properties of your systems, but not to reach structural convergence.

II.5.3 Full potential- linearized augmented plane wave (FP-LAPW) + local orbitals method

II.5.3.1 Linearized augmented plan wave basics functions

The solution of many electron problems has been changed to an eigen-value problem of single particle Kohn-Sham equation Eq II.42:

$$\left(-\frac{1}{2}\nabla^2 + V_{ext}(r) + \int \frac{\rho(r)}{|r_1 - r_2|} dr_2 + V_{XC}(r)\right)\phi_i(r) = \varepsilon_i \phi_i(r) \qquad \text{Eq II. 96}$$

A lot of methods have been proposed for solving Eq II.97 for different applications, geometries, symmetries, chemical elements and materials requiring different approximations [191]. The eigenvalue problem Eq II.96 is directly related to choosing basis function sets $\{\psi_G(k,r)\}$ for all reciprocal lattice vectors up G to the largest value of K_{max},

$$\varphi_{k,v}(r) = \sum_{|k+G| \leq K_{max}} C_{k,v}^{G} \phi_G(k,r) \qquad \text{Eq II. 97}$$

where $C_{k,v}^{G}$ are vibrational coefficients with the reciprocal lattice vector k for the v^{th} sphere [191]. Using Eq II.97, the partial differential equation Eq II.96 can be solved through algebraic equations which gives the values of $C_{k,v}^{G}$.

The Bloch theorem gives the most straightforward suggestion for three dimensional periodic solids, which would be to expand the wave function into plane wave or Fourier series, respectively,

$$\phi_G(k,r) = e^{i(k+G)r} \qquad \text{Eq II. 98}$$

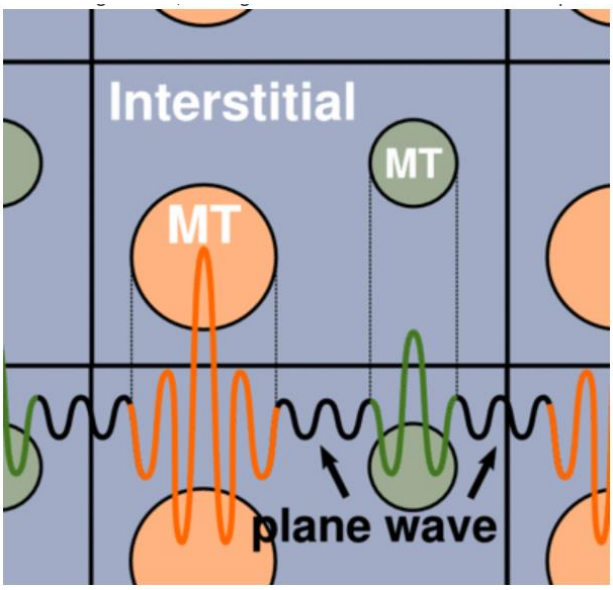

Figure II.2 Space division both in the APW and LAPW methods [192].

Slater developed the augmented plane wave (APW) method in which the space is partitioned into spheres centered at each atom site, which is strongly varying but nearly spherical, the so-called muffin-tin (MT) sphere, and into the remaining interstitial region as in Figure II.5 [192]. Koelling and independently Andersen proposed a linearization method in the radial functions inside the MT sphere, i.e., the basis functions inside the spheres are linear combinations of $u_l(r)Y_{l,m}(\theta,\phi)$ and its radial derivative $u'_l(r)Y_{l,m}(\theta,\phi)$ [193, 194].

$$\phi_G(k,r) = \frac{1}{\Omega}e^{i(k+G)r} \qquad r \in Interstitial$$

$$= \sum_{l,m}\left\{A^v_{l,m}u_l(r) + B^v_{l,m}u'_l(r)\right\}Y_{l,m}(\theta,\phi) \qquad r \in \text{MT} \qquad \text{Eq II. 99}$$

The radial function $u_l(r)$ satisfies

$$-\frac{d^2}{dr^2} + \frac{l(l+1)}{r^2} + V_v(r) - \varepsilon_l\}ru_l(r,\varepsilon_l) = 0 \qquad \text{Eq II. 100}$$

where $V_v(r)$ is the spherically symmetric potential inside the v^{th} sphere and ε_l is the angular momentum dependent energy parameter. The spherical harmonics $Y_{l,m}(\theta,\phi)$, which is used to illustrate an atomic orbital of hydrogen atom, is the solution of the angular part of Laplace's equation $\nabla^2 f = 0$. These functions are matched to the values and derivatives of the plane-waves on the sphere boundaries and the basis functions augmented in the way are the linearized APW (LAPW) method. Harmann and Weinert have introduced the full potential-LAPW (FP LAPW)

method, which solves the non-spherical potential problem by partitioning the region to vacuum, interstitial and MT sphere regions [195, 196].

II.5.3.2 Augmented plan wave + local orbitals (APW + lo) basis functions

Recently, Sjösted, Nordström and Singh [197] proposed an alternative way to linearize the APW method in which the continuous derivative condition is released. In this method, the eigenvalue problem of the original APW method is linearized by choosing fixed linearization energies (ε_l) for the APW basis functions in Eq II.97. Then, the flexibility of the basis set with respect to the reference energy is obtained by adding a set of local orbitals (lo):

$$\phi_{APW}^{lo}(r) = 0 \qquad r \in Interstitial$$

$$= \sum_{l,m} \{A_{l,m} u_l(r^\alpha, \varepsilon_l) + B_{l,m} u'_l(r^\alpha, \varepsilon_l)\} Y_{l,m}(r^\alpha) \qquad r \in \text{MT} \qquad \text{Eq II. 101}$$

using the same linearization energies. The coefficients are obtained by requiring the function to be zero at the sphere boundary.

The APW basic functions keep the convergence behavior of the original APW method while the local orbitals (lo) make it flexible with respect to choice of the reference energy. Therefore, the complete APW+lo basis set consists of two different types of basis functions, the 'APW' one (Eq II.96) at fixed linearization energies and the 'lo' one (Eq II.101). As in the LAPW method, when different states with the same l (semi-core states) have to be treated, a second set of local orbitals of the form:

$$\phi_{APW}^{lo}(r) = 0 \qquad r \in Interstitial$$

$$= \sum_{l,m} \{A_{l,m} u_l(r^\alpha, \varepsilon_l) + C_{l,m} u_l{}^{(2)}(r^\alpha, \varepsilon_l{}^{(2)})\} Y_{l,m}(r^\alpha) \qquad r \in \text{MT} \qquad \text{Eq II. 102}$$

that can be added. The coefficients are determined by matching the function to zero at the muffin-tin radius, with no condition on the slope.

II.5.3.3 Wien2k code

Wien2k is amongst the famous packages using FP-LAPW methods [198]. As can be seen from the illustrated flowchart of wien2k (Figure II.3), the code is divided in two parts. The

first part (Top row of Figure II.3) analyzes the input files, while the second part performs a self-consistent calculation. The input routine starts from a structure file containing structural information of the system such as lattice parameters, atomic positions, and muffin-tin radii. Based on this input file, the subroutines called NN, SGROUP and SYMMETRY check for overlap between the different muffin-tin spheres and determine the symmetry of the unit cell. In the next step, LSTART calculates the atomic densities for all atoms in the unit cell, which would be used by KGEN in combination with the other input files to determine a suitable k-mesh. Finally, in the final initialization step called DSTART, which consists of a starting electron density ρ, constructed based on a superposition of the atomic densities. During this initialization all the necessary parameters are fixed as well: the exchange-correlation approximation (LDA, GGA, LSDA), $R_{MT}K_{max}$, l_{max} and the energy parameter that separates the core states from the valence states. In order to perform an optimal use of computation time, a good choice of $R_{MT}K_{max}$ and the k-mesh is needed. For instance, the calculation should be accurate, but not more accurate than needed and fast, but not faster than the required accuracy permits. Once the starting density is generated, the self-consistent calculation can start. This process is divided into several subroutines, which are repeated over and over until convergence is reached and the calculation is self-consistent. LAPW0 starts with calculating the Coulomb and the exchange-correlation potential. Next, LAPW1 solves the secular equation for all the k-values in the k-mesh and finds by diagonalization of the Kohn-Sham equation the eigenvalues and eigenfunctions of the valence states.

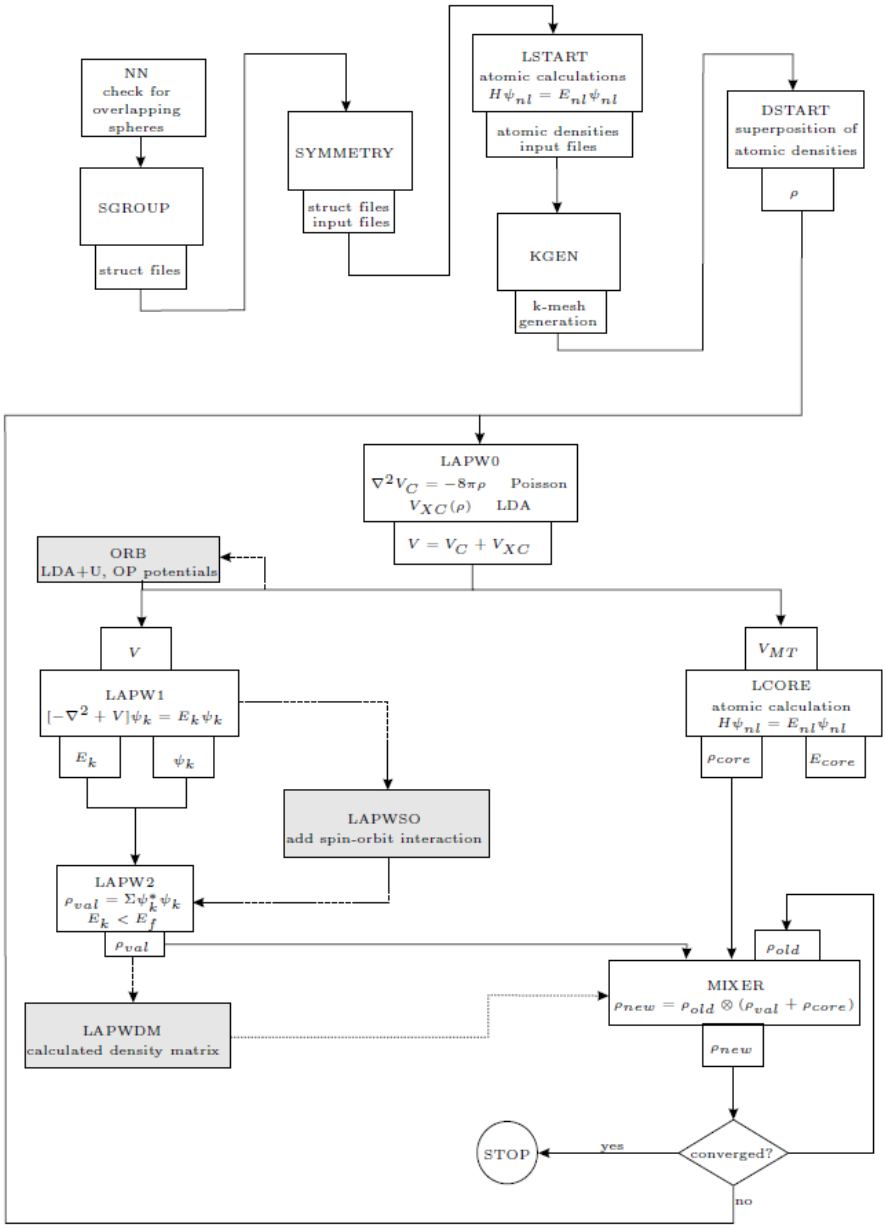

Figure II.3 Program flow in WIEN2k [198]

The following subroutine, LAPW2 determines the Fermi energy that separates filled from unfilled states. Once this energy is known the eigenfunctions resulting from LAPW1 can be used to construct a valence density:

$$\rho_{val}(\vec{r}) = \sum_{\varepsilon_{\vec{k},i} < E_F} \phi^*_{\vec{k},i}(\vec{k})\phi_{\vec{k},i}(\vec{k}) \qquad \text{Eq II. 103}$$

The states and energies of the core electrons are calculated separately in a regular atomic calculation in the LCORE subroutine, which results in a total core density ρ_{core}. Both densities ρ_{val} and ρ_{core} combined give the total density, $\rho_{total} = \rho_{core} + \rho_{val}$. Since this density often

differs a lot from the old density ρ_{old}, they are mixed by MIXER to avoid large fluctuations between iterations that would lead to divergence: $\rho_{new} = \rho_{old} \otimes (\rho_{core} + \rho_{val})$. Once the end of the cycle is reached, Wien2k algorithm checks for convergence between the old and the new density. If they differ from each other a new iteration would started with the new density as input density. This procedure would repeated until the old and new density are consistent. When this is the case, the self-consistency cycle ends and the self-consistent solution of the equation equals ρ_{new}. This program flow corresponds to the trajectory in full lines shown in Figure II.3. The subroutines reached by the dashed lines are optionally.

Finally, additional packages are available to facilitate deeper analysis of the calculated results, e.g. the determination of the density of states, X-Ray spectra, and band structure calculation.

II.5.4 plane wave and pseudo potentials basis

II.5.4.1 plane waves method

The plane wave basis, associated with periodic boundary conditions are relatively suitable for the study of solids to the extent that they comply with Bloch theorem. As indicated in the preceding paragraph, the plane-wave decomposition of wave functions $\phi_{\vec{k}}^{n}(\vec{r})$ consist to express these wave functions using Fourier series:

$$\phi_{\vec{k}}^{n}(\vec{r}) = \Omega^{-\frac{1}{2}} \sum_{\vec{k}} C_{\vec{K}}^{n,\vec{k}} e^{i(\vec{K}+\vec{k}).\vec{r}} \qquad \text{Eq II. 104}$$

with n=1,...,*Ne*.

where $\vec{K}$ and $\vec{k}$ represents a vector from the reciprocal lattice and a wave vector from the same reciprocal lattice belonging to the first Brillouin zone respectively.

In theory, the plane waves employed base should be infinite. However, in practice the base used is finite. The number of plane waves N_{pw}, can in principle be obtained from the number of vectors $\vec{k}$ and $\vec{K}$. In practice, it is defined from a breaking energy (we call it cut-off) E_{cut}, which represents a stopping criterion that corresponds to the minimization of the error committed at the kinetic energy (plane waves being eigenfunctions of the kinetic energy operator):

$$\frac{\hbar^2}{2m_e}\left|\vec{k}+\vec{K}\right|^2 < E_{cut} \qquad \text{Eq II. 105}$$

that imposes to the following expression for plane waves number:

$$N_{pw} \approx N_k \times \frac{1}{2}\pi^2 \Omega E_{cut}^{\frac{3}{2}} \qquad \text{Eq II. 106}$$

where N_k is the number of vectors $\vec{k}$ by which the Brillouin zone is sampled and Ω is the volume of the simulation cell. The basis used will include even more of plane waves when E_{cut} is high. The calculation will be all the more precise but the calculation time will also be even more important. An alternative way of limiting the number of plane waves is to use the value K_{max} by imposing the condition $K < K_{max}$ to all K vectors game $\vec{K}$ (i.e. sphere of radius K_{max} centered at the origin of the reciprocal lattice, all reciprocal lattice vectors who are in this sphere are included in the base).

II.5.4.2 Pseudopotential method

The plane waves basis use the same resolution in each region of space so that to describe both ionic cores (i.e. core surrounded by internal electronic cloud) and partially localized electronic states around them, the number of vectors $\vec{K}$ needed would be relatively localized to carry out the solving of Kohn-Sham equations. One way around this difficulty is to use the pseudopotentials method. This method relies on the assumption that the physical properties and chemical properties of a system are essentially governed by the valence electrons (i.e. the outermost electrons) while ionic hearts can be considered "Frozen" in their atomic configurations. The method of pseudopotentials consist just to use the valence electrons, which then move in an effective external potential produced by these inert ionic cores called pseudopotential. This pseudopotential try to reproduce the interaction generated by the true potential of the valence electrons without explicitly including in the core electrons.

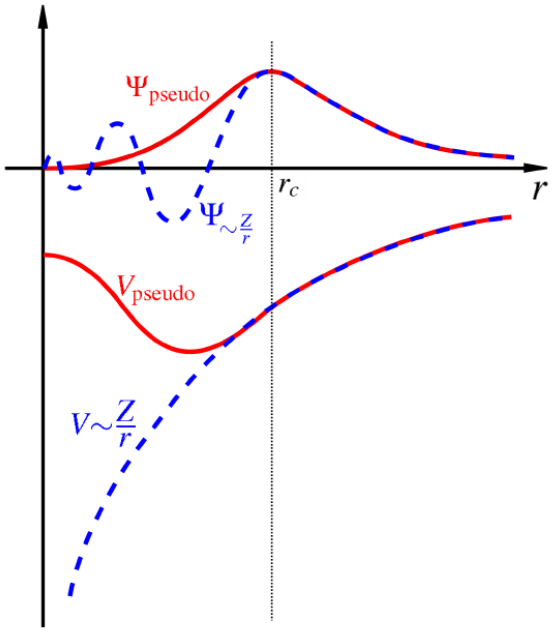

Figure II.4 schematic representation of the replacement of a wave function all electrons ($\psi \sim \frac{Z}{r}$) and core potential ($V \sim \frac{Z}{r}$) by a pseudo-wave-function (ψ_{pseudo}) and by a pseudopotential (V_{pseudo}), respectively. This operation leads to the elimination of nodes and oscillations of the wave function resulting from orthonormalization conditions, thereby treating pseudo-functions using a reduced number of plane wave compared to the actual case of wave functions.

The wave functions oscillating in the core region (Figure II.4), resulting from the constraint orthogonality with core states (Pauli repulsion principle) and that would relatively be difficult to describe from a plane wave basis (number of vectors $\vec{K}$ very high), are replaced by pseudo-wave functions that are devoid of nodes in the core region. The pseudopotential is therefore constructed so that the characteristics of the phase shift produced on the pseudo-wave functions are identical to those resulting from the action of the ionic core on the real wave functions valence, while generating pseudo-wave functions devoid of oscillations in the ionic core region. Beyond this ionic core region delimited by r_c, the pseudo-wave functions must be identical to real valence wave functions, which are also called, with reference to this pseudopotential "all electrons".

These pseudo-wave functions are smoother or "soft" that the real wave functions and may therefore be properly represented by using a number of vectors $\vec{K}$ much lower than the one needed in the treatment of real wave functions. This operation leads to the elimination of nodes and oscillations of the wave function resulting from orthonormalization conditions, thereby treating pseudo-functions using a reduced number of plane wave compared to the actual case of wave functions. If the pseudopotential is adjusted so that the built-in region of ionic core

corresponding to the pseudo-wave-function is equal to the integrated charge associated with the true wave function, the pseudopotential is said norm conserving. Thus, although pseudopotential method greatly simplifies the description of valence electrons, the use of norm conserving pseudopotentials preserved guarantees a correct consideration of this outer electron shell. Such pseudopotentials are also highly transferable, that is to say, they can be used to predict the chemical properties of an atom in a wide range of situations (e.g. bulk, surface).

So far, as the norm conserving pseudopotentials are not based on the preliminary experimental knowledge of a chemical element, it can be constructed for any element of the periodic table. However, the use of the pseudopotential norm conserved is very costly in the case of transition metals or rare earths. Because, these atoms have localized orbitals and require a large number of plane waves. It is then necessary to use pseudopotentials not norm conserving. This pseudopotential are characterized by arbitrarily smooth waves in pseudo functions regions of the heart (e.g. Vanderbilt pseudopotentials also called "ultrasoft" (USPP: ultrasoft pseudopotentials [199])). Further, Blöch [200] helped improve the concept of pseudopotential by combining this method with the method LAPW to form pseudopotentials type "PAW" (Projector Augmented-Wave).

The use of pseudopotentials can greatly reduce the number of plane waves needed to treat a periodic system. However, in some cases it may be desirable to consider all of the electrons in the system. In this case, if this methodology is not appropriate then it is necessary to resort to an all electrons methods, which are the LAPW method (Linearized Augmented Plane Wave) and "APW + lo'.

II.5.4.3 QUANTUM ESPRESSO (QE) code

QUANTUM ESPRESSO package is an open source computer code for electronic structure calculations and materials modeling [201]. It is freely available to researchers around the world under the terms of the GNU General Public License. QE code is based on density functional theory and its approximations, which enables calculation of quantum mechanical systems. Hence, it is very practical for crystal structure and surface structure calculations, which are the main tool of quantum chemistry measurements. Quantum espresso package is written mostly in Fortran 95, Fortran 77 and C programing languages. Parallelization is also possible by MPI (message passing interface) libraries [201] which reduces computational cost considerably. Gianozzi et al. [201] implemented many different concepts in the code. These useful implementations are ground state energy calculation of Kohn Sham orbitals,

pseudopotential approximations for the exchange correlation potentials, supercell approach, structural optimization schemes, ab initio molecular dynamics schemes, calculation of magnetic systems, and density functional perturbation theory calculations. It has several different codes in it, which are devoted for different type of calculations. These codes are called PWscf, CP, PHonon, Atomic, PWcond, GIPAW, XSPECTRA, Wannier90, PostProc, PWggui. The input file consist of three namelists, 'Control', 'System' and 'Electrons'. Control should indicate the calculation type, whereas System namelist defines the structural and electronic properties of the system, and Electrons namelist defines which algorithms would be used for the self consistent solutions. There is other mandatory fields such as the input cards that are shown in last three titles called atomic species (includes type of the atomic species and used pseudopotentials), atomic positions (the crystal lattice structure), and kpoints (number of points used for the brillouin zone integration in the reciprocal space). In order to run this input file one must use the executable program 'pw.x' as: pw.x <inputfile> outputfile.

II.5.4.3 VASP code

The Vienna Ab-initio Simulation Package (VASP) performs ab-initio density functional theory calculations [202,203]. It is by far one of the most popular computational codes for calculations of infinite systems such as solid states and condensed matters. VASP uses plane wave basis set rather than localized basis set. The PAW method or ultra-soft pseudopotentials are used to describe the interaction between ion and non-valence electron so that the size of the basis set can be reduced. The self-consistency cycles and choices of numerical methods to calculate the electronic Kohn-Sham ground state in VASP are quite efficient and robust. Periodic boundary conditions are used to treat infinite numbers of atoms. The package also includes the Monkhorst Pack to sample the Brillouin zone. The VASP offers support for a large variety of platforms, such as Pentium, Athlon, IBM, HP, and Cray. All these features make the package very suitable for computations of extended large systems. In principle, in paralleled computing the more processors are used, the faster the calculation is. However, for the computer clusters, there is always a critical number of CPUs (depending on the processor type), larger than which the computation speed does not increase linearly with the number of CPUs used. For example, computing on four nodes might be two times faster than computing on two nodes, but computing on eight nodes does not necessarily improve the efficiency by as much as four times. A typical VASP calculation requires at least four basic input files, INCAR, POTCAR, POSCAR and KPOINTS

CHAPTER III: STRAIN AND SIZE EFFECTS ON SnO_2 ELECTRONIC PROPERTIES

Table of contents

CHAPTER III: STRAIN AND SIZE EFFECTS ON SnO_2 ELECTRONIC PROPERTIES

III.1 Strain effect on the electronic properties of bulk SnO2

III.1.1 Modeling and application of strain

Figure III.4 presents the crystal structure of bulk cassiterie SnO_2, which crystallizes in the rutile-type structure (space group P42/mnm) (see **Chapter I** part **I.2.1 Structural properties** for more details**)**. The lattice coordinates of one Sn atom position located at (0,0,0) and the two positions of O atoms located at (u,u,0), where u=0.3056 [204].

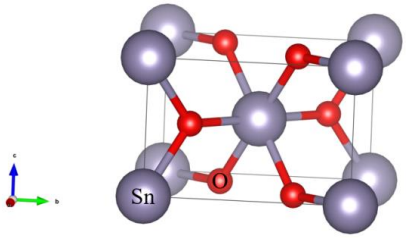

Figure III.1 Crystal Structure of SnO2 Unit Cell. Red and Grey Balls Are O and Sn Atoms Respectively

Our calculated equilibrium lattice constants used as input in the calculation are $\boldsymbol{a_0} = \boldsymbol{b_0} = 4.76$ Å and $\boldsymbol{c} = 3.29$ Å. Under biaxial strain, as illustrated in Figure III.2, $\boldsymbol{a}$ and $\boldsymbol{b}$ lattice constants were given different fixed-values in order to simulate either a compression or a tension, while the relaxation of the crystal is freely performed along the $\boldsymbol{c}$ axis for each $\boldsymbol{a}(\boldsymbol{b})$ given value. In this figure case, the biaxial strain can be expressed as:

$$\varepsilon_{xx}(\%) = \varepsilon_{yy}(\%) = \frac{a(b) - a_0(b_0)}{a_0(b_0)} \qquad \text{Eq III. 1}$$

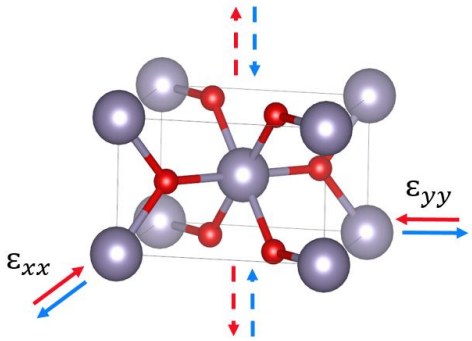

Figure III.2 Illustration of applied biaxial strain on SnO_2 Unit-cell, The Sn, and O Atoms Are Represented by Gray, And Red Spheres Respectively. Red-Solid and Blue-Solid Arrows Present The Compressive and Tensile Strain Respectively. Black-Dashed Arrows Indicates The *c* Lattice Movement Under Compressive (Red) and Tensile Strain (Blue)

We then considered a series of biaxial strain ranging from -6% to +6% imposed in the ***ab*** plane, where negative strain values represent a compressive strain while positive strain values represent a tensile strain.

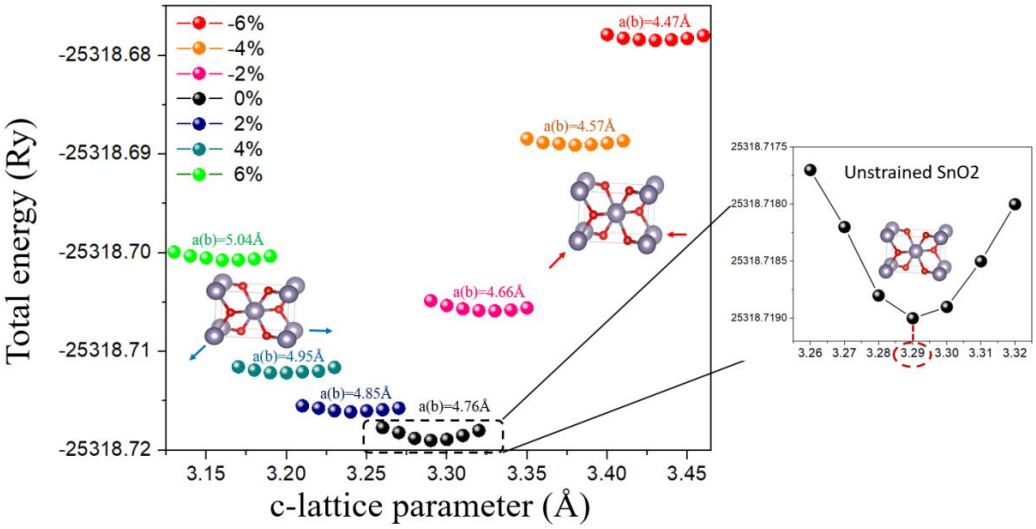

Figure III.3 Munghanam Fit of SnO2 Under Various Values of Strain. The Zoom-in is The Munghanam Fit of Unstrained SnO2

As can be observed from the Munghanam fit presented in Figure III.3, the unstrained SnO_2 exhibit the most stable crystal, while either compressive or tensile strained SnO_2 have higher total energies, and then less stable structures. Figure III.4 shows the variation of the ***c*** lattice parameter and its corresponding unit-cell volume under different values of $\varepsilon_{xx}(\varepsilon_{yy})$. As can be seen, the ***c*** lattice parameter increases under biaxial compressive strain and shrinks under biaxial tensile strain, whereas, SnO_2 unit-cell volume increases or decreases linearly as a function of the strain percent.

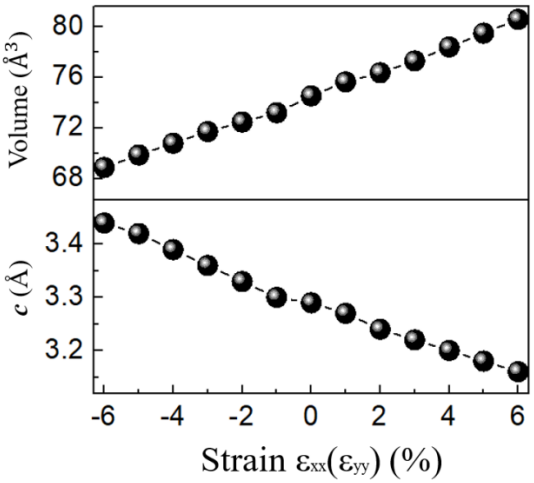

Figure III.4 Calculated ***c*** Lattice Parameter and its Corresponding Unit-Cell Volume of SnO_2 Under Different Strain Values

Thus we can conclude that the ***c*** lattice parameter variation shows a relatively weak ability to keep the crystal volume constant when the ***ab*** plane is distorted causing therefore a structural deformation of the SnO_2 unit-cell.

III.1.2 Electronic properties

Figure III.8 shows the calculated band structure of SnO2 under various strain values along high symmetry directions of the Brillouin zone. In the present calculation, the valence band maximum (VBM) is set equal to $E\text{-}E_F = 0$ eV, where E_F is the Fermi level energy. It is noticed from the band structure that the VBM and the conduction band minimum (CBM) occur at the Γ point, which clearly demonstrates that SnO2 remains a direct band gap semiconductor under strain, a fact that is of immense benefit to photonic and optoelectronic applications since optical transitions can be maintained in the absence of phonons contribution [205,206]. The calculated band gap of unstrained SnO2 is 3.593 eV, a value that is close to the experimental one [207], *i.e.* 3.6 eV. From Figure III.5, we can clearly notice that the band gap decreases under tensile strain, but increases under compressive strain.

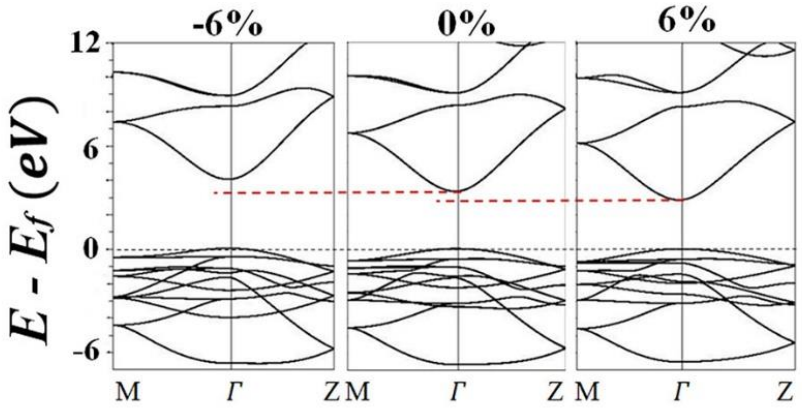

Figure III.5 Calculated Band Structure of SnO2 Under Three Strain Values. The Dashed Red Lines Show The Shift of The CBM as a Function Of Strain

The projected densities of states (DOS) of strained and unstrained SnO2 are presented in Figure III.6. In general, under compressive and tensile strain, valence and conduction bands seem to blue- and red-shift respectively. In addition, the blue-shift of the conduction band (CB) is higher than that of the valence band (VB). This progressive increase of the CB leads to a significant increase of the band gap energy. However, analogical description can be undertaken in the case of a tensile strain where a progressive and rapid decrease of the CB seems to lead to a band gap reduction. In each case, the valence band width either expands or retracts depending on the strain value demonstrating again the efficiency of an applied strain to provoke a motion

of the energy band structure. First, it is seen that the VB is mainly composed of O-2p states and admixture of Sn-4p,d states, whereas the CB is formed by O-2p and Sn-5s states hybridization, the nature of which does not change under biaxial strain (tensile or compressive).

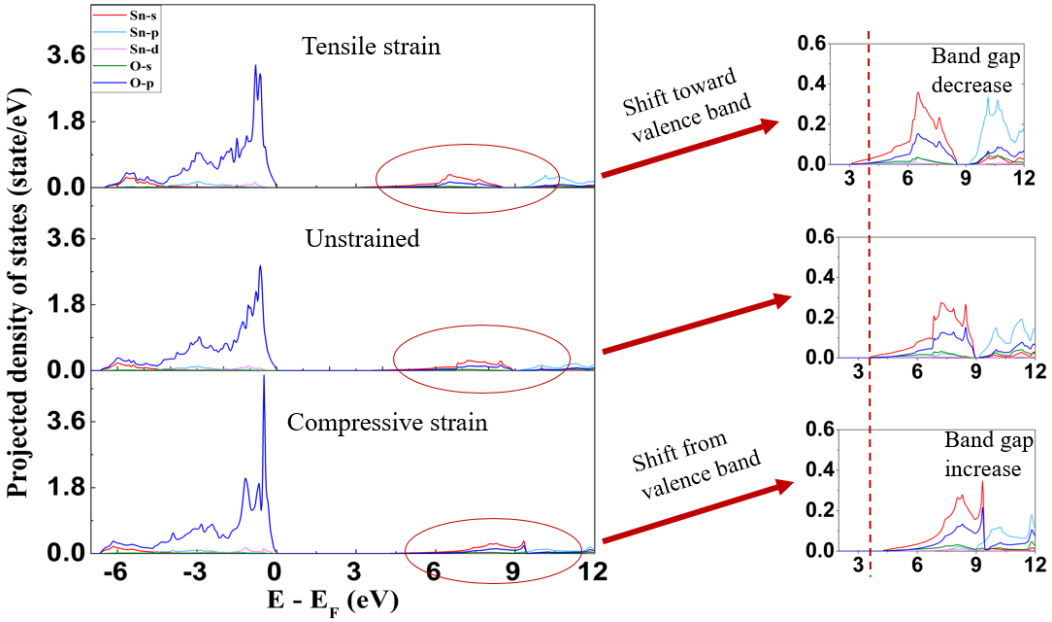

Figure III.6 Calculated Density of States (DOS) of SnO2 Under Three Strain Values. The Dashed Red Line Shows The Shift of The CBM as a Function of Strain

Second, this hybridization provides covalent bonding interaction between Sn and O. Indeed, the band gap reflects directly the strength of the covalent bond; stronger the covalent interaction is, wider is the band gap. A better picture of these effects is illustrated in the charge density distributions, shown in Figure III.7, viewed along the [110] axis. We can notice that an increase in the compressive strain is accompanied with an increase of the charge distribution. In addition, the Sn-O bond becomes shorter (stronger) which increases the charge density induced by this shrunk volume, and then explains the band gap energy increase. Opposite behavior is demonstrated in the case of a tensile biaxial strain, when the Sn-O bond become longer (weaker), and then the charge density become lower due to volume expansion.

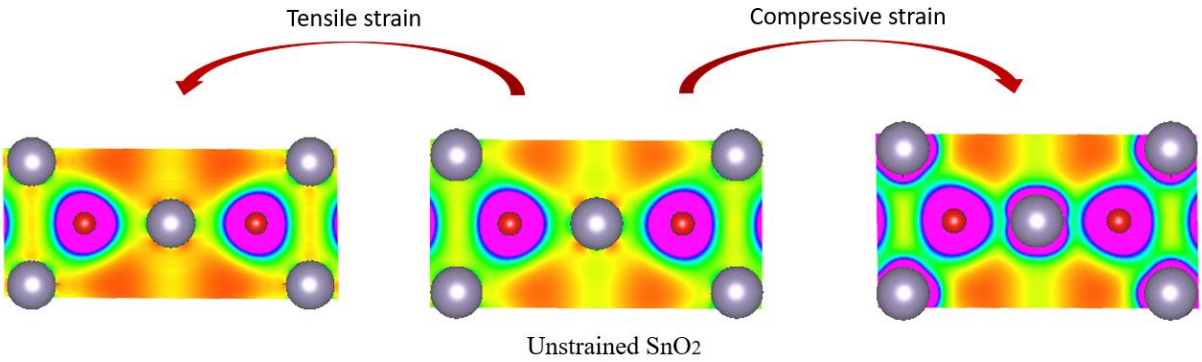

Figure III.7 Calculated Charge Density Distribution in The (110) Plane of Strained and Unstrained SnO2. Red and Grey Balls Are O and Sn Atoms Respectively

To further appreciate the strain effect on the band gap, we examine the variation of the VBM and CBM energies with strain, as plotted in Figure III.8. These energies decrease with expansion and increase with compression. In addition, the slope of the CBM plot is slightly smaller (i.e. more negative) than that of the VBM plot. This results in a nearly linear behavior of the band gap (inset).

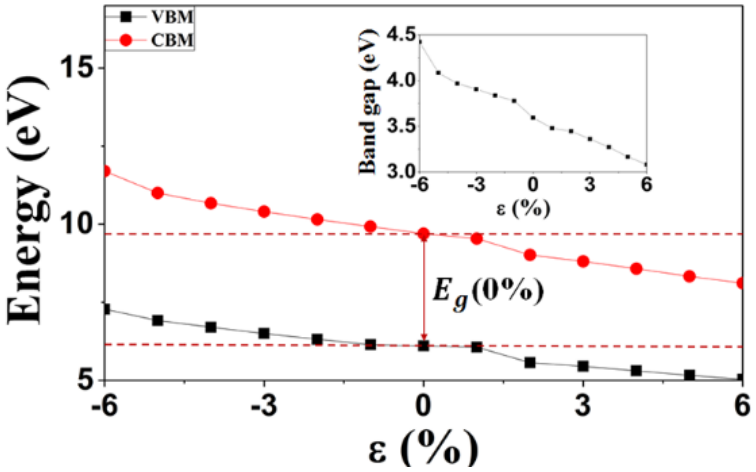

Figure III.8 Calculation of The Valence Band Maximum (VBM) and Conduction Band Minimum (CBM) Under Strain, The Inset Is The Calculated Band Gap Energy of SnO2 as Function of Strain.

Consequently, the band gap energy undergoes a clear modulation under biaxial strain varying from 4.42 to 3.08 eV as the strain value varies from -6% to +6%, respectively, which is in agreement with reported experimental and theoretical studies [208,209]. It is therefore concluded that the band gap of SnO2 can be effectively modulated by lattice strain which may also have huge benefit to other important applications such as optoelectronic devices and thermoelectric generators [210-212].

III.2 Thickness effect on the electronic properties of SnO2 ultra-thin films

In the present section, we aim to examine the effect of size and thickness on the electronic properties of SnO2 thin-films. For such a purpose, we have considered films with different thicknesses ranging from 0.3 nm (1 layer) to 2.5 nm (8 layers). In order to investigate the electronic properties of SnO2 thin-films, two cases will be treated in the following sections, namely; un-passivated SnO_2, which is the case of exfoliated SnO_2, and passivated SnO_2 films by pseudo hydrogens atoms on the surface, which is the case of hetero- epitaxially grown SnO_2.

III.2.1 Un-Passivated SnO2 film

III.2.1.1 Structural properties

Figure III.9 represents the crystalline structures of SnO2 films before and after relaxation.

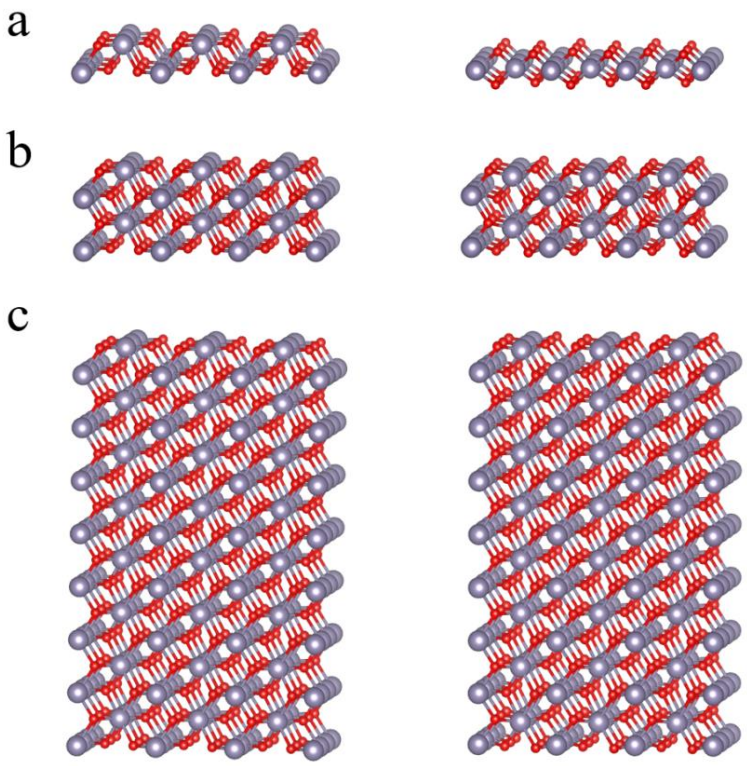

Figure III.9 Structure of Un-passivated SnO2 Films Before (Left) and After (Right) Relaxation in Different Sizes. Thickness of films is (a) 0.3 nm, (b) 0.6 nm, (c) 2.5 nm. Gray Spheres Present Sn Atoms, and Red Spheres Present O Atoms.

As the number of layers increases, the films crystalline structure become similar to that of bulk-SnO_2, especially, for eight layers film and more. Particularly, the film of one layer has

changed completely its morphology, where each Sn atom is encountered by four equidistant O atoms, forming a new crystalline structure.

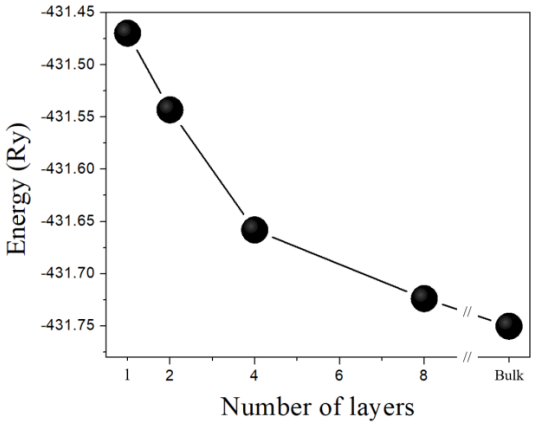

Figure III.12 Calculated energy of Un-Passivated SnO2 in different sizes.

From Figure III.10, one can see that the film energy decreases as the number of layers increases, and when this latter became eight layers or higher, the film energy start to converge to SnO_2-bulk energy.

III.2.1.2 Electronic properties

In order to examine the electronic properties of SnO2 films, total and projected density of states (DOS) have been calculated.

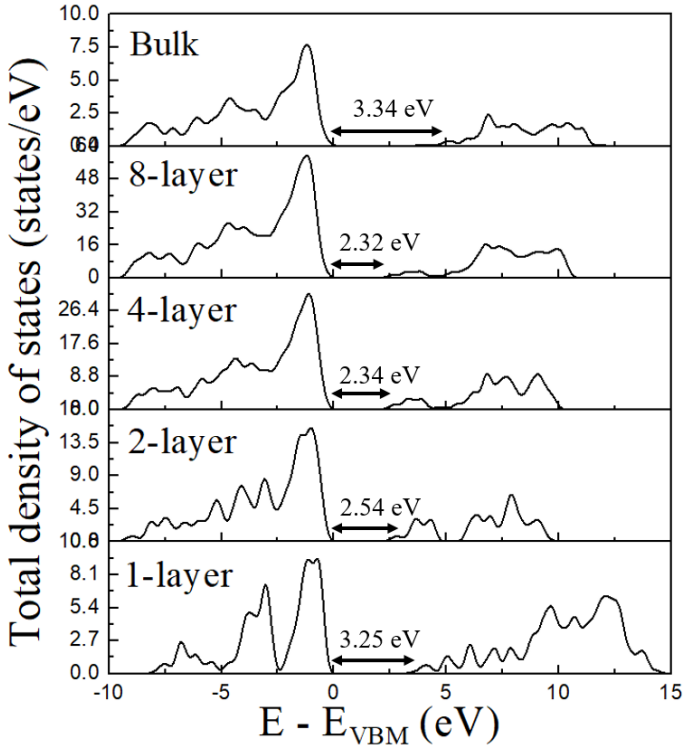

Figure III.11 Calculated Total Density of States of Un-passivated SnO2 Films in Different Sizes.

As presented in Figure III.11, as the thickness increases, the conduction band seem to shift toward lower energies, which leads to a significant decrease of the band gap energy. This later seems to do not follow a regular trend from 1-layer to bulk, it decreases radically from a large value of 3.25 eV (1-layer) to 2.32 eV (8-layer) with no convergence to the bulk band gap. Since the CBM and VBM of SnO2 are mainly formed by s-states of Sn and p-states of O, their projected and local density of states have been calculated and presented in Figure III.12.

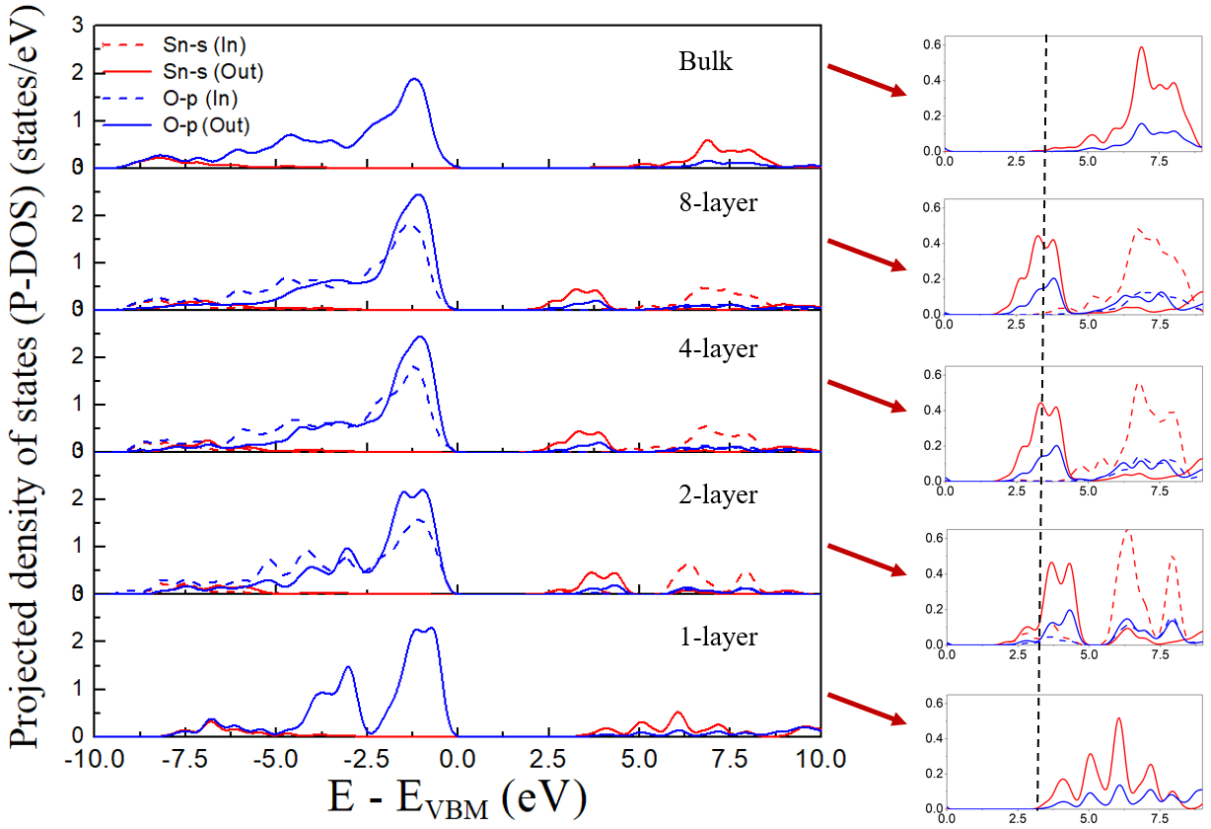

Figure III.12 Calculated Projected and Local Density of States (left) and Zoom-in The CBM (right) of SnO2 Films in Different Sizes. Dashed and Straight Curves Present Density of States of Atoms Located Inside the Structure and at The Surface of the Structure Respectively. Dashed Black Line Presents the Shift of the CBM as a Function of SnO_2 Film Thickness.

First, it is seen that the density of states of the atoms located in bulk (In) of the film and the atoms located at the surface (Out) are different. In all cases, the CBM is mainly formed by the (Out) atoms states, which leads to smaller band gaps in comparison with the bulk band gap. Second, as the thickness increases the CBM shift towards lower energies resulting in bang gap narrowing. To further understand the effect of the active surface of SnO_2 films on its electronic properties, we calculated the charge density distributions, shown in Figure III.13, viewed along the [110] axis. We can notice that as the film size decreases the Sn-O bond becomes shorter (stronger), which induces higher charge density distribution, and explains the bandgap energy increase. However, the denser charge distribution that could be seen at the upper layers of each

film surfaces, results in an excess of electronic states, which explain the narrowed band gap in comparison with SnO_2-bulk bandgap.

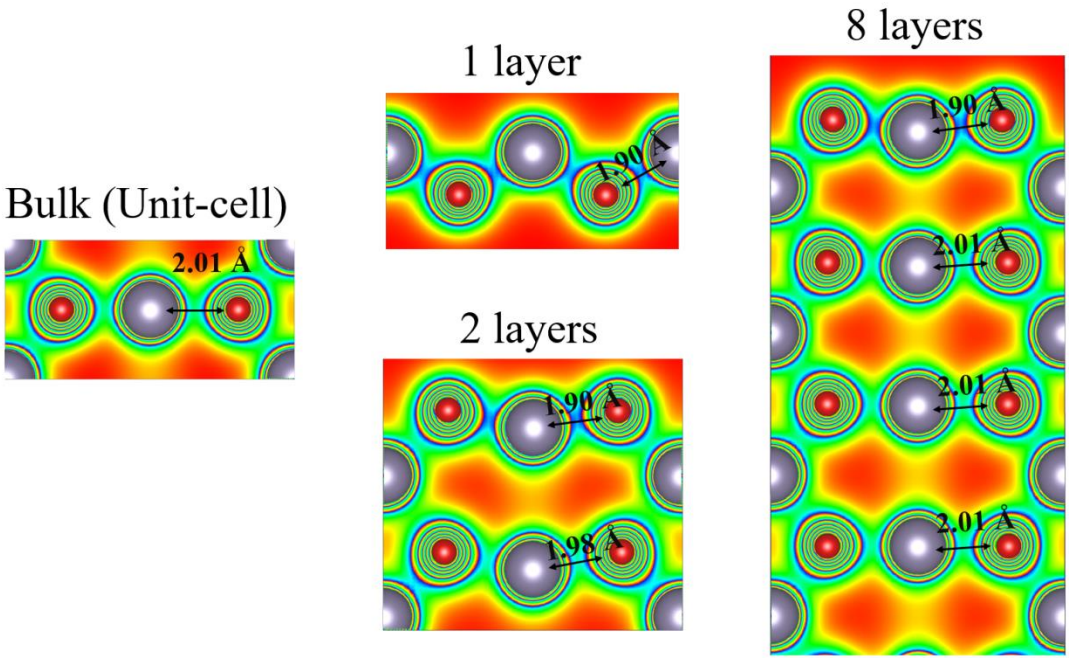

Figure III.13 Calculated Charge Density Distribution in The (110) Plane of SnO2 Films in Various Sizes. Red and Grey Balls are O and Sn Atoms Respectively.

As presented in Figure III.13, as a function of film thickness, the band gap decreases as the film thickness increases with no convergence to the bulk band gap. Therefore, the band gap respect the quantum confinement effect only for the films, which results from charge being squeezed into a size smaller than the exciton Bohr radius of SnO_2 [213], *i.e.* 2.7 nm, leading to band gap decrease as the film thickness increases.

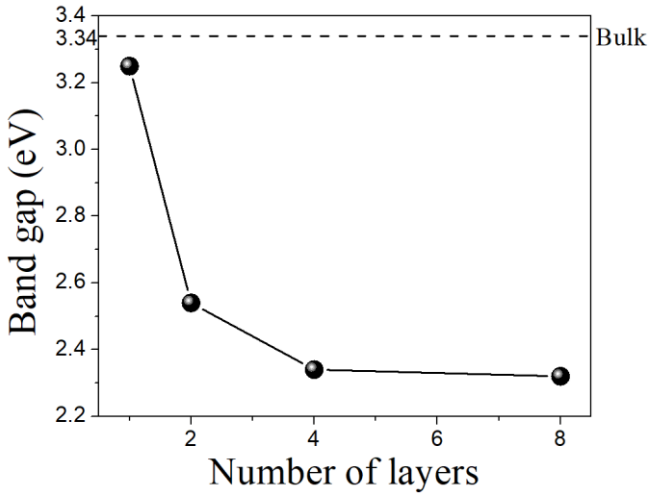

Figure III.14 Calculated band gap values of Un-Passivated SnO2 in different sizes.

Such behavior have not resulted only by film thickness and size, but also from the active charges and dangling bonds existing at the surface. We can conclude that we have two effects. In one hand, is the active Sn-s and O-p states of the atoms located at the surface, which leads to smaller band gap in comparison with bulk bandgap. In the other hand, the effect of thickness where the band gap of films decreases as the thickness increases due to quantum confinement.

III.2.2 Passivated SnO2 thin films

III.2.2.1 Structural properties

To passivate dangling bonds at the surface, fake hydrogen atoms with fractional nuclear charges and electrons were needed to keep the system charge neutral. For SnO2 that is a tetrahedral crystal, each dangling bond need a hydrogen-like atom with Z = (8 - m)/4, where m is the number of valence electrons [214]. Precisely, Sn and O dangling bonds were passivatedd with pseudo-hydrogen atoms with 1 and 1/2 nuclear charge respectively. The film structures before and after optimization are shown in Figure III.15.

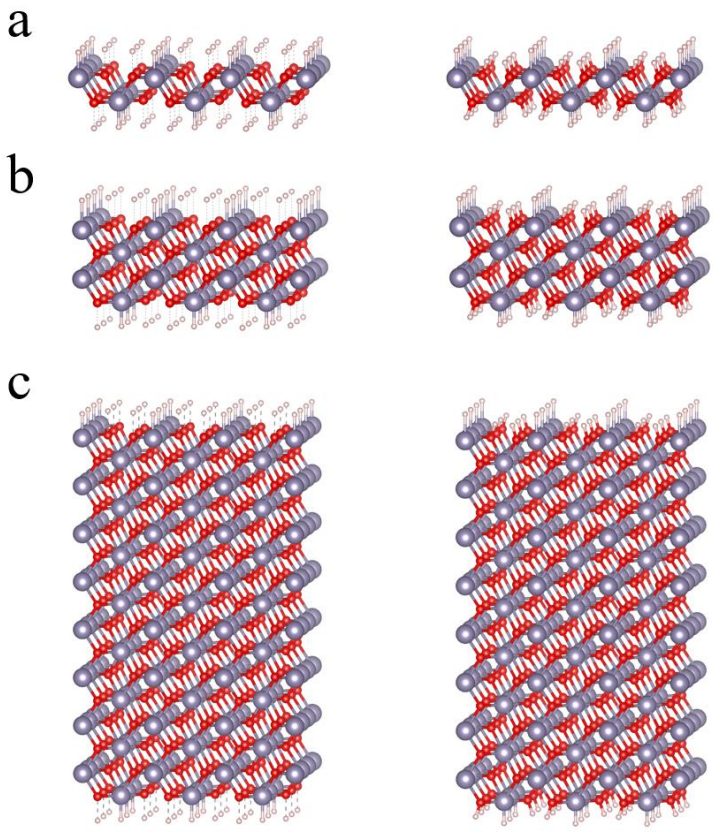

Figure III.15 Structure of Passivated SnO2 Films Before (Left) and After (Right) Optimization in Different Sizes. Thickness of Films Are (a) 0.3 nm, (b) 0.6 nm, (c) 2.5 nm. Gray Spheres Present Sn Atoms, and Red spheres Present O Atoms.

In contrast with un-passivated SnO2 films, the crystalline structure of passivated SnO2 films did not change after optimization, which might allow studying only the effect of film thickness on SnO2 electronic properties.

III.2.2.2 Electronic properties

Projected density of states (P-DOS) have been calculated in order to understand the electronic properties of SnO2 passivated films.

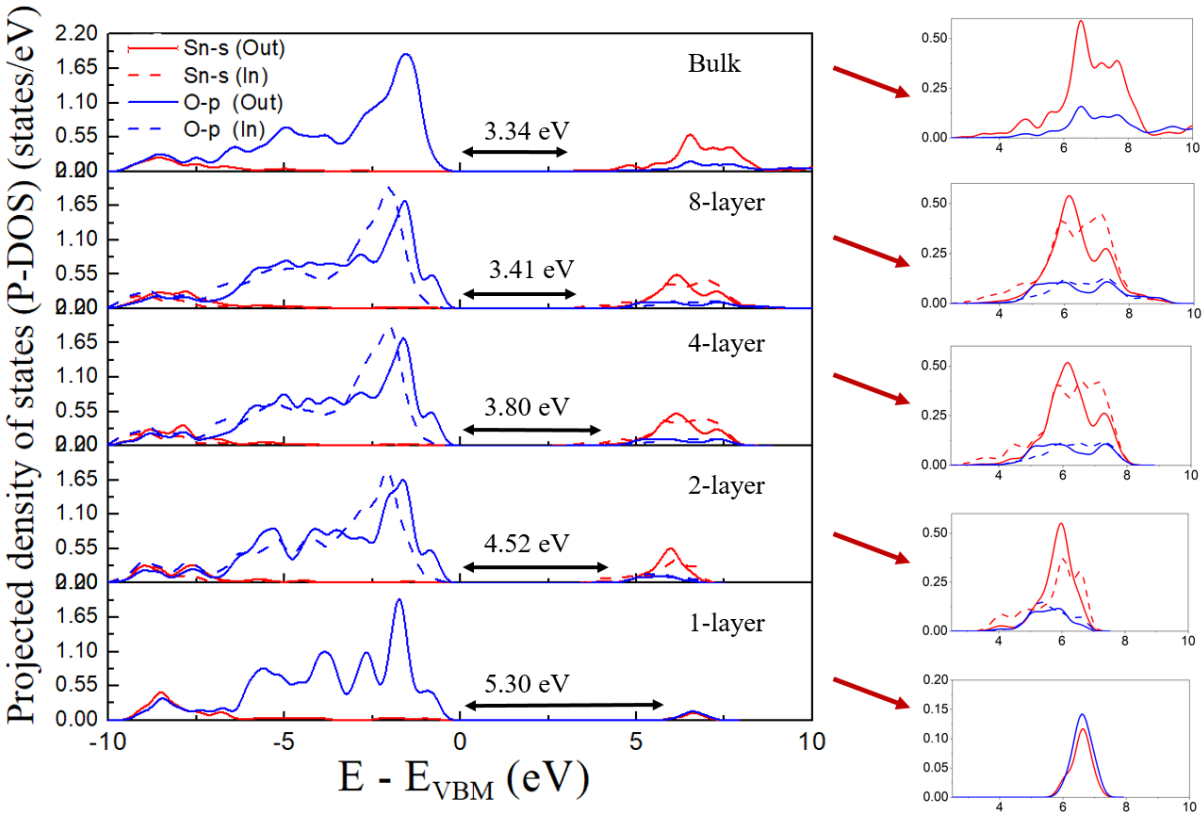

Figure III.16 Calculated Projected and Local Density of States (left) and Zoom-in The CBM (right) of Passivated SnO2 Films in Different Sizes. Dashed and Straight Curves Present Density of States of Atoms Located Inside the Structure and at The Surface of the Structure Respectively.

As presented in Figure III.16, the band gap of SnO2 films The CBM shift toward the VBM, which results in band gap decrease from 5.3 eV (1 layer) to 3.34 eV (bulk). In contrast with the case of un-passivated SnO2 films, it is seen that for each film the P-DOS of the atoms located at the surface occupy the same energy level of those located inside. Which means that the surface of films maintained its charge neutrality thanks to Hydrogen passivation.

Figure III.17 presents the charge distribution viewed along the [110] axis. We can notice that the charge distribution at the surface of films were nearly similar to that of bulk. Although, as the thickness decreases, denser charge distribution around Sn and O atoms can be seen, even if they are bonded by same distances.

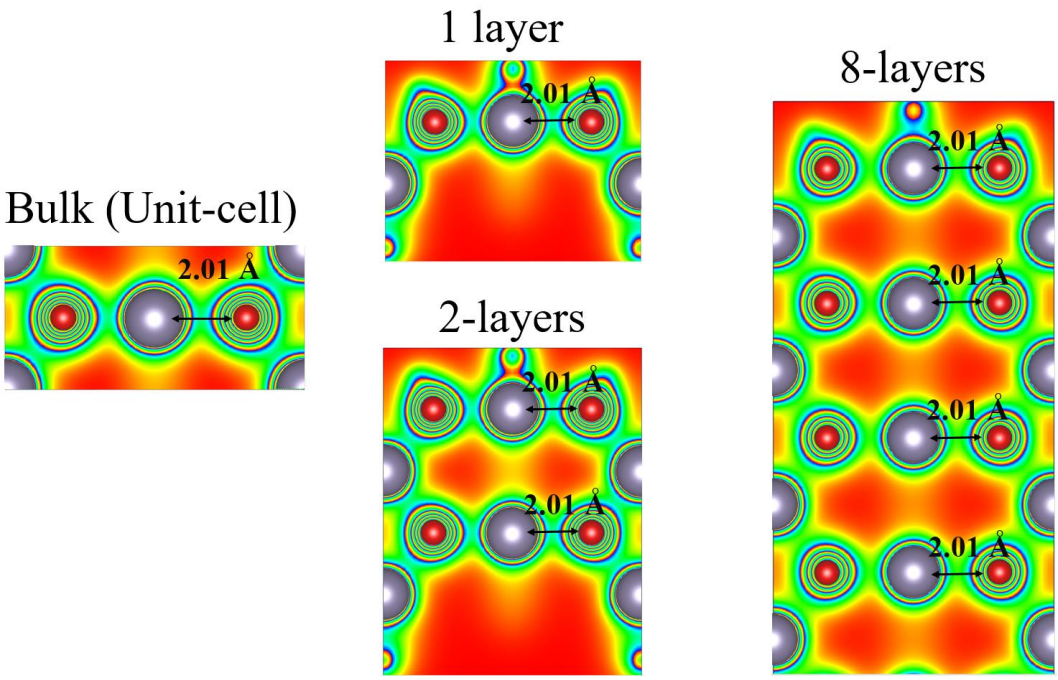

Figure III.17 Calculated Charge Density Distribution in The (110) Plane of Passivated SnO2 films in various sizes. Red and Grey Balls Are O and Sn Atoms Respectively.

As presented in Figure III.18, The band gap increases gradually from 3.34 eV to 5.23 eV with decreasing film thickness, and as this later increases, the band gap energy decreases toward the band gap of bulk. Since all the studied films are smaller than the exciton Bohr radius for SnO2 (2.7 nm) [213], the resulted increase of the band gap as the size decreases could be attributed to the quantum confinement effect, as reported previously in several studies [215,216].

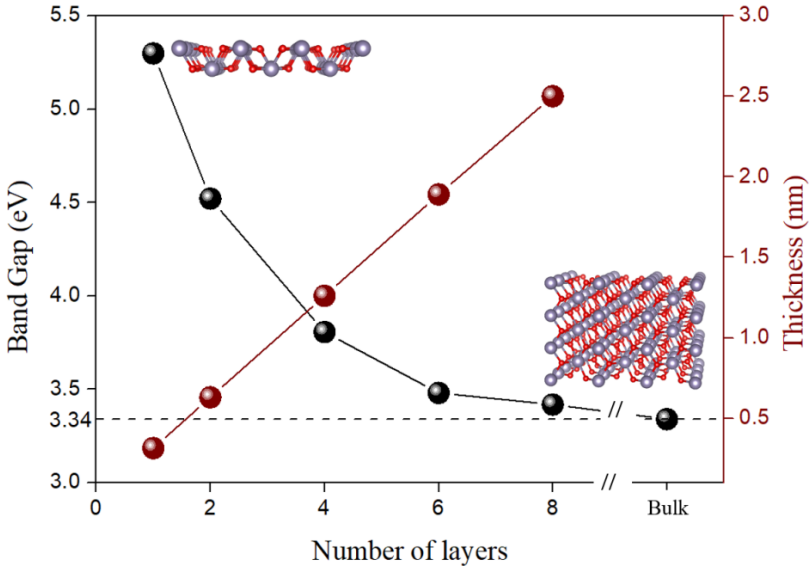

Figure III.18 Calculated band gap values of Passivated SnO2 in Different Sizes

III.2.2.3 Strain and size combined effect on the electronic properties of Passivated SnO2 thin-films

In the present section, we aim to study the effect of thickness together with strain on SnO2 electronic properties. As illustrated In Figure III.19, a range of strain values from -6% (Red arrows) to +6% (Blue arrows) were gradually applied along the ***ab*** plane of SnO2-films.

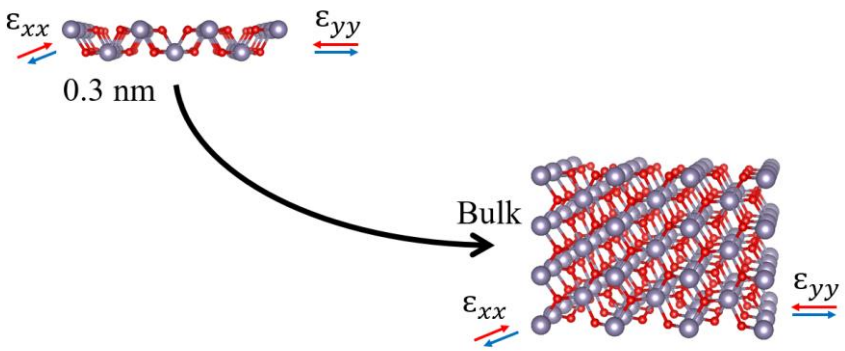

Figure III.19 Illustration of Applied Biaxial Strain Along ab Plane of SnO2 Thin-Films and Bulk

As explained in section (**III.2 Effect of strain on the electronic properties of SnO2 Bulk)**, applied biaxial strain causes structural deformation mostly interatomic bonds distortion, which is the major responsible of electronic properties and band gap alteration. A good picture of these effects is illustrated in the charge density distributions of passivated SnO2 films in various sizes under compressive and tensile shown in Figure III.20.

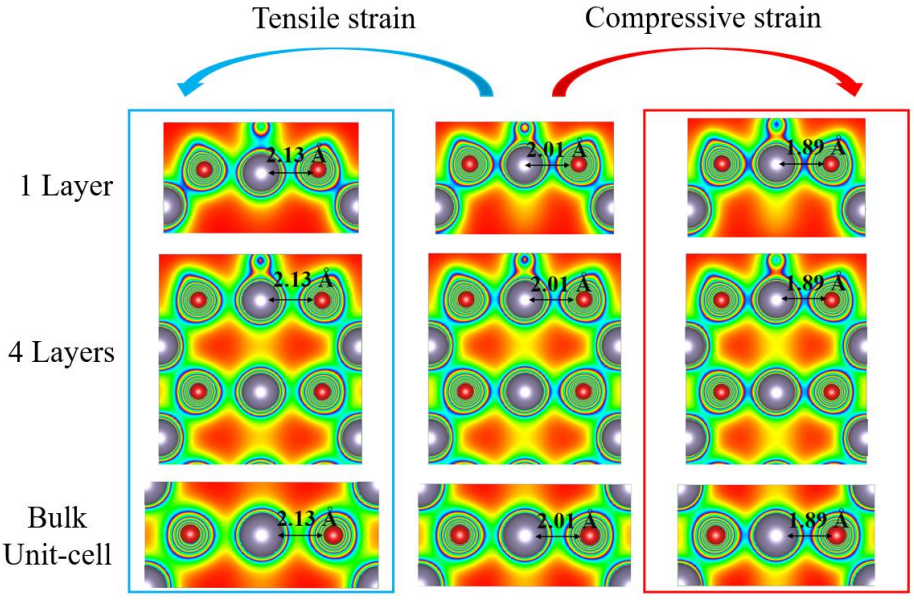

Figure III.20 Calculated Charge Density Distribution in The (110) Plane of Passivated SnO2 films in various sizes under strain. Red and Grey Balls Are O and Sn Atoms Respectively.

Applying biaxial strain on nanostructured SnO2 generates multiple effects; one is that the charge density distribution increases as the size decreases from SnO2 bulk to 1layer film, which could be explained by quantum confinement. In the other hand, for each film, charge density distribution become denser under compressive strain due to shorter (stronger) Sn-O bond, while opposite behavior is observed in the case of a tensile strain.

The calculated band gap energy of passivated SnO2 thin-films under strain is presented in Figure III.21. As the film thickness increases the band gap energy decreases toward the bulk band gap. In addition, for each film, under compression, because of covalent bonding strengthening and charge condensation the band gap increases. Again, an opposite behavior is demonstrated in the case of tensile strain.

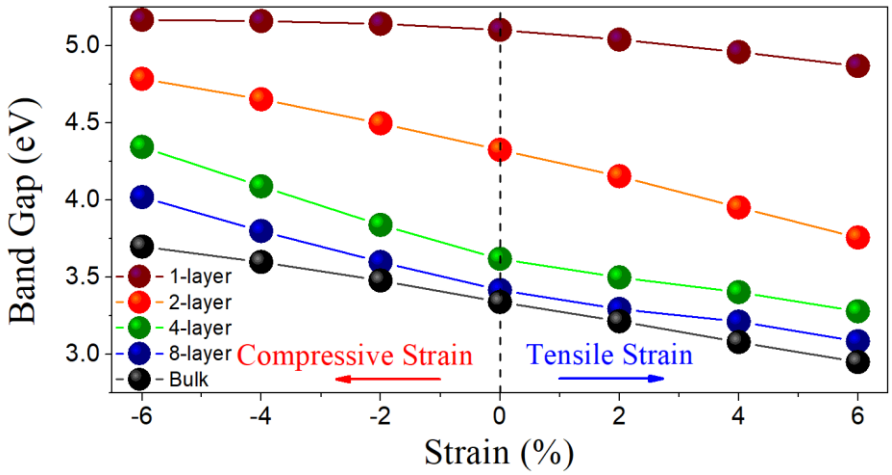

Figure III.21 Calculated band gap energy of Passivated SnO2 film under strain.

Chapter Conclusion

In conclusion, we have studied theoretically the effect of thickness and biaxial strain on SnO2 properties. For bulk, due to a compressive (tensile) strain, a strong (weak) hybridization of O-p and Sn-s in the conduction band is obtained because of dense (less) charge distribution around atoms causing therefore a band gap energy modulation.

While for thin-films, the band gap decreases with increasing thickness, which is contributed to the effect of quantum confinement. Although, in the case of un-passivated films new states appeared near the CBM, leading to smaller band gaps in comparison of those of passivated films.

Lastly, the band gap energy of biaxial strained SnO2 thin-films follow similar trend of that of bulk. Under compression, the bandgap of thin-films increases, while it decreases under tensile strain. Therefore, compressed thinner film have the large band gap, whereas expanded thicker film have the narrowed one.

CHAPTER IV: ENHANCED THERMOELECTRIC PROPERTIES OF STRAINED SNO_2 BULK

Table of contents

CHAPTER IV: ENHANCED THERMOELECTRIC PROPERTIES OF STRAINED SNO_2

IV.1 Thermoelectric effects

IV.1.1 Seebeck effect

The Seebeck effect was discovered in 1821 by the German physicist Thomas Johann Seebeck [217], when he found that a circuit made from two different electrically conducting materials, with junctions at different temperatures would deflect a compass magnet. Thomas Seebeck initially believed this was due to magnetism induced by the temperature difference and thought it might be related to the Earth's magnetic field.

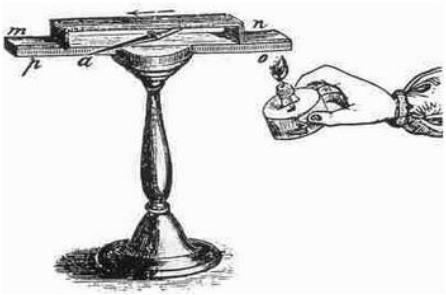

Figure IV.1 Instrument used by Seebeck to observe the deflection of a compass needle (a) due to a thermoelectric induced current from heating the junction of two different metals (n and o).

However, it was quickly realized that a "Thermoelectric Force" induced an electrical current, which by Ampere's law deflects the magnet. More specifically, as shown in Figure IV.2 the temperature difference ΔT causes charge carriers diffusion from the warm side to the cold side, leading to electric potential (voltage) production, which can drive an electric current in a closed circuit.

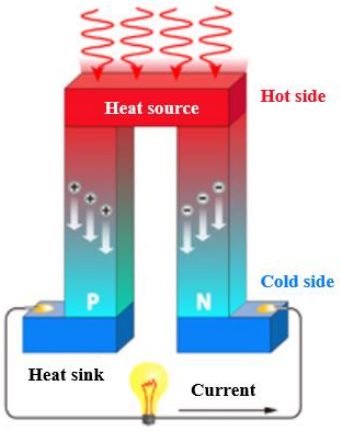

Figure IV.2 Illustration of Seebeck effect.

Therefore, the induced *dV* voltage is proportional to the temperature difference between the hot side and the cold side. This proportionality constant (***S***) is known as the Seebeck coefficient and expressed as:

$$S = -\frac{V_H - V_C}{T_H - T_C} = -\frac{dV}{dT} \qquad \text{Eq.IV.1}$$

Where V_H and V_C are the voltages at the hot side and cold side respectively; and T_H and T_C are the temperatures of the hot side and the cold side respectively. The sign of Seebeck coefficient ***S*** usually depends on the semiconducting type of the material. For instance, ***S*** is positive in p-type semiconductors. While, in n-type semiconductors ***S*** is negative.

IV.1.2 Peltier effect

The Peltier effect is a thermoelectric effect discovered in 1834 by Jean-Charles Peltier [218]. It describes the phenomenon of heat transfer in the presence of an electric current at the junction of two different electrically conducting materials. As presented in Figure IV.3, when an electric current passes through the junction connecting two materials, there is a release of heat or a heat absorption according to the direction of the current.

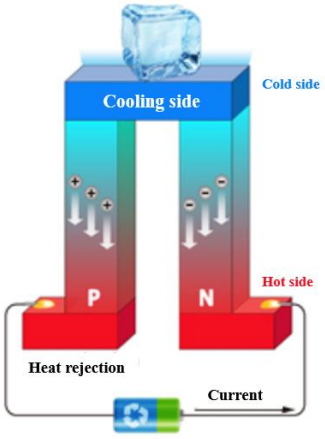

Figure IV.3 Illustration of Peltier effect

The quantity of heat Q released at the junction of two materials N and P, per unit of time, is proportional to the applied current I, and expressed as:

$$Q = \Pi_{NP}.I \qquad \text{Eq.IV.2}$$

where Π_{NP} is the relative Peltier coefficient of materials N and P, which is defined by:

$$\Pi_{NP} = |\Pi_N - \Pi_P| \qquad \text{Eq.IV.3}$$

IV.1.3 Thomson effect

Thomson effect is discovered by the physicist William Thomson (later Lord Kelvin) in 1851 [219], he issued a comprehensive explanation of the Seebeck and Peltier Effects and described their interrelationship (known as the Kelvin Relations). In the Thomson effect, heat Q is absorbed or produced when current I flows in a material with a temperature gradient ΔT. Hence, the heat is proportional to both the electric current and the temperature gradient. The proportionality constant, known as the Thomson coefficient is related by thermodynamics to the Seebeck coefficient:

$$Q = -\beta_{\text{th}}.I.\,\Delta T \qquad \text{Eq.IV.4}$$

where β_{th} is the Thomson coefficient.

Kelvin's relationship showed that the three effects Seebeck, Peltier and Thomson were interdependent. These three coefficients are linked by the following relations:

$$\Pi = \text{S}.T \qquad \text{Eq.IV.5}$$

$$\frac{dS}{dT} = \frac{\beta_{th}}{T} \qquad \text{Eq.IV.6}$$

The relation IV.5 demonstrates the reversibility between the Seebeck and the Peltier effects, which makes it possible to determine the Peltier coefficient via the Seebeck coefficient. Heat transfer can be determined from voltage and temperature measurements that are much simpler to perform. Kelvin's relations show that the three Seebeck, Peltier and Thomson effects exist simultaneously in any material when subjected to a temperature difference and an electric current.

IV.2 Energy conversion

Thermoelectricity allows the direct generation of electrical energy from a heat source (Seebeck effect) or cooling generation from electrical energy (Peltier effect). In this section, further details about thermoelectric device and conversion have been provided.

IV.2.1 Thermoelectric module and working principle

The thermoelectric module is composed by thermoelectric pairs (thermocouples), which are connected electrically in series and thermally in parallel. Each pair is formed by two dissimilar semiconductor materials, one of P-type ($\boldsymbol{S} > 0$), and the other of N-type ($\boldsymbol{S} < 0$).

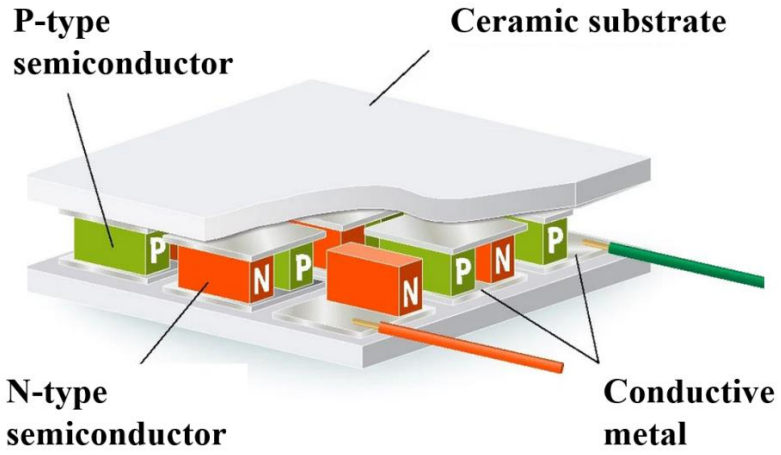

Figure IV.4 Illustration of Thermoelectric Module

In the case of thermoelectric generators, one end of the system is kept at hot temperature T_H while the other end is kept cold at T_C, with $T_C < T_H$. This applied temperature gradient to both sides generates an electrical voltage through Seebeck effect, which leads to an electric current. The efficiency of thermoelectric generator is defined by the ratio of the electric power (P) generated by the thermoelectric module to the thermal power (Q_H) yielded by the hot source:

$$\eta = \frac{P}{Q_H} = \frac{T_H - T_C}{T_H} \frac{\sqrt{1+ZT}-1}{\sqrt{1+ZT}+T_c/T_H} \qquad \text{Eq.IV.7}$$

Where ZT is the figure of merit, T_H and T_C are the temperatures of the hot and cold sides respectively. As reported by Han et al. [220] and shown in Figure IV.5, thermoelectric generator efficiency is limited by the Carnot efficiency $\eta_C = \frac{T_H - T_C}{T_H}$.

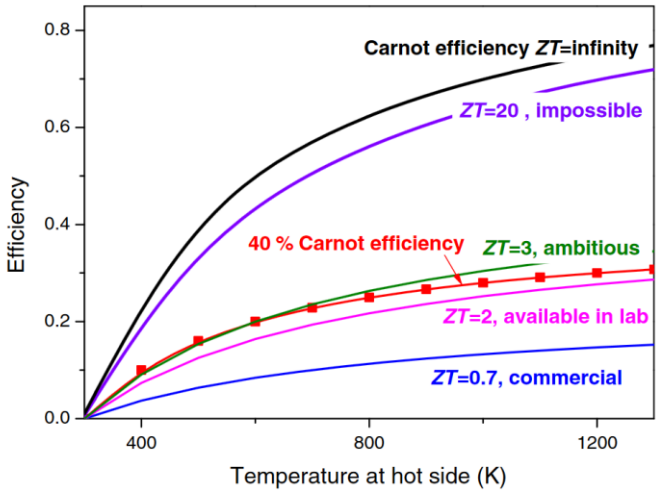

Figure IV.5 Conversion efficiency of TE materials with changing temperature difference and ZT, assuming that the cold side temperature is 300 K. The red curve is the 40 % Carnot efficiency. Reported by Han et al. [220]

The best thermoelectric modules marketed are composed of alloys, for example, $(Bi, Sb)_2$ $(Te, Se)_3$, which operate at temperatures below 450K [221,222]. These modules reach a Figure of merit of ZT ≈ 1 which corresponds to a conversion efficiency of η = 15%. This later is considered too small in comparison with another renewable energy technologies, such as photovoltaic cells that have a conversion efficiency up to 18% [223]. Therefore, to maximize η, the thermoelectric materials must have high ZT values together with large temperature gradient.

IV.2.2 Figure of Merit ZT

As mentioned in the previous section, the Figure of merit is the parameter that governs the conversion efficiency. According to equation IV.8, the dimensionless figure of merit depends on transport properties of the two materials integrated in the elementary thermoelectric pair (N and P).

$$ZT = \frac{S^2\sigma}{k} T \qquad \text{Eq.IV.8}$$

where S, σ, κ and T represent Seebeck coefficient, electrical conductivity, thermal conductivity, and the absolute temperature respectively. These three parameters are the norms that determine the thermoelectric material quality. Therefore, good thermoelectric material must have high Seebeck coefficient **S** and electrical conductivity **σ**, and low thermal conductivity **κ**.

IV.2.2.1 Seebeck coefficient (Thermoelectric power)

The Seebeck coefficient can be considered as the entropy per charge carrier over temperature or more simply as the measure of heat that is carried along with a unit charge, S ≈ C/q, where C is the specific heat and q is the elementary charge. The Seebeck coefficient, ***S*** can be expressed by the Mott formula as:

$$S \approx \frac{C_e}{q} \approx \frac{\pi^2 {k_B}^2}{3e} T \left(\frac{d \ln(\sigma(E))}{dE}\right)_{E=E_F} \quad \text{Eq.IV.9}$$

where $\sigma(E)$ is the energy dependent conductivity. For the case of metals or degenerate semiconductors (parabolic band, energy-independent scattering approximation), the Seebeck coefficient can be expressed as:

$$S = \frac{8\pi^2 {k_B}^2}{3eh^2} m^* T \left(\frac{\pi}{3n}\right)^{3/2} \quad \text{Eq.IV.10}$$

As can be seen from Eq.IV.10, The Seebeck coefficient depends on the charge carriers effective mass m^*, and inversely proportional to charge carriers concentration. Therefore, in term of Seebeck coefficient, an optimal semiconductor should have large bandgap with high effective mass and low charge carriers concentration.

IV.2.2.2 Electrical conductivity

The electrical conductivity σ is given by the following formula:

$$\sigma = n.e.\mu \quad \text{Eq.IV.11}$$

where n and μ are respectively the charge carriers concentration and mobility, and e is the elementary charge. Charge carriers mobility vary according to the elementary charge e, the effective mass m *, and the time scattering τ as expressed by the following relation:

$$\mu = \frac{e.\tau}{m^*} \quad \text{Eq.IV.12}$$

Materials containing elements with similar electronegativity have a longer relaxation time, which leads to an increase in electrical conductivity [229]. The effective mass m*, depends on the width of the energy bands [231].

$$m^* = \frac{\overline{h}^2}{d^2E/dk^2} \quad \text{Eq.IV.13}$$

Narrow band gap leads to lower m* value, resulting in higher mobility and electrical conductivity compared to wide band gap. Therefore, In terms of the expressions IV.12 and IV.13, electrical conductivity of semiconductors can be improved by narrowing the band gap and increasing the charge carriers mobility.

IV.2.2.3 Thermal conductivity

In a crystalline solid, the transfer of heat can be ensured by the motion of the charge carriers and the lattice vibrations (phonons), described as electronic contribution k_e and phonons contribution k_L [232]. Total thermal conductivity is defined as:

$$k = k_e + k_L \qquad \text{Eq.IV.14}$$

According to the Wiedemann-Franz law, the electronic contribution k_e depends on the concentration of the charge carriers and it is directly related to the electrical conductivity:

$$k_e = L.\sigma.T \qquad \text{Eq.IV.15}$$

where *L* is the Lorentz factor.

According to the Debye model, lattice thermal conductivity (phonons contribution) corresponds to the propagation of phonons in the three dimensions of space through the crystal lattice:

$$k_L = \frac{1}{3}.C_p.v_s.l_{ph} = \frac{1}{3}.C_p.{v_s}^2.\tau_{ph} \qquad \text{Eq.IV.16}$$

where C_p is the specific heat, v_s is the phonon speed, l_{ph} and τ_{ph} are the average free path and the average relaxation time of phonons. The contribution of phonons as a function of temperature depends on the dominant interactions that occur in the crystal. At low temperatures, the average free path of the phonons is limited by the size of crystal and the concentration of defects and impurities. While at high temperature (T ≥ 300K), the phonons speed and the specific heat are independent of the temperature.

Apart from the general requirements for materials, such as good thermal, and mechanical stability, the main requirement for good thermoelectric materials revolves around the equation $ZT = \frac{S^2\sigma}{k} T$, such as high Seebeck coefficient ***S*** and electrical conductivity σ, and low thermal conductivity κ. As can be noticed from the formulas (IV.10), (IV.11), and (IV.15), Seebeck coefficient, electrical conductivity σ, and electronic thermal conductivity κe depend

on the charge carriers concentration n. Figure IV.6 illustrates the charge carriers concentration dependence of the three parameters, and their influence on the Figure of merit ZT.

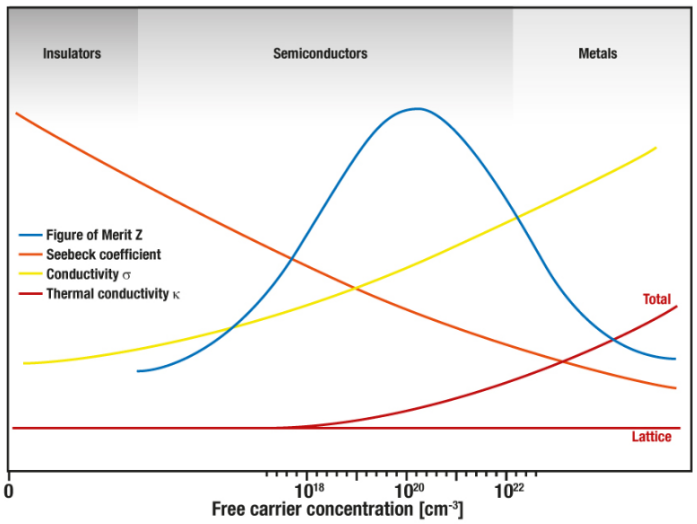

Figure IV.6 Qualitative influence of carrier concentration on the key material parameters: Seebeck coefficient S, electrical conductivity σ, thermal conductivity κ, and Figure of merit ZT for insulators, semiconductors and metals.

From the figure, we can see that an optimal Figure of merit ZT can be achieved around $n \approx 10^{19} cm^3$, in the range of semiconductors.

IV.3 Thermoelectric applications and materials

IV.3.1 Thermoelectric applications

During and after the world wars I and II, thermoelectricity has been actively studied for applications such as cooling and power generation for military and civil purposes [224]. Later, commercial applications for thermoelectric materials appeared such as radios and refrigerators using thermoelectric modules based on Bi_2Te_3. After the 70s, several types of devices based on thermoelectric modules are marketed for different applications such as small refrigerators and car seat cooling/heating systems. A well-known example in this period is that of Radioisotope Thermoelectric Generators (RTG) used by many space probes of NASA [225-227]. These thermoelectric generators can provide electrical power of a few hundred watts by converting the heat produced by radioactive sources such as plutonium 238Pu. Although thermoelectric generators have low efficiency (less than 10%), the advantages such as compactness, lightness and durability make them the better choice compared to other systems.

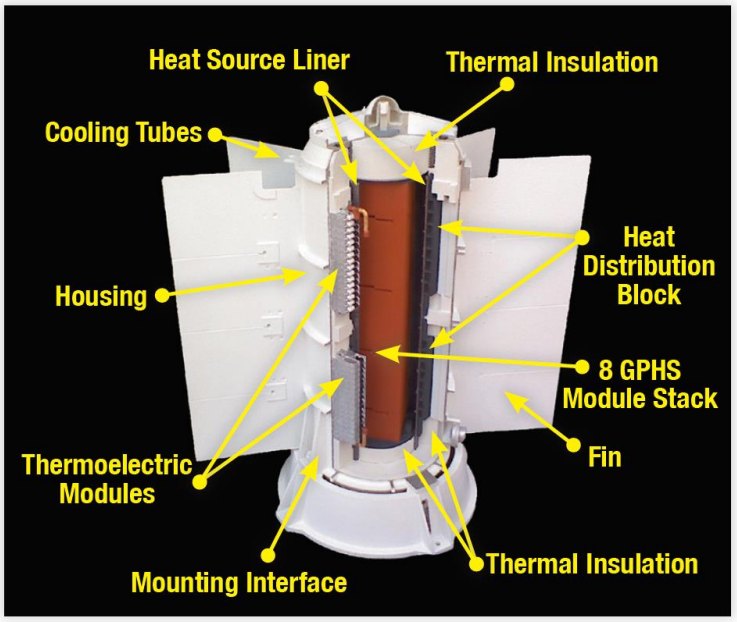

Figure IV.7 Multi-Mission Radioisotope Thermoelectric Generator (MMRTG) Model [227].

Since 2000, scientific discovery of new materials renewed the interest for new thermoelectric applications, mainly the production of electrical energy from waste heat sources such as industrial processes or vehicles. For instance, nearly 70% of wasted energy released for cars, could be recovered to feed it into the vehicle's on-board power system in the form of electrical energy using a thermoelectric generator.

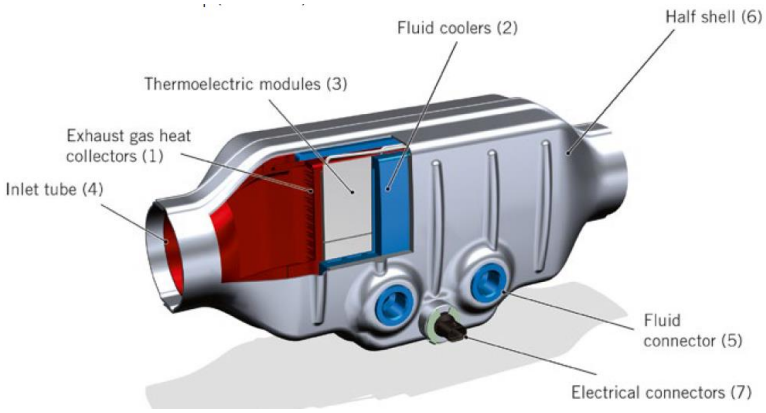

Figure IV.8 Automotive Thermoelectric Generator Model [228].

Famous automakers such as BMW, and General Motors, as well as many research laboratories such as University of Michigan, University of South Florida and Oak Ridge Laboratory have achieved great success in new thermoelectric generators applications [228-230].

IV.3.2 Conventional thermoelectric materials

Conventional thermoelectric materials can be classified into three groups in terms of the temperature range of their operation. First, low temperature materials (< 450K) such as Bismuth (Bi), Antimony (Sb), Tellurium (Te), and Selenium (Se) based alloys. Second, medium temperature materials (< 850 K) such as Lead (Pb) based alloys. Finally, high temperature conventional materials that operate up to 1300 K such as Silicon Germanium (SiGe) alloys. Over three decades from 1960 to 1990, increased ZT ~ 1 were achieved only for the $(Bi_{1-x}Sb_x)_2(Se_{1-y}Te_y)_3$ alloy family remaining the best commercial material with conversion efficiency of $\eta \sim 15$. During this period, the field of thermoelectrics remained stagnant and received little attention from the scientific research community worldwide. However, the thermoelectric industry grew slowly around applications for space missions, laboratory equipment, and medical applications, where cost and energy efficiency were not as important as energy availability, reliability, predictability, as well as the quiet operation of the equipment. [231,232]

IV.3.3 Advanced thermoelectric materials

In the early 1990s, research interest have been focused on improving the performance of thermoelectric materials by reducing their thermal conductivity and improving their power factor. Hicks and Dresselhaus [232], reported nano-structuring as a potential approach for novel thermoelectric materials. Their findings have triggered research on discovering advanced bulk thermoelectric materials and low-dimensional materials in order to develop high-performance thermoelectric devices. The phonon-glass/electron-crystal (PGEC) materials [233] have been considered as the most prominent of the new families of advanced thermoelectrics, as they have high electrical properties as crystalline materials and good thermal properties as amorphous, for example, Skutterudites, Clathrates, Heussler alloys, complex chalcogenides and oxides [231]. In addition, huge efforts have been focused in low-dimensional materials approach, mainly by lattice thermal conductivity reduction and power factor enhancement via nano-structuring and quantum confinement effects.

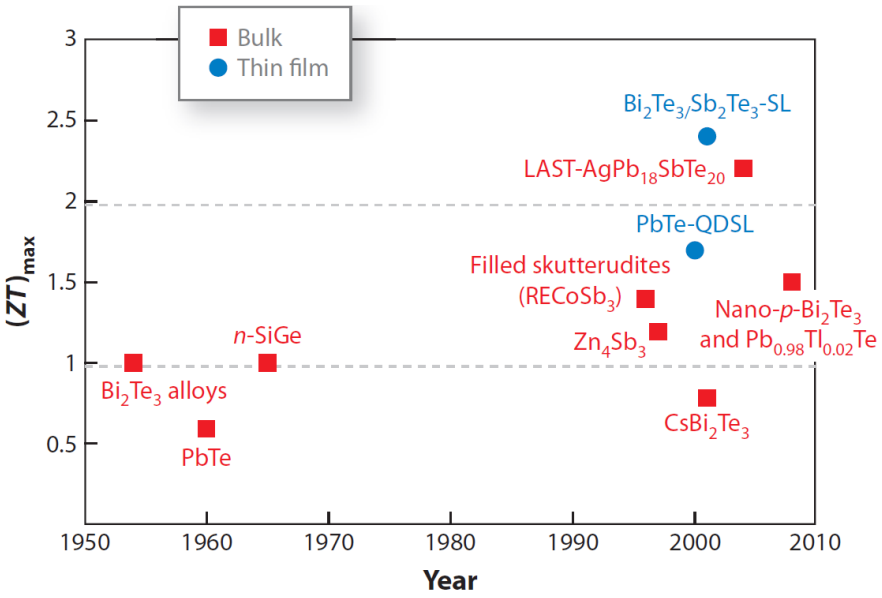

Figure IV.9 The figure of merit, *ZT*, as a function of the time frame of several key TE materials relative to their discovery year, thus showing many of the recent advancements in both thin-film and bulk thermoelectric materials. Abbreviations: LAST, PbAgSbTe compounds; QDSL, quantum dot superlattice; SL, superlattice. Reported from Reference [234].

Figure IV.9 shows the timeline of Figure of merit evolution of several thermoelectric materials [234]. The main goals of the current research efforts are to find advanced materials that either increase the thermoelectric devices efficiency, or have the capability of operating in new and broader temperature ranges, especially at lower temperatures (T < 250 K) and higher temperatures (T > 800 K). Thermoelectric applications at high temperature are limited to one candidate mainly SiGe alloys with maximum Figure of merit ZT around 1000 K. Although, its instability and dopant precipitation issues limit its use for high-temperature heat sources. Despite all the scientific efforts in order to discover new materials with high thermoelectric performance, the current commercial thermoelectric modules are still based on conventional materials, such as compounds based on heavy-elements (Bi-Te, Pb-Te or Si-Ge), which must address toxicity and high cost problems.

Recently, oxide materials have gained huge interest to address toxicity and cost issues, and to be promising candidates for thermoelectric materials new generation. Among oxide semiconductors, SnO_2 presents a potential candidate thanks to its high surface area/volume ratio for nanoparticles [235,236], chemical stability, and low cost. SnO_2 research have been motivated by several applications. In fact, it is already applied in several fields such as gas sensors, transparent conducting thin films, solar cells and light emitting diodes, [237,238]. The limiting point of SnO_2 integration in thermoelectric applications is its low thermoelectric

performance mainly caused by its large thermal conductivity [239,240], *i.e.*≳40$Wm^{-1}K^{-1}$. To overcome such an obstacle, reported studies have shown that SnO_2 thermoelectric efficiency can be improved by doping [241-243], where transport properties can be enhanced by the introduction of free charge carriers in the conduction band. In addition, it was recently demonstrated that strain also plays an important role in modulating the energy band structure and electronic properties [244-247].

Inspired by such a finding, we attempt to take advantage from the ability of an applied biaxial strain to modulate the band gap of SnO_2 (See **CHAPTER III: STRAIN ENGINEERING: Strain and size effect on SnO_2 electronic properties**, section **III.2 Effect of strain on the electronic properties of SnO_2 Bulk** for more details), and elaborate a computational strategy to enhance the SnO_2 figure of merit (ZT) since the latter is directly related to the band structure. Therefore, in the present chapter, we explore the thermoelectric properties of SnO_2 in its bulk state under biaxial strain using density functional theory calculations over a wide range of temperatures.

IV.4 Enhanced thermoelectric properties of strained SnO_2 bulk

In the present section, we aim to discuss the effect of biaxial strain on the transport properties of SnO_2 bulk. As shown in Figure IV.10, the unit-cell volume linearly increases as a function of strain although the ***c*** lattice parameter is found to follow an inverted tendency. The applied strain along the ***ab*** plane causes a structural deformation of the SnO_2 unit-cell, which is due to the weak ability of the ***c*** lattice parameter to keep the crystal volume constant.

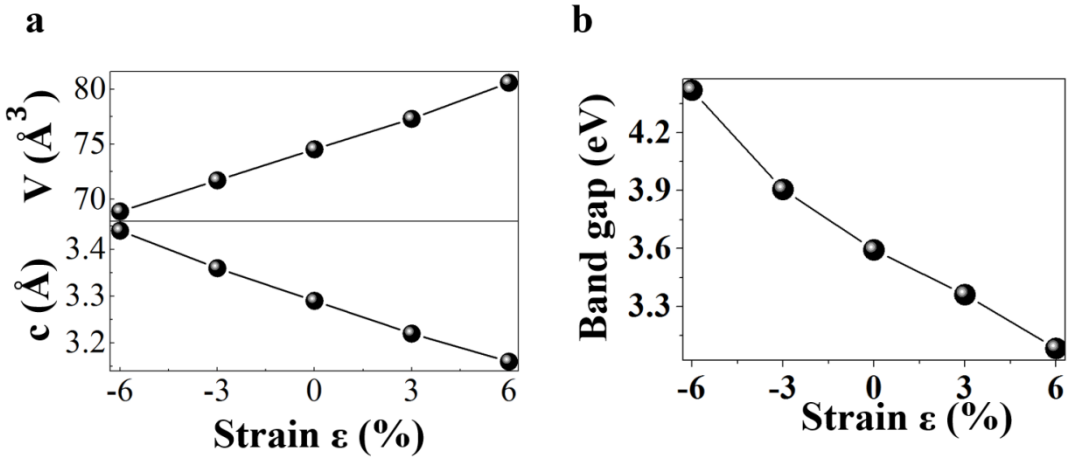

Figure IV.10 Calculation of (a) the ***c*** lattice parameter and its corresponding unit-cell volume, and (b) band gap energy of SnO_2 under various strain values.

Under compression, a shorter (stronger) covalent bonding interaction results in a wider bandgap energy, while a tensile strain yields to an opposite behavior (See **CHAPTER III: STRAIN ENGINEERING: Strain and size effect on SnO_2 electronic properties**, section **III.2 Effect of strain on the electronic properties of SnO_2 Bulk** for more details).

IV.4.1 Effective mass of strained SnO_2 bulk

Figure IV.11 shows the effective mass of electrons (Red) and holes (Blue) under biaxial strain. The calculated effective mass of unstrained SnO_2 is 0.282/m0 and 0.867/m0 for electrons and holes respectively, which is in agreement with previous reports [248]. Our results display a similar variation of the band gap energy under strain to that of the effective mass, which is mainly due to the fact that the effective mass is directly related to the electronic band structure. Indeed, compressive strain results in higher effective mass values due to the continuous increase of the band gap, while under tensile strain, narrow band gap yields to a decrease of the effective mass. The mobility of the thermally excited electrons and holes is inversely depend on the effective mass [249], hence from our calculated effective mass we found that the compressive strain caused a low carrier mobility while tensile strain load to high carrier mobility.

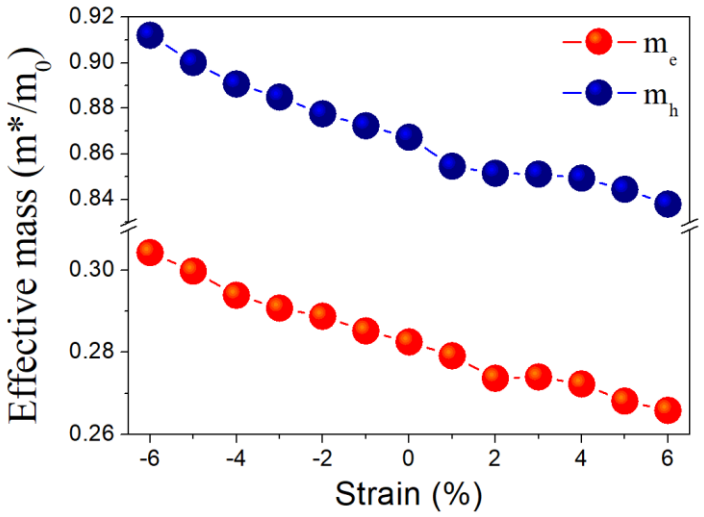

Figure IV.11 Calculated effective mass of electrons and of SnO_2 as a function of strain.

IV.4.2 Transport properties of strained SnO_2 bulk

For the transport properties calculations from 50K to 700K, we used the Boltzmann transport equation within the relaxation time approximation as implemented in the BoltzTraP package [250], which has successfully predicted the temperature and carrier concentration dependence of transport properties for other thermoelectric materials [251-253]. The calculated electrical conductivity (σ/τ) and thermal conductivity (κ/τ) are relaxation time dependent.

To explore the strain effect on thermoelectric properties, Seebeck coefficient (thermopower) is calculated as a function of wide range of temperatures, and presented in Figure IV.12. As noticed, the absolute value of our calculated Seebeck coefficient |S| is around 213 μV.K^{-1} at 300 K for an unstrained SnO_2 which is very close to the absolute experimental one [243] *i.e.* 195 μV.K^{-1}, validating therefore our approach.

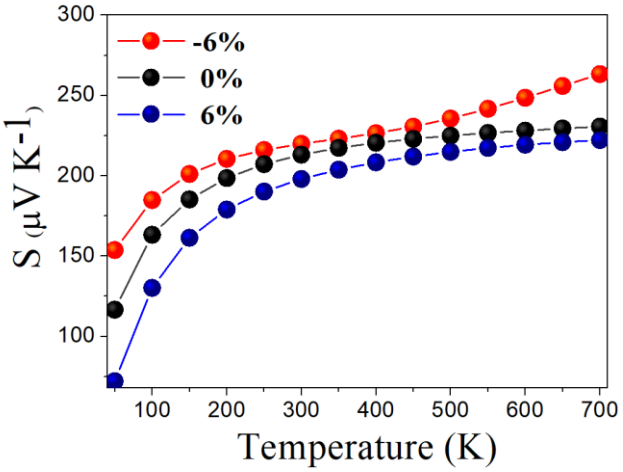

Figure IV.12 Calculated Seebeck coefficient of unstrained (0%), compressive (-6%), and tensile (6%) strained SnO_2 over a wide range of temperature.

Since the Seebeck coefficient is directly related to the band structure [254,255], our calculated values are following a similar trend as those obtained for bandgap energy values over the same strain range. Indeed, compressive strain results in higher Seebeck coefficients in absolute value for all temperature values due to the continuous increase of bandgap energy, while under tensile strain, reduced bandgaps yield to a decrease of Seebeck coefficient.

In contrast with the above Seebeck coefficient behavior, the electrical conductivity exhibits an opposite tendency with respect to the applied strain. As shown in Figure IV.13, under biaxial tensile strain, the electrical conductivity shows larger values as compared to unstrained SnO_2. This finding can mainly be explained by an increase of the effective mass observed in Figure IV.8 leading to a low carrier mobility, which yields to a lower conductivity [256].

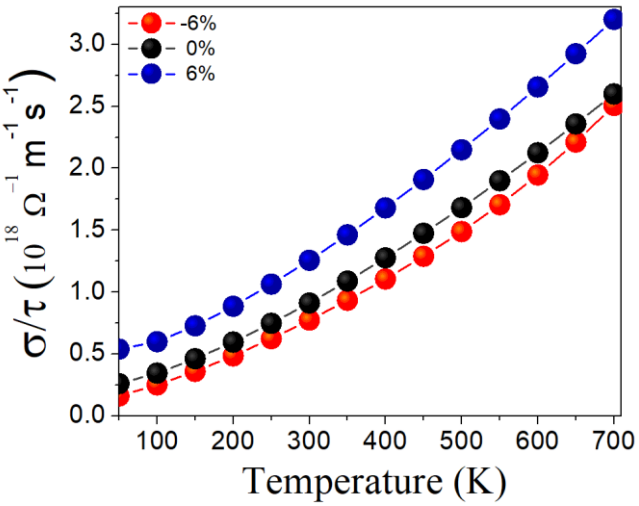

Figure IV.13 Calculated electrical conductivity of unstrained (0%), compressive (-6%), and tensile (6%) strained SnO_2 over a wide range of temperature.

On the other hand, as shown in Figure IV.14, the electronic thermal conductivity κ follows under strain the same trend as electrical conductivity. In addition, κ displays a progressive increase with temperature due to the thermally excited electron-hole pairs, and becomes more important at high temperatures under compression.

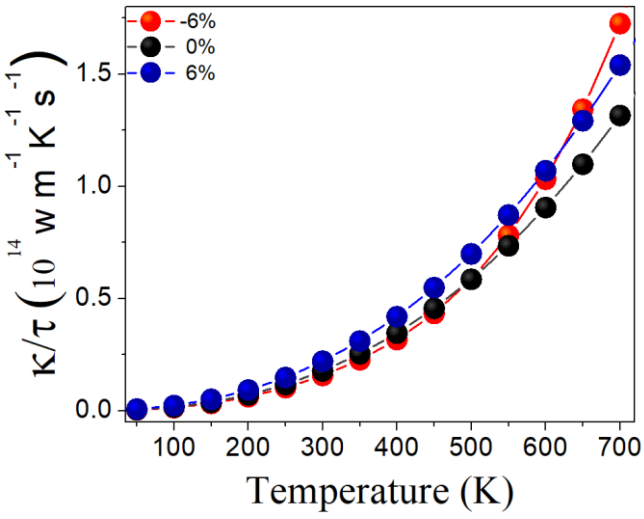

Figure IV.14 Calculated thermal conductivity of unstrained (0%), compressive (-6%), and tensile (6%) strained SnO_2 over a wide range of temperature.

Finally, to examine the biaxial strain effect on the thermoelectric performance we calculated the figure of merit (ZT) for SnO_2 under different strain " ε" values. As shown in Figure IV.15, the ZT value of unstrained SnO_2 is around 0.7, a value that is small as compared to other materials such as SnTe, SnSe [257].

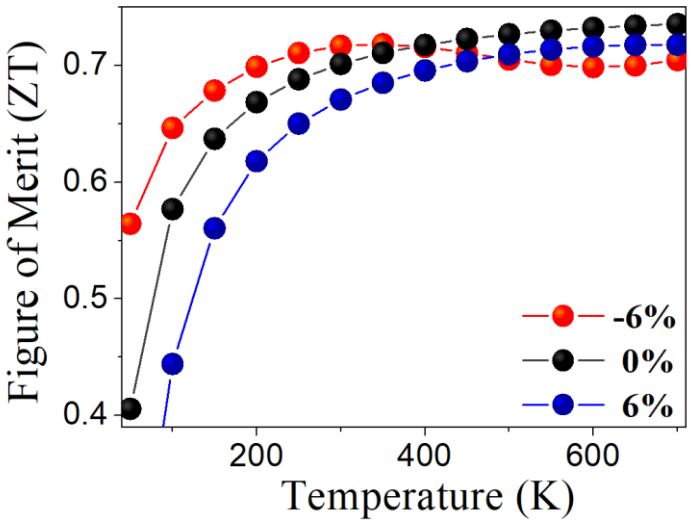

Figure IV.15 Calculated figure of merit (ZT) of unstrained (0%), compressive (-6%), and tensile (6%) strained SnO_2 over a wide range of temperature.

Due to the interplay between the Seebeck coefficient, electrical and thermal conductivities, our figure of merit displays a modulated variation under strain. Surprisingly, compressive strain gives raise to higher ZT values for temperatures below 400 K. This important result is mainly explained by the combination of a high Seebeck coefficient with a low thermal conductivity of strained SnO_2. Therefore, we can undoubtedly conclude that the thermoelectric efficiency of SnO_2 can be successfully improved by simply applying a biaxial strain, a finding that is very promising for room-temperature thermoelectric gas sensors applications [258], for instance.

Chapter conclusion

In conclusion, the biaxial strain effect on SnO_2 electronic and thermoelectric properties has been studied using first-principles calculations. Under compressive strain, our calculated bandgap was found to increase due to the formation of short and strong, covalent bonds while it decreases under an applied tensile strain. A wide bandgap is shown to yield a high Seebeck coefficient and a large effective mass that lowers the electrical conductivity. However, our calculated figure of merit (ZT) was found to be higher under compressive strain due to such a large Seebeck coefficient and low thermal conductivity for temperatures below 400K.

CHAPTER V: COMBINED STRAIN AND SIZE EFFECT ON THE ELECTROCHEMICAL PROPERTIES OF SnO_2 FOR HYDROGEN PRODUCTION

Table of contents

CHAPTER V: COMBINED STRAIN AND SIZE EFFECT ON THE ELECTROCHEMICAL PROPERTIES OF SnO_2 FOR HYDROGEN PRODUCTION

The need to reduce the environmental impact of fossil fuels in combination with its market instability increase the demand for new clean and sustainable energy sources needed to cover the world energy needs. The global energy needs increase rapidly according to the world population [259].

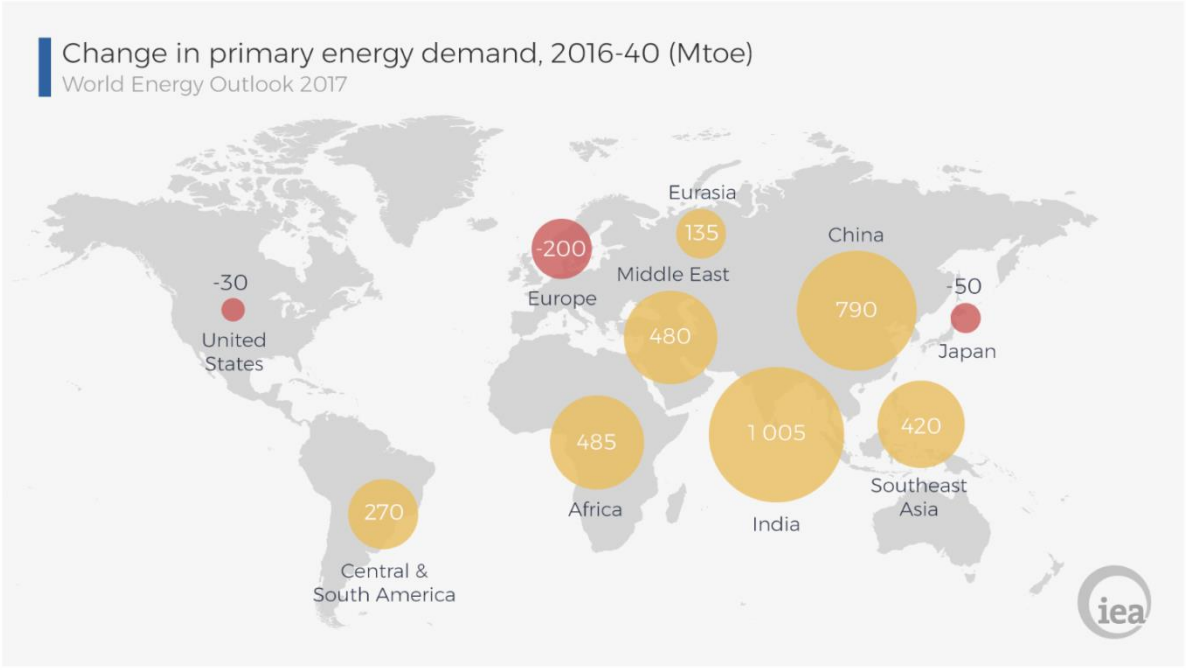

Figure V.1 Change in primary energy demand from 2016 to 2040 by Million tones (Mtoe) [259].

Increasing demand for clean and sustainable energy generates an urgent need to develop advanced methods with low cost and high efficiency for renewable energy conversion, such as wind energy conversion, photovoltaic process, and photo-catalytic water splitting and treatment. In fact, Photocatalysis has recently seen a growing interest within researchers as it serves in most promising technologies for water treatment and energy harvesting such as pollutants degradation, and hydrogen production [260-262].

V.1 Heterogeneous photocatalysis

Since the early 20th century, photocatalysis gained a great interest from scientists, as it serves in many promising environmental applications ranging from photo-electrocatalytic production of hydrogen and renewable energy to disinfection of water (See Figure V.2).

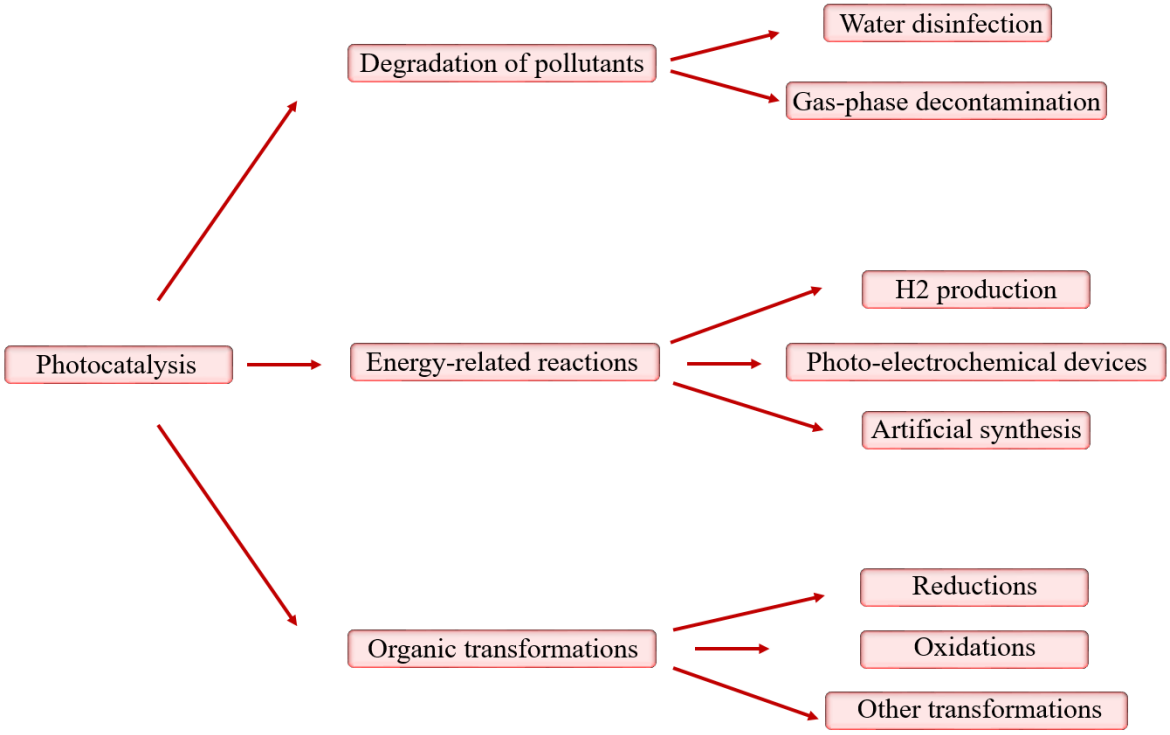

Figure V.2 Scheme of Photocatalysis applications

The photocatalysis process consists of acceleration of chemical reactions by mainly two ways, homogenous photocatalysis where the reactants and the photocatalyst are in the same phase, and heterogeneous photocatalysis where the photocatalyst and the reactants are in different phases. The heterogeneous photocatalysis process begins when a solid semiconductor absorbs a photon of an energy equal or higher than its bandgap ($h\upsilon \geq Eg$), the generated photo-excited electrons migrate from valence to conduction band [263,264]. The photonic excitation leaves behind an exciton with a hole in the valence band and electron in the conduction band (electron-hole pair). After, the photo-excited electrons and holes migrate to the semiconductor surface. At the surface, the photocatalyst is able to donate the electron to an electron acceptor (A), usually molecular oxygen. In turn, a donor species (D) can be oxidized by the valence band hole. The photocatalytic reactions are given by:

$$\text{Semiconductor} \xrightarrow{h\nu \geq E_g} e^-_{CB} + h^+_{VB}$$

$$h^+_{VB} + D \longrightarrow D^{\cdot +}$$

$$e^-_{CB} + A \longrightarrow A^{\cdot +}$$

$$e^-_{CB} + h^+_{VB} \longrightarrow \Delta \text{ and/or } h\nu$$

A successful photocatalyst process usually depends on three important factors, light irradiation, photocatalyst properties, and the interfacial charge transfer occurring at its surface. These charge transfer processes depend mainly on band edges positions of the valence and the conduction band relative to the redox potential of the adsorbed species [265]. Although parameters such as charge separation, mobility, and recombination of photo-generated electrons and holes may affect the photocatalytic process [266,267] (See Figure V.3).

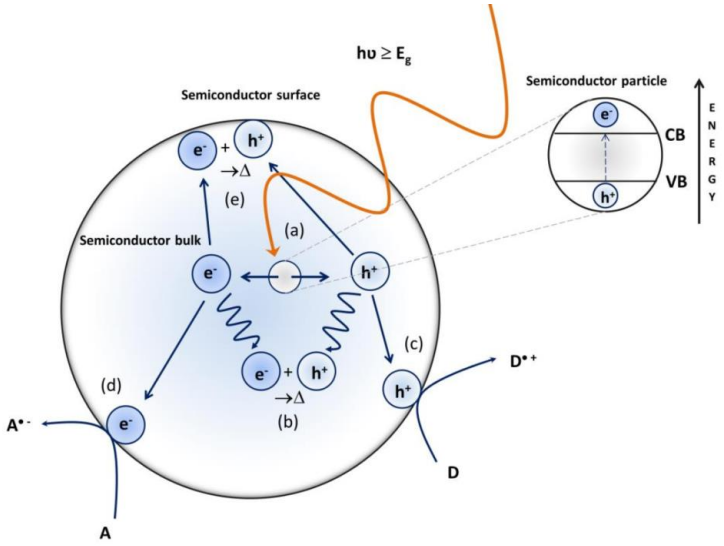

Figure V.3 Illustration of semiconducting metal oxide particle photo-excitation (a), electron-hole recombination within the semiconductor bulk (b), oxidation of surface adsorbed electron donors (c), reduction of surface adsorbed hole acceptors (d), and electron-hole recombination at the semiconductor surface (e).

V.2 Hydrogen production via photo-electrochemical water splitting

Since the discovery of the first hydrogen production from water by Fujishima and Honda in 1972 [268,269] the photo-electrochemical (PEC) water splitting has become an active research area for producing hydrogen [270-272]. Photo-electrochemical water splitting is effectively an artificial version of the photosynthesis scheme found in plants. As illustrated in Figure V.4, the photo-electrochemical cell consists of photo-electrodes used to generate a

potential which drives catalytic reactions, namely, the evolution of hydrogen (at the photo-cathode) and oxygen (at the photo-anode).

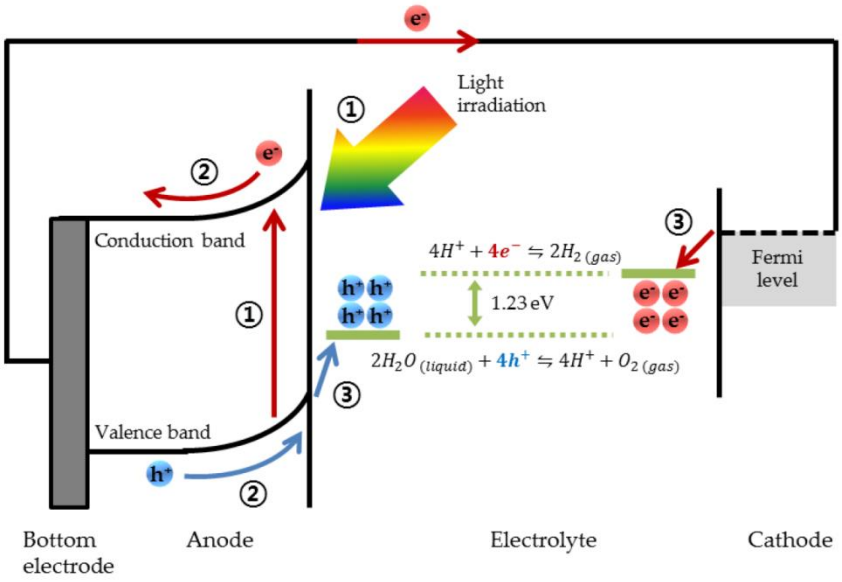

Figure V.4 Schematic representation of the photo-electrochemical (PEC) water splitting process in a common PEC water splitting system consisting of a photo-anode and a metal counterpart. Reported by Jeong et al. [273]

Amongst the important properties needed for water splitting process, the band edges alignment. For instance, to facilitate both the reduction and the oxidation of (H_2O) by photo excited electrons and holes, the conduction band minimum (CBM) should be located below the redox potential level of $H^+/H2$ (0 V vs NHE), the valence band maximum (VBM) should be above the redox potential level of H_2O/O_2 (1.23 V vs NHE), and the band-gap should be larger than 1.23 eV [274-276], which is the value of the standard Gibbs free energy change ΔG^0 needed for water decomposition:

$$H_2O = 1/2\ O_2 + H_2; \qquad \Delta G^0 = +237\ kJ/mol$$

V.2.1 Photo-electrochemical water splitting applications

In addition to its use for water treatment, photocatalysis has found several environmental applications such as air purification, atmospheric gases elimination (e.g. nitrogen oxides (NOx)), and self-cleaning surfaces (e.g. glass, metals, concretes, cements) [277-284]. Further, photocatalysis has been used for cancer treatment, hydrogen production, and organic compounds synthesis [285-288]. In particular, hydrogen production via photo-electrochemical water splitting has gained huge interest due to the enormous benefits of hydrogen in many fields and applications.

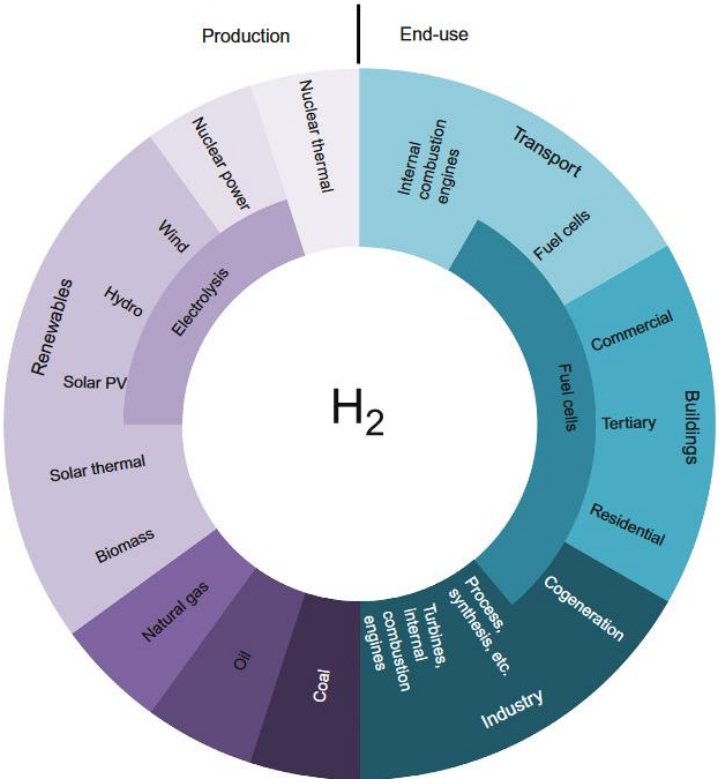

Figure V.5 Scheme for hydrogen production and uses Adapted from 2011connaissancedesenergies.com, from AFHYPAC—UE [289]

In the field of environmental conservation, the main use of hydrogen is removing the naturally sulfur contained in oil to produce cleaner fuels. In addition, hydrogen is a clean source of energy with great potential for applications in the aerospace industry. For instance, NASA has relied upon hydrogen gas as rocket fuel to deliver crew and cargo to space as is the fuel that concentrates the most energy (e.g. 1kg of hydrogen contains three times more energy than 1kg of gasoline) [290]. Besides, hydrogen has been used as fuel on board vehicle propelled by an electric motor. For industrial applications, hydrogen is used as a carrier gas (gas for transporting active gases) for the manufacture of electronic devices. Besides, in chemical industry, hydrogen can be combined with nitrogen to make ammonia, and it can be used as a reagent in the composition of textile fibers such as nylon, polyurethane foams and various plastics. Moreover, in glass industry, hydrogen is extensively used in the float glass process in the manufacture of flat glasses used for flat screens.

Figure V.6 Report on the global industrial gases market for the glass industry from 2017-2021 [291].

V.2.2 Materials for photocatalytic water splitting

Since the first solar-driven splitting of water into oxygen and hydrogen, TiO_2 was the most intensively used and studied photo-catalyst semiconductor combining several optimistic features such as non-toxicity, low cost and an excellent stability against photo-corrosion [268,292,293] making it the most prevalent photo-catalyst material. TiO_2 can be used in two ways, as suspended nanoparticles or as immobilized on solid substrates immersed inside reactors. The main benefits of TiO2 particles are the high area-to-volume ratios and the high specific production of reactive species. Indeed, TiO2 nanoparticles are the most widespread form of TiO2 used in water and wastewater research so far. Nevertheless, the separation of TiO2 nanoparticles from the liquid phase is required after water treatment. The post-separation of TiO_2 triggers the need for other complex and expensive processes such as filtration or coagulation whose efficiency depends on the nanoparticles size.

In comparison with TiO2 nanoparticles, immobilized TiO2 provides a simpler photocatalytic process, as it avoids filtration and recovery of dispersed nanoparticles after photocatalytic reactions. Therefore, developing photocatalytic devices based thin films is desirable thanks to their low cost and high efficiency. As mentioned, TiO2 presents the most convenient photocatalyst for water splitting. Nevertheless, the fast recombination of TiO_2 photo-generated electron/hole due to its low electron mobility (~1 cm^2 V^{-1} S^{-1}) represents a serious obstacle for its efficiency [294,295].

To face such an handicap SnO2 is a serious option since it has a superior electron mobility (~200-250 cm^2 V^{-1} S^{-1}) and high electron transfer efficiency [295,296] preventing therefore a rapid electron-hole recombination. Indeed, SnO2 has recently been tested for photo-

catalytic production of H_2 [297-301]. However, its band energy did not match the redox potential of water (H2O). As reported in Figure V.7, the conduction band minimum (CBM) of SnO2 compared to other semiconductors such as ZnO and TiO2 is located above the redox potential level of H^+/H_2 (outlined in red), which presents a serious disadvantage and complicates its wide application in photocatalysis especially for water splitting and hydrogen evolution reaction (HER) [302].

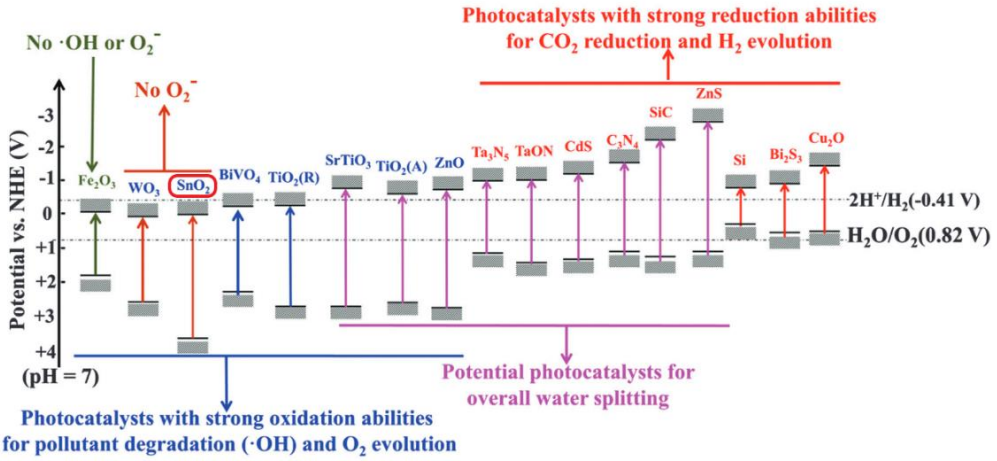

Figure V.7 Band positions and potential applications of some typical photo-catalysts (at pH = 7 in aqueous solutions). Reported by Li et al. [303].

To face such a difficulty, one can modulate the energy band structure of SnO_2 by use of strain when SnO_2 is deposited as a thin film on a foreign substrate [304,305]. In fact, such a strategy minimizes the industrial cost since it avoids the recovery to the removal of dispersed nanoparticles after photocatalytic reaction, as it is usually the case. Therefore, the development of thin films based photo-catalysts becomes of great interest for novel photocatalytic systems [306-309].

Inspired by such a funding, we attempt to take advantage from our previous results regarding the capability of an applied biaxial strain to adjust the electronic properties of strained SnO2 bulk and thin films (See **CHAPTER III: STRAIN ENGINEERING: Strain and size effect on SnO_2 electronic properties**, section **III.3.2.3. Strain and size combined-effect on the electronic properties** for more details), and elaborate a computational strategy to enhance the SnO_2 electrochemical properties since the latter is directly related to the band gap and electronic properties. Therefore, in the present chapter, the effect of a biaxial strain on the photo-electrochemical properties of SnO2 bulk and thin-films have been investigated using density functional theory calculations, especially the improvement of the redox potential level of H^+/H2.

V.3 Photo-electrochemical properties of strained SnO_2

In the present section, we aim to discuss the effect of thickness together with biaxial strain on the electrochemical properties of SnO_2. As a start of the present study, the band gap energy of SnO2 film in different thin-film thicknesses (from 0.3 nm (one layer) to 2.5 nm (8 layers)) has been calculated.

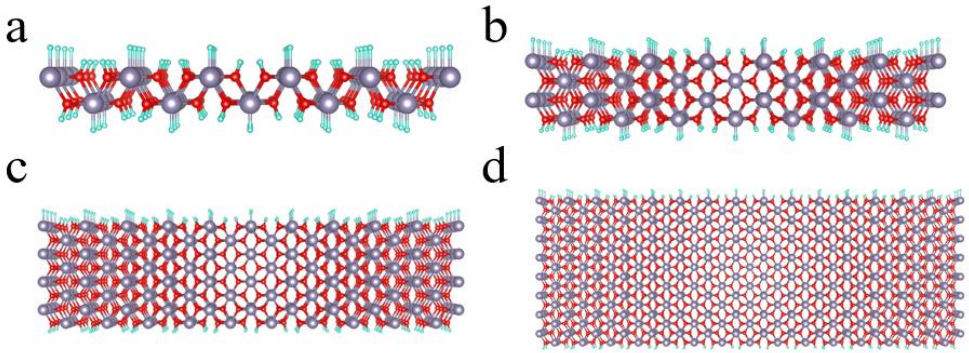

Figure V.8 Structure of Hydrogen-passivated SnO2 films in different sizes. Thickness of films are (a) 0.3 nm, (b) 0.6 nm, (c) 1.25 nm, (d) 2.5 nm. Gray spheres present Sn atoms, red spheres present O atoms, and the blue spheres present the pseudo-hydrogen atoms.

As presented in Figure V.9, The calculated band gap of SnO2 bulk is 3.34 eV, a value that is close to the experimental one *i.e.* 3.6 eV [310]. The band gap increases gradually from 3.34 eV to 5.23 eV with decreasing film thickness, and as this later increase, the band gap energy decreases toward the band gap of SnO2 bulk. Since all the studied films are smaller than the exciton Bohr radius for SnO2 (2.7 nm) [311], the resulted increase of the band gap as the size decreases could be attributed to the quantum confinement effect, as reported previously in several studies [304,312].

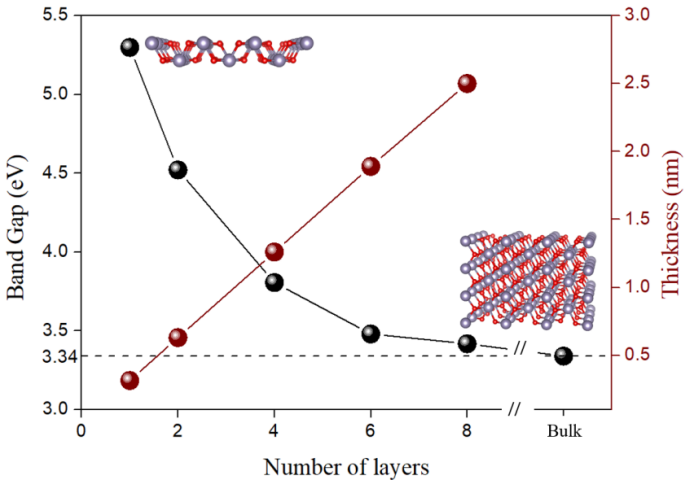

Figure V.9 Calculated band gap values of SnO2 in different sizes.

Further, we applied a range of biaxial strain "ε" along the ***ab*** plane of SnO2 bulk and thin-films. This later was varied in order to simulate either a compression (negative strain values) or a tension (positive strain values), while the relaxation of the crystal is freely performed along the ***c*** axis for each ***a***(***b***) fixed. In this figure case, the biaxial strain can be expressed as:

$$\varepsilon_{xx}(\%) = \varepsilon_{yy}(\%) = \frac{a(b) - a_0(b_0)}{a_0(b_0)} \qquad \text{Eq.V.1}$$

Calculated band gap energy of bulk and passivated SnO2 thin-films under strain is presented in Figure V.10 As the film thickness increases the band gap energy decreases toward the bulk band gap. In addition, for each film, under compression, because of covalent bonding strengthening and charge condensation the band gap increases. Again, an opposite behavior is demonstrated in the case of tensile strain. (See **CHAPTER III: STRAIN ENGINEERING: Strain and size effect on SnO_2 electronic properties**, section **III.3.2.3. Strain and size combined-effect on the electronic properties** for more details)

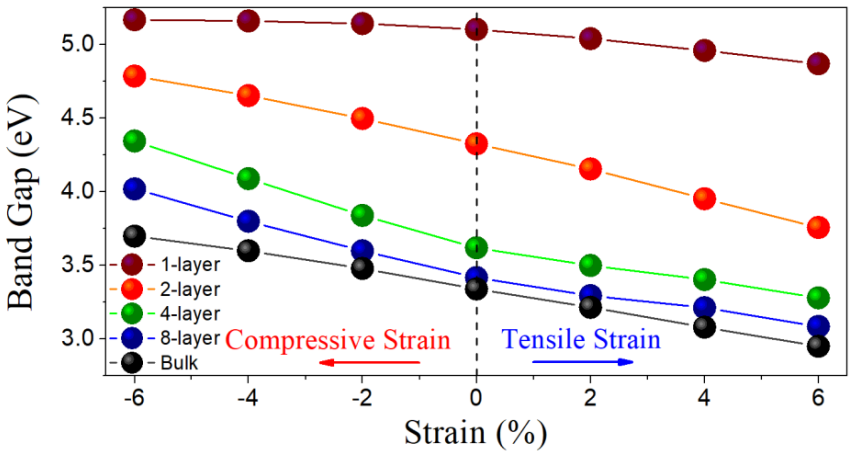

Figure V.10 Calculated band gap energy of Passivated SnO2 film under strain.

The design of a photo-electrochemical material is directly based on its electronic properties through three important criteria. The absorption capability, the charge carrier mobility, and the band edge positions of the photo-electrochemical material, which are related to the material band gap and band structure. Therefore, in the present chapter we aim to discuss the effect of thickness together with an applied biaxial strain on the photo-electrochemical properties of SnO_2 ultra-thin films.

V.3.1 Absorption of strained SnO2 bulk thin-films

The absorption capability of a material is related directly to its band gap energy. Indeed, as presented in Figure V.11, the absorption of SnO2 is limited to the ultraviolet light due to its large band gap (e.g. 3.6 eV for SnO2 bulk). As the thickness decreases from bulk to one layer thin film, the band gap increases, which results in absorption shift from visible light.

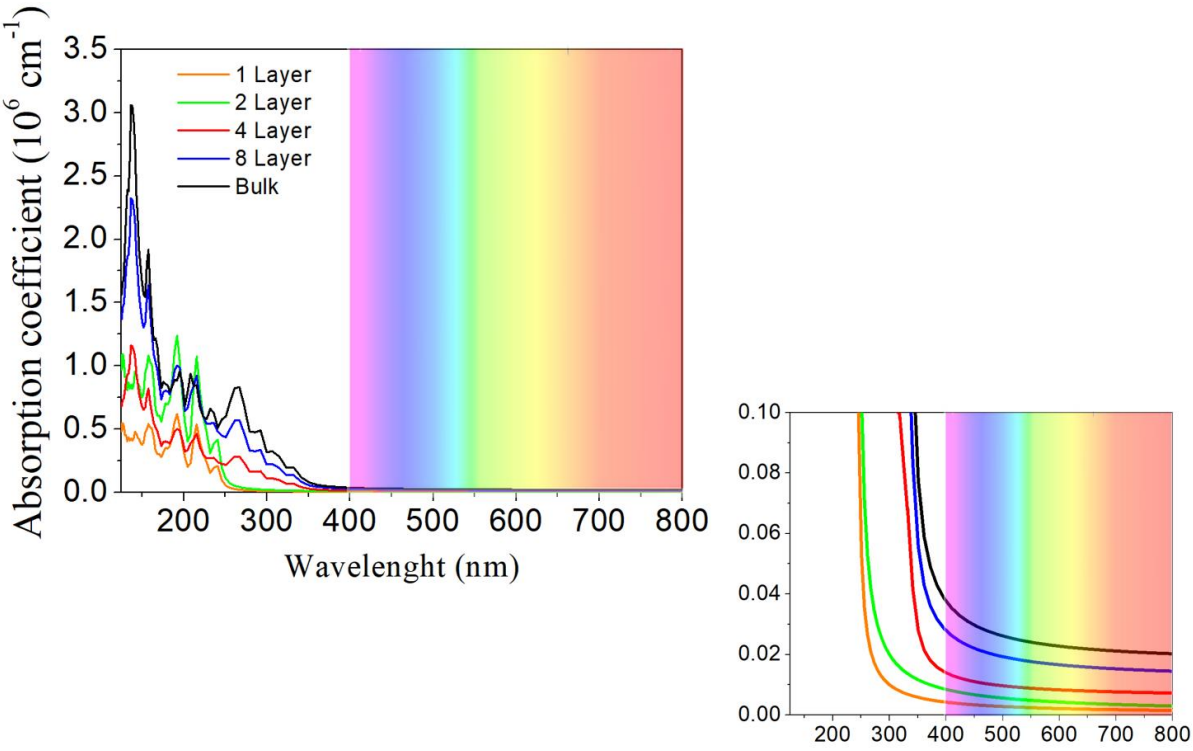

Figure V.11 Calculated absorption of SnO2 thin films in different sizes (left) and zoom in the absorption coefficient near visible light (right)

However, visible-light absorption can be improved by applying a tensile strain, as the later can decrease the band gap energy. In fact, as presented in Figure V.12, for SnO_2 thin films and bulk, tensile strain seems to increase enhance the visible-light absorption especially in the case of SnO_2 bulk thanks to band gap decreasing, these results are of big benefit to SnO_2 in order to widen its photocatalytic application.

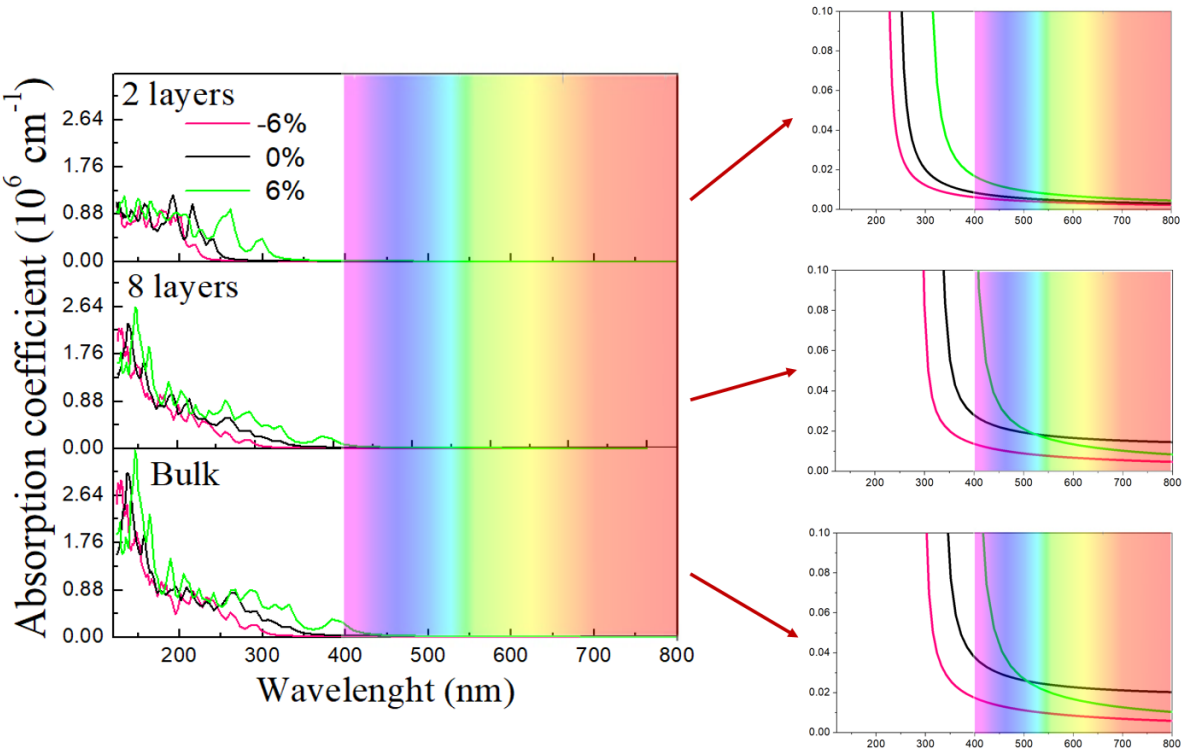

Figure V.12 Calculated absorption of SnO2 thin films, 2 layers film (Top), 8 layers film (Middle), and bulk (Below) under strain (Left). Zoom in the absorption coefficient near visible light (right)

V.3.2 Charge carrier concentration and mobility of strained SnO2 bulk and thin films

After light absorption, photo-excited electrons and holes mobilize to migrate and reach the film surface, and their mobility can define their capability to be transferred to the surface. The charge carrier mobility is highly related to the band structure, band gap energy and effective mass. For instance, wide band gap leads to high effective mass, which yields to a lower charge carriers mobility. In fact, the calculated charge carrier mobility as a function of strain for each SnO2 thin film is presented in Figure V.13. Our results display an opposite trend to our calculated band gap energy under strain. In one hand, as the thickness increases, due to the band gap decrease, electrons and holes mobility increases, in the other hand, for each SnO2 thin film compressive strain results in lower mobility values for electrons and holes due to the continuous increase of band gap, while under tensile strain, narrow band gap seems to increase the mobility.

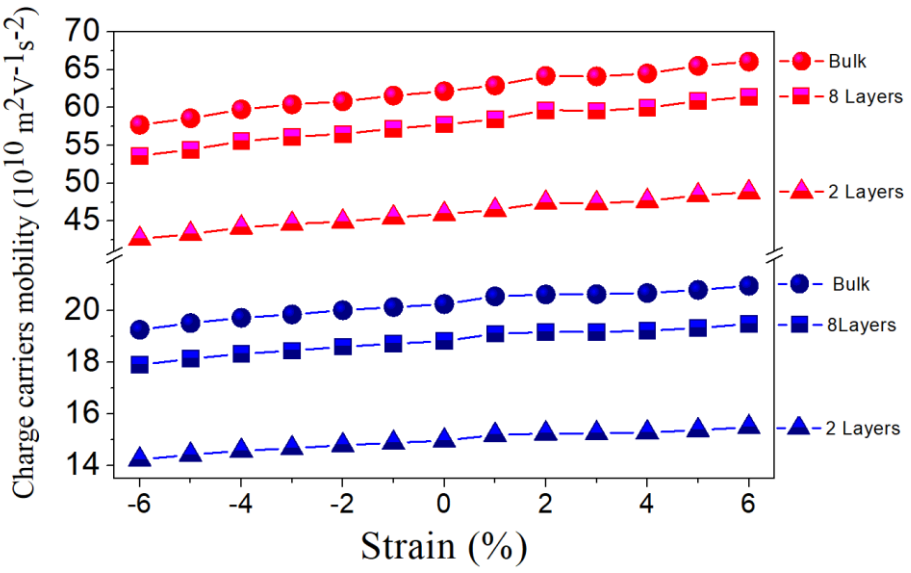

Figure V.13 Calculated mobility of electrons (Red) and holes (Blue) of SnO_2 thin films and bulk under strain.

Beside mobility of charge carriers, their concentration presents a crucial parameter for photo-electrochemical reactions. Table.1 presents the electrons and holes concentrations for unstrained, 6% and -6% strained SnO_2 Thin films, it is noticed that the SnO_2 is remained n-type semiconductor under strain for bulk and thin films. Again, as thickness increases the concentrations of holes and electrons increase due to the band gap decrease. Also, the electrons and holes concentrations increase under tensile strain for SnO_2 bulk as well as thin films.

Table V.1 Calculated concentration and mobility of charge carriers of SnO2 thin films under strain.

Carriers concentration		-6%	0%	6%
2 Layers	n (m^{-3})	$5.46\ 10^{13}$	$1.87\ 10^{18}$	$9.39\ 10^{19}$
	p (m^{-3})	$8.67\ 10^{3}$	$7.16\ 10^{4}$	$4.28\ 10^{7}$
8 Layers	n (m^{-3})	$7.82\ 10^{15}$	$3.18\ 10^{19}$	$2.64\ 10^{21}$
	p (m^{-3})	$9.15\ 10^{4}$	$5.28\ 10^{6}$	$2.53\ 10^{10}$
Bulk	n (m^{-3})	$3.85\ 10^{16}$	$4.16\ 10^{20}$	$6.81\ 10^{21}$
	p (m^{-3})	$1.2\ 10^{5}$	$1.19\ 10^{7}$	$1.43\ 10^{12}$

The previous results show the strong effect of band gap modulation on optical properties, and introduce tensile strain as a good technique to improve the probability of generated electrons and holes transferring to the surface, and consequently to enhance the photo-catalytic properties.

Since electronic and optical properties of SnO_2 are mechanically tunable, it is worthwhile exploring the effect of strain on its valence and conduction band edges in order to enhance its suitability for photo-catalytic application.

V.3.3 Band edges positions of strained SnO2 bulk and thin-films

Band edge positions are the parameters that govern the ability of a semiconductor to transfer the photo-generated electrons to the adsorbed species on its surface. Therefore the positions of valence and conduction band edges were calculated using the concept of the semiconductor electronegativity and Nernst equation. Then the conduction and valence band edges can be expressed by:

$$E_{CB}^{0} = X(\mathrm{S}) - E^{0} - \frac{1}{2}E_{\mathrm{g}}, \quad \text{Eq.V.2}$$

$$E_{CB} = E_{CB}^{0} - 0.05911 * \left(pH - pH_{pzc}\right) \quad \text{Eq.V.3}$$

$$E_{VB} = E_{CB} + E_{\mathrm{g}} \quad \text{Eq.V.4}$$

Where Eg is the band gap, E^0 is the scale factor relating the reference electrode redox level to the absolute vaccum scale (AVS) (E^0 ~ 4.5 eV for normal hydrogen electrode (NHE)) and $pH_{pzc}$is the pH value at the point of zero charge ($pH_{pzc}(SnO_2)$ = 5) [313]. Although this method cannot give precise absolute values as it neglects the structural factors, it may estimate the relative positions of NHE.

Figure V.14 presents the CB and VB edges of SnO_2 thin films as a function of its thicknesses for different values of *pH*. Band edge alignments of SnO_2 bulk for $pH = pH_{pzc}$ shows that the VBM is more positive than the redox potential of O_2/H_2O (1.23V) while the CBM lies above the redox potential of H^+/H_2 (0V), which mean that the pure SnO2 in neutral environment cannot be used for hydrogen evolution reaction (HER). As thickness decreases the VB edge is more positive than the redox potential of O_2/H_2O (1.23V) for all *pH* values, while the CB edge lies below the redox potential of H^+/H_2 (0V) only for films thinner than 1.26 nm (4 layers). Although, by increasing the pH value ($pH \geq 10$), CB edge of larger films could reach the reduction potential of H^+/H_2.

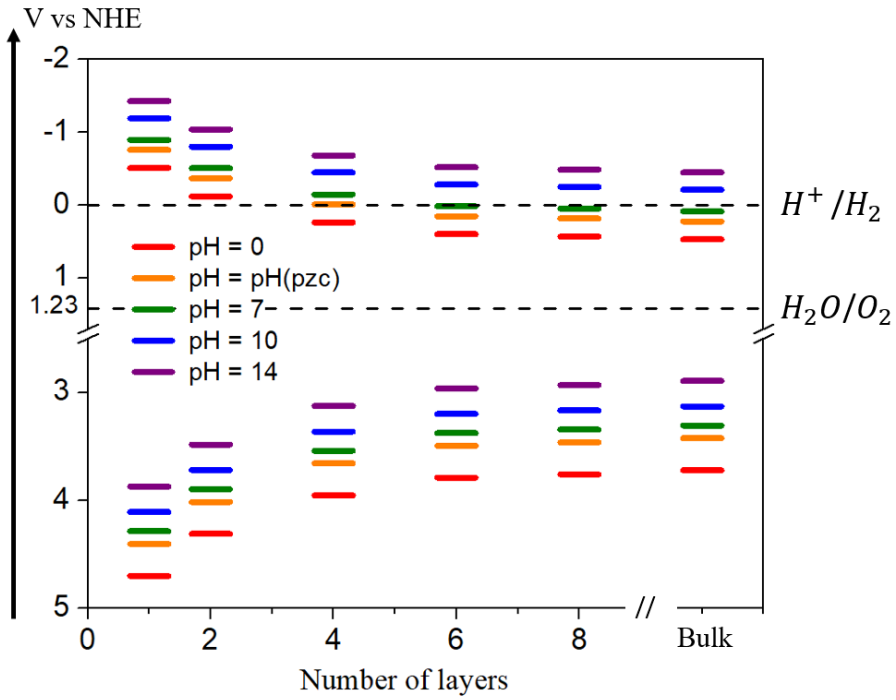

Figure V.14 Calculated band edges position of SnO2 in different sizes for various pH values.

Furthermore, as presented in Figure V.15, biaxial strain could improve the CB edge position. Indeed, CB edge of SnO2 bulk is suitable under compressive strain for pH ≥ 7 and under tensile strain for pH > 10. For SnO_2 film of 8 layers, CB edge is suitable under compressive strain for pH $\geq pH_{pzc}$ and under tensile strain for pH ≥ 10. While for SnO2 film of 2 layers, CB edge is suitable under compressive strain for pH ≥ 0 and under tensile strain for pH $\geq pH_{pzc}$. Therefore, large pH values and/or large bandgap can make the redox potentials energetically more favorable for water splitting. Since the band edges change as a function of band gap and pH, CBM edge position could be suitable for hydrogen production either by increasing the band gap and/or the pH value.

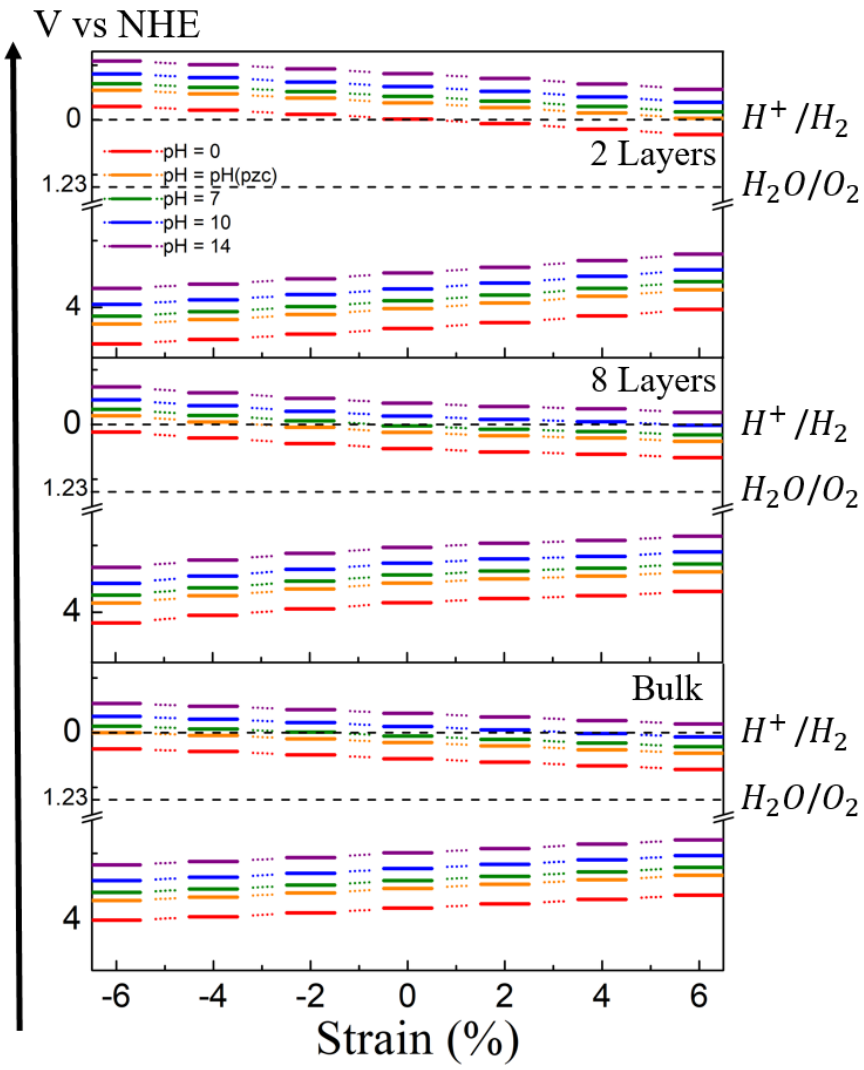

Figure V.15 Calculated band edges position of SnO_2 2 layers film (Top), 8 layers film (Middle), and bulk (Bottom) under strain for various pH values.

Chapter conclusion

In summary, the effect of size together with biaxial strain on SnO2 electrochemical properties have been studied using first-principles calculations. Narrow band gap is demonstrated to yield higher charge carrier mobility, while for the band edge alignments the redox potential for hydrogen reduction has been enhanced in the case SnO_2 films thinner than 1.26 nm (4 layers). Elsewhere, compressive strain for $pH \geq 7$ or larger pH value ($pH \geq 10$) under tensile strain could enhance the band edge positions relative to the water (H_2O/H2) redox levels. Finally, we believe that tensile strained-SnO_2 can for instance be acheived by depositing a thin film on a substrate with larger lattice parameters, making therefore such a compound a suitable candidate for H_2 production applications without the need for nanoparticles filtration as it usually the case of static photocatalysis.

CHAPTER VI: COMPARATIVE STUDY OF CARBON MONOXIDE (CO) ADSORPTION ON STRAINED SnO2 SURFACES

Table of contents

CHAPTER VI: COMPARATIVE STUDY OF CARBON MONOXIDE (CO) ADSORPTION ON SnO_2 SURFACES

During the past decades, the development of industrial and chemical activities resulted in toxic gases emissions that pollute environment leading to a serious threat of humans' health and life. Outdoor air pollution may cause diseases, allergies and even death to humans and other living organisms such as animals and food crops, and may damage the natural or built environment. Human health diseases and death from outdoor air pollution have been estimated to increase from 3.4 million in 1990 to 4.2 million death in 2016 [314].

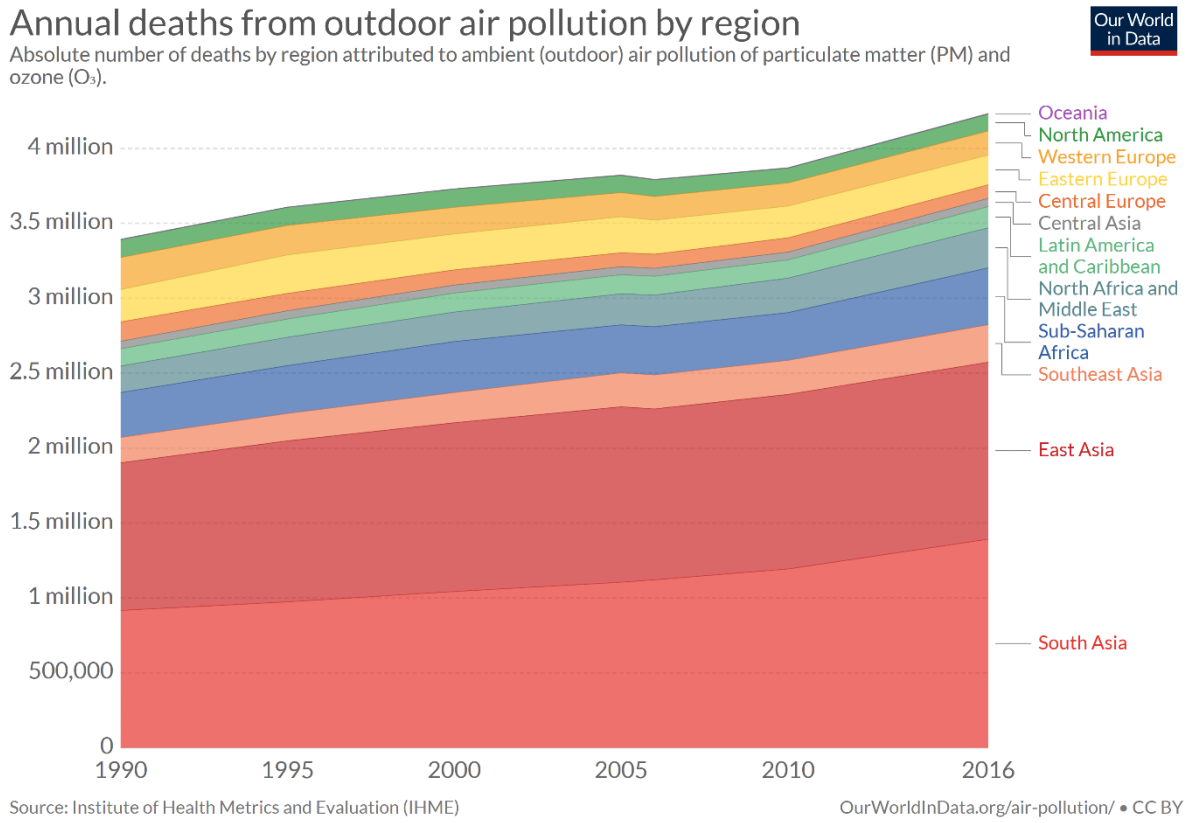

Figure VI.1 Number of deaths by region attributed to outdoor air pollution [314]

Besides, indoor air pollution is considered also as one of the world's largest environmental problems. Based on the reports of the Institute for Health Metrics and Evaluation (IHME), 1.6 million people died prematurely in 2016 from illness attributable to household air pollution [314].

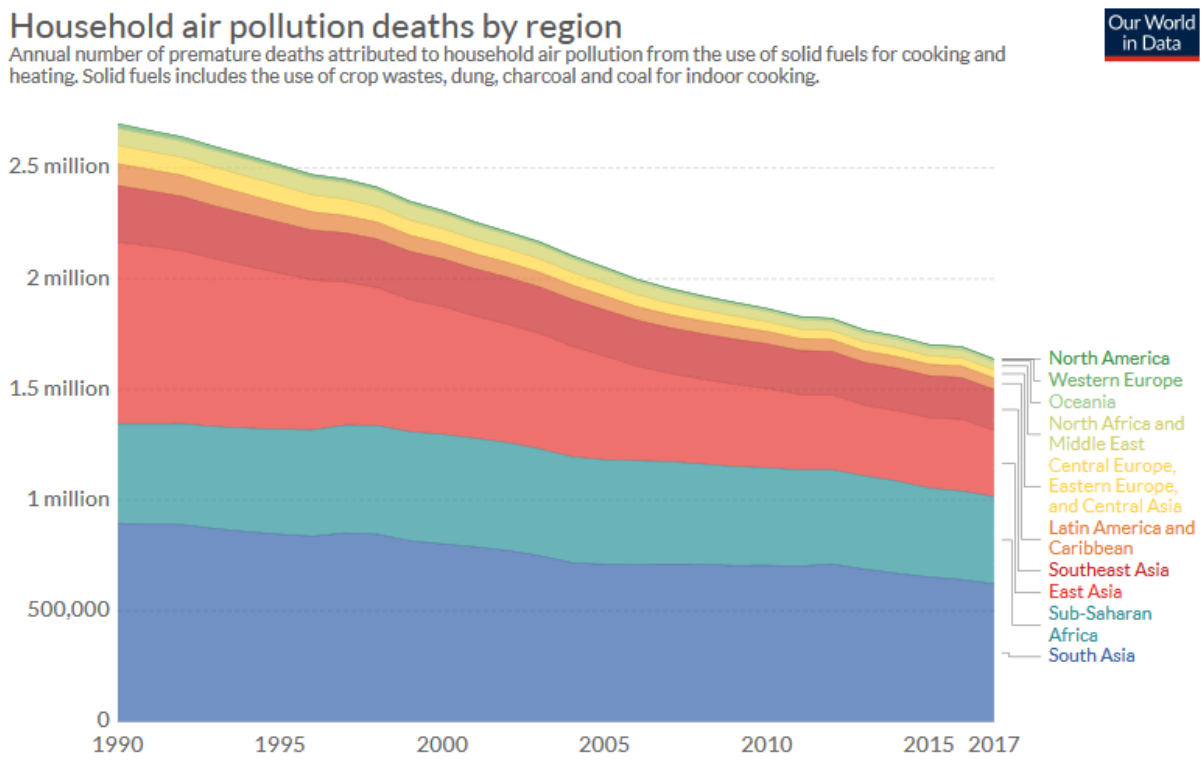

Figure VI.2 Number of deaths by region attributed to indoor air pollution [314]

Indoor air pollution is caused by the inefficient use of solid fuels for cooking and cleaning, .It is predominantly women and young children who are killed by indoor air pollution. According to the World Health Organization (WHO), these deaths are attributable to different diseases such as Pneumonia, stroke, ischemic heart disease, chronic obstructive pulmonary disease (COPD), and lung cancer [315].

Therefore, the development of effective monitoring system to supervise air quality and control heating, ventilating, and air conditioning (HVAC) are needed in order to ensure maximum safety for human life. Among toxic gases, carbon monoxide (CO) is the most common type of fatal air poisoning. Indeed, its exposure at concentrations of about 30 ppm can result in the weakening of heart conditions, reduction in ability to perform manual tasks and general drowsiness, and at concentrations greater than 35 ppm for extended durations (>24h) CO exposure can result in headache, irritability, blurred vision, lack of coordination, nausea, dizziness, breathlessness, then death [316].

In the recent decades, scientists have developed small and flexible devices in order to detect the limit of hazardous substances in the atmosphere, which are widely known as gas sensors. The so-called gas sensors have been developed based on different sensing mechanisms, such as electrochemical sensors, catalytic combustion sensors, infrared sensors and diffusion

fuel cell sensors [317-324]. Amongst, Metal Oxide (MOx) gas sensors have gained significant interest since they are based on metal oxide semiconductors (MOS) that present attractive materials for functional nano-devices, which are controllable and can be easily transformed in diverse shapes of low dimensionality.

VI.1 Metal Oxide (MOx) gas sensors

Metal Oxide (MOx) gas sensors detect gases by the chemical reactions that take place when the gas comes in direct contact with the sensitive material. MOx gas sensors are generally fabricated by depositing a layer of a metal oxide, typically SnO2 or In2O3, onto a substrate with electrodes and an integrated heater. The first commercialized MOx gas sensors were in 1968 by N.Taguchi [325-326]. After several decades of evolution, MOx gas sensors feature high sensitivity, compact size and low cost [326], and are considered one of the best options for monitoring low concentrations of combustion gases [327].

VI.1.1 Operating principles of Metal Oxides (MOx) gas sensor

The operating principle of MOx gas sensors is based on the electrical properties variation of the metal oxide film exposited to a target gas.

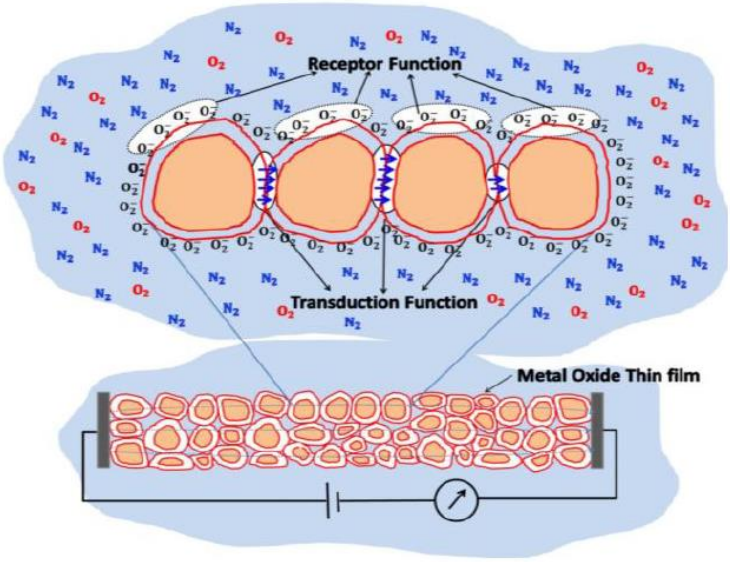

Figure VI.3 Schematic illustration of metal oxide thin film gas sensor.

As shown in Figure VI.3, the reaction of gas molecules with the metal oxide surface involves two key functions. The first one is the detection of the target gas via a gas-solid interaction, which results in electronic change of the oxide surface (*Receptor function*), while the second one is the conversion of the surface reactions into electrical resistance change of the sensor (*Transduction function*).

The change of electrical resistivity of the metal oxide film depends on its semiconducting type (n/p) and the nature of the gas molecules (oxidizing/reducing) in an ambient atmosphere. For instance, oxidizing gases such as NO_2 react as electrons acceptors for n-type semiconductors, which results in an increase of electrical resistivity, while reducing gases such as H_2S, H_2, and CO act as electrons donors, which decreases the electrical resistivity. In the other hand, gases molecules react in a reverse manner with *p*-type semiconductors [328] (See Table VI.1).

VI.1 Effects of Oxidizing/Reducing gases on Semiconductor Properties.

Semiconducting type	Response to oxidizing gases	Response to reducing gases
n-type	Resistance increases	Resistance decreases
p-type	Resistance decreases	Resistance increases

In normal air conditions, the metal oxide surface reacts first with oxygen O2 molecules in air before that they detects target gases. As shown in Figure VI.4, the oxygen molecules in air adsorbate and trap free electrons from the metal oxide surface, which results in inhibiting electrical flow [329,330].

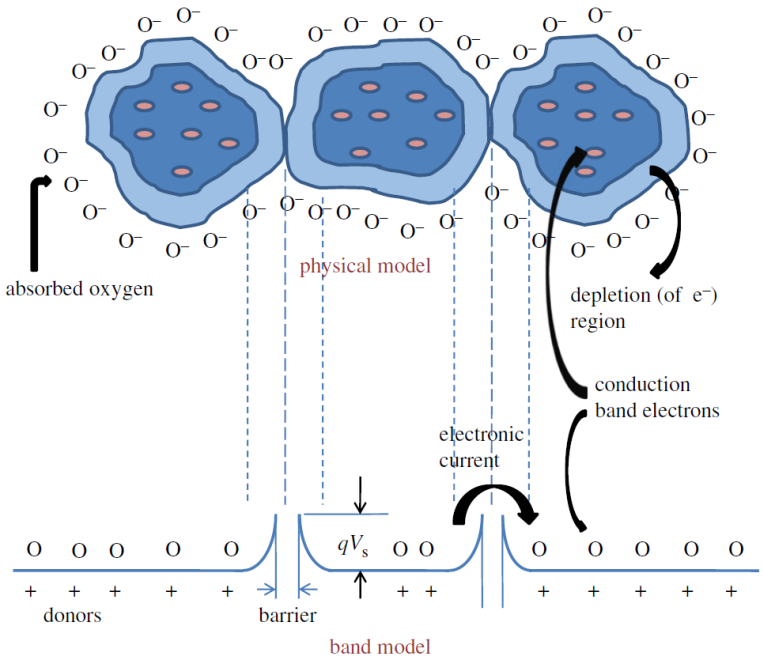

Figure VI.4 Structural and band model for metal oxide grains showing the role of inter-granular contact regions [331].

The negatively charged oxygen ions adsorbed at the surface of the semiconductor oxide, creates a band bending, which generates a surface potential ($-eV_{surface}$) and a depletion layer, building up of Schottky surface barrier that results in free electrons being confined in grains

center. Consequently, the electrical conductance of the film decreases to a minimum. In other words, changes in the width of the depletion layer induce changes in the electrical resistance. In the presence of reducing gases such as CO, CH4, H2S, and H2, they react with the pre-adsorbed O2 at the surface, resulting in release free electrons to the metal oxide surface, causing a reduction in the depletion layer and, as a result, a reduction of the electrical resistance [331]. For example, when CO reacts with chemisorbed oxygen on the metal oxide surface generating CO_2, the amount of adsorbed oxygen will decrease significantly and trapped electrons are released back to the oxide. As a result, the height of Shottky barriers is decreased, which produces an increase in the conductance (or decrease in the resistance) of the sensing layer. Furthermore, there is a clear relation between the depletion layer width and the size of the metal oxide grains. It has been reported that the ratio between the grain size (D) and the Debye length (L_D), which is the scale over which the charge separation happens in a semiconductor, greatly affects the magnitude of the resistance variation [332]. The Debye length is -defined as follows:

$$L_D = \sqrt{\frac{\varepsilon K_B T}{q^2 N_D}} \qquad \text{Eq VI. 1}$$

where ε is the dielectric constant, K_B is the Boltzmann constant, q is the elementary charge and N_D is the density of dopants (either donors or acceptors).

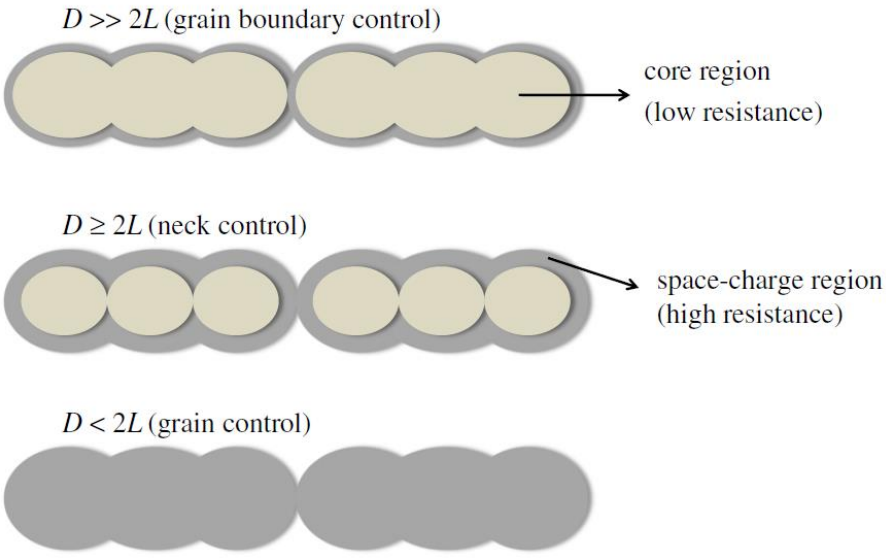

Figure VI.5: Schematic view of the grain boundary control, neck control and grain control

If the grain size is larger than two times the Debye length (D>>2L_D), the depletion of the surface between the grain boundaries control the conductivity is really small (grain boundary control). In this case, a low response of the sensor is expected because only a small

part of the semiconductor is affected. When grain size became comparable with the Debye length (but still larger, D ≥ $2L_D$), the necks become more resistant and they start to control the gas sensitivity (neck control). Finally, when D < $2L_D$, the whole grain is depleted, the energy bands are almost flat, changes in the oxygen concentration affects the entire semiconductor and thus, a high response is obtained [333] (See shown in Figure VI.5).

Adsorption of gas molecules on solid surfaces can be classified into physisorption or chemisorption [334]. The former is induced by weak van der Waals forces and can be transferred (with subsequent bond activation) into the latter one, which involves a chemical bonding with the atoms at the surface. Adsorbed molecules can undergo a dissociation process to form smaller molecular or atomic fragments on the surface. As a result, the system evolves to a state for lowering the total energy. Nevertheless, having a clear picture of how the gas molecules interact with the MOx surface is not enough to quantitatively explain the change of electrical properties in the solids.

VI.1.2 Key characteristics of Metal Oxides (MOx) gas sensors

The key characteristics of all gas sensors are sensitivity, selectivity, reversibility, response time and recovery time, which depend on the method of preparation of the sensitive material.

VI.1.2.1 Sensitivity of Metal Oxides (MOx) gas sensors

The sensitivity (S) of a gas sensor is a measure of the lowest detected change on electrical properties toward a gas. The sensitivity of metal oxide is defined as:

$$S_{RG} = \frac{R_{gas}}{R_{air}} \qquad \text{Eq VI. 2}$$

$$S_{OG} = \frac{R_{air}}{R_{gas}} \qquad \text{Eq VI. 3}$$

where S_{RG} and S_{OG} are sensitivities for reducing and oxidizing gases respectively, R_{air} and R_{gas} are electrical resistances of the sensor in the air and upon exposure to the target gas respectively.

VI.1.2.2 Selectivity of Metal Oxides (MOx) gas sensors

The selectivity of metal oxides could be defined as a comparison between sensitivity for two target gases under same conditions. Generally, metal oxides gas sensors exhibit poor selectivity as their operation depends in most cases, on the reaction of reducing gases with pre-adsorbed oxygen molecules. The selectivity can be expressed as:

$$\text{Selectivity } (S_l) = \left| \frac{S_{gas(a)} - S_{gas(b)}}{S_{gas(a)}} \right| \qquad \text{Eq VI. 4}$$

VI.1.2.3 Response and recovery time of Metal Oxides (MOx) gas sensors

The response time is usually defined as the time taken to achieve 90% of the final change in resistance following the change of gas concentration, while the recovery time is defined as the time that the sensor takes to recover a 90% of the initial value of the resistance when exposed to clean air. The response time is an important parameter since it can determine the commercial applicability of the sensor. Unfortunately, it is probably the most difficult parameter to measure in a reproducible manner, as it requires special gas flow systems, which are designed to ensure that step changes in gas concentration are faster than the response time of the sensor, especially when dealing with highly adsorptive and reactive gases.

VI.1.2.4 Stability of Metal Oxides (MOx) gas sensors

The stability is defined as the ability of the sensor to maintain their properties in a long period. It has been reported that chemical surface reaction may produce a long-term drift (poisoning) affecting the performance of the sensor [335]. There are several factors leading to gas sensors instability [336], such as design errors, structural changes (variations of grain size or grain network), phase shifts (the segregation of additives doped with sensing materials), poisoning triggered by chemical reactions and variation of the surrounding environment. Several methods have been considered in order to make the sensor more stable and reduce the response time. For example, using metals with good chemical and thermal stability, optimizing elemental composition and grain size of sensing materials and utilizing specific technologies during surface pretreatment of sensors.

VI.1.3 Sensing mechanism of Carbon Monoxide (CO) in MOx gas sensors

Carbon monoxide (CO) is an odorless and colorless gas, which is considered as one of the most dangerous and fatal gases that can cause sudden illness and death. CO is mainly produced by incomplete combustion of fuels, emission of automobile exhausts, and the burning of domestic fuels. As mentioned in the previous section, the sensing mechanism of MOx gas sensors to reducing gases such as CO is attributed to the chemisorption of oxygen located at the metal oxide surface and the target gas molecules. Thus when a metal oxide sensor is exposed to a carbon monoxide gas atmosphere, CO molecules usually react with the pre-adsorbed oxygen species by the following reaction [337-344]:

$$CO_{(gas)} + O^-_{(ads)} \rightarrow CO_{2(gas)} + e^- \qquad \text{Re VI. 1}$$

As a result, the surface oxygen concentration is reduced, and electrons that were initially trapped by oxygen anions are released back into the metal oxide, leading to an increase in the conductivity of the sensor, as shown in Figure VI.6.

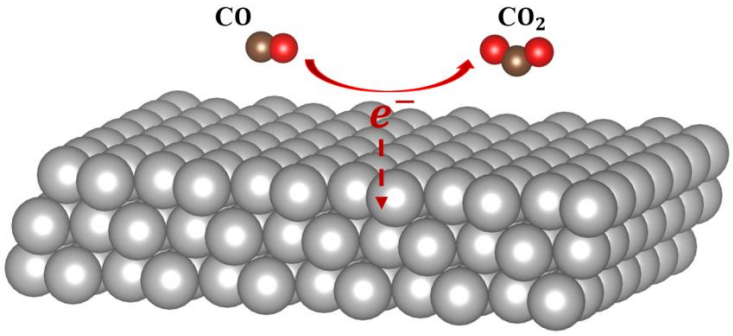

Figure VI.6 The mechanism of metal oxide sensor response to carbon monoxide CO

VI.2 SnO_2 in Metal Oxides (MOx) gas sensors

Among metal oxides, SnO_2 is considered as a potential material for gas sensing due to its promising properties, high selectivity and sensitivity, easy designing and implementation, and low cost [345]. Until now, researchers are still developing and reporting SnO_2 in different morphologies by doping and nano-structuring in order to enhance its sensitivity [346–348]. For example, Kolmakov et al. [349] investigated on SnO_2 nanowires and found that the smallest optimum diameter was around 60 nm for the adsorption of oxygen. Further, Wang et al. [350] reported high stability, selectivity and sensitivity of Pd-loaded SnO_2 nanostructures, as well as fast recover properties when detecting carbon monoxide gases. Moreover, Maeng et al. [351]

reported highly sensitive SnO_2 nano-slab network for NO_2 sensing. Further, Du et al. [352] studied the sensitivity dependence of SnO_2 film on its thickness. Besides, various hybrid materials like SnO_2/reduced graphene oxide composites, and reduced graphene oxide-multi walled carbon nanotubes-tin oxide nanoparticles hybrids have been employed for high performance low temperature NO_2 sensing [353,354]. During the last decade, intense research has been conducted to understand the electronic and mechanical features that govern the sensing behavior of SnO_2 towards various gases (NOx, ethanol, methanol, ammonia, acetone, CO, H_2 etc.) including trace amounts of toxic gases establishing the great suitability and huge potential of SnO_2 for gas sensing applications [355–360]. Therefore, it is relevant and valuable to deeply study and understand the sensing mechanism of SnO_2 to toxic gases. For such reason, in the present chapter we aim to predict and understand the sensing mechanism of CO through its adsorption on unstrained and strained (110), (100), and (101) SnO_2 surfaces.

VI.3 The sensing mechanism of Carbon Monoxide (CO) on SnO_2 surfaces

VI.3.1 CO adsorption on relaxed (110), (101), and (100) SnO_2 surfaces.

VI.3.1.1 Preparation and stability of relaxed SnO_2 surfaces

In this section, we focus on exploring the sensing mechanism of SnO_2 low-index surfaces to Carbon Monoxide (CO) molecule. First, we performed energy calculations for SnO_2 surfaces [(100), (110), and (101)] shown in Figure VI.7.

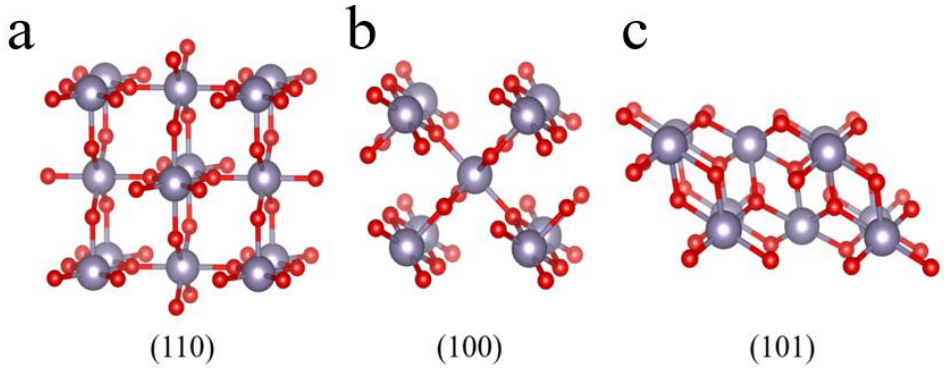

Figure VI.7 crystalline structure of (110) (a), (100) (b), and (101) (c) SnO_2 surfaces. Grey and red balls represent the Sn and O atoms respectively.

Usually the surface energy E_{surf} can be defined as the energy of the surface slab related to its bulk reference [361–368] as expressed by:

$$E_{surf} = \frac{E_{slab} - nE_{bulk}}{2A} \qquad \text{Eq VI. 5}$$

where E_{slab} is the total energy of the surface slab, E_{bulk} is the total energy of the bulk, n is the number of SnO_2 formula units in the slab, and A is the surface area with a factor of 2 due to each slab containing two surfaces.

From our calculated surface energies presented in Table VI.2, one can see that the stabilities of the SnO_2 surfaces are in the order $(110) > (100) > (101)$, and the most stable SnO_2 surface is (110) because it has the lowest number of dangling bonds in comparison to (100) and (101) surfaces. Our results are in good agreement with other reported results [368–370]. However, also (100) and (101) surfaces are relevant and widely investigated for toxic gases sensing by many researchers [371–374]. Therefore, it is worthy to do a comparative study of CO sensing mechanism on the three SnO_2 surfaces (110), (100), and (101).

Table VI.2 The calculated surface energy of SnO_2 (J/m^2).

Surfaces	(110)	(100)	(101)
Surface energy	1.027[a]	1.095[a]	1.439[a]
	1.040[b]	1.140[b]	1.330[b]
	1.035[c]	1.128[c]	1.461[c]

[a]Calculated energies
[b]From Ref. [369]
[c]From Ref. [371]

In the following, we discussed adsorption possibilities of CO on each SnO_2 surface. For all cases we used stoichiometric SnO_2 surfaces of 1 nm using the periodic slab model. The adsorption energy E_{ads} that measures a configuration stability is defined as:

$$E_{ads} = E_{slab} + E_{adsorbate} - E_{slab/adsorbate} \quad \text{Eq VI. 5}$$

where E_{slab}, $E_{adsorbate}$ and $E_{slab/adsorbate}$ are the total energies of the free slab, adsorbate, and the slab with the adsorbate respectively. According to Eq VI.5, positive adsorption energy consists of energetically favorable configuration, while negative one consists of unfavorable adsorption configuration. We note that different sites and configurations have been tested for the three surfaces of SnO_2, but only the optimized geometries of stable CO adsorption modes ($E_{ads} > 0$) have been discussed in the following sections.

VI.3.1.2 Adsorption of CO on relaxed SnO_2 (110)

Starting with the (110) surface of SnO_2 that consists of three parallel planes ($O/Sn_2O_2/O$), and has three possible adsorption sites: five-coordinated Sn top site (Sn_{5c}), two-coordinated O bridge site (O_{2c}), and three-coordinated O in-plane site (O_{3c}) (See Figure VI.8).

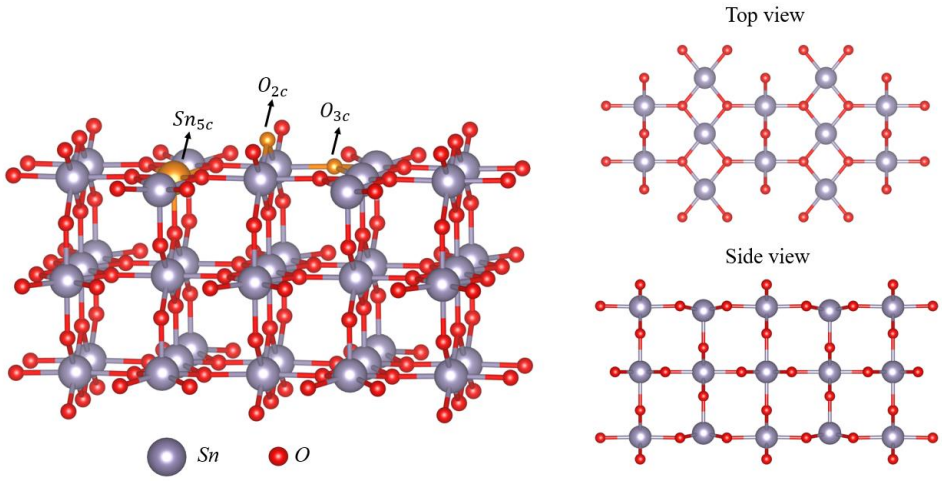

Figure VI.8 The (110) surface of SnO_2, gold atoms indicate the possible adsorption sites.

As shown in Figure VI.9, four adsorption configurations of CO on the oxygen bridge site (O_{2c}) have been considered: (A1) CO top O_{2c} with C down, (A2) CO along y axis with C top O_{2c}, (A3) CO along x axis with C top O_{2c}, (A4) CO along x axis.

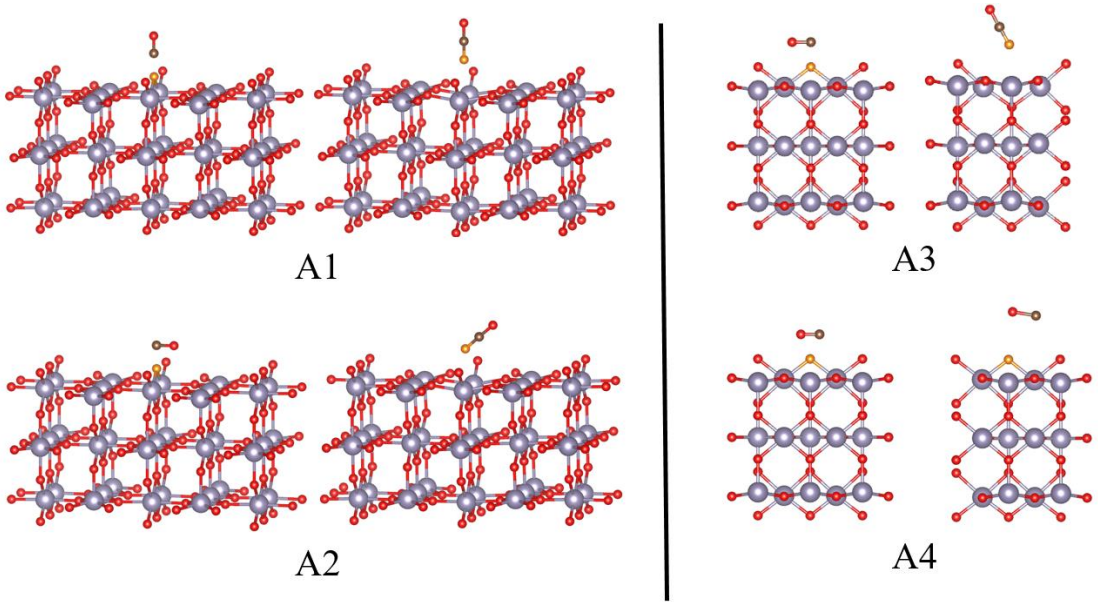

Figure VI.9 Adsorption of CO on O_{2c} site (indicated with gold atoms) of SnO_2 (1 1 0) surface. The left drawings are the configurations of initial adsorption and the right ones are those of optimized adsorption.

As can be seen from Figure VI.9, the modes A1, A2, and A3 present chemical adsorption resulting in formation of CO_2 molecule with the adsorption energies 1.07 eV, 1.05 eV, 1.05 eV respectively, while A4 mode exhibit smaller adsorption energy 0.01 eV without CO_2 formation. The A1, A2, and A3 modes present the strongest binding energy when the C atom of the CO molecule is on top O_{2c} of the surface, while mode A4 exhibits a much smaller adsorption

energy. According to our calculation, it is also found that the highest adsorption energy and the most stable configuration is mode A1 when CO is localized on O_{2c} perpendicularly.

For the five-coordinated Sn_{5c} site, six possible configurations have been considered as shown in Figure VI.10: (B1) CO top Sn_{5c} with C down, (B2) CO top Sn_{5c} with O down, (B3) CO along y axis with C top Sn_{5c}, (B4) CO along x axis with C top Sn_{5c}, (B5) CO along x axis, (B6) CO along y axis

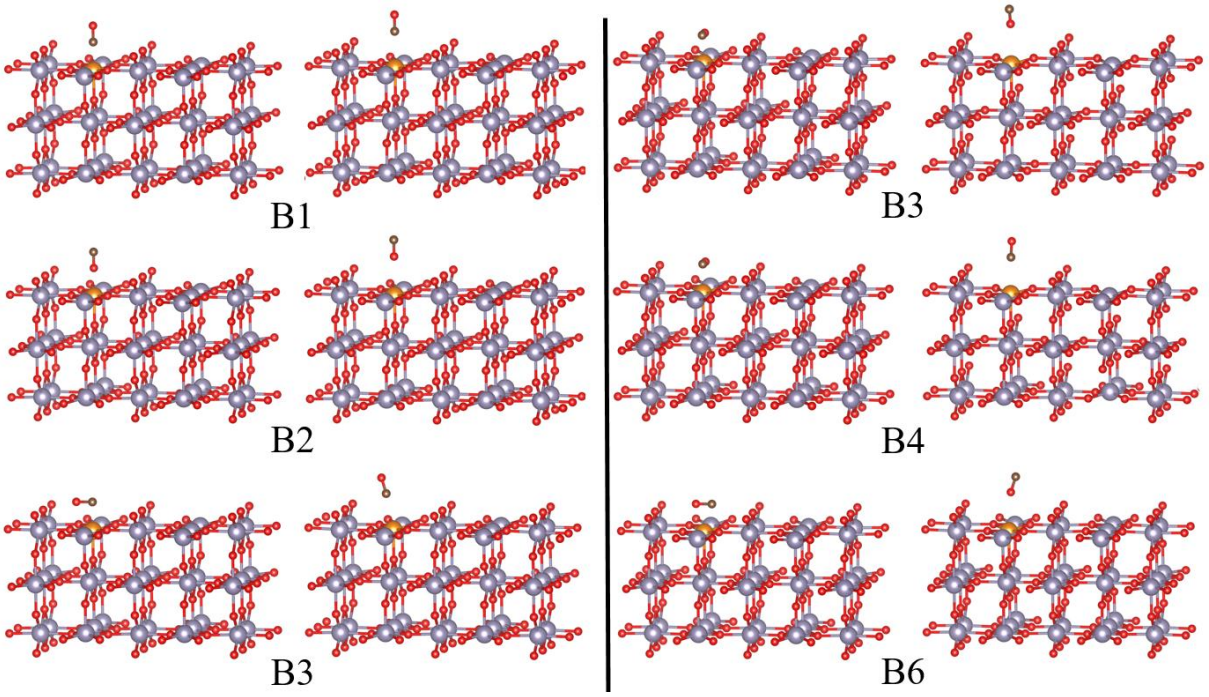

Figure VI.10 Adsorption of CO on Sn_{5c} site (indicated with gold atoms) of SnO2 (1 1 0) surface. The left drawings are the configurations of initial adsorption and the right ones are those of optimized adsorption

The B1, B3, and B5 modes display an important physisorption with the adsorption energies 0.40 eV, 0.38 eV, 0.39 eV respectively, while modes B2, B4, and B6 exhibit weak adsorption energy 0.11 eV for the three modes. The most stable modes (B1, B3, and B5) are when the CO molecule adsorbs with C-down orientation, while the modes (B2, B4, B6) with O-down orientation are the less stable. It is also found that the highest adsorption energy and the most stable configuration is mode B1 when CO (C-down) is localized on Sn_{5c} perpendicularly.

For the three-coordinated O_{3c} site, we considered one possible configuration that is CO adsorption top O_{3c} with C-down orientation.

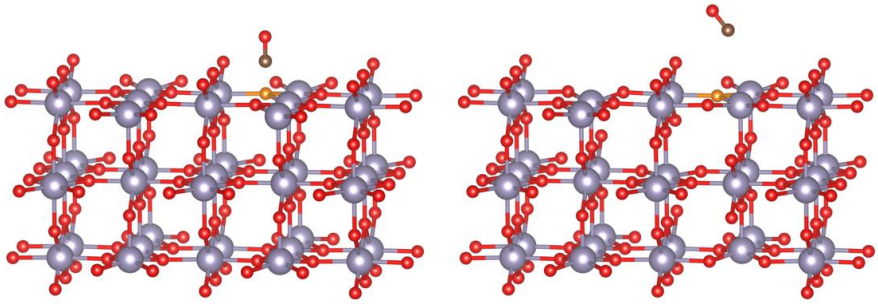

Figure VI.11 Adsorption of CO on O_{3c} (indicated with gold atom) site of SnO_2 (1 1 0) surface. The left drawing is the configuration of initial adsorption and the right one is that of optimized adsorption.

The adsorption energy for the configuration presented in Figure VI.11 is 0.16 eV; such small adsorption energy compared to that of O_{2c} and Sn_{5c} sites are likely due to the coordination of O_{3c}. Our results and the previous observed configurations of CO adsorption on (110) surface are similar to those of Lu et al. [375], and Wang et al. [376].

VI.3.1.3 Adsorption of CO on relaxed SnO_2 (101)

The studied (101) surface of SnO_2 consists of four parallel planes O/Sn/O, and it has two possible adsorption sites, top site (Sn_{5c}) and bridge site (O_{2c}) as in (110) surface (See Figure VI.12).

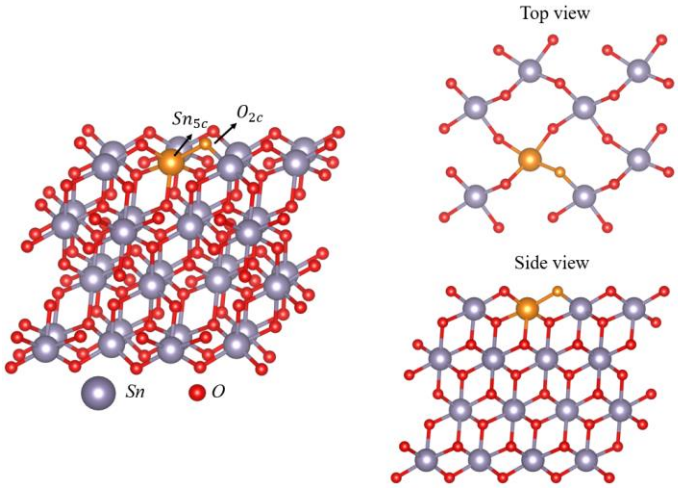

Figure VI.12 The (101) surface of SnO_2, gold atoms indicate the possible adsorption sites.

Four possible adsorption configurations of CO on the oxygen bridge (O_{2c}) are shown in Figure VI.13: (C1) CO top O_{2c} with C down, (C2) CO along y axis with C top O_{2c}, (C3) CO along x axis with C top O_{2c}, (C4) CO along y axis.

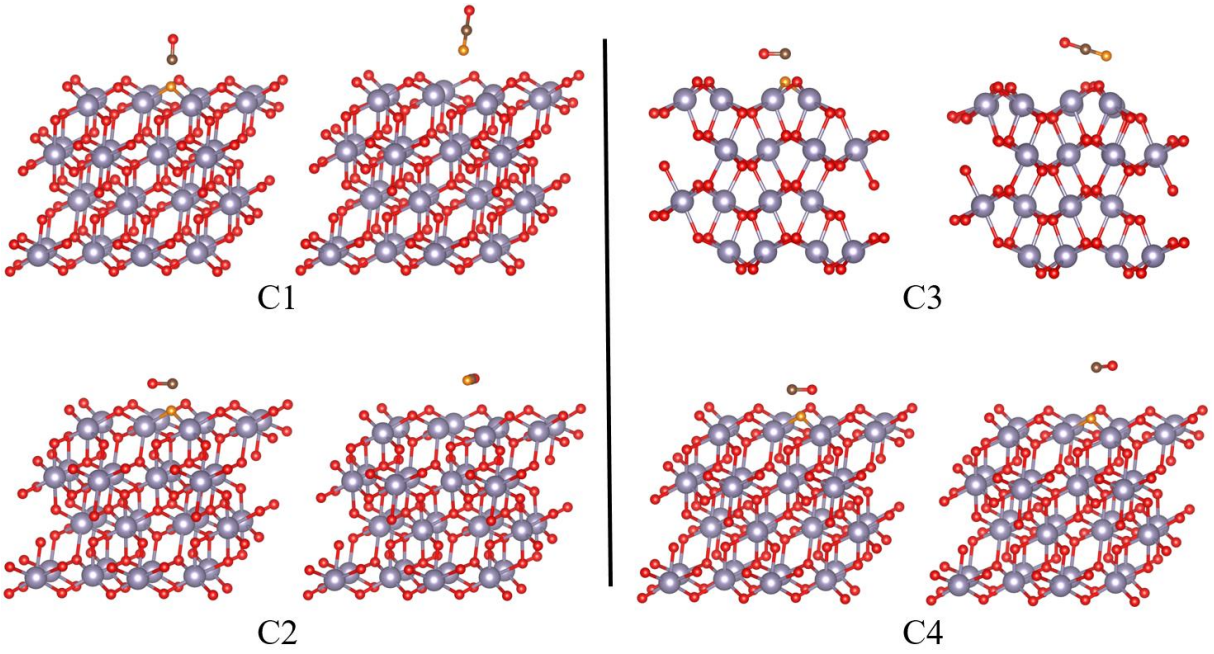

Figure VI.13 Adsorption of CO on O_{2c} site (indicated with gold atoms) of SnO2 (1 0 1) surface. The left drawings are the configurations of initial adsorption and the right ones are those of optimized adsorption.

For C1, C2, and C3 modes, the interaction of C of CO molecule with O_{2c} site leads to the formation of CO_2 molecule leaving a vacancy on the surface, while C4 mode presents weak binding energy (0.04 eV). The adsorption energy is 1.45 eV for C1, 1.44 eV for C2, 1.42 eV for C3, which means that C1 mode presents the most stable configuration.

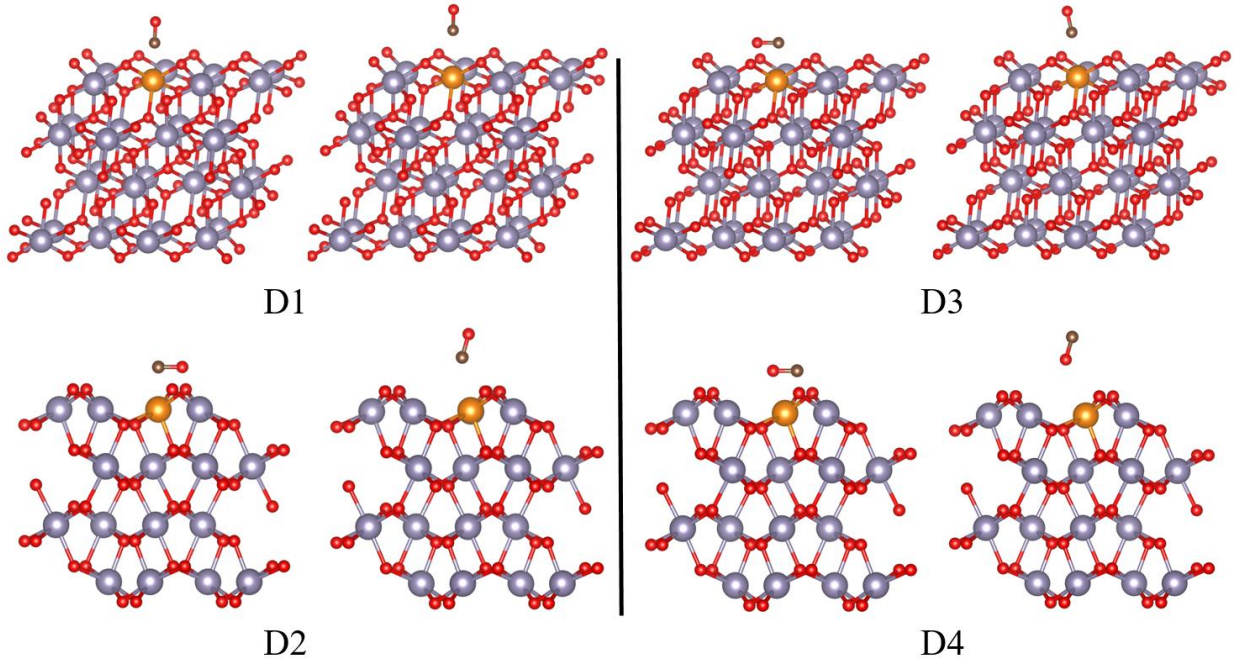

Figure VI.14 Adsorption of CO on Sn_{5c} site (indicated with gold atoms) of SnO2 (1 0 1) surface. The left drawings are the configurations of initial adsorption and the right ones are those of optimized adsorption.

As presented in Figure VI.14, four possible configurations have been considered for the five-coordinated Sn_{5c} site: (D1) CO top Sn_{5c} with C down, (D2) CO along x-axis with C top Sn_{5c}, (D3) CO along y-axis with C top Sn_{5c}, (D4) CO along x-axis. As for the Sn_{5c} of (110) surface, the adsorption modes with C-down orientation display the strongest physorptions. The Adsorption energies of D1, D2, and D3 modes are 0.45 eV, 0.44 eV, 0.40 eV respectively, while for mode D4 the adsorption energy is 0.12 eV. The most stable configuration is mode D1 when CO (C-down) is localized on Sn_{5c} perpendicularly.

VI.3.1.4 Adsorption of CO on relaxed SnO_2 (100)

As presented in Figure VI.15, the (100) surface of SnO_2 consists of four parallel planes O/Sn/O, and it has two possible adsorption sites, top site (Sn_{5c}) and bridge site (O_{2c}) as in (110) and (101) surfaces (See Figure VI.12).

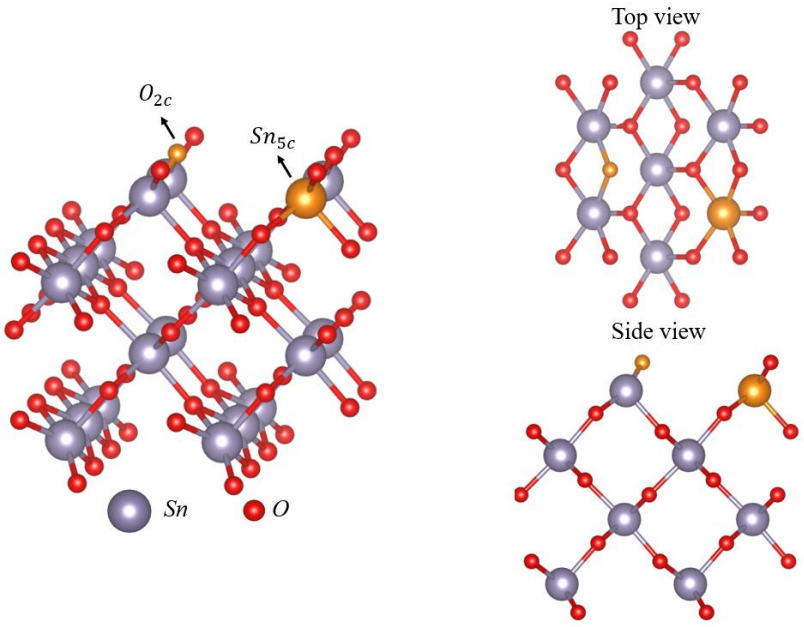

Figure VI.15 The (100) surface of SnO_2, gold atoms indicate the possible adsorption sites.

Starting by O_{2c} site, we considered four adsorption configurations of CO: (E1) CO top O_{2c} with C down, (E2) CO along y axis with O top O_{2c}, (E3) CO along y axis with C top O_{2c}, (E4) CO along x axis.

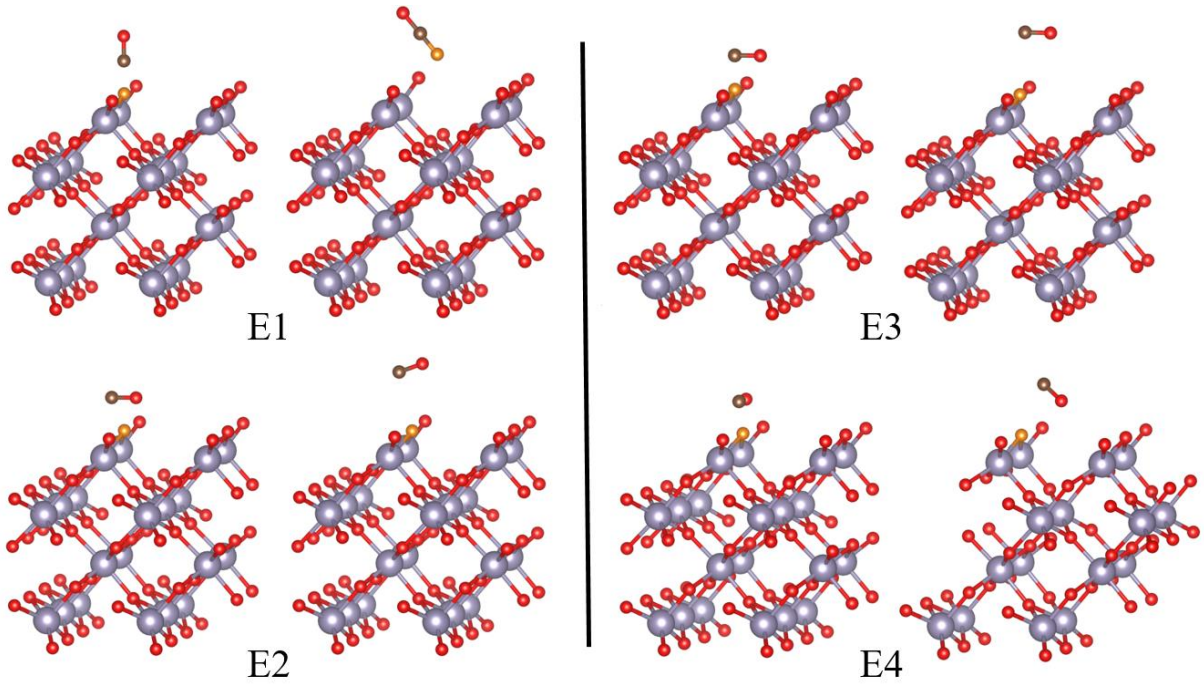

Figure VI.16 Adsorption of CO on O_{2c} site (indicated with gold atoms) of SnO_2 (1 0 0) surface. The left drawings are the configurations of initial adsorption and the right ones are those of optimized adsorption.

As can be seen from Figure VI.16, the chemisorption behavior observed in the case of (110) and (101) surfaces has been observed only in mode E1 when the CO molecule adsorbs top the site with C-down orientation. While for the mode E2, E3, and E4 weak binding energy have been found (0.06 eV).

For the five-coordinated Sn_{5c} site, we considered six possible configurations: (F1) CO top Sn_{5c} with C down, (F2) CO top Sn_{5c} with O down, (F3) CO perpendicular to Sn row with C top Sn_{5c}, (F4) CO perpendicular to Sn row with O top Sn_{5c}, (F5) CO along x-axis with C top Sn_{5c}, (F6) CO along x-axis. F1, F3, and F5 modes display an important physisorption with the adsorption energies 0.34 eV, 0.32 eV, 0.31 eV respectively, while for modes F2, F4, and F6, exhibit weak adsorption energies of 0.06 eV, 0.05 eV, and 0.05 eV respectively. It is clearly observed that the most stable configurations are when the C atom of CO adsorbs exactly top the Sn_{5c} site.

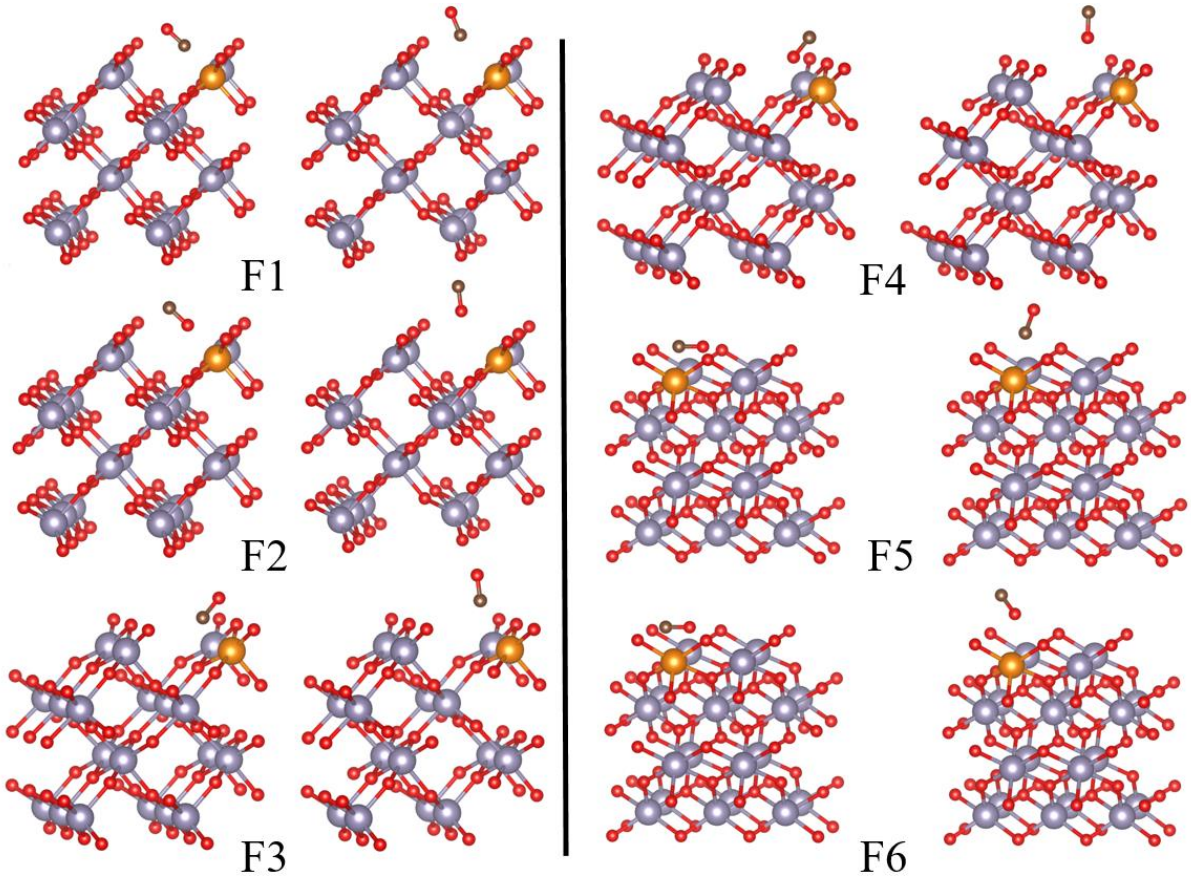

Figure VI.17 Adsorption of CO on Sn_{5c} site (indicated with gold atoms) of SnO_2 (1 0 0) surface. The left drawings are the configurations of initial adsorption and the right ones are those of optimized adsorption.

The observed behavior of CO adsorption on (100) surface is the same as in the case of (110) and (101) surfaces, which is chemisorption on O_{2c} site and physisorption on Sn_{5c} site, however, the adsorption energies of CO on SnO_2 surfaces are in the order (101) > (110) > (100).

VI.3.2 CO adsorption on strained (110), (101), and (100) SnO_2 surfaces.

VI.3.2.1 Preparation and stability of strained SnO_2 surfaces

First, we performed energy calculations of (100), (110), and (101) SnO_2 surfaces under compressive (-4%) and tensile (4%) biaxial strain. The calculated surface energies presented in Table VI.5, show that the stabilities of the SnO_2 surfaces remain their order (110) > (100) > (101) under strain.

Table VI.3 The calculated surface energy of strained SnO_2.

	(110) surface	(100) surface	(101) surface
Compressive strain	1.038	1.103	1.447
Unstrained	1.027	1.095	1.439
Tensile strained	1.035	1.096	1.446

However, for each surface, these energies increase either under tensile or compressive strain. In addition, the magnitude of the energies increase under tensile strain is smaller than that of the energies under compressive strain. Further, in order to examine the effect of strain on the adsorption of CO on SnO_2 surfaces, we discussed only the two most stable CO adsorption configurations (one on the O_{2c} site and one on the Sn_{5c} site) for each surface separately.

VI.3.2.1 Adsorption of CO on strained SnO_2 (110)

Figure VI.18 presents the CO adsorption on the O_{2c} site (Mode A1) under compressive and tensile strain.

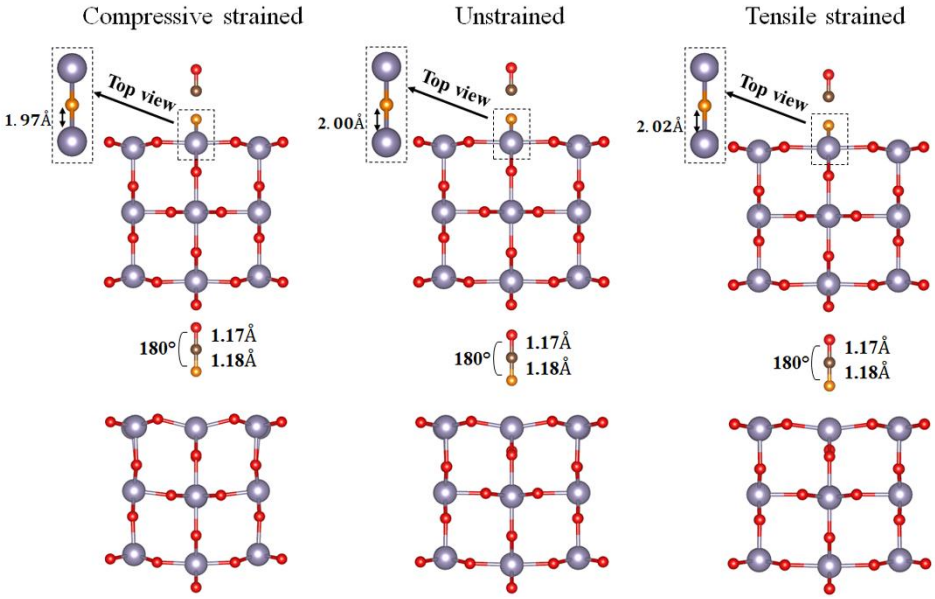

Figure VI.18 Side view of CO adsorption on the O_{2c} site (Mode A1) under strain. The top drawings are the configurations before adsorption and the bottom ones are the configurations after adsorption. Gold atoms indicate the O_{2c} site.

As can be seen from Figure VI.18, the distance between O_{2c} and its two Sn neighbors before CO adsorption increases under tensile strain and decreases under compressive strain. In order to calculate the charges released Δq to the surface after CO adsorption we have carried out a Bader charge analysis [377].

Table VI.4 The calculated adsorption energy Eads and charge transfer Δq of CO adsorption on the O_{2c} site (Mode A1) under strain.

	Distance Sn-O (Å)	Eads (eV)	Δq (e^-)
Compressive strained	1.97	1.01	0.986
Unstrained	2.00	1.07	1.038
Tensile strained	2.02	1.12	1.065

Table VI.4 presents adsorption energies and charge transfer Δq of CO adsorption on the O2c site under strain. Under tensile strain, longer distance between O_{2c} and its Sn neighbors

(Sn-O_{2c} = 2.02 Å) displays weaker interatomic bonding, which may facilitate the O_{2c} release to CO molecule and induce higher charge transfer to the surface (1.09 e^-). While under compressive strain, opposite behavior is observed due to shorter interatomic (Sn-O_{2c}) distance. Figure VI.19 presents a detailed illustration of CO adsorption on the Sn_{5c} site (Mode B1).

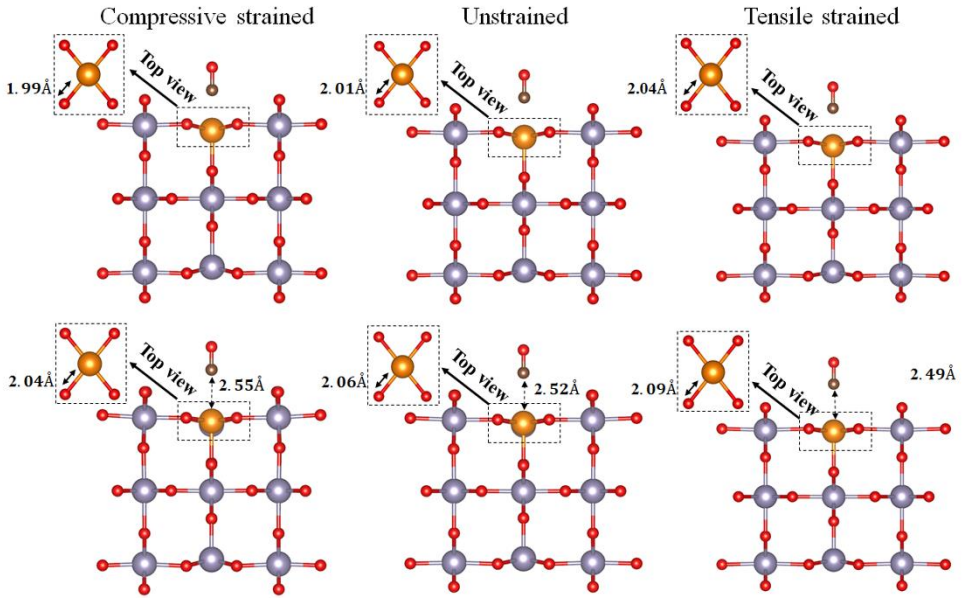

Figure VI.19 Side view of CO adsorption on the Sn_{5c} site (Mode B1) under strain. The top drawings are the configurations before adsorption and the bottom ones are the configurations after adsorption. Gold atoms indicate the Sn_{5c} site.

Under no strain, the CO adsorption on the Sn_{5c} induces minor structural modifications in both the adsorbate and surface geometries compared to that on the O_{2c} site.

Table VI.5 The calculated adsorption energy Eads and charge transfer Δq of CO adsorption on the Sn_{5c} site (Mode B1) under strain.

	Distance Sn-O (Å)	Distance CO-Surface (Å)	Eads (eV)	Δq (e^-)
Compressive strained	1.99	2.55	0.38	0.050
Unstrained	2.01	2.52	0.40	0.058
Tensile strained	2.04	2.49	0.43	0.066

As can be seen from Figure VI.19, alongside with the results presented in Table VI.5, the increase of Sn_{5c}-O bond under tensile strain promotes charge exchanges with the adsorbate CO molecule. Indeed, the charge transfer from CO molecule to the surface is higher under tensile strain that can be explained by the shorter distance from CO molecule to the surface. Our results indicate that the adsorption process did not change under strain. Further, tensile strain boosts the adsorption of the CO molecule for both the O_{2c} and Sn_{5c}. As mentioned previously, the surface energy before CO adsorption increases under both tensile and

compressive strain. However, under tensile strain, CO adsorption induces a decrease of the surface energy ($E_{slab/adsorbate}$) more than that in the case of unstrained surface, which explain the continuous increase of adsorption energy according to equation Eq VI.5. While under compressive strain, the surface energy after adsorption ($E_{slab/adsorbate}$) is higher than that of unstrained surface, which results in lower adsorption energy.

VI.3.2.2 Adsorption of CO on strained SnO_2 (101)

Figure VI.20 presents the CO adsorption on the O_{2c} site (Mode C1) under compressive and tensile strain.

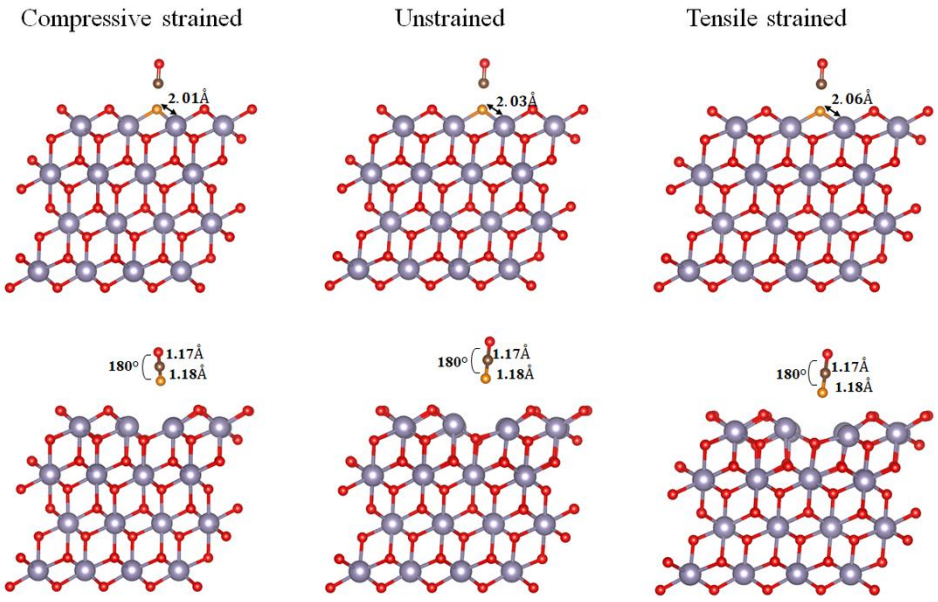

Figure VI.20 Side view of CO adsorption on the O_{2c} site (Mode C1) under strain. The top drawings are the configurations before adsorption and the bottom ones are the configurations after adsorption. Gold atoms indicate the O_{2c} site.

As have been observed in the case of the (110) surface, the (O_{2c}-Sn) distance increases under tensile strain and decreases under compressive strain. From Table VI.6 one can deduces that longer Sn-O_{2c} (2.06 Å) bonding length under tensile strain that results in weaker bonding configuration at the surface induce easy O2c release to CO molecule and higher charge transfer to the surface (1.072 e^-). While under compressive strain opposite behavior is observed.

Table VI.6 The calculated adsorption energy Eads and charge transfer Δq of CO adsorption on the O_{2c} site (Mode C1) under strain.

	Distance Sn-O (Å)	Eads (eV)	Δq (e^-)
Compressive strained	2.01	1.39	1.001
Unstrained	2.03	1.45	1.043
Tensile strained	2.06	1.49	1.072

For CO adsorption on the Sn5c site (Mode D1), detailed illustration is presented in Figure VI.21

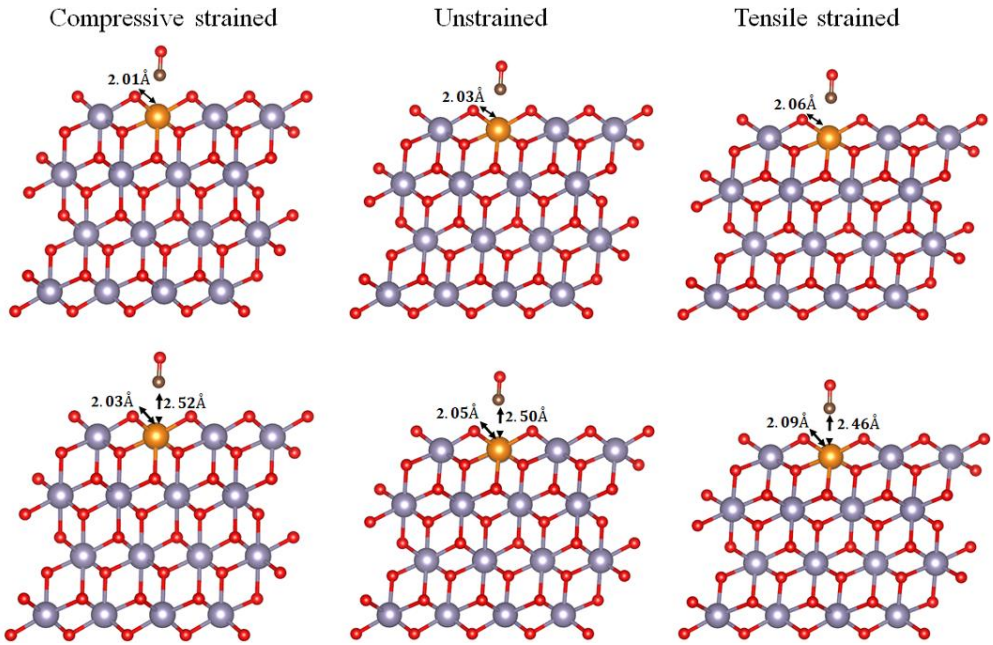

Figure VI.21 Side view of CO adsorption on the Sn5c site (Mode D1) under strain. The top drawings are the configurations before adsorption and the bottom ones are the configurations after adsorption. Gold atoms indicate the Sn5c site.

Again, Sn5c-O distance increases under tensile strain and decreases under compressive strain. Therefore, as presented in Table VI.7, one can has the same inference as in the case of the (110) surface; increased Sn5c-O bond under tensile strain helps charge transfer from the adsorbate CO molecule to the surface.

Table VI.7 The calculated adsorption energy Eads and charge transfer Δq of CO adsorption on the Sn5c site (Mode D1) under strain.

	Distance Sn-O (Å)	Distance CO-Surface (Å)	Eads (eV)	Δq (e^-)
Compressive strained	2.01	2.52	0.41	0.081
Unstrained	2.03	2.50	0.45	0.086
Tensile strained	2.06	2.46	0.47	0.092

Indeed, as have been obtained in the case of strained (110) surface, the charge transfer from CO molecule to the surface is higher under tensile strain that can be confirmed by the shorter distance from CO molecule to the surface. Our results indicate that the (101) surface presents higher sensitivity compared to the (110) surface either strained or unstrained. This disparity may due to the difference in their morphology. For example, in the (101) surface, Sn

atoms form wells with its neighbors oxygen atoms that can increase the charge transfer more than in plat surface as it is the case of the (110) surface.

VI.3.2.3 Adsorption of CO on strained SnO_2 (100)

The CO adsorption on the O_{2c} site (Mode E1) under compressive and tensile strain is presented in figure VI.22.

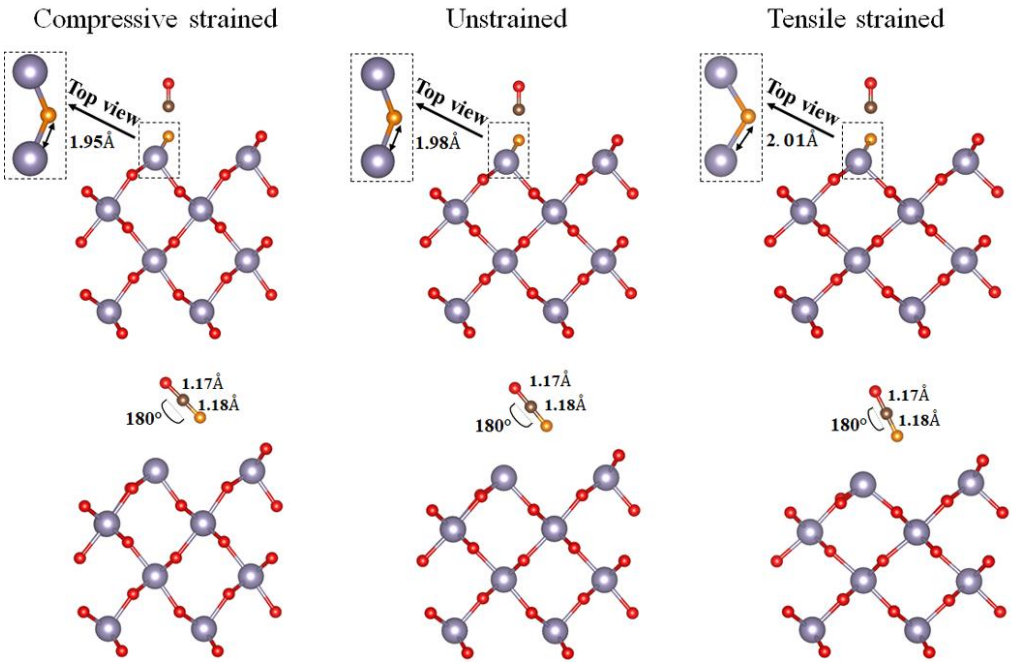

Figure VI.22 Side view of CO adsorption on the O_{2c} site (Mode E1) under strain. The top drawings are the configurations before adsorption and the bottom ones are the configurations after adsorption. Gold atoms indicate the O_{2c} site.

Again, from figure VI.22, we can observe the same behavior as in the case of the (101) and (110) surfaces, under tensile strain the (O_{2c}-Sn) distance increases, which results in weaker interatomic bonding, facilitates O_{2c} release to the CO molecule, and induces higher charge transfer to the surface (1.019 e^-).

Table VI.8 The calculated adsorption energy Eads and charge transfer Δq of CO adsorption on the O_{2c} site (Mode E1) under strain.

	Distance Sn-O (Å)	Eads (eV)	Δq (e^-)
Compressive strained	1.95	0.98	0.950
Unstrained	1.98	1.02	0.990
Tensile strained	2.01	1.05	1.019

Detailed illustration of CO adsorption on the Sn_{5c} site (Mode F1), is presented in Figure VI.23

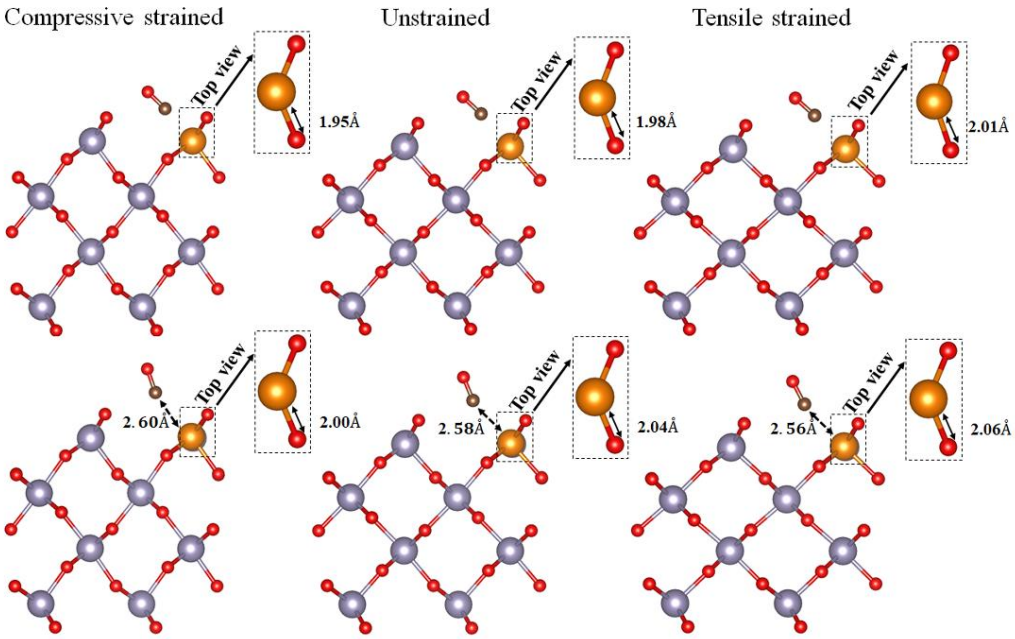

Figure VI.23 Side view of CO adsorption on the Sn_{5c} site (Mode F1) under strain. The top drawings are the configurations before adsorption and the bottom ones are the configurations after adsorption. Gold atoms indicate the Sn_{5c} site.

Same as in the case of CO adsorption on the Sn_{5c} site of strained (101) and (110) SnO_2 surfaces, tensile strain results in longer Sn_{5c}-O distance, which boosts charge transfer from the CO molecule to the surface as can be confirmed by the shorter distance from CO molecule to the surface (See Table VI.9).

Table VI.9 The calculated adsorption energy Eads and charge transfer Δq of CO adsorption on the Sn_{5c} site (Mode F1) under strain.

	Distance Sn-O (Å)	Distance CO-Surface (Å)	Eads (eV)	Δq (e^-)
Compressive strained	1.95	2.56	0.31	0.040
Unstrained	1.98	2.58	0.34	0.046
Tensile strained	2.01	2.60	0.37	0.052

VI.3.2.5 Discussion and comparison of CO adsorption on strained (110), (101), and (100) SnO_2 surfaces.

Our findings shows that the Sn-O bond length plays an important role in CO adsorption. In fact, as summarized in Table VI.10, for the three surfaces, tensile strain results in weak interatomic bonding at the surface, which facilitates CO adsorption on both O_{2c} and Sn_{5c} sites.

Table VI.10 The calculated adsorption energy Eads and charge transfer Δq of CO adsorption on strained SnO_2 surfaces.

Surfaces		-4%		0%		4%	
	Modes	Eads (eV)	Δq (e^-)	Eads (eV)	Δq (e^-)	Eads (eV)	Δq (e^-)
(110)	A1	1.01	0.986	1.07	1.038	1.12	1.065
	B1	0.38	0.050	0.40	0.058	0.43	0.066
(101)	C1	1.39	1.001	1.45	1.043	1.49	1.072
	D1	0.41	0.081	0.45	0.086	0.47	0.092
(100)	E1	0.98	0.950	1.02	0.990	1.05	1.019
	F1	0.31	0.040	0.34	0.046	0.37	0.052

Unstrained (101) SnO_2 surface has the longer Sn-O distance compared to the (110) and (100) surfaces resulting in a weaker interatomic bonding, which may facilitates CO adsorption and induces higher charge transfer. In contrast, the unstrained (100) surface that has the shortest Sn-O bond length, has the lowest adsorption energy and the lesser charge transfer. In addition, the CO adsorption on tensile strained SnO_2 surfaces induces the higher charge transfer and the most stable adsorption configurations, when compressive strain results in opposite behavior. Similar results have been reported by D. Ma et al. for hydrogen adsorption on CeO2 (111) under strain [377]. Although, the stability of CO adsorption on SnO_2 surfaces maintain their order $(101) > (110) > (100)$ under strain. Our results clearly demonstrate that lattice strain could tune the adsorption energy of CO on SnO_2 surfaces and the weakening of the Sn–O bond at the surface under tensile strain may facilitate the CO interaction with SnO_2 surfaces in order to enhance its sensing performance.

Chapter Conclusion

In conclusion, we have studied the interaction of CO molecule with strained SnO_2 surfaces. First, we performed energy calculations for the (100), (110), and (101) SnO_2 surfaces, our results revealed that the order of their stabilities is $(110) > (100) > (101)$, and they maintain this order under strain. Further, we performed various adsorption configurations of CO on SnO_2 surfaces. Our findings show that two types of adsorption could occur similarly on the three SnO_2 surfaces, one is the physisorption of CO on Sn_{5c} site and the other is CO chemisorption on O_{2c} site. Besides, calculated adsorption energies together with Bader charge analysis revealed that the (101) surface present the highest charge transfer from CO molecule, due to the Sn-O low bonding. Under tensile strain, the weakening of the Sn–O bond at the surface enhances the adsorption energy and the charge transfer, which facilitate SnO_2 interaction with CO molecule. Moreover, the stability of CO molecule adsorption on SnO_2 surfaces maintain its order $((101) > (110) > (100))$ under strain. Finally, based on our findings, we believe that tensile strain that can be acheived by depositing SnO_2 thin film on a substrate with larger lattice parameters, is a good strategy to enhance SnO_2 suitablity for CO sensing.

GENERAL CONCLUSION

In the present thesis, first-principles calculations have been employed in order to predict the physical properties of strained SnO_2. We have introduced strain as an efficient method that demonstrated its ability to modulate the electronic band structure of SnO_2 and solve its limitations for solar energy applications and toxic gas sensing.

First, our calculations on the effect of an applied biaxial strain ranging from -6% to 6% on the *ab* plane of SnO_2 bulk, show that under compressive strain, a strong hybridization of O-p and Sn-s in the conduction band is obtained because of dense charge distribution around atoms causing therefore a bandgap energy increase, while an opposite behavior have been observed under tensile strain. In the other hand, for thin-films, the band gap decreases with increasing thickness due to the quantum confinement effect. The obtained band structure modulation and bandgap increase/decrease under compressive/tensile strain, affects directly the optical and transport properties of SnO_2.

Indeed, for thermoelectric applications, transport properties of SnO_2 bulk under strain have been calculated. Our results show that wider bandgap resulting from the compressive-strained SnO_2 yield to a high Seebeck coefficient and a large effective mass that lowers the electrical conductivity. This interplay leads to a variation of the figure of merit (ZT) under strain that reaches its higher value under compression for temperatures below 400 K.

In terms of photo-catalytic water splitting process, visible light absorption and band edges related to the redox potential of water have been calculated. We found that a narrowed bandgap of tensile-strained SnO_2 yield to enhanced visible light absorption and higher charge carrier mobility. However, for the band edge alignments, the redox potential for hydrogen reduction has been enhanced in the case of SnO_2 films thinner than 1.26 nm (4 layers). Elsewhere, compressive strain for $pH \geq 7$ or larger pH value ($pH \geq 10$) under tensile strain could enhance the band edge positions relative to the water (H_2O/H_2) redox levels.

Regarding the sensing mechanism of Carbon Monoxide (CO) on SnO_2 surfaces, a comparative study of CO molecule interaction with strained (110), (101), and (100) SnO_2 surfaces have been performed. Our results show that the (101) surface induces the highest charge transfer during the CO adsorption in comparison with the (110) and (100) surfaces. In addition, we found that for the (110), (101), and (100) SnO_2 surfaces, tensile strain tends to increase the charge transfer from CO molecule to the surface and facilitates its adsorption due to the weakening of the surface Sn–O bond.

Finally, through the present thesis, we attempted to demonstrate the ability of strain as a solution to adjust the energy band structure of SnO_2. Indeed, we have presented enhanced physical properties for thermoelectric, photocatalytic, and gas sensing applications. Through this work, we aimed to provide a useful insight to improve SnO_2 for future development of high performance SnO_2-based devices. Although, we believe that calculations for quasi-real sizes of SnO_2 in addition to SnO_2-Substrat hetero-structures could give better understanding on the effect of strain on SnO_2 properties, but, these issues are very demanding in computational resources and time. However, we believe that the results provided in the present thesis are very promising which may open the way to future experimental realizations of strained-SnO2 based devices.

REFERENCES

[1] https://www.who.int/health-topics/climate-change#tab=tab_1
[2] W. C. Turkenburg, A. Faaij. Renewable energy technologies. *World Energy Assessment. New York: UNDP*, 219-272, 2000.
[3] D. M. Rowe. CRC Handbook of Thermoelectrics; CRC Press, Florida, 1995.
[4] K. Kusagaya, M. Takashiri. Investigation of the Effects of Compressive and Tensile Strain on n-Type Bismuth Telluride and p-Type Antimony Telluride Nanocrystalline Thin Films for Use in Flexible Thermoelectric Generators. *J. Alloys Compd.*, *653*, 480–485, 2015.
[5] K. Zhao, Y. Wang, C. Xin, Y. Sui, X. Wang, Y. Wang, Z. Liu, B. Li. Pressure-Induced Anomalies in Structure, Charge Density and Transport Properties of Bi2Te3: A First Principles Study. *J. Alloys Compd.* , *661*, 428–434, 2016.
[6] M. N. Chong, B. Jin, C. W. Chow, C. Saint. Recent developments in photocatalytic water treatment technology: a review. *Water Res*., 44, 2997-3027, 2010.
[7] M. T. Amin, A. A. Alazba, U. Manzoor. A review of removal of pollutants from water/wastewater using different types of nanomaterials. *Adv. Mater. Sci. Eng*. 2014.
[8] R. Daghrir, P. Drogui, D. Robert. Photoelectrocatalytic technologies for environmental applications. *J. Photochem. Photobiol. A: Chemistry*., 238, 41-52, 2012.
[9] A. Fujishima, & K. Honda. Electrochemical photolysis of water at a semiconductor electrode. *Nature*, 238, 37-38, 1972.
[10] J. Liqiang, S. Xiaojun, S. Jing, C. Weimin, X. Zili, D. Yaoguo, & F. Honggang. Review of surface photovoltage spectra of nano-sized semiconductor and its applications in heterogeneous photocatalysis. *Sol. Energ. Mat. Sol. Cells*., 79, 133-151, 2003.
[11] T. Tachikawa, M. Fujitsuka, & T. Majima. Mechanistic insight into the TiO2 photocatalytic reactions: design of new photocatalysts. *J. Phys. Chem. C*., 111, 5259-5275, 2007.
[12] A. K. Chandiran, M. Abdi-Jalebi, M. K. Nazeeruddin, M. Grätzel. Analysis of electron transfer properties of ZnO and TiO2 photoanodes for dye-sensitized solar cells. *ACS Nano*, 8, 2261-2268, 2014.
[13] P. Tiwana, P. Docampo, M. B. Johnston, H. J. Snaith, L. M. Herz. Electron mobility and injection dynamics in mesoporous ZnO, SnO2, and TiO2 films used in dye-sensitized solar cells. *ACS Nano*, 5, 5158-5166, 2011.
[14] C. G. Fonstad, R. H. Rediker. Electrical properties of high-quality stannic oxide crystals. *Journal of applied physics*, 42, 2911-2918, 1971.
[15] O. Madelung, U. Rössler, M. Schulz, Tin dioxide (SnO_2) band structure, band parameters. Non-Tetrahedrally Bonded Elements and Binary Compounds I. 41C, 1-9.
[16] C. Poulier, D. Smith, J. Absi, Thermal conductivity of pressed powder compacts: tin oxide and alumina, *J. Eur. Ceram. Soc*. 27, 475–478, 2007.
[17] S. Fayette, D. Smith, A. Smith, C. Martin, Influence of grain size on the thermal conductivity of tin oxide ceramics, *J. Eur. Ceram. Soc.* 20, 297–302, 2002.
[18] B. Babu, A. N. Kadam, R. V. S. S. N. Ravikumar, C. Byon. Enhanced visible light photocatalytic activity of Cu-doped SnO2 quantum dots by solution combustion synthesis. *J. Alloys Compd.*, 703, 330-336, 2017.
[19] Li, S., Yu, L., Man, X., Zhong, J., Liao, X., & Sun, W. The Synthesis and band gap changes induced by the doping with rare-earth ions in nano-SnO2. *Mat. Sci. Semicon. Proc.*, 71, 128-132, 2017.
[20] T. T. X. Vo, T. N. H. Le, Q. N. Pham, C. Byl, D. Dragoe, M. G. Barthés-Labrousse, D. Bérardan, N. Dragoe, N. Preparation and Study of the Thermoelectric Properties of Nanocrystalline Sn1−xTaxO2($0 \leq x \leq 0.04$). *Phys. Status Solidi*. 212, 2776–2784, 2015.
[21] J. Bardeen, W. Shockley. Deformation potentials and mobilities in non-polar crystals, *Phys. Rev.*, 80, 72–80, 1950.
[22] J. Welser, J.L. Hoyt, and J.F. Gibbons. NMOS and PMOS transistors fabricated in strained silicon/relaxed silicon-germanium structures. *In Proc. Intl. Electron Devices Meeting*, 1000-1002, 1992.
[23] J. Welser, J.L. Hoyt, and J.F. Gibbons. Electron Mobility Enhancement in Strained-Si N-Type Metal-Oxide-Semiconductor Field-Effect Transistors. *IEEE Electron Device Lett.,* 15, 100-102, 1994.
[24] F. Guffarth, R. Heitz, A. Schliwa, O. Stier, N. N. Ledentsov, A. R. Kovsh, D. Bimberg. Strain engineering of self-organized InAs quantum dots. *Phys. Rev. B*, 64, 085305, 2001.
[25] M. Z. Hossain. Quantum conductance modulation in graphene by strain engineering. *Appl. Phys. Lett.*, *96*, 143118, 2010.
[26] Y. Wang, X. Sun, Z. Chen, Z. Cai, H. Zhou, T. M. Lu, J. Shi. Defect-engineered epitaxial VO2±δ in strain engineering of heterogeneous soft crystals. *Sci. Adv.*, *4*, 3679, 2018
[27] Y. Y. Hui, X. Liu, W. Jie, N. Y. Chan, J. Hao, Y. T. Hsu, S. P. Lau. Exceptional tunability of band energy in a compressively strained trilayer MoS2 sheet. *ACS nano*, *7*, 7126-7131, 2013.

[28] Y. Wang, C. Cong, W. Yang, J. Shang, N. Peimyoo, Y. Chen, T. Yu. Strain-induced direct–indirect bandgap transition and phonon modulation in monolayer WS2. *Nano Research, 8*, 2562-2572, 2015.
[29] G. Plechinger, F. X. Schrettenbrunner, J. Eroms, D. Weiss, C. Schueller, T. Korn. Low-temperature photoluminescence of oxide-covered single-layer MoS2. *Phys. Status Solidi* RRL, 3, 126, 2012
[30] G. Plechinger, A. Castellanos-Gomez, M. Buscema, H. S. van der Zant, G. A. Steele, A. Kuc, T. Korn. Control of biaxial strain in single-layer molybdenite using local thermal expansion of the substrate. *2D Mater.* 2, 015006, 2015.
[31] G. H. Ahn, M. Amani, H. Rasool, D. H. Lien, J. P. Mastandrea, J. W. Ager III, A. Javey. Strain-engineered growth of two-dimensional materials. *Nat. commun., 8*, 608, 2017.
[32] M. A. Bissett, M. Tsuji, H. Ago. Strain engineering the properties of graphene and other two-dimensional crystals. *Phys. Chem. Chem. Phys., 16*, 11124-11138, 2014.
[33] Q. Yan, P. Rinke, A. Janotti, M. Scheffler, C. G. Van de Walle. Effects of strain on the band structure of group-III nitrides. *Phys. Rev. B, 90*, 125118, 2014.
[34] K. P. Dhakal, S. Roy, H. Jang, X. Chen, W. S. Yun, H. Kim, J. H. Ahn. Local strain induced band gap modulation and photoluminescence enhancement of multilayer transition metal dichalcogenides. *Chem. Mater., 29*, 5124-5133, 2017.
[35] S. F. Rus, T. Z. Ward, A. Herklotz. Strain-induced optical band gap variation of SnO2 films. *Thin Solid Films*, 615, 103-106, 2016.
[36] M. Zhang, M. Xu, M. Li, Q. Zhang, Y. Lu, J. Chen, Y. He. SnO2 epitaxial films with varying thickness on c-sapphire: Structure evolution and optical band gap modulation. *Appl. Surf. Sci.*, 423, 611-618, 2017.
[37] O. Madelung, U. Rössler, M. Schulz, Tin dioxide (SnO_2) band structure, band parameters. Non-Tetrahedrally Bonded Elements and Binary Compounds I. 41C, 1–9.
[38] Gracia, L., Beltrán, A., & Andrés, J. (2007). Characterization of the high-pressure structures and phase transformations in SnO2. A density functional theory study. The Journal of Physical Chemistry B, 111(23), 6479-6485.
[39] S.Ono, T. Tsuchiya, K. Hirose, Y. Ohishi, Phase transition between the CaCl2-type and a- PbO2-type structures of germanium dioxide. Physical review B. 2003. 68, 134108.
[40] Haines, J., Léger, J. M., & Schulte, O. (1996). Pa Modified Fluorite-Type Structures in Metal Dioxides at High Pressure. Science, 271(5249), 629-631.
[41] Z. M. Jarzebski, Physical properties of SnO2 materials: 1. Preparation and defect structure, Journal of the Electrochemical Society, 123, Iss. 7 (1976) p. 199-205.
[42] Hamad BA. First-principle calculaions of structural and electronic properties of rutile-phase dioxides (MO2), M = Ti, V, Ru, Ir and Sn. Eur Phys JB 2009;70:163.
[43] Z. W.Chen, Z. Jiao, M. H. Wu, C. H. Shek, C. M. L. Wu, J. K. L. Lai, Microstructural evolution of oxides and semiconductor thin films, Progress in Materials Science 56(7) (2011) 901-1029.
[44] M. Kwoka, L. Ottaviano, M. Passacantando, S. Santucci, G. Czempik, J. Szuber, XPS study of the surface chemistry of L-CVD SnO2 thin films after oxidation, Thin Solid Films 490(1) (2005) 36-42.
[45] Stéphane ASTIE, Integration d'un capteur de gaz à oxide semi-conducteur sur silicium, these, LAAS, décembre 1998.
[46] K. G. Godinho, A. Walsh, G. W. Watson, Energetic and electronic structure analysis of intrinsic defects in SnO2. Journal of Physical Chemistry C 113(1) (2009) 439-448
[47] Kittel, Introduction to Solid State Physics 8th edition, page 194-196
[48] Kim, Y. S., Marsman, M., Kresse, G., Tran, F., & Blaha, P. (2010). Towards efficient band structure and effective mass calculations for III-V direct band-gap semiconductors. *Physical Review B, 82*(20), 205212.
[49] J.P. Joly, L. Gonszalez-Cruz, Y. Arnaud, Bulletin de la société chimique de France (1986) p. 11-17.
[50] Rakhshani, A. E., Makdisi, Y., & Ramazaniyan, H. A. (1998). Electronic and optical properties of fluorine-doped tin oxide films. Journal of Applied Physics, 83(2), 1049-1057.
[51] Shanthi, E., Dutta, V., Banerjee, A., & Chopra, K. L. (1980). Electrical and optical properties of undoped and antimony-doped tin oxide films. Journal of Applied Physics, 51(12), 6243-6251.
[52] Spence, W. (1967). The UV absorption edge of tin oxide thin films. Journal of Applied Physics, 38(9), 3767-3770.
[53] Sundaram, K. B., & Bhagavat, G. K. (1981). Optical absorption studies on tin oxide films. Journal of Physics D: Applied Physics, 14(5), 921.
[54] Rahal, A., Benramache, S., & Benhaoua, B. (2013). Preparation of n-type semiconductor SnO2 thin films. Journal of Semiconductors, 34(8), 083002.
[55] B. Harton, Nature, 1999, 400, 797.
[56] M. Misono, C. R. Acad, Sci. Ser. IIc: Chim., 2000, 3, 471.

[57] A. I. Ahmed, S. A. El-Hakam, A. S. Khder and W. S. Abo El-Yazeed, J. Mol. Catal. A Chem., 2013, 366, 99–108.
[58] V. S. Marakatti, P. Manjunathan, A. B. Halgeri and G. V. Shanbhag, Catal. Sci. Technol., 2016, 6,2268–2279.
[59] Z. Zhang, L. Wang, Y. Jin, F. Xiao and S. Wang, Part. Part. Syst. Charact., 2016, 33, 519–523.
[60] A. Bhattacharjee, M. Ahmaruzzaman and T. Sinha, Spectrochim. Acta - Part A Mol. Biomol. Spectrosc., 2015, 136, 751–760.
[61] A. Bhattacharjee and M. Ahmaruzzaman, Mater. Lett., 2015, 145, 74–78.
[62] Y. Sun, F. Lei, S. Gao, B. Pan, J. Zhou and Y. Xie, Angew Chem Int Ed Engl, 2013, 52, 10569–10572.
[63] J. Xu, D. Aili, Q. Li, C. Pan, E. Christensen, J. O. Jensen, W. Zhang, G. Liu, X. Wang and N. J.Bjerrum, J. Mater. Chem. A, 2013, 1, 9737.
[64] Wang, C., Shao, C., Zhang, X., & Liu, Y. (2009). SnO2 nanostructures-TiO2 nanofibers heterostructures: controlled fabrication and high photocatalytic properties. Inorganic Chemistry, 48(15), 7261-7268.
[65] Dou, X., Sabba, D., Mathews, N., Wong, L. H., Lam, Y. M., & Mhaisalkar, S. (2011). Hydrothermal synthesis of high electron mobility Zn-doped SnO2 nanoflowers as photoanode material for efficient dye-sensitized solar cells. Chemistry of Materials, 23(17), 3938-3945.
[66] R. Pan, S. Pan, J. Zhou and Y. Wu, Appl. Surf. Sci., 2009, 255, 3642–3647.
[67] Zhao, Q., Ju, D., Deng, X., Huang, J., Cao, B., & Xu, X. (2015). Morphology-modulation of SnO 2 hierarchical architectures by Zn doping for glycol gas sensing and photocatalytic applications. Scientific reports, 5, 7874.
[68] Sadeghzadeh-Attar, A. (2018). Efficient photocatalytic degradation of methylene blue dye by SnO 2 nanotubes synthesized at different calcination temperatures. Solar Energy Materials and Solar Cells, 183, 16-24.
[69] G. H. Guai, M. Y. Leiw, C. M. Ng and C. M. Li, Adv. Energy Mater., 2012, 2, 334−338.
[70] G. H. Guai, Y. Li, C.M. Ng, C.M. Li and M. B. Chan-Park, Chem. Phys. Chem., 2012, 13,
[71] Ahmad, M. S., Pandey, A. K., & Rahim, N. A. (2017). Advancements in the development of TiO2 photoanodes and its fabrication methods for dye sensitized solar cell (DSSC) applications. A review. Renewable and Sustainable Energy Reviews, 77, 89-108.
[72] Park, K. H., & Dhayal, M. (2009). High efficiency solar cell based on dye sensitized plasma treated nano-structured TiO2 films. Electrochemistry Communications, 11(1), 75-79.
[73] J. J. Teh, S. L. Ting, K. C. Leong, J. Li and P. Chen, ACS Appl. Mater. Interfaces, 2013, 5, 11377−11382
[74] Basu, K., Benetti, D., Zhao, H., Jin, L., Vetrone, F., Vomiero, A., & Rosei, F. (2016). Enhanced photovoltaic properties in dye sensitized solar cells by surface treatment of SnO 2 photoanodes. Scientific reports, 6, 23312.
[75] Milan, R., Selopal, G. S., Epifani, M., Natile, M. M., Sberveglieri, G., Vomiero, A., & Concina, I. (2015). ZnO@ SnO 2 engineered composite photoanodes for dye sensitized solar cells. Scientific reports, 5, 14523.
[76] Xu, Z., Li, T., Liu, Q., Zhang, F., Hong, X., Xie, S., ... & Guo, W. (2018). Controllable and large-scale fabrication of rectangular CuS network films for indium tin oxide-and Pt-free flexible dye-sensitized solar cells. Solar Energy Materials and Solar Cells, 179, 297-304.
[77] Chen, H., Liu, T., Wang, B., Liu, Z., Li, Y., Zhao, Q., ... & Guo, Z. (2018). Highly efficient charge collection in dye-sensitized solar cells based on nanocomposite photoanode filled with indium-tin oxide interlayer. Advanced Composites and Hybrid Materials, 1(2), 356-363.
[78] Wang, Y. C., & Cho, C. P. (2015). Improved performance of dye-sensitized solar cells with patterned fluorine-doped tin oxide electrodes. Energy, 89, 277-282.
[79] Poizot, P., Laruelle, S., Grugeon, S., Dupont, L. & Tarascon, J. M. Nano-sized transition-metaloxides as negative-electrode materials for lithium-ion batteries. Nature 407, 496–499 (2000).
[80] Tarascon, J. M. & Armand, M. Issues and challenges facing rechargeable lithium batteries. Nature 414, 359–367 (2001).
[81] Arico`, A. S., Bruce, P., Scrosati, B., Tarascon, J.-M. & Van Schalkwijk, W. Nanostructured materials for advanced energy conversion and storage devices. Nat. Mater. 4, 366–377 (2005).
[82] P. Meduri, C. Pendyala, V. Kumar, G. U. Sumanasekera and M. K. Sunkara, Nano Lett.,2009, 9, 612-616.
[83] Liu, C., Li, F., Ma, L. P. & Cheng, H. M. Advanced Materials for Energy Storage. Adv. Mater. 22, E28–E62 (2010).
[84] Reddy, M., Subba Rao, G. & Chowdari, B. Metal Oxides and Oxysalts as Anode Materials for Li Ion Batteries. Chem. Rev. 113, 5364–5457 (2013).
[85] Han, S., Jang, B., Kim, T., Oh, S. M. & Hyeon, T. Simple Synthesis of Hollow Tin Dioxide Microspheres and Their Application to Lithium-Ion Battery Anodes. Adv. Funct. Mater. 15, 1845–1850 (2005).

[86] Wen, Z., Wang, Q., Zhang, Q. & Li, J. In Situ Growth of Mesoporous SnO2 on Multiwalled Carbon Nanotubes: A Novel Composite with Porous-Tube Structure as Anode for Lithium Batteries. Adv. Funct. Mater. 17, 2772–2778 (2007).
[87] Chen, J. S.& Lou, X. W. D. SnO2-Based Nanomaterials: Synthesis and Application in Lithium-Ion Batteries. Small 9, 1877–1893 (2013).
[88] Wang, Z., Luan, D., Boey, F. Y. C. & Lou, X. W. Fast formation of SnO2 nanoboxes with enhanced lithium storage capability. J. Am. Chem. Soc. 133, 4738–4741 (2011).
[89] The developments of SnO2/graphene nanocomposites as anode materials for high performance lithium ion batteries: A review Yuanfu Deng a, b, *, Chengcheng Fang c, Guohua Chen b, c, d, **
[90] High capacity and stable all-solid state Li ion battery using SnO2-embedded nanoporous carbon Hiroo Notohara1, Koki Urita1, Hideyuki Yamamura2 & Isamu Moriguchi1
[91] Confined SnO2 quantum-dot clusters in graphene sheets as high-performance anodes for lithium-ion batteries Chengling Zhu1, Shenmin Zhu1, Kai Zhang1, Zeyu Hui1, Hui Pan1, Zhixin Chen2, Yao Li1, Di Zhang1 & Da-Wei Wang3
[92] Paek, S.-M., Yoo, E. & Honma, I. Enhanced cyclic performance and lithium storage capacity of SnO2/graphene nanoporous electrodes with three dimensionally delaminated flexible structure. Nano Lett. 9, 72–75 (2008).
[93] J.Deng, C. Yan, L. Yang, S. Baunack, S. Oswald, H. Wendrock, Y. Mei, and O. G. Schmidt, ACS Nano, 2013, 7, 6948–6954.
[94] J. Sun, L. Xiao, S. Jiang, G. Li, Y. Huang, and J. Geng, Chem. Mater., 2015, 27, 4594–4603
[95] H. Xue, J. Zhao, J. Tang, H. Gong, P. He and H. Zhou, Chem. Eur.J., 2016, 22, 4915–4923.
[96] B. Huang, X. Li, Y. Pei, S. Li, X. Cao, R. C. Masse and G. Cao, Small, 2016, 12, 1945–1955.
[97] F. Lamberti, L. Brigo, M. Favaro, C. Luni, A. Zoso, M. Cattelan, S. Agnoli, G. Brusatin, G. Granozzi, M. Giomo and N. Elvassore, ACS Appl. Mater. Interfaces, 2014, 6, 22769−22777 RSC Advances Page 28 of 44 RSC Advances Accepted Manuscript Published on 15 November 2016. Downloaded by UNIVERSITY OF OTAGO on 15/11/2016 12:40:32.View Article Online DOI: 10.1039/C6RA21444D 29
[98] V. Dharuman, J. H. Hahn, K. Jayakumar and W. Teng, Electrochim. Acta, 2013, 114, 590–597.
[99] N. T. Darwish, Y. Alias and S. M. Khor, Appl. Surf. Sci., 2015, 325, 91–99.
[100] K. Grochowska, K. Siuzdak, J. Karczewski and G.Ľiwiński, Appl. Surf. Sci., 2015, 357, 1684–1691.
[101] H.-K. Seo, S. G. Ansari, S. S. Al-Deyab and Z. A. Ansari, Sensors Actuators B Chem., 2012, 168,149–155.
[102] J. I. A. Rashid, N. A. Yusof, J. Abdullah, U. Hashim and R. Hajian, Mater. Sci. Eng. C, 2014, 45,270–276.
[103] M. K. Patel, J. Singh, M. K. Singh, V. V. Agrawal, S. G. Ansari and B. D. Malhotra, J. Nanosci. Nanotechnol., 2012, 12, 1–8.
[104] Y. Masuda, T. Ohji and K. Kato, ACS Appl. Mater. Interfaces, 2012, 4, 1666–1674.
[105] B. Liu and J. Liu, Langmuir, 2015, 31, 371–377.
[106] Z. Gao and N. C. Tansil, Nucleic Acids Res., 2005, 33, e123.
[107] P. M. Armistead and H. H. Thorp, Anal. Chem., 2000, 72, 3764−3770.
[108] X. Wei, X. Ma, J. J. Sun, Z. Lin, L. Guo, B. Qiu and G. Chen, Anal. Chem., 2014, 86, 3563−3567.
[109] M. K. Patel, J. Singh, M. K. Singh, V. V. Agrawal, S. G. Ansari and B. D. Malhotra, J. Nanosci. Nanotechnol., 2013, 13, 1671−1678.
[110] Q. Qi, T. Zhang, S. Wang and X. Zheng, Sens. Actuators B: Chem., 2009, 137, 649–655.
[111] P. Ivanov, E. Llobet, X. Vilanova, J. Brezmes, J. Hubalek and X. Correig, Sens. Actuators B:Chem.,2004, 99, 201–206.
[112] R. L. Vander Wal, G. W. Hunter, J. C. Xu, M. J. Kulis, G. M. Berger and T. M. Ticich, Sens.Actuators B: Chem., 2009, 138, 113–119.
[113] Efimov, A., Volkov, I., Varfolomeev, A., Vasiliev, A., & Ivanov, V. (2016). Tin Oxide Nanoparticles Produced by Spark Ablation: Synthesis and Gas Sensing Properties. Oriental Journal of Chemistry, 32(6), 2909-2913.
[114] H. Li, W. Xie, T. Ye, B. Liu, S. Xiao, C. Wang, Y. Wang, Q. Li and T. Wang, ACS Appl. Mater.Interfaces, 2015, 7, 24887–24894.
[115] C. O. Park and S. A. Akbar, J. Mater. Sci.2003, 38, 4611-4637.
[116] E. Kanazawa, M. Kugishima, K. Shimanoe, Y. Kanmura, Y. Teraoka, N. Miura, and N. Yamazoe, Sens. Actuators B, 2001, 75, 121-124.
[117] Q. Wang, C. Wang, H. Sun, P. Sun, Y. Wang, J. Lin and G. Lu, Sensors Actuators B Chem., 2016, 222, 257–263.

[118] S. Maeng, S. W. Kim, D. H. Lee, S. E. Moon, K. C. Kim and A. Maiti, ACS Appl. Mater. Interfaces, 2014, 6, 357–363.
[119] H. Zhang, J. Feng, T. Fei, S. Liu and T. Zhang, Sensors Actuators, B Chem., 2014, 190, 472–478.
[120] S. Liu, Z. Wang, Y. Zhang, C. Zhang and T. Zhang, Sensors Actuators, B Chem., 2015, 211, 318–324.
[121] Liu, X., Chen, N., Han, B., Xiao, X., Chen, G., Djerdj, I., & Wang, Y. (2015). Nanoparticle cluster gas sensor: Pt activated SnO 2 nanoparticles for NH 3 detection with ultrahigh sensitivity. Nanoscale, 7(36), 14872-14880.
[122] Saboor, F. H., Ueda, T., Kamada, K., Hyodo, T., Mortazavi, Y., Khodadadi, A. A., & Shimizu, Y. (2016). Enhanced NO2 gas sensing performance of bare and Pd-loaded SnO2 thick film sensors under UV-light irradiation at room temperature. Sensors and Actuators B: Chemical, 223, 429-439.
[123] Li, C., Lv, M., Zuo, J., & Huang, X. (2015). SnO2 highly sensitive CO gas sensor based on quasi-molecular-imprinting mechanism design. Sensors, 15(2), 3789-3800.
[124] Kou, X., Xie, N., Chen, F., Wang, T., Guo, L., Wang, C., ... & Lu, G. (2018). Superior acetone gas sensor based on electrospun SnO2 nanofibers by Rh doping. Sensors and Actuators B: Chemical, 256, 861-869.
[125] Xiao, L., Xu, S., Yu, G., & Liu, S. (2018). Efficient hierarchical mixed Pd/SnO2 porous architecture deposited microheater for low power ethanol gas sensor. Sensors and Actuators B: Chemical, 255, 2002-2010.
[126] Bhatnagar, M., Dhall, S., Kaushik, V., Kaushal, A., & Mehta, B. R. (2017). Improved selectivity of SnO2: C alloy nanoparticles towards H2 and ethanol reducing gases; role of SnO2: C electronic interaction. Sensors and Actuators B: Chemical, 246, 336-343.
[127] Miller, D. R., Williams, R. E., Akbar, S. A., Morris, P. A., & McComb, D. W. (2017). Measuring optical properties of individual SnO 2 nanowires via valence electron energy-loss spectroscopy. Journal of Materials Research, 32(13), 2479-2486.
[128] Peelaers, H., Kioupakis, E., & Van de Walle, C. G. (2012). Fundamental limits on optical transparency of transparent conducting oxides: Free-carrier absorption in SnO2. *Applied Physics Letters*, *100*(1), 011914.
[129] Babu, B., Kadam, A. N., Ravikumar, R. V. S. S. N., & Byon, C. (2017). Enhanced visible light photocatalytic activity of Cu-doped SnO2 quantum dots by solution combustion synthesis. Journal of Alloys and Compounds, 703, 330-336.
[130] Li, S., Yu, L., Man, X., Zhong, J., Liao, X., & Sun, W. (2017). The Synthesis and band gap changes induced by the doping with rare-earth ions in nano-SnO2. Materials Science in Semiconductor Processing, 71, 128-132.
[131] Zhang, M., Xu, M., Li, M., Zhang, Q., Lu, Y., Chen, J., ... & He, Y. (2017). SnO2 epitaxial films with varying thickness on c-sapphire: Structure evolution and optical band gap modulation. Applied Surface Science, 423, 611-618.
[132] Ganose, A. M., & Scanlon, D. O. (2016). Band gap and work function tailoring of SnO 2 for improved transparent conducting ability in photovoltaics. *Journal of Materials Chemistry C*, *4*(7), 1467-1475.
[133] Tsubota, T., Kobayashi, S., Murakami, N., & Ohno, T. (2014). Improvement of Thermoelectric Performance for Sb-Doped SnO 2 Ceramics Material by Addition of Cu as Sintering Additive. *Journal of electronic materials*, *43*(9), 3567-3573.
[134] Poulier, C.; Smith, D.; Absi, J. Thermal Conductivity of Pressed Powder Compacts: Tin Oxide and Alumina. J. Eur, Ceram. Soc. 2007, 27, 475–478.
[135] Fayette, S.; Smith, D.; Smith, A.; Martin, C. Influence of Grain Size on the Thermal Conductivity of Tin Oxide Ceramics. J. Eur, Ceram. Soc. 2000, 20, 297–302.
[136] Kanatzidis, M. G. (2015). Advances in thermoelectrics: From single phases to hierarchical nanostructures and back. Mrs Bulletin, 40(8), 687-695.
[137] He, J., & Tritt, T. M. (2017). Advances in thermoelectric materials research: Looking back and moving forward. Science, 357(6358), eaak9997.
[138] A. I. Vakis, V. A. Yastrebov, J. Scheibert, L. Nicola, D. Dini, C. Minfray, J. F. Molinari. Modeling and simulation in tribology across scales: An overview. *Tribology International*, *125*, 169-199, 2018.
[139] E. Schrödinger. An undulatory theory of the mechanics of atoms and molecules. *Phys. Rev.*, 28, 1049-1070, 1926.
[140] F. Schwabl. Quantenmechanik (QM I): Eine Einführung. *Springer*, 2007.
[141] D.J. Griffiths. Introduction to quantum mechanics. *Pearson international edition*, 2005.
[142] M. Born. On the quantum mechanics of collision processes. *Zeitschrift fuer Physik*, 37, 863-867, 1926.
[143] W. Pauli. The connection between spin and statistics. *Phys. Rev.*, 58,716-722, 1940.
[144] A. Jabs. Connecting spin and statistics in quantum mechanics. *Found. Phys.*, 40, 776-792, 2010.
[145] W. Pauli. On the connexion between the completion of electron groups in an atom with the complex structure of spectra. *Zeitschrift für Physik*, *31*, 765, 1925.
[146] N. Zettili. Quantum Mechanics: Concepts and Applications. Wiley-VCH, 2003.

[147] E. Fermi. Eine statistische methode zur bestimmung einiger eigenschaften des atoms und ihre anwendung auf die theorie des periodischen systems der elemente, *Zeitschrift für Physik*, *48*, 73-79, 1928.
[148] L. H. Thomas. On the capture of electrons by swiftly moving electrified particles. *Proceedings of the Royal Society of London. Series A*, 114, 561-576, 1927.
[149] R. G. Parr, W. Yang. Density-functional theory of atoms and molecules, *OxfordUniversity, New York*., 1989.
[150] E. K. Gross and R. M. Dreizler. Density functional theory. *Springer Science & Business Media*, 337, 2013.
[151] R. G. Parr. Density functional theory. *Annual Review of Physical Chemistry*, 34, 631656, 1983.
[152] T. Ziegler. Approximate density functional theory as a practical tool in molecular energetics and dynamics. *Chem. Rev.*, 91, 651-667, 1991.
[153] P. Geerlings, F. D. Proft, W. Langenaeker. Conceptual density functional theory. *Chem. Rev.*, 103, 1793-1874, 2003.
[154] P. Hohenberg, W. Kohn. Inhomogeneous electron gas. *Phys. Rev.*, 136, B864-B871, 1964.
[155] W. Kohn, L. J. Sham. Self-consistent equations including exchange and correlation effects. *Phys. Rev.*, 140, A1133-A1138, 1965.
[156] A. E. Mattsson. In pursuit of the" divine" functional. *Science*, *298*, 759-760, 2002.
[157] D. M. Ceperley, B. J. Alder. Ground state of the electron gas by a stochastic method. *Phys. Rev. Lett.*, 45, 566-569, 1980.
[158] J. P. Perdew, A. Zunger. Self-interaction correction to density-functional approximations for many-electron systems. *Phys. Rev. B*, 23, 5048, 1981.
[159] J. Harris, R. O. Jones. The surface energy of a bounded electron gas. *Journal of Physics F: Metal Physics*, 4, 1170, 1974.
[160] D. C. Langreth, J. P. Perdew. The exchange-correlation energy of a metallic surface. *Solid State Communications*, 17, 1425-1429, 1975.
[161] J. Harris. Adiabatic-connection approach to kohn-sham theory. *Phys. Rev. A*, 29, 1648, 1984.
[162] J. P. Perdew, Y. Wang. Pair-distribution function and its coupling-constant average for the spin-polarized electron gas. *Phys. Rev. B*, 46, 12947, 1992.
[163] J. P. Perdew, Y. Wang. Accurate and simple analytic representation of the electron-gas correlation energy. *Phys. Rev. B*, 45, 13244, 1992.
[164] S. H. Vosko, L. Wilk, M. Nusair. Accurate spin-dependent electron liquid correlation energies for local spin density calculations: a critical analysis. *Canadian Journal of Physics*, 58, 1200-1211, 1980.
[165] A. D. Becke. Density-functional exchange-energy approximation with correct asymptotic behavior. *Phys. Rev. A*, 38, 3098, 1988.
[166] J. P. Perdew, J. A. Chevary, S. H. Vosko, K. A. Jackson, M. R. Pederson, D. J. Singh, C. Fiolhais. Atoms, molecules, solids, and surfaces: Applications of the generalized gradient approximation for exchange and correlation. *Phys. Rev. B*, 46, 6671, 1992.
[167] J. P. Perdew, K. Burke, M. Ernzerhof. Generalized gradient approximation made simple. *Phys. Rev. Lett.*, 77, 3865, 1996.
[168] Y. Zhang, W. Yang, Comment on "Generalized gradient approximation made simple". *Phys. Rev. Lett.*, *80*, 890, 1998.
[169] B. H. L. B. Hammer, L. B. Hansen, J. K. Nørskov. Improved adsorption energetics within density-functional theory using revised Perdew-Burke-Ernzerhof functionals. *Phys. Rev. B*, 59, 7413, 1999.
[170] J. P. Perdew, A. Ruzsinszky, G. I. Csonka, O. A. Vydrov, G. E. Scuseria, L. A. Constantin, X. Zhou, K. Burke. Restoring the density-gradient expansion for exchange in solids and surfaces. *Phys. Rev. Lett.*, 100, 136406, 2008.
[171] A. Ruzsinszky, G. I. Csonka, G. E. Scuseria. Regularized gradient expansion for atoms, molecules, and solids. *Journal of Chemical Theory and Computation*, 5, 763-769, 2009.
[172] Y. Zhao, D. G. Truhlar. Construction of a generalized gradient approximation by restoring the density-gradient expansion and enforcing a tight Lieb–Oxford bound. *J. Chem. Phys.*, 128, 184109, 2008.
[173] A. D. Becke. Density-functional thermochemistry. III. The role of exact exchange. *J. Chem. Phys.*, 98, 5648, 1993.
[174] J. Heyd, G. E. Scuseria and M. Ernzerhof. *J. Chem. Phys.* 118, 8207, 2003.
[175] A. Svane and O. Gunnarsson, Transition-metal oxides in the self-interaction–corrected density-functional formalism. *Phys. Rev. Lett.* 65, 1148, 1990.
[176] S. Massida, M. Posternak and A. Baldereschi, Hartree-Fock LAPW approach to the electronic properties of periodic systems. *Phys. Rev. B*, 48, 5058, 1993.
[177] L. Hedin, New method for calculating the one-particle Green's function with application to the electron-gas problem. *Phys. Rev.*, 139, A796, 1965.
[178] V. I. Anisimov, F. Aryasetiawan, A. I. Lichtenstein, First-principles calculations of the electronic structure and spectra of strongly correlated systems: the LDA+ U method. *J. Phys. Condens. Matter*, 9, 767, 1997.
[179] J. C. Slater, Quantum Theory of Atomic Structure, *McGraw-Hill, New York*, 1960.

[180] F. M. F. de Groot, J. C. Thole, G. A. Sawatzky, 2p x-ray absorption of 3d transition-metal compounds: An atomic multiplet description including the crystal field. *Phys. Rev. B*, 42, 5459, 1990.
[181] V. I. Anisimov, J. Zaanen, O. K. Andersen, Band theory and Mott insulators: Hubbard U instead of Stoner I. *Phys. Rev. B*, 44, 943, 1991.
[182] M. T. Czyzyk, G. A. Sawatzky, Local-density functional and on-site correlations: the electronic structure of La2CuO4 and LaCuO3. *Phys. Rev. B*, 49, 14211, 1994.
[183] V. I. Anisimov, I. V. Solovyev, M. A. Korotin, M. T. Czyzyk, G. A. Sawatzky, Density-functional theory and NiO photoemission spectra. *Phys. Rev. B*, 48, 16929, 1993.
[184] E. R. Ylvisaker, W. E. Pickett and K. Koepernik, Anisotropy and magnetism in the LSDA+ U method. *Phys. Rev. B*, 79, 035103, 2009.
[185] A. D. Becke, E. R. Johnson. A simple effective potential for exchange. *J. Chem. Phys.*, 124, 221101, 2006.
[186] F. Tran, P. Blaha. Accurate band gaps of semiconductors and insulators with a semilocal exchange-correlation potential. *Phys. Rev. Lett.*, 102, 226401, 2009.
[187] D. Koller, F. Tran, P. Blaha. Merits and limits of the modified Becke-Johnson exchange potential. *Phys. Rev. B*, 83, 195134, 2011.
[188] D. J. Singh. Electronic structure calculations with the Tran-Blaha modified Becke-Johnson density functional. *Phys. Rev. B*, 82, 205102, 2010.
[189] G. D. Mahan. Condensed Matter in a Nutshell, *Princeton University Press*, 2011.
[190] H. J. Monkhorst, J. D. Pack, Special points for Brillouin-zone integrations. *Phys. Rev. B*, 13, 5188, 1976.
[191] S. Blügel, G. Bihlmayer. *NIC series*, 31, 85-129, 2006. URL http://hdl.handle.net/ 2128/2943.
[192] K. Dewhurst, S. Sharma Dewhurst. Development of the Elk LAPW Code.
[193] O. Andersen. Linear methods in band theory. *Phys. Rev. B*, 12, 3060, 1975.
[194] D. Koelling, G. Arbman. Use of energy derivative of the radial solution in an augmented plane wave method: application to copper. *J. Phys. F: Metal Phys.*, 5, 2041, 1975.
[195] D. R. Hamann, M. Schlüter, C. Chiang. Norm-conserving pseudopotentials. *Phys. Rev. Lett.*, 42, 662, 1979.
[196] E. Wimmer, H. Krakauer, M. Weinert, A. J. Freeman. *Phys. Rev. B*, 24, 864, 1981.
[197] E. Sjöstedt, L. Nordström, and D. J. Singh. An alternative way of linearizing the augmented plane-wave method. *Solid State Commun.*, 114, 15-20, 2000.
[198] P. Blaha, K. Schwarz, G. K. Madsen, D. Kvasnicka, J. Luitz. wien2k. An augmented plane wave+ local orbitals program for calculating crystal properties. 2001. (http://susi.theochem.tuwien.ac.at/)
[199] D. Vanderbilt. Soft self-consistent pseudopotentials in a generalized eigenvalue formalism. *Phys. Rev. B*, 41, 7892, 1990.
[200] P. E. Blöchl. Projector augmented-wave method. *Phys. Rev. B*, 50, 17953, 1994.
[201] P. Giannozzi, S. Baroni, N. Bonini, M. Calandra, R. Car, C. Cavazzoni, A. Dal Corso. QUANTUM ESPRESSO: a modular and open-source software project for quantum simulations of materials. *Journal of physics: Condensed matter*, *21*, 395502, 2009. (https://www.quantum-espresso.org/).
[202] G. Kresse, J. Furthmüller. Software VASP. *Phys. Rev. B*, *54*, 169, 1999. (https://www.vasp.at/)
[203] J. Hafner. Ab-initio simulations of materials using VASP: Density-functional theory and beyond. *Journal of computational chemistry*, *29*, 2044-2078, 2008.
[204] A. A. Bolzan, C. Fong, B.1. Kennedy, and C. J. Howard, "Structural studies of rutile-type metal dioxides," Acta Crystallogr., Sect. B: Struct. Sci. 1997, Vol. 53, pp. 373-380.
[205] B. Amin, T. Ahmad, M. Maqbool, S. Goumri-Said, and R. Ahmad, "Ab initio study of the band gap engineering of A11- xGaxN for optoelectronic applications," 1. Appl. Phys. 2011, Vol. 109, p. 023109.
[206] B. Amin, T. Ahmad, M. Maqbool, "Conversion of direct to indirect bandgap and optical response of B substituted InN for novel optical devices applications," J. Lightwave Technol. 2010, Vol. 28, pp. 223-227.
[207] O. Madelung, U. Rössler, M. Schulz, Tin dioxide (SnO_2) band structure, band parameters. Non-Tetrahedrally Bonded Elements and Binary Compounds I. 41C, 1-9.
[208] K. Bakht, T. Mahmood, M. Ahmed, and K. Abid, "Pressure induced electronic and optical properties of rutile SnO 2 b y first principle calculations," Superlattices MicrostrucL 2016, Vol. 90, pp. 236-241.
[209] S. Tingting, Z. Fuchun, and Z. Weihu, "Density Functional Theory Study on the Electronic Structure and Optical Properties of SnO2," Rare Metal Mal. Eng. 2015, Vol. 44, pp. 2409-2414.
[210] H. Wang, Z. M.G ibbs, Y. Takagiwa, and G. J. Snyder, "Tuning bands of PbSe for better thermoelectric efficiency," Energy Environ. Sci. 2014, Vol. 7, pp. 804-811.
[211] R. C. Picu, T. Borca-Tasciuc, and M. C. Pavel, " Strain and size effects on heat transport in nanostructures," J. Appl. Phys. 2003, Vol. 93, pp. 3535-3539.
[212] A. R. Abramson, C. L. Tien, and A. Majumdar, "Interface and strain effects on the thermal conductivity of heterostructures: a molecular dynamics study," 1. Heat Transfer. 2002, Vol. 124, pp. 963-970.
[213] E. J. H. Lee, C. Ribeiro, T. R. Giraldi, E. Longo, E. R. Leite, J. A. Varela. Photoluminescence in quantum-confined SnO2 nanocrystals: evidence of free exciton decay. *Appl. Phys. Lett.* 2004, 84, 1745.
[214] L. W. Wang, J. Li. First-principles thousand-atom quantum dot calculations. *Phys. Rev. B*. 2004, 69, 153302.

[215] M. Zhang, M. Xu, M. Li, Q. Zhang, Y. Lu, J. Chen, Y. He. SnO2 epitaxial films with varying thickness on c-sapphire: Structure evolution and optical band gap modulation. *Appl. Surf. Sci*. 2017, 423, 611-618.
[216] M. Kim, N. Marom, N. Scott Bobbitt, J. R. Chelikowsky. A first-principles study of the electronic and structural properties of Sb and F doped SnO2 nanocrystals. *J. Chem. Phys*. 2015, 142, 044704.
[217] T. Seebeck. Magnetische Polarisation der Metalle und Erze durch Temperatur-Differenz. *Abh. K. Preuss. Akad. Wiss. Berlin.* 265, (1822)
[218] J. C. A. Peltier. Nouvelles expériences sur la caloricité des courant électriques. *Ann. Chim. Phys*. **2**, 371, (1834).
[219] W. Thomson. On a mechanical theory of thermo-electric currents. *Proceedings of the Royal Society of Edinburgh*. (1851), **3**, 91–98.
[220] C. Han, Z. Li, S. Dou. Recent progress in thermoelectric materials. *Chinese science bulletin*. (2014), **59**, 2073-2091.
[221] Y. Chen, X. Hou, C. Ma, Y. Dou, W. Wu. Review of Development Status of Bi2Te3-Based Semiconductor Thermoelectric Power Generation. *Advances in Materials Science and Engineering, 2018*. (2018).
[222] G. J. Snyder, T. S. Ursell, *J. Physics Review Letters*, (2003), 91, 148301.
[223] D.M. Rowe0 Thermoelectrics Handbook - Macro to Nano. *CRC Taylor & Francis, Boca Ratcon.* (2006).
[224] A. F. Ioffe. Semiconductors Thermoelements and Thermoelectric Cooling. *Infosearch Limited*. 39, (1957).
[225] J. Yang, T. Caillat. Thermoelectric materials for space and automotive power generation. *MRS bulletin*, (2006), *31*, 224-229.
[226] G. J. Snyder. Application of the compatibility factor to the design of segmented and cascaded thermoelectric generators. *App. Phys. letters*. (2004), *84*, 2436-2438.
[227] R. Bechtel. Multi-mission radioisotope thermoelectric generator (MMRTG). *NASA Facts*. (2013).
[228] M. Rosenberger, M. Dellner, M. Kluge, K. R. Tarantik. Vehicle integration of a thermoelectric generator. *MTZ worldwide*. (2016). 77, 36-43.
[229] J. Liebl, S. Neugebauer, A. Eder, M. Linde, B. Mazar, W. Stütz. The thermoelectric generator from BMW is making use of waste heat. *MTZ worldwide*, (2009), 70, 4-11.
[230] J. C. Jang, R. G. Chi, S. H. Rhi, K. B. Lee, H. C. Hwang, J. S. Lee, W. H. Lee. Heat pipe-assisted thermoelectric power generation technology for waste heat recovery. *Journal of Electronic Materials*. (2015), *44*(6), 2039-2047.
[231] M. S. Dresselhaus, G. Chen, M. Y. Tang, R. Yang, H. Lee, D. Wang, Z. Ren, J.-P. Fleurial, and P. Gogna. New Directions for Low-Dimensional Thermoelectric Materials. *Advanced Materials*, (2007), 19, 1043-1053.
[232] M. D. Dresselhaus. The evolution of nanothermoelectricity. *MRS Proceedings*, *Cambridge Univ Press*, (2011), 1329, 1.
[233] A. T. Burkov. Measurements of Resistivity and Thermopower: Principles and Practical Realization. *Thermoelectrics Handbook: Macro to* Nano (D. M. Rowe, ed.), *CRC press, Boca Raton.* (2006), 22.
[234] T. M. Tritt. Thermoelectric phenomena, materials, and applications. *Annu. Rev. Mater. Res.*, (2011) 41, 433-448.
[235] T. Krishnakumar, R. Jayaprakash, M. Parthibavarman, A. R. Phani, V. N. Singh, and B. R. Mehta, J. Materials Letters, 63, 896-898 (2009).
[236] E. Shen, C. Wang, E. Wang, Z. Kang, L. Gao, C. Hu, and L. Xu, J. *Materials Letters*, 58, 3761-3764 (2004).
[237] H.J. Snaith, C. Ducati, SnO2 -based dye-sensitized hybrid solar cells exhibiting near unity absorbed photon-to-electron conversion efficiency, *Nano Lett.* 10, (2010), 1259–1265.
[238] Y. Li, W. Yin, R. Deng, R. Chen, J. Chen, Q. Yan, B. Yao, H. Sun, S.-H. Wei, T. Wu, Realizing a SnO2-based ultraviolet light-emitting diode via breaking the dipole-forbidden rule, *NPG Asia Mater*. 4, (2012), 30.
[239] Poulier, D. Smith, J. Absi, Thermal conductivity of pressed powder compacts: tin oxide and alumina, *J. Eur. Ceram. Soc.* 27, (2007), 475–478.
[240] S. Fayette, D. Smith, A. Smith, C. Martin, Influence of grain size on the thermal conductivity of tin oxide ceramics, *J. Eur. Ceram. Soc.* 20, (2000), 297–302.
[241] S. Yanagiya, N.V. Nong, J. Xu, M. Sonne, N. Pryds, Thermoelectric properties of SnO2 ceramics doped with Sb and Zn, *J. Electron. Mater.* 40, (2011), 674–677.
[242] S. Yanagiya, N.V. Nong, M. Sonne, N. Pryds, Thermoelectric properties of SnO2-based ceramics doped with Nd, Hf or Bi, AIP *Conf. Proc.* 1449, (2012), 327–330.
[243] T.T.X. Vo, T.N.H. Le, Q.N. Pham, C. Byl, D. Dragoe, M.-G. Barthes-Labrousse, D. Berardan, N. Dragoe, Preparation and study of the thermoelectric properties of nanocrystalline Sn1−xTaxO2($0 \le x \le 0.04$), *Phys. Status Solidi*, 212, (2015), 2776–2784.
[244] O. Mounkachi, E. Salmani, M. Lakhal, H. Ez-Zahraouy, M. Hamedoun, M. Benaissa, A. Kara, A. Ennaoui, A. Benyoussef, Band-gap engineering of SnO2, *Sol. Energy Mater. Sol. Cells*, 148, (2016), 34–38.
[245] M.M. Soumelidou, I. Belabbas, J. Kioseoglou, P. Komninou, J. Chen, T. Karakostas, Strain and elastic constants of GaN and InN, *Computational Condensed Matter*, 10, (2017), 25–30.

[246] M. Hajji, H. Absike, H. Labrim, H. Ez-Zahraouy, M. Benaissa, A. Benyoussef, Strain effects on the electronic and thermoelectric properties of Bi2Te3: a first principles study, *Computational Condensed Matter*, 16, (2018).
[247] H. Absike, M. Hajji, H. Labrim, B. Hartiti, H. Ez-Zahraouy, Strain effects on the electronic and thermoelectric properties of copper oxide, *Computational Condensed Matter*, 16, (2018), e00322.
[248] Feneberg, M., Lidig, C., Lange, K., White, M. E., Tsai, M. Y., Speck, J. S., ... & Goldhahn, R. Anisotropy of the electron effective mass in rutile SnO2 determined by infrared ellipsometry. *physica status solidi (a)*, (2014), 211(1), 82-86.
[249] Wang, J.; Zhao, R.; Yang, M.; Liu, Z.; Liu, Z. Inverse Relationship between Carrier Mobility and Bandgap in Graphene. *J. Chem. Phys.*, (2013), 138, 084701.
[250] G.K. Madsen, D.J. Singh, BoltzTraP. A code for calculating band-structure dependent quantities, *Comput. Phys. Commun.* 175, (2006), 67–71.
[251] D. Parker, D.J. Singh, Thermoelectric properties of AgGaTe 2 and related chalcopyrite structure materials, *Phys. Rev. B*, 85, (2012), 125209.
[252] D. Zou, S. Xie, Y. Liu, J. Lin, J. Li, Electronic structures and thermoelectric properties of layered BiCuOCh oxychalcogenides (ch = S, Se and Te): first-principles calculations, *J. Mater. Chem.* 1, (2013), 8888–8896.
[253] W. Wu, K. Wu, Z. Ma, R. Sa, Doping and temperature dependence of thermoelectric properties of AgGaTe2: first principles investigations, *Chem. Phys. Lett.* 537, (2012), 62–64
[254] W. Li, G. Zhang, M. Guo, Y.-W. Zhang, Strain-tunable electronic and transport properties of MoS2 nanotubes, *Nano Research*, 7, (2014), 518–527.
[255] Y. Pei, A.D. Lalonde, H. Wang, G.J. Snyder, Low effective mass leading to high thermoelectric performance, *Energy Environ. Sci.* 5, (2012), 7963–7969.
[256] J. Wang, R. Zhao, M. Yang, Z. Liu, Z. Liu, Inverse relationship between Carrier mobility and bandgap in graphene, *J. Chem. Phys*. 138, (2013), 084701.
[257] L.D. Zhao, S.H. Lo, Y. Zhang, H. Sun, G. Tan, C. Uher, M.G. Kanatzidis, Ultralow thermal conductivity and high thermoelectric figure of merit in SnSe crystals, *Nature*, 508, (2014), 373–377.
[258] L. Sun, W.L. Luan, T.C. Wang, W.X. Su, L.X. Zhang, Room-temperature CO thermoelectric gas sensor based on Au/Co3O4 catalyst tablet, *Nanotechnology*, 28, (2017), 075501
[259] World Energy Outlook 2017, Available from https://www.iea.org/weo2017/.
[260] M. N. Chong, B. Jin, C. W. Chow, C. Saint. Recent developments in photocatalytic water treatment technology: a review. *Water Res*. 2010, 44, 2997-3027.
[261] M. T. Amin, A. A. Alazba, U. Manzoor. A review of removal of pollutants from water/wastewater using different types of nanomaterials. *Adv. Mater. Sci. Eng*. 2014.
[262] R. Daghrir, P. Drogui, D. Robert. Photoelectrocatalytic technologies for environmental applications. *J. Photochem. Photobiol. A: Chemistry*. 2012, 238, 41-52.
[263] S. T. Martin, H. Herrmann, W. Choi and M. R. Hoffmann, Journal of the Chemical Society, Faraday Transactions, 1994, 90, 3315-3322.
[264] S. T. Martin, H. Herrmann and M. R. Hoffmann, J. Chem. Soc., Faraday Trans., 1994, 90, 3323-3330.
[265] A. L. Linsebigler, G. Lu and J. T. Yates Jr, Chemical Reviews, 1995, 95, 735-758.
[266] H. Park, H. I. Kim, G. H. Moon, W. Choi. Photoinduced charge transfer processes in solar photocatalysis based on modified TiO2. *Energy & Environmental Science*. 2016, *9*, 411-433.
[267] J. Xu, Y. Teng, F. Teng. Effect of surface defect states on valence band and charge separation and transfer efficiency. *Scientific reports*. 2016, 6.
[268] A. Fujishima, & K. Honda. Electrochemical photolysis of water at a semiconductor electrode. Nature. 1972, 238, 37-38.
[269] A. Fujishima, & K. Honda. Electrochemical evidence for the mechanism of the primary stage of photosynthesis. Bull. Chem. Soc. Jpn. 1971, 44, 1148-1150.
[270] S. U. Khan, M. Al-Shahry, & W. B. Ingler. Efficient photochemical water splitting by a chemically modified n-TiO2. *Science*. 2002, 297, 2243-2245.
[271] Z. Zou, J. Ye, K. Sayama, & H. Arakawa. Direct splitting of water under visible light irradiation with an oxide semiconductor photocatalyst. *Nature*. 2001, 414, 625-627.
[272] X. SHI, H. JEONG, S. J. OH, et al. Unassisted photoelectrochemical water splitting exceeding 7% solar-to-hydrogen conversion efficiency using photon recycling. *Nat. Commun*. 2016, 7.
[273] S. Jeong, J. Song, S. Lee. Photoelectrochemical Device Designs toward Practical Solar Water Splitting: A Review on the Recent Progress of BiVO4 and BiFeO3 Photoanodes. *Applied Sciences*, 2018, 8, 1388.
[274] Y. Qu, & X. Duan Progress, challenge and perspective of heterogeneous photocatalysts. *Chem. Soc. Rev*. 2013, 42, 2568-2580.
[275] O. Carp, C. L. Huisman, & A. Reller. Photoinduced reactivity of titanium dioxide. *Prog. Solid State Chem*. 2004, 32, 33-177.

[276] A. Fujishima, T. N. Rao, & D. A. Tryk. Titanium dioxide photocatalysis. *J. Photochem. Photobiol., C*. 2000, 1, 1-21.
[277] T. Ibusuki, K. Takeuchi, Removal of low concentration nitrogen oxides through photoassisted heterogeneous catalysis, Journal of Molecular Catalysis, 88, 1994, 93-102.
[278] N. Negishi, K. Takeuchi, T. Ibusuki, Surface structure of the TiO2 thin film photocatalyst, Journal of Materials Science, 33, 1998, 5789-5794.
[279] P. Yaron, Application of TiO2 photocatalysis for air treatment: Patents' overview, Applied Catalysis B: Environmental, 99, 2010, 448-460.
[280] P. Pichat, J. Disdier, C. Hoang-Van, D. Mas, G. Goutailler, C. Gaysse, Purification/deodorization of indoor air and gaseous effluents by TiO2photocatalysis, Catalysis today, 63, 2000, 363-369.
[281] O. d'Hennezel, D.F. Ollis, Trichloroethylene-Promoted Photocatalytic Oxidation of Air Contaminants, Journal of Catalysis, 167, 1997, 118-126.
[282] M.L. Sauer, M.A. Hale, D.F. Ollis, Heterogenous photocatalytic oxidation of dilute toluene-chlorocarbon mixtures in air, Journal of Photochemistry and photobiology A: Chemistry, 88, 1995, 169-178.
[283] J. Peral, D.F. Ollis, Heterogeneous photocatalytic oxidation of gas-phase organics for air purification: Acetone, 1-butanol, butyraldehyde, formaldehyde, and m-xylene oxidation, Journal of Catalysis, 136, 1992, 554-565.
[284] X. Ding, S. Zhou, L. Wu, G. Gu, J. Yang, Formation of supra-amphiphilic self-cleaning surface through sun-illumination of titania-based nanocomposite coatings, Surface and Coatings Technology, 205, 2010, 2554-2561.
[285] H. Sakai, R. Baba, K. Hashimoto, Y. Kubota, A. Fujishima, Selective killing of a single cancerous T24 cell with TiO2 semiconducting microelectrode under irradiation, Chem. Lett. 1995, 185-186.
[286] R. Cai, K. Hashimoto, Y. Kubota, A. Fujishima, Increment of photocatalytic killing of cancer cells using TiO2 with the aid of superoxide dismutase, Chem. Lett 1992, 427-430.
[287] A. Kudo, Photocatalysis and solar hydrogen production, Pure Appl. Chem 79, 2007, 1917-1927.
[288] J.S. Hubbard, J.P. Hardy, G.E. Voecks, E.E. Golub, Photocatalytic synthesis of organic compounds from CO and water: Involvement of surfaces in the formation and stabilization of products, Journal of Molecular Evolution, 2, 1973, 149-166.
[289] Hydrogen production and uses Adapted from 2011connaissancedesenergies.com, from AFHYPAC—UE, Available from https://www.connaissancedesenergies.org/fiche-pedagogique/hydrogene-energie
[290] Space Applications of Hydrogen and Fuel Cells, Available from https://www.nasa.gov/content/space-applications-of-hydrogen-and-fuel-cells.
[291] J. Maida. Global Industrial Gases Market for Glass Industry 2017-2021, *Technavio Research*, 2017
[292] J. Liqiang, S. Xiaojun, S. Jing, C. Weimin, X. Zili, D. Yaoguo, & F. Honggang. Review of surface photovoltage spectra of nano-sized semiconductor and its applications in heterogeneous photocatalysis. *Sol. Energ. Mat. Sol. Cells*. 2003, 79, 133-151.
[293] T. Tachikawa, M. Fujitsuka, & T. Majima. Mechanistic insight into the TiO2 photocatalytic reactions: design of new photocatalysts. *J. Phys. Chem. C*. 2007, 111, 5259-5275.
[294] A. K. Chandiran, M. Abdi-Jalebi, M. K. Nazeeruddin, M. Grätzel. Analysis of electron transfer properties of ZnO and TiO2 photoanodes for dye-sensitized solar cells. *ACS Nano*. 2014, 8, 2261-2268.
[295] P. Tiwana, P. Docampo, M. B. Johnston, H. J. Snaith, L. M. Herz. Electron mobility and injection dynamics in mesoporous ZnO, SnO2, and TiO2 films used in dye-sensitized solar cells. *ACS Nano*. 2011, 5, 5158-5166.
[296] C. G. Fonstad, R. H. Rediker. Electrical properties of high-quality stannic oxide crystals. *Journal of applied physics*. 1971, 42, 2911-2918.
[297] L. Zhu, M. Hong, G. W. Ho. Hierarchical assembly of SnO2/ZnO nanostructures for enhanced photocatalytic performance. *Sci. rep*. 2015, 5, 11609.
[298] A. Kar, A. Patra. Recent development of core–shell SnO2 nanostructures and their potential applications. *J. Mater. Chem. C*. 2014, *2*, 6706-6722
[299] M. M. Khan, S. A. Ansari, M. E. Khan, M. O. Ansari, B. K. Min, M. H. Cho. Visible light-induced enhanced photoelectrochemical and photocatalytic studies of gold decorated SnO2 nanostructures. *New J. Chem.* 2015, 39, 2758-2766.
[300] Z. Zhang, C. Gao, Z. Wu, W. Han, Y. Wang, W. Fu, E. Xie. Toward efficient photoelectrochemical water-splitting by using screw-like SnO2 nanostructures as photoanode after being decorated with CdS quantum dots. *NANO ENERGY*. 2016, 19, 318-327.
[301] L. Zhu, M. Hong, G. W. Ho. Hierarchical assembly of SnO2/ZnO nanostructures for enhanced photocatalytic performance. *Sci. rep*. 2015, 5, 11609.
[302] V. Stevanović, S. Lany, D. S. Ginley, W. Tumas, & A. Zunger. Assessing capability of semiconductors to split water using ionization potentials and electron affinities only. Phys. Chem. Chem. Phys. 2014, 16, 3706-3714.
[303] Li, X., Yu, J., & Jaroniec, M. (2016). Hierarchical photocatalysts. Chemical Society Reviews, 45(9), 2603-2636.

[304] Zhang, M., Xu, M., Li, M., Zhang, Q., Lu, Y., Chen, J., ... & He, Y. (2017). SnO2 epitaxial films with varying thickness on c-sapphire: Structure evolution and optical band gap modulation. Applied Surface Science, 423, 611-618.
[305] Rus, S. F., Ward, T. Z., & Herklotz, A. (2016). Strain-induced optical band gap variation of SnO 2 films. Thin Solid Films, 615, 103-106.
[306] H. Dong, G. Zeng, L. Tang, C. Fan, C. Zhang, X. He, Y. He. An overview on limitations of TiO2-based particles for photocatalytic degradation of organic pollutants and the corresponding countermeasures. *Water Res.* 2015, 79, 128-146.
[307] A. Di Mauro, M. Cantarella, G. Nicotra, G. Pellegrino, A. Gulino, M. V. Brundo, G. Impellizzeri. Novel synthesis of ZnO/PMMA nanocomposites for photocatalytic applications. *Sci. rep*. 2017, 7, 40895.
[308] A. Shokuhfar, M. Alzamani, E. Eghdam, M. Karimi, S. Mastali. SiO2-TiO2 Nanostructure Films on Windshields Prepared by Sol-Gel Dip-Coating Technique for Self-Cleaning and Photocatalytic Applications. *J. Nanosci. Nanotechnol*. 2012, 2, 16-21.
[309] S. Abanades, P. Charvin, F. Lemont, G. Flamant. Novel two-step SnO2/SnO water-splitting cycle for solar thermochemical production of hydrogen. *Int. J. Hydrog. Energy*. 2008, 33, 6021-6030.
[310] O. Madelung, U. Rössler, M. Schulz, Tin dioxide (SnO_2) band structure, band parameters. Non-Tetrahedrally Bonded Elements and Binary Compounds I. 41C, 1-9.
[311] E. J. H. Lee, C. Ribeiro, T. R. Giraldi, E. Longo, E. R. Leite, J. A. Varela. Photoluminescence in quantum-confined SnO2 nanocrystals: evidence of free exciton decay. *Appl. Phys. Lett.* 2004, 84, 1745.
[312] M. Kim, N. Marom, N. Scott Bobbitt, J. R. Chelikowsky. A first-principles study of the electronic and structural properties of Sb and F doped SnO2 nanocrystals. *J. Chem. Phys*. 2015, 142, 044704.
[313] M. T. Uddin, Y. Sultana, & M. A. Islam. Nano-sized SnO_2 photocatalysts: synthesis, characterization and their application for the degradation of methylene blue dye. *J Sci Res*. 2016, 8, 399-411.
[314] Global Burden of Disease Collaborative Network. Global Burden of Disease Study 2016 (GBD 2016) Results. Seattle, United States: Institute for Health Metrics and Evaluation (IHME), 2017. www.ourworldindata.org/air-pollution
[315] WHO (2014) – Fact sheet N°292 – Household air pollution and health. Updated March 2014. Available in https://www.who.int/en/news-room/fact-sheets/detail/household-air-pollution-and-health
[316] B. A. Wittenberg, J. B. Wittenberg. Effects of carbon monoxide on isolated heart muscle cells. *Research report (Health Effects Institute)*, (62), 1-12, 1993.
[317] S. K. Pandey, K. H. Kim, K. T. Tang. A Review of Sensor-Based Methods for Monitoring Hydrogen Sulfide, TrAC, *Trends Anal. Chem.*, 32, 87−99, 2012.
[318] N. Docquier, S. Candel. Combustion control and sensors: a review, *Progress in Energy and Combustion Science*, 28, 107-150, 2002.
[319] R. Moos. A Brief Overview on Automotive Exhaust Gas Sensors Based on Electroceramics, *Int. J. Appl. Ceram. Technol.*, 2, 401- 413, 2005.
[320] M. Folke, L. Cernerud, M. Ekstrom, B. Hok, Critical review of non-invasive respiratory monitoring in medical care, *Med. Bio. Eng. Comput.*, 41, 377-383, 2003.
[321] Solid State Gas Sensors - Industrial Application, M. Fleischer, M. Lehmann (Eds.), Springer, Berlin Heidelberg, 2012.
[322] R. A. Potyrailo, C. Surman, N. Nagraj, A. Burns. Materials and Transducers Toward Selective Wireless Gas Sensing, *Chemical Reviews*, 111, 7315-7354, 2011
[323] Transparency Market Research, Gas Sensors Market - Global Industry Size, Share, Trends, Analysis And Forecast, 2012-2018, 2013.
[324] J. Chou, Hazardous Gas Monitors - A Practical Guide to Selection, Operation and Applications. *McGraw-Hill and SciTech Publishing*, 1999.
[325] N. Taguchi, GAS DETECTING ELEMENT AND METHOD OF MAKING IT, in: U.S. Patent (Ed.), 3 644 795, 1970.
[326] N. Taguchi, in: J. Patent (Ed.), 45-38200, 1962.
[327] X. Liu, S. Cheng, H. Liu, S. Hu, D. Zhang, H. Ning. A survey on gas sensing technology. *Sensors*, *12*, 9635-9665, 2012.
[328] G. F. Fine, L. M. Cavanagh, A. Afonja, R. Binions. Metal oxide semi-conductor gas sensors in environmental monitoring. *sensors*, *10*, 5469-5502, 2010.
[329] A. Vergara, E. Llobet. Sensor selection and chemo-sensory optimization: toward an adaptable chemo-sensory system. *Frontiers in neuroengineering*, *4*, 19, 2012.
[330] S. Sharma, M. Madou. A new approach to gas sensing with nanotechnology. *Philosophical Transactions of the Royal Society A: Mathematical, Physical and Engineering Sciences*, *370*, 2448-2473, 2012.

[331] F. E. Annanouch, Z. Haddi, S. Vallejos, P. Umek, P. Guttmann, C. Bittencourt, E. Llobet. Aerosol-Assisted CVD-Grown WO3 Nanoneedles Decorated with Copper Oxide Nanoparticles for the Selective and Humidity-Resilient Detection of H2S. *ACS Applied Materials & Interfaces*, *7*, 6842-6851, 2015.
[332] Rothschild, A.; Komem, Y., The effect of grain size on the sensitivity of nanocrystalline metal-oxide gas sensors. *Journal of Applied Physics*, *95* (11), 6374-6380, 2004.
[333] M. E. Franke, T. J. Koplin, U. Simon. Metal and Metal Oxide Nanoparticles in Chemiresistors: Does the Nanoscale Matter. *Small*, 2, 36-50, 2006.
[334] E.M. Freer, O. Grachev, X. Duan, S. Martin, D.P. Stumbo. High-yield self-limiting single-nanowire assembly with dielectrophoresis, *Nat. Nano*, 5, 525-530, 2010.
[335] A. C. Romain, J. Nicolas. Long term stability of metal oxide-based gas sensors for e-nose environmental applications: An overview. *Sensors and Actuators B: Chemical*, *146*, 502-506, 2010.
[336] G. Korotcenkov, B. K. Cho. Instability of metal oxide-based conductometric gas sensors and approaches to stability improvement (short survey). *Sensors Actuators, B Chem*. 156, 527–538, 2011.
[337] A. Labidi, E. Gillet, R. Delamare, M. Maaref, K. Aguir. Ethanol and ozone sensing characteristics of WO3 based sensors activated by Au and Pd. *Sens. Actuators B Chem.*, 120, 338–345, 2006
[338] R.S. Khadayate, M. T. Chaudhari, S. K. Disawal, P. P. Patil. Sensing behavior printed WO3 thick films for four organic vapors. *Invertis J. Sci. Technol.*, 2, 185–189, 2009.
[339] P. P. Sahay, S. Tewari, S. Jha, M. Shamsuddin. Sprayed ZnO thin films for ethanol sensors. *J. Mater. Sci.*, 4791–4793, 2005.
[340] L. Mädler, T. Sahm, A. Gurlo, J. D. Grunwaldt, N. Barsan, U. Weimar, S. E. Pratsinis. Sensing low concentrations of CO using flame-spray-made Pt/SnO2 nanoparticles. *J. Nanopart. Res.*, 8, 783–796, 2006.
[341] A. A. Firooz, A. R. Mahjoub, A. A. Khodadadi. Highly sensitive CO and ethanol nanoflower-like SnO2 sensor among various morphologies obtained by using single and mixed ionic surfactant templates. *Sens. Actuators B Chem.*, 141, 89–96, 2009.
[342] N. Singh, A. Ponzoni, R. K. Gupta, P. S. Lee, E. Comini. Synthesis of In2O3–ZnO core–shell nanowires and their application in gas sensing. *Sens. Actuators B Chem.*, 160, 1346–1351, 2011.
[343] M. H. Seo, M. Yuasa, T. Kida, J. S. Huh, N. Yamazoe, K. Shimanoe. Microstructure control of TiO2 nanotubular films for improved VOC sensing. *Sens. Actuators B Chem.*, 154, 251–256, 2011.
[344] H. J. Kim, J. H. Lee. Highly sensitive and selective gas sensors using p-type oxide semiconductors: Overview. *Sens. Actuators B Chem.*, 192, 607–627, 2014.
[345] R. L. Vander Wal, G. W. Hunter, J. C. Xu, M. J. Kulis, G. M. Berger, T. M. Ticich. Metal-oxide nanostructure and gas-sensing performance. *Sens.Actuators B: Chem.*, 138, 113–119, 2009.
[346] H. Li, W. Xie, T. Ye, B. Liu, S. Xiao, C. Wang, Y. Wang, Q. Li and T. Wang. Temperature-dependent abnormal and tunable pn response of tungsten oxide–tin oxide based gas sensors. *ACS Appl. Mater. & Interfaces*, 7, 24887–24894, 2015.
[347] C. O. Park and S. A. Akbar. Ceramics for chemical sensing. *J. Mater. Sci.*, 38, 4611-4637, 2003.
[348] E. Kanazawa, M. Kugishima, K. Shimanoe, Y. Kanmura, Y. Teraoka, N. Miura, and N. Yamazoe. Mixed-potential type N2O sensor using stabilized zirconia-and SnO2-based sensing electrode. *Sens. Actuators B*, 75, 121-124, 2001.
[349] A. Kolmakov, Y. Zhang, G. Cheng, M. Moskovits. Detection of CO and O2 using tin oxide nanowire sensors. *Adv. Mater.*, 15, 997–1000, 2003.
[350] Q. Wang, C. Wang, H. Sun, P. Sun, Y. Wang, J. Lin and G. Lu. Microwave assisted synthesis of hierarchical Pd/SnO2 nanostructures for CO gas sensor. *Sensors Actuators B Chem.*, 222, 257–263, 2016.
[351] S. Maeng, S. W. Kim, D. H. Lee, S. E. Moon, K. C. Kim and A. Maiti. SnO2 nanoslab as NO2 sensor: identification of the NO2 sensing mechanism on a SnO2 surface. *ACS Appl. Mater. & Interfaces*, 6, 357–363, 2014.
[352] X. Du, S. M. George. Thickness dependence of sensor response for CO gas sensing by tin oxide films grown using atomic layer deposition. *Sens. Actuators B Chem*., 135, 152–160, 2008.
[353] H. Zhang, J. Feng, T. Fei, S. Liu and T. Zhang. Enhancing NO2 gas sensing performances at room temperature based on reduced graphene oxide-ZnO nanoparticles hybrid. *Sensors Actuators, B Chem.*, 190, 472–478, 2014.
[354] S. Liu, Z. Wang, Y. Zhang, C. Zhang and T. Zhang. High performance room temperature NO2 sensors based on reduced graphene oxide-multiwalled carbon nanotubes-tin oxide nanoparticles hybrids. *Sensors Actuators, B Chem.*, 211, 318–324, 2015.
[355] X. Liu, N. Chen, B. Han, X. Xiao, G. Chen, I. Djerdj, Y. Wang. Nanoparticle cluster gas sensor: Pt activated SnO2 nanoparticles for NH3 detection with ultrahigh sensitivity. *Nanoscale*, 7, 14872-14880, 2015.

[356] F. H. Saboor, T. Ueda, K. Kamada, T. Hyodo, Y. Mortazavi, A. A. Khodadadi, Y. Shimizu. Enhanced NO2 gas sensing performance of bare and Pd-loaded SnO2 thick film sensors under UV-light irradiation at room temperature. *Sensors and Actuators B: Chemical*, 223, 429-439, 2016.
[357] C. Li, M. Lv, J. Zuo, X. Huang. SnO2 highly sensitive CO gas sensor based on quasi-molecular-imprinting mechanism design. *Sensors*, 15, 3789-3800, 2015.
[358] X. Kou, N. Xie, F. Chen, T. Wang, L. Guo, C. Wang, G. Lu. Superior acetone gas sensor based on electrospun SnO2 nanofibers by Rh doping. *Sensors and Actuators B: Chemical*, 256, 861-869, 2018.
[359] L. Xiao, S. Xu, G. Yu, S. Liu. Efficient hierarchical mixed Pd/SnO2 porous architecture deposited microheater for low power ethanol gas sensor. *Sensors and Actuators B: Chemical*, 255, 2002-2010, 2018.
[360] M. Bhatnagar, S. Dhall, V. Kaushik, A. Kaushal, B. R. Mehta. Improved selectivity of SnO2: C alloy nanoparticles towards H2 and ethanol reducing gases; role of SnO2: C electronic interaction. *Sensors and Actuators B: Chemical*, 246, 336-343, 2017.
[361] S. P. Bates, G. Kresse, and M. J. Gillan. A systematic study of the surface energetics and structure of TiO2 (110) by first-principles calculations. *Surf. Sci.* 385, 386, 1997.
[362] J. Oviedo and M. J. Gillan. The energetics and structure of oxygen vacancies on the SnO2 (110) surface. *Surf. Sci.* 467, 35, 2000.
[363] J. Oviedo and M. J. Gillan. Reconstructions of strongly reduced SnO2 (1 1 0) studied by first-principles methods. *Surf. Sci.* 513, 26, 2002.
[364] L. S. Roman, R. Valaski, C. D. Canestraro, E. C. S. Magalhaes, C. Persson, R. Ahuja, E. F. da Silva, I. Pepe, A. F. da Silva. Optical band-edge absorption of oxide compound SnO2. *Appl. Surf. Sci.* 252, 5361, 2006.
[365] M. Batzill. Surface science studies of gas sensing materials: SnO2. *Sensors*, *6*, 1345-1366, 2006.
[366] M. Batzill and U. Diebold. The surface and materials science of tin oxide. *Progress in surface science*, *79*, 47-154, 2005.
[367] M. Batzill, K. Katsiev, U. Diebold, Surface morphologies of SnO2 (110). *Surface science*, 529, 295-311, 2003.
[368] M. Batzill, K. Katsiev, J. M. Burst, U. Diebold, A. M. Chaka, B. Delley. Gas-phase-dependent properties of SnO2 (110),(100), and (101) single-crystal surfaces: Structure, composition, and electronic properties. *Phys. Rev. B*, 72, 165414, 2005.
[369] J. D. Prades, A. Cirera, J. R. Morante, J. M. Pruneda, P. Ordejón. Ab initio study of NOx compounds adsorption on SnO2 surface. *Sensors and Actuators B: Chemical*, *126*, 62-67, 2007.
[370] Y. Duan. Electronic properties and stabilities of bulk and low-index surfaces of SnO in comparison with Sn O 2: A first-principles density functional approach with an empirical correction of van der Waals interactions. *Physical Review B*, *77*, 045332, 2008.
[371] L. Mahdavian. Highly sensitive SnO2 (100) nano-crystal CH3OH/C2H5OH gas sensor operating at different temperatures: Monte Carlo studies. *Journal of Computational and Theoretical Nanoscience*, *8*, 2356-2361, 2011.
[372] L. Mahdavian. Thermodynamic study of alcohol on SnO2 (100)-based gas nano-sensor. *Physics and Chemistry of Liquids*, *49*, 626-638, 2011.
[373] M. Batzill, K. Katsiev, J. M. Burst, Y. Losovyj, W. Bergermayer, I. Tanaka, U. Diebold. Tuning surface properties of SnO2 (1 0 1) by reduction. *Journal of Physics and Chemistry of Solids*, *67*, 1923-1929, 2006.
[374] J. M. Ducéré, A. Hemeryck, A. Estève, M. D. Rouhani, G. Landa, P. Ménini, B. Chaudret. A computational chemist approach to gas sensors: Modeling the response of SnO2 to CO, O2, and H2O Gases. *Journal of computational chemistry*, *33*, 247-258, 2012.
[375] Lu, Z., Ma, D., Yang, L., Wang, X., Xu, G., & Yang, Z. (2014). Direct CO oxidation by lattice oxygen on the SnO 2 (110) surface: a DFT study. *Physical Chemistry Chemical Physics*, *16*(24), 12488-12494.
[376] Wang, X., Qin, H., Chen, Y., & Hu, J. (2014). Sensing mechanism of SnO2 (110) surface to CO: density functional theory calculations. *The Journal of Physical Chemistry C*, *118*(49), 28548-28561.
[377] D. Ma, Z. Lu, Y. Tang, T. Li, Z. Tang, Z. Yang. Effect of lattice strain on the oxygen vacancy formation and hydrogen adsorption at CeO2 (111) surface. *Physics Letters A*, 378, 2570-2575, 2014.